

Institut für Physik  
der Technischen Universität München  
Lehrstuhl Prof. Dr. W. Götze

# Asymptotic Laws near Higher-Order Glass-Transition Singularities

Matthias Sperl

Vollständiger Abdruck der von der Fakultät für Physik der Technischen Universität München zur Erlangung des akademischen Grades eines  
**Doktors der Naturwissenschaften (Dr. rer. nat.)**  
genehmigten Dissertation.

Vorsitzender: Univ.-Prof. Dr. W. Petry  
Prüfer der Dissertation: 1. Univ.-Prof. Dr. W. Götze  
2. Univ.-Prof. Dr. J. L. van Hemmen

Die Dissertation wurde am 3. April 2003 bei der Technischen Universität München eingereicht und durch die Fakultät für Physik am 3. Juni 2003 angenommen.



# Contents

List of Figures	5
List of abbreviations, acronyms and symbols	7
Chapter 1. Introduction	9
Chapter 2. Equations of motion	13
1. Density-autocorrelation function	13
2. Glass-transition singularities	16
3. Coupled quantities	17
Chapter 3. Static-structure factors	19
1. Static-structure factor and Wiener-Hopf factorization	19
2. Structure factors for short-ranged attraction within MSA	21
3. Structure factors for short-ranged interaction within PYA	25
4. Remarks	27
Chapter 4. Glass-transition diagrams	29
1. Glass-transition diagram of the SWS	29
2. Glass-transition diagrams for different potentials	36
3. Reentry phenomenon	41
Chapter 5. Asymptotic expansions	45
1. General formulas	45
2. Logarithmic decay	49
3. Critical decay at an $A_3$ -singularity	54
4. Critical decay at an $A_4$ -singularity	59
5. $A_2$ -singularity and coupled quantities	61
6. Dynamics in a one-component model	65
7. Dynamics in a two-component model	72
Chapter 6. Logarithmic relaxation in the SWS	87
1. Logarithmic decay at the $A_4$ -singularity	87
2. Subdiffusive power law in the MSD	95
3. Logarithmic decay at an $A_3$ -singularity	98
4. Critical decay at higher-order singularities	101
Chapter 7. Line crossing in the SWS	107
1. MSD at a crossing	107
2. Correlation function at a crossing	115
Chapter 8. Experimental aspects	121

1. Depletion Attraction	121
2. Reentry phenomenon	121
3. Location of the glass-transition diagram in the phase diagram	122
4. Logarithmic decay in MD	124
Chapter 9. Conclusion	129
Appendix A. Comments on the asymptotic expansion	131
1. Laplace transform of logarithms	131
2. Parameters $C_j$ for Eq. (5.31)	132
3. Critical decay for the $F_{13}$ -model	132
Appendix B. Numerical Algorithms	135
1. Determination of glass-glass transitions	135
2. Characteristic parameters for higher-order singularities	136
Appendix. Bibliography	139

## List of Figures

3.1	Factor function $Q(r)$ in MSA for the SWS at the $A_4$ -singularity.	24
3.2	Factor function $Q(r)$ in PYA for the SWS at the $A_4$ -singularity.	27
3.3	Factor functions for different $A_4$ -singularities.	28
4.1	Glass-transition diagram for the SWS.	30
4.2	Glass-form factors for the SWS.	32
4.3	Elastic moduli at a glass-glass transition for $\delta = 0.03$ .	33
4.4	Exponent parameter $\lambda$ for the SWS.	34
4.5	Comparison of PYA and MSA at the $A_4$ -singularity.	35
4.6	Glass-transition diagram for the HCY.	37
4.7	Attractive potentials and glass-transition diagrams.	38
4.8	Structure factors at different $A_4$ -singularities	39
4.9	Localization lengths at the $A_4$ -singularity for SWS and HCY.	40
4.10	Elastic moduli at the $A_4$ -singularity of SWS and HCY.	41
4.11	Reentry for SWS, TRI, AOS and HCY.	42
5.1	Glass-transition diagram for the $F_{13}$ -model.	65
5.2	Logarithmic decay in the $F_{13}$ -model.	67
5.3	Decay in the $F_{13}$ -model for constant separation $\varepsilon_1$ .	68
5.4	Critical decay at the $A_3$ -singularity in the $F_{13}$ -model.	70
5.5	$t_0$ for the critical decay in the $F_{13}$ -model.	72
5.6	An $A_3$ -singularity in the two-component model.	74
5.7	Logarithmic decay at the $A_3$ -singularity in the two-component model.	75
5.8	Logarithmic and power law decay in the two-component model.	77
5.9	Critical decay at the $A_3$ -singularity in the two-component model.	78
5.10	The $A_4$ -singularity in the two-component model.	80
5.11	Logarithmic decay in the first correlator at the $A_4$ -singularity.	81
5.12	Logarithmic decay in the second correlator at the $A_4$ -singularity.	82
5.13	Critical decay at the $A_4$ -singularity in the two-component model.	84
5.14	Parameters $\mu_2$ and $\mu_3$ for the two-component model.	86

6.1	Parameters $\mu_3$ , $\mu_4$ , and $\kappa$ in the SWS.	88
6.2	Wave-vector dependent amplitudes at the $A_4$ -singularity.	89
6.3	Lines of vanishing quadratic correction at the $A_4$ -singularity.	90
6.4	Logarithmic decay at the $A_4$ -singularity.	92
6.5	Logarithmic decay, variation of wave vector $q$ .	93
6.6	Logarithmic decay, variation of control parameters $\mathbf{V}$ .	95
6.7	Subdiffusive power law in the MSD.	96
6.8	Deviations from power law behavior in the MSD.	97
6.9	Wave-vector dependent amplitudes at the $A_3$ -singularity.	99
6.10	Lines of vanishing quadratic correction at the $A_3$ -singularity.	100
6.11	Critical decay at a $A_3$ -singularity in the SWS .	102
6.12	Critical decay at the $A_4$ -singularity in the SWS.	104
7.1	Isodiffusivity curves for $\delta = 0.03$ for PYA and MSA	108
7.2	MSD for the SWS at the crossing.	109
7.3	Parameters for the critical decay at $A_2$ -singularities.	111
7.4	Parameters for the von Schweidler-law description.	112
7.5	Subdiffusive power law at the $A_3$ -singularity.	114
7.6	Parameters for the asymptotic description at the crossing.	116
7.7	Logarithmic decay at a crossing point.	117
7.8	Wave-vector test for logarithmic decay.	119
8.1	Glass-transition diagram from computer simulation data.	123
8.2	Rescaled correlators from simulation data.	125
8.3	Glass-form factors from simulation.	127
B.1	Eigenvalue at glass-glass transitions.	136
B.2	Parameter $\mu_2$ at higher-order singularities in the SWS.	137

## List of abbreviations, acronyms and symbols

AOS	Asakura-Oosawa system
HCY	hard-core Yukawa system
HSS	hard-sphere system
lhs	left-hand side
MCT	mode-coupling theory
MD	molecular-dynamics simulation
MSA	mean-spherical approximation
MSD	mean-squared displacement
OZ	Ornstein-Zernike relation
PYA	Percus-Yevick approximation
rhs	right-hand side
SHSS	sticky-hard-sphere system
SWS	square-well system
TRI	triangular system

### Mathematical notation

$x^c$	quantity $x$ at an $A_2$ -singularity
$x^\circ$	quantity $x$ at an $A_3$ -singularity
$x^*$	quantity $x$ at an $A_4$ -singularity
convex	$f''(x) > 0$
concave	$f''(x) < 0$





## Introduction

Standard text books on solid state physics usually start out by assuming long-range crystalline order in the solid under consideration. They introduce a lattice for the positions of the atoms and characterize the lattice structure by Bragg reflection in some scattering experiment. The existence of Bragg peaks allows to differentiate between a crystalline solid and an amorphous liquid where Bragg peaks are absent because there is no long-range order. There are, however, also *amorphous solids* that can be discriminated from a liquid by the fact that they can sustain shear stress without yielding. The static structure of these amorphous solids — also called glasses — is not very much different from a liquid, so a measurement of the structure would not clearly reveal whether the system is in the liquid or in the glass state. There are in particular no divergences of thermodynamic quantities at the liquid-glass transition as they occur at classical thermodynamic phase transitions.

For the reasons above one has to look at dynamical variables to gain insight into the transition from a liquid to a glass. We will use the framework of correlation functions to discuss the dynamics in a given system. Correlation functions can be measured in experiments, e.g., in dynamic light scattering, and calculated from computer simulation what facilitates the comparison to theory [1]. While the correlation functions vary only little in the dilute regime and decay to zero almost exponentially, the relaxation time changes by orders of magnitude in time when the transition to a glass is approached. At an ideal liquid-glass transition the relaxation time actually diverges and the system arrests.

Mode-coupling theory for ideal glass transitions (MCT) describes the slow dynamics of density-autocorrelation functions close to the transitions [2–4]. The long-time limits of the correlation functions yield algebraic equations that exhibit structurally stable singularities singularities of MCT are equivalent to the bifurcations in the real roots of real polynomials when the coefficients are changed continuously [5]. The simplest possible singularity is the *fold* bifurcation where generically the smooth variation of a single control parameter causes a discontinuous change in the solution for the long-time limit. This behavior can be identified with the transition from a liquid, where the long-time limit of the correlation function is zero, to a glass, where this limit is finite. Close to the singularities the equations of motion can be expanded in asymptotic series which in the case of the fold yields a two-step decay with two related power laws for the short-time and the long-time decay [3]. These universal laws are independent of the details of the system under study and have been applied frequently to a variety of experiments and computer simulation studies [6].

The paradigm example for a glass transition is the transition in the hard-sphere system (HSS). In this system the interaction potential among the particles is zero

unless their mutual separation becomes smaller than their diameter where the potential becomes infinitely repulsive, thus preventing the particles from overlapping. The HSS is the system MCT was applied to first [2], and it is also the system for which the most detailed predictions have been worked out [7]. The hard sphere potential can be realized experimentally to a high degree in sterically stabilized colloids [8], and the predictions of MCT were tested thoroughly in dynamic light scattering experiments in that system [9–12] yielding strong support for the theory [13]. The arrest in the HSS can be understood by the so-called cage effect. In a dense liquid, a particle is surrounded by a number of other particles and can only diffuse over a larger distance if these neighbors rearrange and give space to the first particle. For this rearrangement the neighboring particles require their neighbors to move out of the way, and so forth. If density exceeds a critical value, this rearrangement is no longer possible. A glass transition occurs.

MCT can exhibit also singularities of higher order than the fold. Namely, *cusp* and *swallowtail* singularities were predicted recently for systems where the hard-core repulsion is supplemented with a short-ranged attraction [14–16]. Close to the higher-order glass-transition singularities, the asymptotic power-law solutions are replaced by decay laws involving logarithms in time. Different asymptotic expansions for the decay laws at higher-order singularities shall be elaborated and tested in this work. Subsequently, the newly derived laws are applied to a model system with short-ranged attraction, the square-well system (SWS), where the hard core repulsion is supplemented by an attractive potential of constant depth and finite range.

The arrest in the SWS can originate from two different sources. The first mechanism is the repulsion of the hard core that leads to a glass transition as in the HSS. The second mechanism leading to the arrest is bond formation introduced by the attractive part of the potential. This latter transition was proposed as relevant for the transition to a gel [15]. A gel is characterized as an amorphous state that despite its low density can support its weight and resist weak external forces, and thus qualifies as a solid. Its formation from the liquid state (also called sol) is driven by the attraction among its building units. When colloidal particles are the constituents of the gel one speaks of a *colloidal gel*. Both glass and gel transitions have been studied frequently in colloidal dispersions. It was observed that the dynamics at the gel transition shows features similar to the glass transition [17, 18]. When both mechanisms of arrest are of the same importance, at high density and for strong attraction, a discontinuous transition between glass and gel is predicted by MCT which is intimately connected with emergence of the cusp singularity.

The shapes of the potentials required for the discussion of the higher-order singularities are rather far apart from the classical Lennard-Jones potential where the range of the attraction is of the order of the particle diameter and the repulsion is comparably soft. The short-ranged attraction considered here takes place within a fraction of less than 20% of the diameter and the repulsion is required to be substantially steeper than in the Lennard-Jones system. These potentials can be realized in computer simulation and in colloidal systems where, e.g., the addition of a small amount of polymer leads to an effective attraction among the colloidal particles [19–21]. The typical thermodynamic phase diagram for such short-ranged potential does not contain gas-liquid separation and the critical point is metastable

with respect to the fluid-crystal transition. This phase behavior is well established in experiments [21, 22]. In the crystal phase there is the possibility of an isostructural transition among crystals of the same crystalline order but different lattice constants. This was so far only found in computer simulation studies [23–26] and corroborated by density functional theory [27, 28]. It is intriguing that the higher-order glass-transition singularities in MCT are predicted for similar values of the control parameters.

Though logically disconnected from the study of higher-order singularities, there is a particularly intriguing phenomenon MCT predicts for systems like the SWS that encourages the use of this theory. At high density and small to moderate strength of the attraction it is possible to melt a glass by increasing the attraction at fixed density. This is equivalent to melting by cooling [14, 16]. Since the system arrests again after further increasing the attraction this phenomenon was termed *reentry*. This scenario was subsequently confirmed by independent experiments and computer simulation studies and is by now well established [29–33]. That MCT can describe correctly such a subtle effect of the attraction on the liquid-glass transition allows to seriously consider the existence of higher-order glass-transition singularities.

Higher-order singularities were also known for schematic MCT models. In these models the microscopic details are neglected in the coupling parameters [3]. For simple one- and two-component systems cusp and swallowtail singularities could be identified [34]. These were associated with a leading-order  $-\ln t$  decay of the correlation functions or equivalently  $1/f$ -noise in the fluctuation spectra. However, corrections alter this behavior qualitatively and need to be discussed to understand the relaxation scenarios. For cusp singularities the inverse square of the logarithm was found as an asymptotic solution and extended to multiparameter scaling laws using Weierstrass' elliptic functions [35]. Dielectric-loss data for certain polymers was interpreted by this leading-order scaling-law description [36, 37]. For similar systems data was analyzed using the equivalent scaling laws for a swallowtail singularity [38–40]. However, the critical decay at the cusp and swallowtail singularities is described unsatisfactorily by the leading order result and has to be complemented by corrections [35, 41].

Logarithmic decays were reported in recent light scattering experiments [42, 43] and computer simulation studies [33, 44] of colloidal and micellar systems that motivate the present work.

The basic equations of MCT are introduced briefly in Ch. 2. A necessary input to these equations is the static-structure factor of the disordered system, which is calculated for potentials with short-ranged attraction in Ch. 3. The glass-transition singularities of these systems are presented in Ch. 4, which motivates the asymptotic expansions carried out in Ch. 5. The decay laws at the higher-order singularities are first tested in one- and two-component systems, Ch. 5 Secs. 6 and 7, before they are applied to the SWS in Ch. 6. Chapter 7 deals with the interplay of *different* glass-transition singularities encountered naturally in a situation close to a higher-order glass-transition singularity. Though the field is just evolving, first experiments are available and a discussion of these shall take place in Ch. 8. The conclusion, Ch. 9, summarizes the main findings of the work stressing the predictions that are assumed to be testable in experiment and computer simulation.



## Equations of motion

Mode-coupling theory (MCT) describes the dynamics of glass-forming systems in terms of correlation functions. For the structural arrest at a glass transition the correlation function for the density is the most important one. If the density fluctuations arrest, the system undergoes a glass transition. MCT describes the feedback mechanism leading to arrest via closed equations for the density auto-correlation functions. The equations of motion for the correlation functions are summarized in Sec. 1. A more comprehensive coverage of the derivation is found in Ref. [3].

In the long-time limit the equations of motion yield algebraic equations that exhibit bifurcations we identify with glass-transition singularities. In Sec. 2 some basic properties of these singularities are anticipated that are necessary for the discussion of the glass-transition diagrams in Ch. 4. In Ch. 5 a more comprehensive treatment and one- and two-component examples are presented.

Whereas the arrest of the density fluctuations drives the transition, the signatures of the transition are also displayed by the variables that couple to the density fluctuations. The equations of motion for the tagged particle dynamics shall be summarized in Sec. 3.

### 1. Density-autocorrelation function

We consider a system of  $N$  particles in a volume  $V$  with the number density  $\rho = N/V$ . The particle density is given by  $\rho(\vec{r}, t) = \sum_{j=1}^N \delta(\vec{r} - \vec{r}_j(t))$  or after a Fourier transform with respect to  $\vec{r}$  as  $\rho_{\vec{q}}(t) = \sum_{j=1}^N \exp(i\vec{q}\vec{r}_j(t))/\sqrt{N}$ . Denoting canonical averaging by  $\langle \cdot \rangle$  and the fluctuation of some dynamical variable  $A$  by  $\delta A = A - \langle A \rangle$  we can define the so-called Mori or Kubo scalar product

$$(2.1) \quad (A|B) := \langle \delta A^* \delta B \rangle .$$

The normalized density-autocorrelation function in an isotropic system is then defined as

$$(2.2) \quad \phi_q(t) = (\rho_q(t)|\rho_q) / (\rho_q|\rho_q) ,$$

where  $q = |\vec{q}|$  is the wave-vector modulus. The fluctuations for time zero define the *static structure factor*  $S_q = (\rho_q|\rho_q)$  that can be calculated from the interaction potential. For the potentials of interest in this work, this will be done explicitly in Ch. 3.  $S_q$  depends on external control parameters of the system, e.g., density or temperature, that we combine into a control-parameter vector  $\mathbf{V}$ .

Since the correlation function is determined by the many-body problem that is equivalent to finding  $\rho(\vec{r}, t)$ , we will need approximations to derive equations of motion for  $\phi_q(t)$ . We will reformulate the problem in a way to motivate the approximation. For a system obeying Newtonian dynamics the evolution of a variable

$A$  is conveniently expressed by a Liouville operator,

$$(2.3a) \quad \mathcal{L} = -i \sum_i (\partial_{\vec{p}_i} H \cdot \partial_{\vec{r}_i} - \partial_{\vec{r}_i} H \cdot \partial_{\vec{p}_i}) , \quad \partial_t A(t) = i\mathcal{L}A(t) ,$$

for the Hamiltonian  $H$  of the system. The formal solution for the evolution in time for variable  $A$  is then given by a Liouville equation,

$$(2.3b) \quad A(t) = \exp[i\mathcal{L}t] A(0) .$$

Connected to the density variables is the current  $\vec{j}_q = \sum_{j=1}^N (\vec{p}_j/m) \exp(i\vec{q}\vec{r}_j)/\sqrt{N}$  for particle momenta  $\vec{p}_j$ . The longitudinal part of the current,  $j_q^L = \vec{j}_q \vec{q}/q$ , is given by the derivative of the density,

$$(2.4) \quad \mathcal{L}\rho_q = qj_q^L ,$$

which is a continuity equation and reflects particle conservation. The derivative of the current,  $\mathcal{L}j_q^L$ , represents forces that will be treated by approximation below.

An exact reformulation of the Liouville equation (2.3b) can be given by applying a formalism by Mori and Zwanzig which is derived comprehensively in a number of textbooks [1, 45, 46]. Thereby, the evolution of some variables  $A_j(t)$  is split into a part projected onto the initial  $A_j$  by a projector  $\mathcal{P}$ , obeying idempotency  $\mathcal{P}^2 = \mathcal{P}$ , and a part orthogonal to the chosen variables defining an orthogonal projector  $\mathcal{Q}$ , with  $\mathcal{Q} = 1 - \mathcal{P}$  and  $\mathcal{Q}\mathcal{P} = 0$ . This projection yields equations of motion for the correlation functions  $(A_i(t)|A_j)$  for the selected variables in terms of memory kernels that incorporate the complicated dynamics of the orthogonal space. These memory kernels are subject to further transformation or approximation.

Assuming that the densities and currents are relevant for the glass transition we define the projector using these variables,

$$(2.5) \quad \mathcal{P} := |\rho_q\rangle \frac{1}{S_q} \langle \rho_q| + |j_q^L\rangle \frac{1}{v_0^2} \langle j_q^L| ,$$

with the normalization by the static structure factor  $S_q$  for the  $\rho_q$ , and the thermal velocity  $v_0 = \sqrt{k_B T/m}$  for the currents,  $(j_q^L|j_q^L) = v_0^2$ . We get for the density autocorrelation function

$$(2.6a) \quad \partial_t^2 \phi_q(t) + \Omega_q^2 \phi_q(t) + \int_0^t M_q(t-t') \partial_{t'} \phi_q(t') dt' = 0 ,$$

with the initial conditions  $\phi_q(0) = 1$  and  $\partial_t \phi_q(0) = 0$ . The positive  $\Omega_q = qv_0/\sqrt{S_q}$  denote characteristic frequencies, and the memory kernel  $M_q(t)$  is the fluctuating longitudinal current relaxation kernel [45],

$$(2.6b) \quad M_q(t) = \frac{1}{v_0^2} (\mathcal{Q}\mathcal{L}j_q^L | \exp[-i\mathcal{Q}\mathcal{L}\mathcal{Q}t] | \mathcal{Q}\mathcal{L}j_q^L) .$$

The problem has been transferred to the evaluation of the memory kernel.  $M_q(t)$  is by itself a correlation function for fluctuating forces that are driven by the projected operator  $\mathcal{Q}\mathcal{L}\mathcal{Q}$  instead of the Liouville operator  $\mathcal{L}$ . This kernel will be treated in the following by the so-called mode-coupling approximation.

To simplify  $M_q(t)$  we now apply Kawasaki's mode-coupling factorization [47]. This is motivated in the present context by the observation that the factorization leads to a self-consistent equation that is capable of describing feedback and arrest when both  $\rho$  and  $j^L$  are slow variables [48]. To this end the evolution operator  $\exp[-i\mathcal{Q}\mathcal{L}\mathcal{Q}t]$  in Eq. (2.6b) is replaced by its projection on the subspace of density

pairs  $\delta\rho_{\vec{k}}\delta\rho_{\vec{p}}$  where  $\vec{p} = \vec{q} - \vec{k}$  [49]. The kernel  $M_q(t)$  is then expressed by time-independent so-called coupling vertices, which are given by the overlap of the pair density modes with the fluctuating forces  $\mathcal{QL}j_q^L$ , and a correlation function that involves four dynamical variables. The latter four-variable correlation function is factorized into a product of two-variable correlation functions. This constitutes the mode-coupling approximation. The equations of motion are then given by an approximated memory kernel  $m_q(t)$ . For Newtonian dynamics they read [2, 3]

$$(2.7a) \quad \partial_t^2 \phi_q(t) + \Omega_q^2 \phi_q(t) + \Omega_q^2 \int_0^t m_q(t-t') \partial_{t'} \phi_q(t') dt' = 0 .$$

For Brownian dynamics a similar equation can be derived [50, 51],

$$(2.7b) \quad \tau_q \partial_t \phi_q(t) + \phi_q(t) + \int_0^t m_q(t-t') \partial_{t'} \phi_q(t') dt' = 0 ,$$

with the initial condition  $\phi_q(0) = 1$ . The microscopic time scale  $\tau_q = S_q/(D_0 q^2)$  is given by the short-time diffusion coefficient,  $D_0$ , characterizing the Brownian motion. The mode-coupling approximation results in expressing the kernel  $m_q(t)$  in terms of the correlators  $\phi_q(t)$  [3],

$$(2.7c) \quad m_q(t) = \mathcal{F}_q[\mathbf{V}, \phi_k(t)] .$$

As a consequence of the factorization into pair modes, for the structural relaxation in simple liquids,  $\mathcal{F}_q$  is a bilinear functional of the density correlators [2],

$$(2.7d) \quad \mathcal{F}_q[\tilde{f}] = \frac{1}{2} \int \frac{d^3 k}{(2\pi)^3} V_{\vec{q}, \vec{k}} \tilde{f}_k \tilde{f}_{|\vec{q}-\vec{k}|} ,$$

and the vertex is determined completely by the static structure of the liquid system [52, 53],

$$(2.7e) \quad V_{\vec{q}, \vec{k}} = S_q S_k S_{|\vec{q}-\vec{k}|} \frac{\rho}{q^4} \left[ \vec{q} \cdot \vec{k} c_k + \vec{q} \cdot (\vec{q} - \vec{k}) c_{|\vec{q}-\vec{k}|} \right]^2 .$$

$c_q$  denotes the direct correlation function which is related to the static structure factor in the Ornstein-Zernike relation (OZ)  $S_q = 1/[1 - \rho c_q]$  [45]. In the derivation of the vertex a static triple direct correlation function appears that has to be treated by approximation. It has been simplified by the convolution approximation [45] in Eq. (2.7e) [3]. Introducing a different approximation for that term did not change the results for the HSS significantly [54, 55]. The triple correlation can be calculated in computer simulation and was used as input to MCT [56]. It was found that inclusion of that term improves the results for silica but does practically not change the results for the denser Lennard-Jones system. In the high density regime we are interested in we therefore expect that neglecting  $c_{\vec{q}\vec{k}}^{(3)}$  has a minor effect.

It is the long-time limit of the correlation function,  $\phi_q(t \rightarrow \infty) \rightarrow f_q$ , that determines whether a system is in the liquid regime, where  $f_q = 0$ , or in an arrested state, where  $0 \leq f_q \leq 1$ . In the latter case the variables  $f_q$  characterize the arrested glassy state and the  $f_q$  are therefore called *glass-form factors* or *Debye-Waller factors*. In the long-time limit, the equation of motion (2.7) reduces to an algebraic equation involving only the mode-coupling functional and the glass-form factors [4],

$$(2.8) \quad f_q/(1 - f_q) = \mathcal{F}_q[\mathbf{V}, f] .$$

Equation (2.8) may have multiple solutions  $\tilde{f}_q$ , the glass form factor  $f_q$  is distinguished among these by the maximum property [3].

$$(2.9) \quad \tilde{f}_q \leq f_q, \quad q = 1, \dots, M.$$

For the discussion of the dynamics the value  $f_q^c$  at the singularity is referred to as plateau.

## 2. Glass-transition singularities

Inspecting the mode-coupling functional  $\mathcal{F}$  in Eq. (2.7d) we see that Eq. (2.8) is a closed nonlinear equation in the  $f_q$  with coefficients given by the static structure. It is a key finding of MCT that Eq. (2.8) can have solutions different from  $f_q = 0$  [2]. These solutions with  $f_q \neq 0$  appear discontinuously when control parameters  $\mathbf{V}$  are varied smoothly – Eq. (2.8) exhibits a bifurcation. At the bifurcation the polynomial in Eq. (2.8) is no-longer invertible but exhibits a critical eigenvector with eigenvalue zero. In a one-component system this is equivalent to a vanishing derivative at the bifurcation point. It is possible to show that there is only a single critical eigenvector and that therefore exclusively a certain class of singularities can emerge from Eq. (2.8) [57]. These singularities are of the cuspid hierarchy  $A_l$ ,  $l \geq 2$ . The simplest possible bifurcation is the  $A_2$ -singularity, a *fold*, that is generically encountered if only one control parameter is changed [5]. The most important case of an  $A_2$ -singularity is realized in a liquid-glass transition.

An example exhibiting an  $A_2$ -singularity is the HSS which represents an assembly of particles with diameter  $d$  and a pair potential that is zero for interparticle distances  $r$  larger than  $d$  and infinite for  $r \leq d$ . The only control parameter for the HSS is the packing fraction  $\varphi = \pi d^3 \rho / 6$ . The structure factor for the HSS is available in analytical form [58, 59], and introducing that expression for  $S_q$  and  $c_q$  into Eq. (2.8) a liquid-glass transition can be identified in the HSS for  $\varphi^c = 0.516$  [2]. For increasing the packing fraction beyond the critical value, the glass-form factors grow with the square-root of the distance to the critical point,  $(f_q - f_q^c) \propto \sqrt{\varphi - \varphi^c}$ . This singular variation at the critical point is a result characteristic for the fold bifurcation and is valid close to the transition and for  $f_q$  close to  $f_q^c$ . In a so-called asymptotic expansion around  $f_q^c$  it is possible to describe that variation quantitatively [3],

$$(2.10) \quad f_q - f_q^c = h_q \sqrt{\sigma / \mu_2}, \quad \sigma > 0.$$

The asymptotic expansion introduces a *separation parameter*  $\sigma$  measuring the distance to the singularity in a local coordinate system and a characteristic number  $\mu_2$  which for the MCT-fold bifurcation is also known as *exponent parameter*  $\lambda = 1 - \mu_2$ . The parameter  $\lambda$  is of central importance also for the dynamics at  $A_2$ -singularities [3]. The wave-vector dependence is given by a *critical amplitude*  $h_q$ . The law in Eq. (2.10) becomes invalid when  $\mu_2$  approaches zero which signals the emergence of a higher-order singularity.

Two external parameters need to be varied to locate a generic  $A_3$ -singularity or *cuspl*. Different from the textbook example where cusp singularities appear in pairs, within MCT only one of these two is relevant because the other is not an admissible glass-form factor respecting the maximum property (2.9). Generically the  $A_3$ -singularity is then an endpoint of a line of  $A_2$ -singularities. When two such lines cross, the line connected with the lower critical glass-form factors  $f_q^{(1)c}$



terminates at the crossing, cf. Eq. (2.9). The other line of  $A_2$ -singularities  $f_q^{(2)c}$  extends into the glass phase as a line of glass-glass transitions where the glass-form factors change discontinuously from  $f_q^{(1)} > 0$  to  $f_q^{(2)c} > f_q^{(1)}$ . This discontinuity  $f_q^{(2)c} - f_q^{(1)}$  diminishes along the line of glass-glass transitions as  $f_q^{(1)}$  increases in the glass according Eq. (2.10) while the  $f_q^{(2)c}$  decrease. The point where this discontinuity vanishes is just the  $A_3$ -singularity. The first microscopic model system shown to exhibit an  $A_3$ -singularity was the sticky hard sphere system (SHSS) which has an effective temperature  $\tau$  as second control parameter in addition to the packing fraction  $\varphi$ . The SHSS contains the HSS as a limiting case of infinite  $\tau$ . The cusp occurs in the opposite limit of low effective temperature  $\tau$  [14, 15].

Tuning a third parameter one can merge the endpoint with the crossing point at the  $A_4$ -singularity and observes the scenario of a *swallowtail*. Because of the maximum property (2.9) only one sheet of the familiar swallowtail is realized within MCT. In the square-well system (SWS) the range of the attractive potential is a third parameter that can be changed. One finds a generic  $A_4$ -singularity [16], see also Ch. 4.

### 3. Coupled quantities

Similar to the equations for the density correlator, correlation functions for other variables can also be reformulated using memory kernels and the mode-coupling approximation is invoked in the same way as before [3]. We shall briefly introduce the quantities that are discussed later.

**3.1. Tagged particle motion.** Frequently studied, e.g. in computer simulation, is the dynamics of a single or *tagged* particle with the single particle density  $\rho_q^s(t) = \exp(i\vec{q}\vec{r}_s(t))$ . For the correlation function of a tagged particle,  $\phi_q^s(t) = (\rho_q^s(t)|\rho_q^s)$ , similar equations as Eq. (2.7) have been derived [2, 60],

$$(2.11a) \quad \tau_q^s \partial_t \phi_q^s(t) + \phi_q^s(t) + \int_0^t m_q^s(t-t') \partial_{t'} \phi_q^s(t') dt' = 0,$$

with  $\tau_q^s = 1/(D_0^s q^2)$ . The mode-coupling functional for the tagged particle motion,

$$(2.11b) \quad \mathcal{F}_q^s[f, f^s] = \int \frac{d^3k}{(2\pi)^3} S_k \frac{\rho}{q^4} c_k^s{}^2 (\vec{q}\vec{k})^2 f_k f_{|\vec{q}-\vec{k}|}^s,$$

is also determined by the static structure of the liquid system where  $c_q^s$  is the single-particle direct correlation function [45]. The dynamics of the tagged particle is coupled to the coherent density correlator  $\phi_q(t)$  and for that reason  $\phi_q^s(t)$  also displays the bifurcation dynamics that is driven by  $\phi_q(t)$ . The equation for the long-time limits of the tagged particle correlations function,  $\phi_q^s(t \rightarrow \infty) = f_q^s$ , reads

$$(2.12) \quad f_q^s / (1 - f_q^s) = \mathcal{F}_q^s[f, f^s].$$

In the following, the tagged particle will be assumed as of the same sort as the host fluid. If the host particles are in the liquid state,  $f_q = 0$ , a tagged particle cannot be arrested, in that case Eq. (2.12) implies  $f_q^s = 0$ .

**3.2. Mean squared displacement.** The mean-squared displacement (MSD) is defined by  $\delta r^2(t) = \langle |\vec{r}_s(t) - \vec{r}_s(0)|^2 \rangle$  and describes the average distance a particle has traveled within some time  $t$  [45]. It is obtained either as small wave-number limit of the tagged-particle correlator in Eq. (2.11),  $\phi_q^s(t) = 1 - q^2 \delta r^2(t)/6 + \mathcal{O}(q^4)$  or from the representation of the velocity-autocorrelation function [3, 60],

$$(2.13a) \quad \delta r^2(t) + D_0^s \int_0^t m^{(0)}(t-t') \delta r^2(t') dt' = 6D_0^s t,$$

$m^{(0)}(t) = \lim_{q \rightarrow 0} m_q^s(t) = \mathcal{F}_{MSD}[\phi(t), \phi^s(t)]$ . The mode-coupling functional for the MSD is driven by coherent and tagged particle densities,

$$(2.13b) \quad \mathcal{F}_{MSD}[f, f^s] = \int \frac{dk}{(6\pi^2)} \rho S_k (c_k^s)^2 f_k f_k^s.$$

A characteristic localization length  $r_s$  is defined by the second moment for the relaxation of the distribution of  $\phi_q^s(t)$  [60], which can be identified with the functional in Eq. (2.13b)  $r_s^2 = 1/\mathcal{F}_{MSD}[f, f^s]$ . It is the long-time limit of the MSD and the value at the critical point,  $r_s^c$ , characterizes the arrested structure. The value  $6r_s^c{}^2$  represents the plateau for the dynamics of  $\delta r^2(t)$ . The long-time diffusion coefficient  $D^s$  can be defined from the above correlation functions using  $\lim_{t \rightarrow \infty} \delta r^2(t)/t = 6D^s$  [60],

$$(2.14) \quad \frac{D^s}{D_0^s} = \frac{1}{1 + D_0^s \int_0^\infty m^{(0)}(t) dt}.$$

**3.3. Mechanical Properties.** The elastic moduli quantify the macroscopic mechanical stiffness of both liquids and glasses. The longitudinal modulus  $M_L$  specifies the stiffness for compressions and the transversal one,  $M_T$ , the stiffness for shear deformations. The  $M_T$  is just the shear modulus, also denoted by  $G'$ , that we used to differentiate a solid from a liquid already in the introduction. For a liquid system, the shear modulus vanishes,  $M_T^0 = 0$ . The moduli are defined as constants of proportionality in the linearized stress-strain relation. In systems with Newtonian microscopic dynamics they determine the speed of longitudinal and transversal sound respectively via  $v_{L,T} = \sqrt{M_{L,T}/(\rho m)}$  with  $\rho m$  denoting the mass density. The longitudinal modulus in the liquid reads

$$(2.15) \quad M_L^0 = \rho(k_B T) S_0^{-1},$$

with  $S_0 = \lim_{q \rightarrow 0} S_q$ . In the glass state, the moduli are larger due to additional contributions from the structural arrest,  $M_{L,T} = M_{L,T}^0 + \delta M_{L,T}$ . The additional contributions are given by the glass-form factor for the arrested state [3],

$$(2.16) \quad \delta M_{L,T} = \rho(k_B T) \lim_{q \rightarrow 0} \sum_{\vec{k} + \vec{p} = \vec{q}} S_k S_p f_k f_p \{ [\vec{k} c_k + \vec{p} c_p] \cdot \vec{e}_{\vec{q}}^{\perp,T} \}^2 (\rho/2q^2).$$

Here  $\vec{e}_{\vec{q}}^{\perp,T}$  are unit vectors parallel and perpendicular to  $\vec{q}$ , respectively. The limit leads to

$$(2.17a) \quad \delta M_{L,T} = \rho(k_B T) \int_0^\infty dk \{ \rho [S_k f_k k / (2\pi)]^2 w_{L,T}(k) \},$$

$$(2.17b) \quad w_L(k) = c_k^2 + \frac{2}{3} (k c_k') c_k + \frac{1}{5} (k c_k')^2,$$

$$(2.17c) \quad w_T(k) = \frac{1}{15} (k c_k')^2.$$

## Static-structure factors

The static-structure factor  $S_q$  constitutes the input to the equations of MCT for the structural relaxation in liquids. This quantity is not derived within MCT but taken from different approximate theories. The appearance of higher-order singularities depends on the incorporation of different features of the interaction potential into the structure factor. Therefore, the structure factors used later shall be derived in this chapter for several short-ranged potentials using two different approximations and both analytical and numerical solutions. The formalism used below yields a transparent representation of the structure factors in terms of the Fourier transform of simple polynomials. This allows for a direct explanation of some features in the vertices of MCT. The approximations used below are known to introduce inconsistencies in the equation of state derived from the structure factors and more refined approximation schemes are available to improve the behavior of the thermodynamic quantities [61]. Here, the priority is given to keep the structure factor simple and transparent and nevertheless incorporate the essential structural features.

### 1. Static-structure factor and Wiener-Hopf factorization

The probability of finding one of the  $N - 1$  particles at position  $\vec{r}$  from a first particle at  $\vec{r} = 0$  is given by the *pair distribution function*  $g(\vec{r})$  [45]. For an isotropic system this depends only on the radial distance  $r = |\vec{r}|$ . The Fourier transform of the radial distribution function  $g(r)$  is the static structure factor defined above,

$$(3.1) \quad \rho g(r) = \frac{1}{N} \sum_{n \neq m} \langle \delta(\vec{r} - \vec{r}_n + \vec{r}_m) \rangle, \quad S_q = 1 + \frac{4\pi\rho}{q} \int_0^\infty dr r [g(r) - 1] \sin qr.$$

The knowledge of  $S_q$  allows the evaluation of thermodynamic quantities, e.g., for  $q \rightarrow 0$ , the compressibility of the system is given by [45]

$$(3.2) \quad S_0 = \rho k_B T \chi_T = \chi_T / \chi_T^0,$$

with  $\chi_T^0 = 1/(\rho k_B T)$ , the compressibility of the ideal gas. The location of points where the system is mechanically unstable is given by the divergence of the compressibility at the *spinodal* line where  $S_0^{-1} = 0$ . At these points the input can no longer be used in MCT.

A significant simplification for the calculation of structure factors is given by the introduction of a short-ranged direct correlation function  $c(r)$  by the Ornstein-Zernike relation [45, 62],

$$(3.3a) \quad h(r) = c(r) + \rho \int d\vec{r}' c(|\vec{r} - \vec{r}'|) h(\vec{r}'),$$

where also the total correlation function  $h(r)$  is defined as  $h(r) = g(r) - 1$ . In the present context, Eq. (3.3a) can be motivated by observing that the total correlation  $h(r)$  between two particles consists of their short-ranged direct correlation  $c(r)$  and indirect correlations mediated by the other particles. Equation (3.3a) can be expressed equivalently in the wave-vector-domain,

$$(3.3b) \quad S_q = \frac{1}{1 - \rho c_q}, \quad c_q = \frac{4\pi}{q} \int_0^\infty dr \sin(qr) [rc(r)].$$

Since calculating  $S_q$  involves the solution of a quite involved many-body problem, only limiting cases like  $g(r) \rightarrow \exp[-\beta U(r)]$  for  $\rho \rightarrow 0$ , or  $g(r) \rightarrow 1 - 1/N$  for  $r \rightarrow \infty$  are known exactly. For the strong coupling case, approximations – usually called closure relations – need to be introduced [45, 61]. One particularly successful approximation was introduced by Percus and Yevick (PYA) [63],

$$(3.4a) \quad c(r) = g(r) \{1 - \exp[U(r)/(k_B T)]\}.$$

The closure ensures that  $c(r) = 0$  for vanishing potential  $U(r) = 0$ . For the excluded volume region,  $U(r) = \infty$ , the pair correlation  $g(r)$  is zero while  $c(r)$  remains finite [45]. Also frequently used is the mean-spherical approximation (MSA) [64], where the excluded volume part is described by the exact relation  $g(r) = 0$  for  $0 \leq r < d$  and the interaction tail is given by

$$(3.4b) \quad c(r) = -U(r)/(k_B T), \quad r \geq d.$$

The MSA can be regarded as a leading expansion of the PYA for small coupling but cannot be seen as inferior to PYA *a priori* as a comparison of both approximations for the SWS shows. MSA is reported to be superior to PYA for moderately short-ranged attraction [65], but inferior for shorter ranges [66]. In addition, MSA allowed for a number of analytical solutions, e.g., for Yukawa attraction [67].

The direct correlation function  $c(r)$  usually tends to zero with increasing distance  $r$  much more rapidly than  $h(r)$  or the interaction potential. If  $c(r)$  vanishes beyond some finite range  $R$ , the Ornstein-Zernike relation can be reformulated using the Wiener-Hopf factorization technique [68]. A factor function  $Q(r)$  is introduced which is related to  $h(r)$  and  $c(r)$  involving these functions only over a finite range. The restriction to finite-range  $c(r)$  can be relaxed and the factorization can be seen as general reformulation of the Ornstein-Zernike relation which offers a simple representation of structure factors [69].

For a monodisperse isotropic system, the structure factor is a real function of the wave-vector modulus  $q = |\vec{q}|$ . The inverse of  $S_q$  is factorized into a product of complex conjugated Fourier transforms of a factor function  $Q(r)$  as

$$(3.5a) \quad S_q^{-1} = \hat{Q}(q)^* \hat{Q}(q),$$

$$(3.5b) \quad \hat{Q}(q) = 1 - 2\pi\rho \int_0^\infty dr \exp[iqr] Q(r),$$

where the factor function  $Q(r)$  is real and continuous for  $r \geq 0$ . Anticipating that  $Q(r)$  and  $c(r)$  vanish beyond a distance  $R$  if the potential has a cutoff length and closures of the form Eq. (3.4) are used,  $c(r)$  is expressed in terms of the factor function for  $0 \leq r \leq R$  as

$$(3.6) \quad rc(r) = -Q'(r) + 2\pi\rho \int_r^R ds Q'(s) Q(s-r).$$

The Ornstein-Zernike relation is reexpressed for  $r > 0$ ,

$$(3.7) \quad rh(r) = -Q'(r) + 2\pi\rho \int_0^R ds(r-s)h(|r-s|)Q(s).$$

The structure factor for the HSS has originally been derived on a different route [58]. But it is also expressed by a particular simple factor function consisting of a parabola [68],

$$(3.8a) \quad Q(r) = ar^2/2 + br + c, \quad 0 \leq r \leq d,$$

with the parameters given by the external control parameters

$$(3.8b) \quad a = \frac{1+2\varphi}{(1-\varphi)^2}, \quad b = \frac{-3d\varphi}{2(1-\varphi)^2}, \quad c = \frac{-d^2}{2(1-\varphi)}.$$

The discontinuity in the derivative  $Q'(r)$  at  $r = d$  reflects the jump of  $g(r)$  at contact. One can use Eq. (3.7) to calculate this contact value explicitly  $g_q = Q'(r \rightarrow d_-)/d = a + b/d$  since  $Q'(r \rightarrow d_+) = 0$ .

The SHSS can also be cast in form of a factor function that is reminiscent of the above parabola,

$$(3.9a) \quad Q(r) = ar^2/2 + br + c, \quad 0 \leq r < d,$$

with however different parameters

$$(3.9b) \quad a = \frac{1+2\varphi-\mu}{(1-\varphi)^2}, \quad b = \frac{-3d\varphi+\mu d}{2(1-\varphi)^2}, \quad c = \frac{-d^2}{(1-\varphi)} + \frac{\lambda_B d^2}{12}, \quad \mu = \lambda_B \varphi(1-\varphi).$$

$\lambda_B$  is related to the effective temperature  $\tau$  which is also frequently called *stickiness parameter* [70]. Since  $Q(r) = 0$  for  $r \geq d$ ,  $Q(r)$  exhibits a discontinuity at  $r = d$  and the derivative  $Q'(d)$  incorporates a  $\delta$ -peak as do  $g(r)$  and  $c(r)$ , cf. Eq. (3.6). The Fourier transform  $c_q$ , Eq. (3.3b), acquires a term  $\propto \sin(qd)/q$  and leads to a divergence in the functional  $\mathcal{F}_q$ , cf. Eq. (2.7). One can resolve this difficulty by taking a finite range for the attraction [16].

## 2. Structure factors for short-ranged attraction within MSA

All the potentials considered below shall have a hard core repulsion at  $r = d$  and an attractive tail with potential depth  $u_0$  and potential range  $\Delta$ . The attraction may have the following functional form in the interaction shell,

$$(3.10) \quad U(r) = -u_0 \left[ \frac{d+\Delta-r}{\Delta} \right]^{n-1}, \quad d < r \leq d+\Delta.$$

This represents the SWS for  $n = 1$ , the triangular system (TRI) for  $n = 2$ , and the Asakura-Oosawa system (AOS) for  $n = 3$ . The external control parameters are packing fraction  $\varphi = \pi\rho d^3/6$ , attraction strength  $\Gamma = u_0/(k_B T)$ , and attraction range  $\delta = \Delta/d$ .

**2.1. First order solution within MSA.** Using  $h(r) + 1 = g(r) = 0$  within the hard-core diameter  $d$ , Eq. (3.7) splits into three equations. Abbreviating  $G(r) = rg(r)$ , one finds for the inner core

$$(3.11a) \quad Q'(r) = ar + b - 2\pi\rho \int_{r+d}^{d+\Delta} ds G(s-r)Q(s), \quad 0 \leq r \leq \Delta.$$

The middle interval in  $r$  resembles the result familiar from the HSS,

$$(3.11b) \quad Q'(r) = ar + b, \quad \Delta \leq r \leq d,$$

and for the attraction shell one obtains

$$(3.11c) \quad Q'(r) = ar + b - G(r) + 2\pi\rho \int_0^{r-d} ds G(r-s)Q(s).$$

For  $r \geq d + \Delta$  the factor function  $Q(r)$  vanishes. The coefficients  $a$  and  $b$  are defined by finite integrals over the factor functions,

$$(3.11d) \quad a = 1 - 2\pi\rho \int_0^{d+\Delta} ds Q(s), \quad b = 2\pi\rho \int_0^{d+\Delta} ds s Q(s).$$

To proceed, the MSA-closure relation from Eq. (3.4b) is substituted into Eq. (3.6) for the potentials (3.10) and an integration over  $r$  is performed, which yields for the attraction shell

$$(3.12a) \quad Q(r) = 2\pi\rho \int_r^{d+\Delta} ds Q(s) Q(s-r) + S(r), \quad d \leq r \leq d + \Delta,$$

$$(3.12b) \quad S(r) = \frac{u_0}{k_B T} \int_r^{d+\Delta} ds s \left[ \frac{d + \Delta - s}{\Delta} \right]^{n-1}, \quad d \leq r \leq d + \Delta.$$

The integration in Eq. (3.12b) can be done analytically for integer values  $n > 0$ . By substituting  $r = d + \Delta x$ , the different orders in  $\delta$  show up explicitly as  $x$  is of order unity,

$$(3.12c) \quad S(r) = (\Gamma\delta) \frac{d^2}{n} (1-x)^n \left[ 1 + \delta \frac{1+nx}{1+n} \right], \quad x = \frac{r-d}{\Delta}.$$

For keeping the product  $\Gamma\delta$  fixed, which is motivated by the limit taken in the SHSS, the leading order in  $\delta$  in Eq. (3.12c) is  $\delta^0$ . Retaining only terms of this order in Eq. (3.11) yields the leading-order solution, where the hard-core region is still represented by a parabola,

$$(3.13a) \quad Q(r) = ar^2/2 + br + c, \quad 0 \leq r \leq d,$$

and the attraction shell is given by a polynomial,

$$(3.13b) \quad Q(r) = \frac{\Gamma\delta d^2}{n} \left( \frac{d + \Delta - r}{\Delta} \right)^n, \quad d \leq r \leq d + \Delta,$$

with the parameters  $a = a_1$ ,  $b = b_1$ , and  $c = c_1$ ,

$$(3.13c) \quad a_1 = \frac{1+2\varphi}{(1-\varphi)^2} - \frac{12\varphi}{(1-\varphi)} \frac{\Gamma\delta}{n}, \quad b_1 = \frac{-3d\varphi}{2(1-\varphi)^2} + \frac{6\varphi d}{(1-\varphi)} \frac{\Gamma\delta}{n}, \quad c_1 = \frac{-d^2}{2(1-\varphi)} + \frac{\Gamma\delta d^2}{n}.$$

$Q(r)$  is now continuous at  $r = d$  and joins the solution  $Q(r) = 0$  for  $r \geq d + \Delta$  continuously at  $r = d + \Delta$ . This way, the problems associated with the limit of infinitely short-ranged attraction have been resolved. In the limit  $\delta \rightarrow 0$ , while keeping  $\Gamma\delta$  fixed, Baxter's solution (3.9) is recovered with  $\lambda_B = \Gamma\delta/n$ . The spinodal line is given from setting  $a = 0$ ,

$$(3.14) \quad \frac{\Gamma\delta}{n} = \frac{1+2\varphi}{12\varphi(1-\varphi)},$$

which yields a critical point at

$$(3.15) \quad \varphi^{\text{crit}} = (\sqrt{3} - 1)/2 \approx 0.366, \quad \Gamma^{\text{crit}} = \frac{n}{6\delta} \frac{1}{2 - \sqrt{3}}.$$

The value for the packing fraction is independent of the potential and higher than the value for the SHSS,  $\varphi^{\text{crit}} = (3/\sqrt{2} - 1) \approx 0.121$  [70]. Therefore, the critical point (3.15) is in better agreement with computer simulation data [71].

**2.2. Second order solution for the SWS in MSA.** For the case of the SWS,  $n = 1$ , also the next-to-leading order result has been derived [16, 41] and shall be quoted here. In this order, Eq. (3.13a) still holds for  $\Delta \leq r \leq d$  with modified parameters, but  $Q(r)$  at the inner core has an additional cubic term,

$$(3.16a) \quad Q(x) = \frac{1}{2}ax^2 + bx + c + 2\varphi(\Gamma\delta)^2 \cdot \delta \cdot \left[1 - \frac{x}{\delta}\right]^3, \quad 0 \leq x \leq \delta, \quad x = r/d.$$

and for the outer shell,  $1 \leq x \leq 1 + \delta$ , a quadratic term is added to the leading order result,

$$(3.16b) \quad Q(x) = (\Gamma\delta) \left[1 - \frac{x-1}{\delta}\right] + (\Gamma\delta) \delta \left\{ \frac{1}{2} \left[1 - \left(\frac{x-1}{\delta}\right)^2\right] + 6\varphi c_1 \left[1 - \frac{x-1}{\delta}\right]^2 \right\}.$$

The parameters also acquire terms of higher order in  $\delta$ ,  $a = a_1 + (\Gamma\delta) \delta a_2$ ,  $b = b_1 + (\Gamma\delta) \delta b_2$ , and  $c = c_1 + (\Gamma\delta) \delta c_2$ . Setting  $d$  to unity these parameters read

$$(3.16c) \quad a_1 = [6\varphi(5\varphi - 2) - 72c_1\varphi^2(1 - \varphi)] / (1 - \varphi)^2,$$

$$(3.16d) \quad b_1 = [9\varphi(1 - 2\varphi) + 36c_1\varphi^2(1 - \varphi)] / (1 - \varphi)^2,$$

$$(3.16e) \quad c_1 = [1 - 7\varphi + 12c_1\varphi(1 - \varphi)] / (2(1 - \varphi)).$$

The MSA and the PYA in Eq. (3.4) differ only in the treatment of the direct correlation function  $c(r)$  in the range  $d \leq r \leq d + \Delta$ . Considering only a small attraction range,  $\Delta \ll d$ , the pair distribution function in that range can be approximated by the value at contact,  $g(r) \approx g(r = d)$  and the direct correlation function for the PYA is  $c_{\text{PYA}} = g_d(1 - \exp[-\Gamma])$ . Identifying  $c_{\text{PYA}}$  with the value for the MSA for an effective value for the parameter  $\Gamma$ ,  $c_{\text{MSA}} = -\Gamma^{\text{eff}}$ , yields a mapping of the external control parameter  $\Gamma$  that allows to calculate a solution within MSA where another solution for the PYA exists [16],

$$(3.17) \quad \Gamma_{\text{eff}}^{\text{MSA}} \approx [1 - \exp(-\Gamma)] g_d.$$

**2.3. Numerical solution.** To check the validity of the expansion presented above and for covering also larger values for  $\Delta$ , the structure factors are also calculated numerically. For a numerical treatment, the closure relations, Eqs. (3.4) are substituted into Eq. (3.6) and Eq. (3.11c). For the PYA this leads to

$$(3.18a) \quad e^{U(r)/k_{\text{B}}T} G(r) = ar + b - 2\pi\rho \int_r^{d+\Delta} ds Q'(s) Q(s-r) + 2\pi\rho \int_0^{r-d} ds G(r-s) Q(s), \quad d \leq r \leq d + \Delta.$$

For the MSA closure one obtains

$$\begin{aligned}
 G(r) = & \quad ar + b - 2\pi\rho \int_r^{d+\Delta} ds Q'(s) Q(s-r) \\
 & + 2\pi\rho \int_0^{r-d} ds G(r-s) Q(s) \\
 (3.18b) \quad & -U(r) \frac{r}{k_B T}, \quad d \leq r \leq d + \Delta.
 \end{aligned}$$

The potential  $U(r)$  is taken from Eq. (3.10) and for the solution of the respective closure relations, Eqs. (3.11) and Eq. (3.18a) or Eq. (3.18b), are solved iteratively for  $Q(r)$  and  $G(r)$  [16]. The three intervals in  $r$  are discretized into a grid of 1000 equally spaced points. The iteration is terminated if the relative error in the parameter  $a$  between the successive steps is smaller than  $10^{-12}$ .  $\hat{Q}(q)$  is obtained by a simplified Filon integration [72] of Eq. (3.5b), and  $S_q$  is then given by Eq. (3.5a).

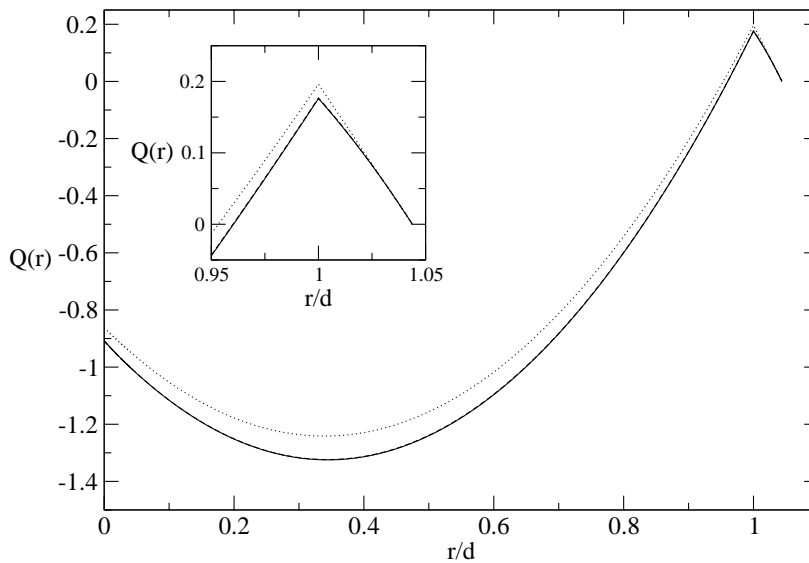


FIGURE 3.1. Factor function  $Q(r)$  for the SWS in MSA at the  $A_4$ -singularity (4.1). The leading order expansion, Eq. (3.13), is shown as dotted line, the next-to-leading order, Eq. (3.16), as dashed line which is almost indistinguishable from the numerical result, Eq. (3.18b), (full line). The inset views an enlargement around  $r/d = 1$ .

For the SWS we compare the numerical solution in MSA with the analytical ones in Fig. 3.1. We use the factor functions for this comparison since  $Q(r)$  is more sensitive than  $S_q$  for which examples are shown later in Fig. 4.8. The control parameters are chosen at the special point given by Eq. (4.1) which will be important later on. The agreement between numerical solution (full line) and the next-to-leading-order result (3.16) (dashed) is excellent, both curves cannot be distinguished in the large panel and also in the inset they are quite close. When larger well widths are considered the deviations increase but do not exceed the 3%-level



for  $\delta = 0.25$ . The dotted line shows the result for the SWS in MSA when only the leading-order result of Sec. 2.1 is considered. The qualitative features of  $Q(r)$  are still captured reasonably well but the deviations are getting larger and reach 8% at the minimum around  $r = 0.5$  and 13% at the attraction shell,  $r/d = 1$ . The results for the other systems, TRI and AOS are similar.

### 3. Structure factors for short-ranged interaction within PYA

Looking at the functional form of Eq. (3.13) and the fact that in a reasonable region in control-parameter space MSA and PYA can be mapped on top of each other, it seems possible to apply the expansion from above also to the PYA. Since the PYA is also reasonable for repulsive interaction, we set  $\Gamma = u_0/(k_B T)$  in the following, where  $u_0$  can be both positive and negative. Then  $\Gamma > 0$  implies repulsion and  $\Gamma < 0$  denotes attraction.

For the SWS in zeroth order at  $r = 1$  for both MSA and PYA,  $Q(r)$  changes from the parabola known from the HSS to a linear function between  $r = d$  and  $r = d + \Delta$ . This motivates the following Ansatz for the factor function in that region,

$$(3.19) \quad Q(r) = -\frac{Q_1}{n} \left( \frac{d + \Delta - r}{\Delta} \right)^n, \quad d \leq r \leq d + \Delta.$$

For the MSA, the prefactor would be  $Q_1 = -\Gamma \delta d^2$ . The derivative is

$$(3.20) \quad Q'(r) = Q_1/\Delta \left( \frac{d + \Delta - r}{\Delta} \right)^{n-1}, \quad d < r < d + \Delta,$$

and  $Q_1$  is positive for repulsion and negative for SWS. The contact value to leading order is given by the discontinuity in  $Q'(r)$  at  $r = d$ ,

$$(3.21) \quad d g_d = G(r = d) = Q'(r \rightarrow d_-) - Q'(r \rightarrow d_+).$$

As in the case for the MSA, for the PYA the integrals in Eq. (3.18a) are of higher order in  $\delta$ , so the contact value is given by

$$(3.22) \quad G(d) = e^{-\Gamma}(a d + b).$$

$Q'(r \rightarrow d_-)$  is taken from Eq. (3.11b) and combined with Eqs. (3.20) and (3.22). This yields

$$(3.23) \quad Q_1 = (a d + b) \Delta (1 - e^{-\Gamma})$$

for all  $n \geq 1$ . For the parameters  $a$  and  $b$ , the contribution from the integral of Eq. (3.11d) is of higher order in  $\Delta$  for the interaction shell. Therefore, the integral runs only over the parabola as in Eq. (3.9a) and contains the interaction as well as the specific closure only in the definition of the parameter  $c$ . The other parameters read

$$(3.24a) \quad a = \left[ \frac{1 + 2\varphi}{(1 - \varphi)^2} \right] - \frac{6\varphi}{d^2(1 - \varphi)^2} \{d^2 + 2(1 - \varphi)c\},$$

$$(3.24b) \quad b = \left[ \frac{-3d\varphi}{2(1 - \varphi)^2} \right] + \frac{3\varphi}{d(1 - \varphi)^2} \{d^2 + 2(1 - \varphi)c\}.$$

The first terms in the brackets show again the values for the HSS. For the MSA,  $c = c_{\text{HSS}} - \delta \Gamma d^2/n$ , for the PYA we get

$$(3.24c) \quad c = c_{\text{HSS}} - \frac{Q_1}{n} = c_{\text{HSS}} - (a d + b) y, \quad y = \frac{\delta}{n}(1 - e^{-\Gamma}),$$

with  $c_{\text{HSS}} = -0.5 d^2/(1 - \varphi)$ . The solution of Eqs. (3.24) and (3.23) yields the final form of the parameters in leading order,

$$(3.25a) \quad a = a_{\text{HSS}} + \frac{6 \varphi (2 + \varphi) y}{(1 - \varphi)^2 \{(1 - \varphi) - 6 \varphi y\}},$$

$$(3.25b) \quad b = b_{\text{HSS}} - \frac{3 d \varphi (2 + \varphi) y}{(1 - \varphi)^2 \{(1 - \varphi) - 6 \varphi y\}},$$

$$(3.25c) \quad c = c_{\text{HSS}} - \frac{d^2 \varphi (2 + \varphi) y}{2 (1 - \varphi) \{(1 - \varphi) - 6 \varphi y\}}.$$

Different from the MSA solution, within PYA the coupling strength  $\Gamma$  also appears in the denominator and introduces a solvability condition to the parameters in Eq. (3.25),

$$(3.26) \quad \varphi^{\max} [1 + 6 \frac{\delta}{n} (1 - e^{-\Gamma})] = 1.$$

For the HSS,  $\Gamma = 0$ , the boundary  $\varphi^{\max} = 1$  is out of the region of interest. For attraction,  $\Gamma < 0$ , the square brackets are larger than unity and do also not cause any limitation. For repulsion,  $\Gamma > 0$ , solvability is bounded since now  $e^{-\Gamma} \leq 1$ . This boundary  $\varphi^{\max}$  in first order is indeed seen as an instability when solving the structure factor numerically for repulsion according to the algorithm outlined in Sec. 2.3. Inspection of the spinodal lines resulting from Eq. (3.25a) by setting  $a = 0$  reveals that for PYA in this order a critical point is absent in Eq. (3.25) which is clearly inferior to the MSA result.

Figure 3.2 shows the same comparison as in Fig. 3.1 for the PYA. The numerical solution is again shown as full line and compared to the leading-order result from Sec. 3 (dotted), which deviates by 15% at the minimum and by 25% at the attraction shell,  $r/d = 1$ . This is about twice as large as for the corresponding result for the MSA. The definition of an effective attraction strength from Eq. (3.17) allows for comparison to the structure factor of Sec. 2.2 for  $\Gamma_{\text{eff}}^{\text{MSA}} = 5.089$  which is shown by the chain line. The deviations from the numerical solution for PYA are 8% and 15% at the minimum and the attraction shell, respectively. Comparing MSA (dashed line) and PYA at their values for the  $A_4$ -singularity, Eqs. (4.1) and (4.2), shows that the factor functions and hence the resulting structure factors at this points singled out by the later MCT calculations are remarkably similar for both closure relations.

After discussing different closure relations for the SWS above, we compare the factor functions for different potentials fixing again the control parameters by the special point of an  $A_4$ -singularity. The solution of the SWS within PYA from Fig. 3.2 is used as a reference. We choose the numerical solution of the TRI in PYA at the point from Tab. 1 and find deviations of less than 2% at the minimum and 9% at  $r/d = 1$ . It is seen nicely in the inset that the solution for the TRI follows a different functional form than the solutions for the SWS, hence corroborating the form (3.13) and also justifying the Ansatz (3.19). Since the structure factors in leading order, Eq. (3.13), are used for  $n = 1, 2, 3$ , in Ch. 4, we check if these are seriously inferior to the next-to-leading result or the numerical solutions. The result for the SWS according to Eq. (3.13) at the  $A_4$ -singularity, cf. Tab. 1, is displayed as dashed line and shows that the difference to the numerical solution is negligible. Therefore, even the leading approximation (3.13) can be expected to

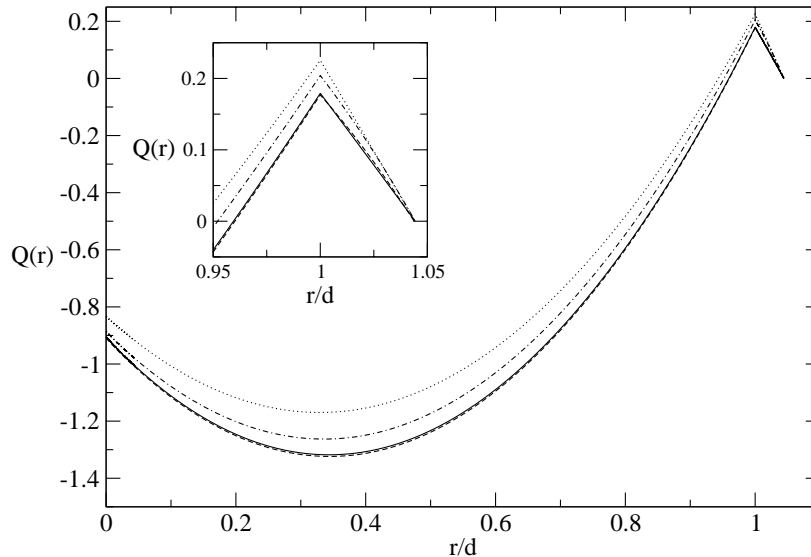


FIGURE 3.2. Factor function  $Q(r)$  in PYA at the point specified in Eq. (4.2). The numerical and the analytical solution (3.19) are shown as full and dotted line, respectively. Factor functions  $Q(r)$  in MSA, Eq. (3.16), yield the chain line when evaluated with the effective coupling  $\Gamma_{\text{eff}}^{\text{MSA}} = 5.089$  according to Eq. (3.17), and the dashed line when calculated for the point specified in Eq. (4.1). The inset shows the region at  $r/d = 1$  enlarged and uses the same line styles.

yield an accurate description of the structure factor in the region we are interested in.

#### 4. Remarks

Having at hand the structure factor in analytical yet approximate form like in Sec. 2.2 might seem superfluous when considering the superiority of the numerical solution if the accuracy of the result is concerned. However, the analytical form has two main advantages. First, the formulation in terms of the factor functions as done above immediately leads to the limit of mechanical stability for simply setting  $a = 0$ . For the rather simple approximation schemes used here, Eq. (3.4), the resulting spinodal is not particularly accurate but allows to control where the input breaks down in later application. Obtaining a spinodal line from the numerical solution requires considerable effort. In addition to the determination of the spinodal line, the analytical solution offers a second advantage: The analysis of the singularities in the factor function makes it possible to derive the asymptotic large- $q$  behavior of  $c_q$  by using a generalization of the Riemann-Lebesgue theorem [73]. This was carried out for the structure factor of Sec. 2.2 and shows that for large enough  $q$ , the direct correlation function  $c_q$  vanishes like  $1/q^2$  as in the HSS [16]. Below some upper cutoff  $q_u = \pi/\delta$ , a slower decrease of  $1/q$  is observed for  $c_q$ . For the limit  $\delta \rightarrow 0$  as done in the SHSS,  $q_u$  diverges and the  $1/q$ -behavior extends to infinity. Since  $c_q$  is a vital input into the vertices of Eq. (2.7e) the large- $q$  asymptote

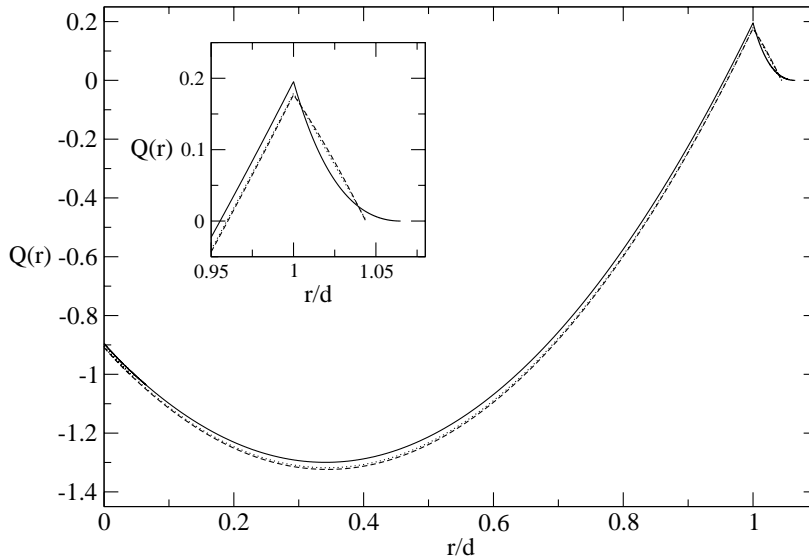


FIGURE 3.3. Factor functions for different approximations and potentials. The numerical result for the SWS in PYA is copied from Fig. 3.2 as dotted curve. The dashed line shows the MSA result for the SWS in leading order (3.13) at the point specified in Tab. 1 on page 41. The numerical solution of the triangular potential (TRI) in PYA is shown as full line for the values indicated in Tab. 1. The inset shows an enlargement of the full panel around  $r/d = 1$ .

determines the convergence of the functional  $\mathcal{F}_q$  in Eq. (2.7d). For  $c_q \propto 1/q$  the integral in Eq. (2.7d) leads to divergent results, and for potentials with finite-ranged attractive potentials a cutoff large enough in  $q$  is required to include the  $1/q$  decay. This explains why for smaller  $\delta$  a higher cutoff in the numerical solution of the mode-coupling functional is necessary. For the same reason, the SHSS cannot be solved within MCT without introducing a numerical cutoff that renormalizes the range of the attraction [14].

For later reference the hard-core Yukawa system (HCY) shall also be introduced here with the convention that  $\delta$  is chosen as the inverse of the conventional screening parameter  $b$ ,

$$(3.27) \quad U(r)/(k_B T) = -\Gamma \exp[-(r-d)/(\delta d)]/(r/d), \quad d < r,$$

The structure factor for that potential is evaluated analytically in the mean-spherical approximation [67].

## Glass-transition diagrams

In this chapter, the structure-factor theory provided in Ch. 3 is used as input for the MCT equations from Ch. 2. The glass-transition diagrams are determined and the static properties associated with the glass-transition singularities are presented. The glass-transition diagram for the square-well system (SWS) was already discussed comprehensively where also further details can be found [16]. The presentation here shall be focused on the higher-order singularities.

The glass-transition diagram for the SWS is complemented by a discussion of the onset of the reentry phenomenon and a comparison of different potentials and closure relations for the structure factors. The comparison of different potentials in Sec. 2 serves two goals. First, the topological stability of the  $A_4$ -singularity is demonstrated by comparing the location and characteristic features of the singularity for a number of potentials which can be regarded as deformations of the potential of the SWS. Second, quantitative changes and qualitative trends can be identified upon variation of the potential, which narrow down deviations that can be expected if the precise form of the potential is unknown as is usually the case in experiments.

The comparison of different closure relations for  $S_q$  gives a margin for the deviations in the MCT results introduced by the derivation of the static structure factor. We compare the results for the closure relations PYA and MSA which incorporate the external control parameters differently. It is found that only the coupling strength  $\Gamma$  has to be rescaled to reasonably match the results for PYA and MSA.

### 1. Glass-transition diagram of the SWS

Calculating glass-transition singularities requires finding the bifurcation points of Eq. (2.8) for varying the control parameters. This is done by the iteration procedure  $f_q^{(n+1)} = \mathcal{F}_q[\mathbf{V}, f_q^{(n)}] / (1 + \mathcal{F}_q[\mathbf{V}, f_q^{(n)}])$  for  $n = 0, 1, \dots$  to determine the set of  $f_q(\mathbf{V})$  at a specific point in control-parameters space. Starting the iteration with  $f_q^{(0)} = 1$  assures that with increasing  $n$  the  $f_q^{(n)}$  decrease monotonically towards the glass-form factors  $f_q(\mathbf{V})$  respecting the maximum theorem in Eq. (2.9) [57]. The method to locate glass-glass-transition points and endpoints is outlined in Appendix B. For the determination of the singularities of the SWS the structure factor from Eq. (3.16) will be used in the following unless stated differently.

Figure 4.1 shows the glass-transition diagram containing the singularities occurring in the SWS. The diagram is organized in cuts of constant well width  $\delta = 0.117, 0.06, 0.04381, 0.03, \text{ and } 0.02$ . For vanishing coupling  $\Gamma$  – which is equivalent to infinite temperature – all curves start at the limiting value of the HSS as indicated,

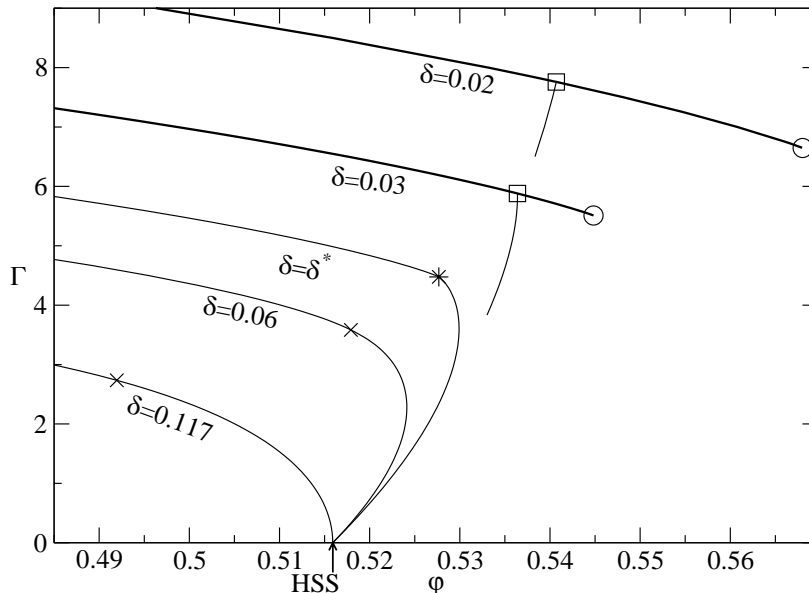


FIGURE 4.1. Glass-transition diagram for the SWS using the structure factor from Eq. (3.16). Five cuts through the three-dimensional diagram are shown for constant well widths  $\delta$  as curves for attraction strength  $\Gamma$  versus packing fraction  $\varphi$ . All curves start at the limit of the HSS for  $\Gamma = 0$  as indicated by the arrow. For  $\delta = 0.117$  and  $0.06$  the curves  $\varphi^c(\Gamma)$  vary smoothly as  $\Gamma$  is increased. The line  $\delta = \delta^* = 0.04381$  hits the  $A_4$ -singularity (\*) specified in Eq. (4.1). Curves for  $\delta > \delta^*$  exhibit a crossing point ( $\square$ ) and an  $A_3$ -endpoint singularity ( $\circ$ ) as demonstrated for  $\delta = 0.03$  and  $\delta = 0.02$  where part of the glass-transition line has been erased to avoid cluttering the figure. The maximum in the exponent parameter  $\lambda$  is assumed at the points marked by crosses ( $\times$ ) for the cuts with  $\delta > \delta^*$ .

$\varphi_{\text{HSS}}^c = 0.516$ . How critical packing fraction  $\varphi^c$  changes when increasing the attraction strength  $\Gamma$  depends on the well width. There is a characteristic range  $\delta_{\text{reentry}}$  separating the case where  $\varphi^c(\Gamma)$  always has a negative slope for  $\delta > \delta_{\text{reentry}}$ . For  $\delta < \delta_{\text{reentry}}$  the curve  $\varphi^c(\Gamma)$  starts with a positive slope at  $\Gamma = 0$ . For the SWS,  $\delta_{\text{reentry}} = 0.117$  and the transition curve for  $\delta = 0.117$  smoothly bends over from the liquid-glass transitions driven by repulsion, where a change in  $\varphi$  leads to the arrest, and the transitions driven by attraction, where a change in  $\Gamma$  is responsible for the arrest.

For  $\delta = 0.06$  another smooth line of liquid-glass-transition singularities is found. This line starts with positive slope in  $\varphi^c(\Gamma)$  and displays the reentry phenomenon already discussed for the SHSS [14]: For fixed density, say  $\varphi = 0.52$ , an arrested state is found for small  $\Gamma \lesssim 1$ . Upon increasing the attraction, around  $\Gamma \approx 1$  the glass is melted and a region of liquid states is encountered before at  $\Gamma \approx 3.5$  another liquid-glass transition takes place. This defines a maximum in  $\varphi^c$  where liquid states

can exist. For  $\delta = 0.06$  this maximum is at  $(\varphi_{\max}^c, \Gamma_{\max}^c) = (0.524, 2.25)$ . For lower  $\delta$  this maximum increases further in  $\varphi$ .

The reentry phenomenon can be related to a dimerization effect where two particles gain a higher probability of being closer together when the attraction is increased. This leaves additional free volume to other particles and thus weakens the cage. This needs to be compensated by a higher density to obtain a glassy state again [14]. For the SWS this can be inferred from the changes in the static structure factor [16]: For higher values of  $\Gamma$  the first peak of the structure factor is lower at the same density and causes a decrease in the coupling vertices of the mode-coupling functional  $\mathcal{F}$  in Eq. (2.7e). To ensure that changes at the peak of the structure factor and not the large- $q$  tail or contributions from small wavelengths are responsible for the reentry, one cuts off the functional at a lower bound of  $q = 4$  and an upper bound of  $q = 20$  and finds that the liquid-glass-transition lines do not change significantly and still display the maximum in  $\varphi^c$ . We conclude that the attraction introduces modifications on the length scale  $d$  which is represented by the peak of the structure factor.

For smaller  $\delta$  and larger attraction strength  $\Gamma$ , contributions from larger  $q$ -values play a more important role, cf. Ch. 3. For the case of  $\delta = 0.02$  and  $0.03$  it is seen in Fig. 4.1 that for these well widths the horizontal and vertical parts of the line of liquid-glass transitions do no longer join smoothly but intersect at a crossing point which is indicated by a square. At the crossing the vertical line stops and the horizontal line extends into the arrested region as a line of glass-glass-transition singularities and eventually terminates in an  $A_3$ -endpoint singularity. In that region, bonding among the particles can become that strong that an additional transition is triggered. Below the glass-glass-transition line the system is arrested because the repulsion of the neighboring particles keeps the particle from leaving the cage formed by its neighbors. Above the glass-glass-transition line the particles localize on a smaller length scale given by the well width  $\delta$  due to the formation of bonds.

We have seen that the liquid-glass-transition lines in the SWS can be smooth for relatively large  $\delta$  or exhibit a crossing for small  $\delta$ . In between there is an exceptional value  $\delta = \delta^*$  where this qualitative change in the transition lines occurs. From that specific point  $\mathbf{V}^* = (\varphi^*, \Gamma^*, \delta^*)$ , where the crossing appears, a line of  $A_3$ -singularities emerges. This special point is the  $A_4$ -singularity and is marked by a star in Fig. 4.1. For the SWS the values for the  $A_4$ -singularity are

$$(4.1) \quad \varphi^* = 0.52768, \quad \Gamma^* = 4.4759, \quad \delta^* = 0.04381.$$

This point in the three dimensional control-parameter space organizes the entire glass-transition diagram and will be of central importance for the dynamics. We note that the values for  $\delta$  where glass-glass transitions occur are quite similar to the ones found in the SWS for isostructural phase transitions which occur between an expanded and a condensed fcc-crystal when  $\delta \lesssim 0.07$  [23, 24].

The attraction dominated transitions predicted by MCT were proposed to be relevant for the transition from a liquid to a gel state by Bergenholtz and Fuchs [15]. To avoid clumsy wording in the following, we will call attraction dominated glass transitions *gel* transitions and reserve the term *glass* transition to the repulsion dominated liquid-glass transitions.

Within MCT the arrested states can be characterized by the glass-form factors  $f_q$ . For the SWS these are shown for  $\delta = 0.06$ ,  $\delta^*$ , and  $0.03$  in Fig. 4.2. To

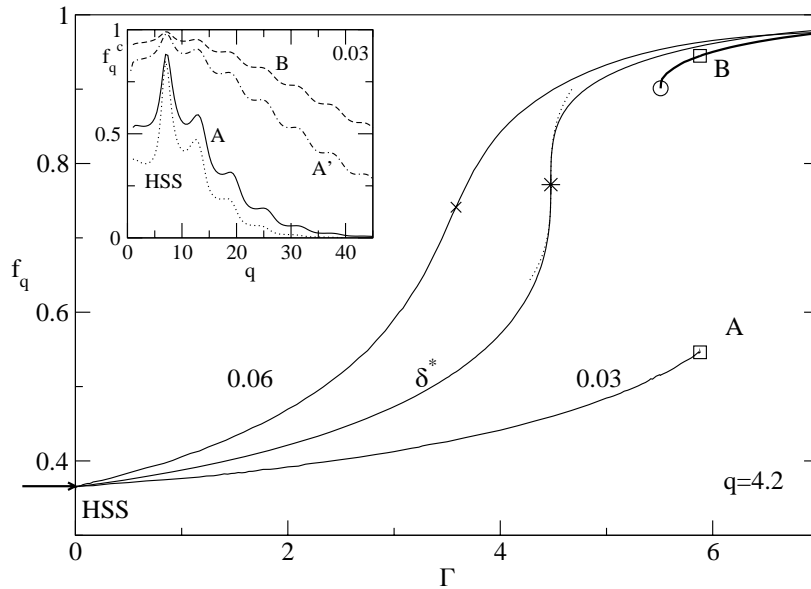


FIGURE 4.2. Glass-form factors  $f_q^c$  at  $q = 4.2$  for the SWS along the constant- $\delta$  cuts from Fig. 4.1 for  $\delta = 0.06$ ,  $\delta^*$ , and  $0.03$ . A cross ( $\times$ ) marks the point of the maximum in  $\lambda$  for  $\delta = 0.06$ . At the  $A_4$ -singularity ( $*$ ), the dotted line shows the variation  $(f^c - f^*) \propto (\Gamma - \Gamma^*)^{1/3}$ . For  $\delta = 0.03$ , two distinct lines are present: From  $\Gamma = 0$  to the crossing ( $\square$ ) at  $\Gamma = \Gamma^\square = 5.88$  the lines of liquid-glass transitions are shown by the light full line. A line of gel transitions (heavy full line) from high values for  $\Gamma$  extends above the crossing and terminates in the  $A_3$ -singularity ( $\circ$ ). The two different values at the crossing point are labeled A and B. The inset shows the two different distributions of  $f_q^c$  at the crossing point for A (full line) and B (dashed line) in comparison to the critical values for the HSS (dotted line). The dash-dotted distribution labeled A' shows the glass-form factors  $f_q$  at  $(\varphi, \Gamma, \delta) = (0.545, 5.5, 0.03)$ .

illustrate the behavior of the distribution of  $f_q^c$  for varying control parameters the value for  $q = 4.2$  is selected but the trends explained in the following apply to all wave vectors. From the limit of vanishing attraction we start from the HSS and cross over smoothly to the gel transitions for  $\delta = 0.06$ . The curve through the  $A_4$ -singularity ( $*$ ) for  $\delta = \delta^*$  is still continuous in the  $f_q^c$  but exhibits a divergent derivative because close to the singularity the variation of the glass-form factor follows a cubic-root law,  $(f^c - f^*) \propto (\Gamma - \Gamma^*)^{1/3}$ , that is characteristic for the  $A_4$ -singularity. The dotted line displays the fit  $0.22(\Gamma - \Gamma^*)^{1/3}$  to the curve. For  $\delta = 0.03$  the variation of the glass-form factors is discontinuous and at the crossing point ( $\square$ ) we encounter two values for  $f_q^c$ . Due to the maximum theorem (2.9) only the higher one is a glass-form factor. Slightly below the crossing we find state A with lower  $f_q^c$ , and at the crossing, state B implies higher  $f_q^c$ . This jump in the  $f_q^c$  is carried on along the glass-glass transition where the  $f_q^c$  decrease as the  $A_3$ -singularity is approached. Just below that line in the glassy regime the  $f_q$  increase



with a square root law (2.10) from their values  $f_q^c$  on the glass-transition. This is illustrated in the inset that shows the evolution from state A to state A'. At the  $A_3$ -singularity the critical values for the gel transition  $f_q^c$  and the noncritical values for the glass transition  $f_q$  are the same and the jump disappears. The inset of Fig. 4.2 shows also the wave-vector dependence of the  $f_q^c$  at the crossing point and for comparison at the HSS at  $\varphi^c = 0.516$ . We see that  $f_q^c$  at the glass state A is quite similar to the HSS. The values at the structure factor peak are almost unchanged and the wings are enhanced by up to 30%. We notice the distribution is becoming broader,  $f_q^c = 0.5$  is assumed for  $q \approx 9$  in the HSS and for  $q \approx 14$  for state A. For state B this happens around  $q \approx 46$  which signals a drastic change in the localization length for the arrested particle at the crossing.

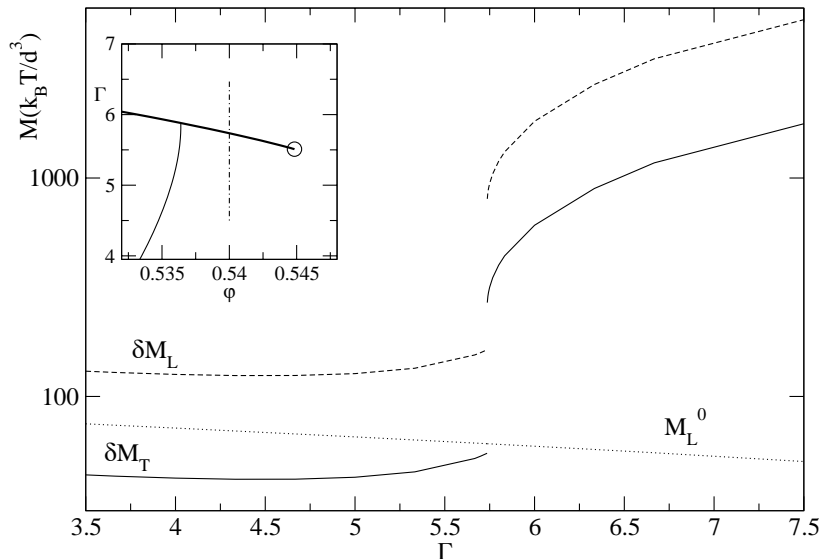


FIGURE 4.3. Longitudinal and transversal elastic moduli at a glass-glass transition for  $\delta = 0.03$ ,  $\varphi = 0.54$  and varying  $\Gamma$ . The lines show the mechanical moduli  $M_L^0$  (dotted),  $\delta M_T$  (full) and  $\delta M_L$  (dashed). The line of glass-glass transitions is crossed at  $\Gamma = 5.736$  as seen in the inset where part of the glass-transition diagram has been replotted from Fig. 4.1 for  $\delta = 0.03$ .

Also the glass-form factors for small  $q$  jump at the crossing as seen in the inset of Fig. 4.2. The zero wave-vector limit of  $f_q$  is related to the longitudinal elastic modulus. The additional contributions to the elastic moduli due to structural arrest are given by Eqs. (2.17). As shown in the inset of Fig. 4.3 we shall look at the moduli for a path at constant  $\varphi = 0.54$  for  $\delta = 0.03$  within the arrested region that eventually crosses the glass-glass-transition line. We observe in Fig. 4.3 that  $M_L^0$ , Eq. (2.15), varies regularly and is in particular unaffected by the glass-glass transition at  $\Gamma = 5.736$ . The additional contributions are different. For increasing the coupling strength  $\Gamma$ , both  $\delta M_T$  and  $\delta M_L$  exhibit a minimum around  $\Gamma \approx 4.5$  that is reminiscent of the reentry phenomenon, since the glass-form factors are smaller at states closer to the liquid-glass transition. At the glass-glass transition



on the glass-transition line. Thus for such small values for  $\delta$ , the largest fraction of the increase in  $\lambda$  takes place on the glass-glass-transition line.

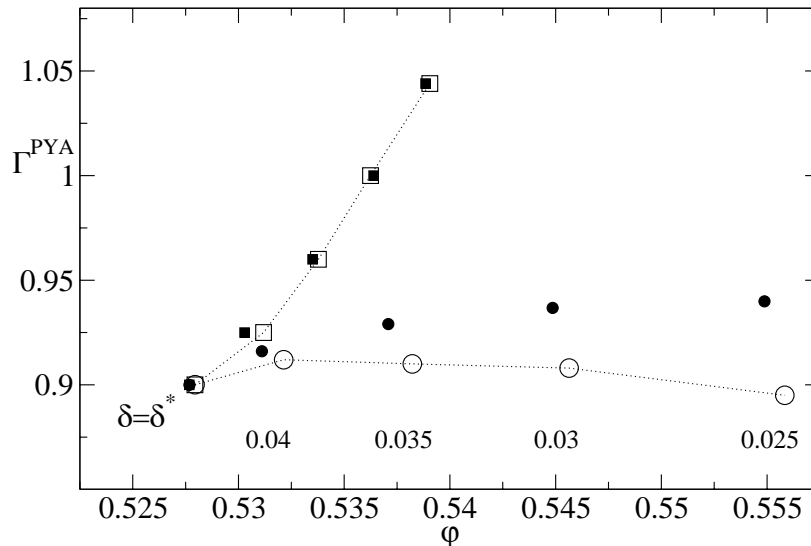


FIGURE 4.5. Comparison of PYA and MSA at  $A_4$ - and  $A_3$ -singularities for the SWS for  $\delta = \delta^*$ , 0.04, 0.035, 0.03, and 0.025. The PYA results are shown with empty symbols for the endpoints ( $\circ$ ) and crossing points ( $\square$ ). The crossing points for MSA ( $\blacksquare$ ) are scaled on top of the PYA result by a  $\delta$ -dependent prefactor,  $\Gamma^{\text{PYA}} = y(\delta) \Gamma^{\text{MSA}}$  with  $y(\delta) \approx 0.1 + 2.34 \delta$ , determined from a least-square fit. The  $A_3$ -endpoints of the MSA ( $\bullet$ ) are scaled in the same way.

Before comparing the SWS to other potentials we examine briefly how the results considered so far depend on the chosen closure relation of the MSA from Eq. (3.4b). For the comparison we use the numerical solution of the structure factor in PYA, Eq. (3.4a). For the PYA the  $A_4$ -singularity is located at

$$(4.2) \quad \varphi^* = 0.52851, \quad \Gamma^* = 0.90275, \quad \delta^* = 0.0442.$$

The location of the  $A_4$ -singularity in PYA and MSA was calculated and compared in Ref. [16] and deviations from the values published there and the one reported here are due to refined numerical procedures and do not exceed 6%. PYA and MSA yield practically the same results for the SWS concerning the glass-transition diagram, the glass-form factors and the exponent parameter [16]. The main difference between the results in PYA and MSA is the treatment of the control parameter  $\Gamma$  and the values for  $\Gamma^*$  disagree considerably in Eqs. (4.1) and (4.2). However, the comparison of the factor functions for the control parameters from Eq. (4.1) and Eq. (4.2) as done in Fig. 3.2 reveals excellent agreement of PYA and MSA at the respective  $A_4$ -singularities already for the static input. The mapping to an effective coupling, Eq. (3.17), yields  $\Gamma_{\text{eff}}^{\text{MSA}} = 5.1$  which is close by 10% to the result in Eq. (4.1).

The discussion in the paragraph above suggests a mapping of the glass-transition diagrams for PYA and MSA by  $\Gamma$ . Figure 4.5 shows such a mapping for  $\delta \leq \delta^*$  for crossing points and higher-order singularities. We keep  $\varphi$  and  $\delta$  fixed and multiply  $\Gamma$  for the MSA-result with a prefactor  $y(\delta)$  to match it with the result from the PYA-calculation. This procedure keeps the limit for the HSS at  $\Gamma = 0$  untouched which is the same in both closures. The endpoint singularities appear roughly at the same  $\Gamma$  after the mapping. The dependence of the prefactor on  $\delta$  is varying regularly between  $y(\delta) \approx 0.2$  at the  $A_4$ -singularities and  $y(\delta) \approx 0.15$  for  $\delta = 0.02$  which can be cast in a  $\delta$ -dependent prefactor  $y(\delta) \approx 0.1 + 2.34 \delta$ . In comparison to the PYA, the MSA underestimates the coupling in  $\Gamma$  which is compensated by higher values of  $\Gamma$  in the results of MCT. This discrepancy gets more pronounced for smaller  $\delta$  and hence  $y(\delta)$  is decreasing.

## 2. Glass-transition diagrams for different potentials

All glass-transition singularities calculated in MCT are topologically stable meaning that variations in the control parameters might change smoothly the location and properties of the singularities but do not challenge their existence. In the following we will see how this topological stability is reflected quantitatively. Despite the global stability, changing the form of the potential might still introduce deviations large enough to be relevant for experiment and simulation.

The comparison shall be done for the potentials (3.10) for  $n = 1, 2, 3$  using the MSA closure relation (3.4b) and the leading-order expansion in  $\delta$ , Eq. (3.13). An additional potential is provided by the HCY in Eq. (3.27) which is also solved for the MSA [67]. The structure factors in PYA are calculated numerically for  $n = 1, 2, 3$  from Eq. (3.18a). For all the potentials and the mentioned different closure relations, the glass-transition singularities like the ones presented in Fig. 4.1 have been calculated and as one additional example Fig. 4.6 displays the glass-transition scenario for the HCY. The scenario is quite similar to the one for the SWS. Starting with larger  $\delta$  there is again a value  $\delta_{\text{reentry}} = 0.30$  where the reentry phenomenon sets in for  $\delta \leq \delta_{\text{reentry}}$ . The curve for  $\delta = 0.30$  ends when  $\Gamma$  is increased until hitting the spinodal line where  $S_q$  diverges for  $q = 0$ . That this was not observed for the corresponding curve for the SWS which reflects the general trend that spinodal lines occur at lower  $\Gamma$  for potentials of longer range [74]. The curve for  $\delta = 0.0250$  represents again a cut through the diagram typical for  $\delta > \delta^*$ . On these lines the exponent parameter is smaller than unity,  $\lambda < 1$ , and for the present case assumes a maximum of  $\lambda = 0.96$ . For the cut  $\delta = \delta^* = 0.0173$  the curve hits the  $A_4$ -singularity indicated by a star (\*). For smaller values of  $\delta < \delta^*$ , the constant- $\delta$  cut consists out of two pieces, a line of glass transitions that terminates at a crossing point ( $\square$ ) and a line of gel transitions that extend into the glassy region as glass-glass transitions and finally terminate at an  $A_3$ -singularity. The line of  $A_3$ -singularities is shown by circles ( $\circ$ ). For  $\delta = 0.0100$  the transition lines are shown as light full line for the glass transition and as heavy full line for the gel transition. Some transition lines in the the HCY have been discussed before, however, without calculating the locations of higher-order singularities [15, 75, 76].

A comparison of the Figs. 4.1 and 4.6 demonstrates the topological stability of the singularities of MCT when the square-well potential is deformed to the Yukawa attraction and the transition diagrams are indeed very similar. This is also true for the glass-transition diagrams for the remaining two systems, TRI and AOS,

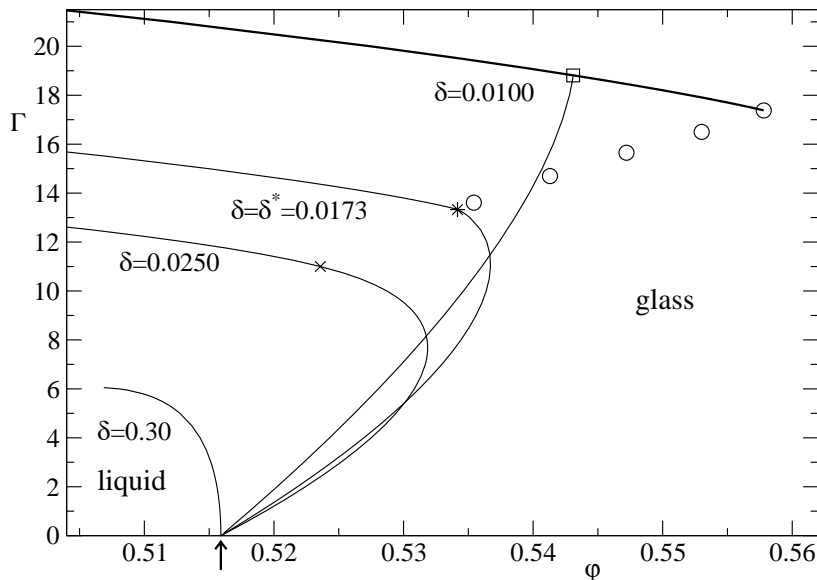


FIGURE 4.6. Glass-transition diagram for the hard-core-Yukawa system (HCY), Eq. (3.27). The  $\Gamma$  versus  $\varphi$  curves show cuts through the surfaces of glass-transition singularities for fixed attraction-range parameter  $\delta$  as indicated. The line for  $\delta = \delta^* = 0.0173$  hits the  $A_4$ -singularity (\*). The line for  $\delta = 0.0100$  exhibits a crossing point ( $\square$ ), and an  $A_3$ -singularity ( $\circ$ ). Four further  $A_3$ -singularities are marked by circles; they refer from left to right to  $\delta = 0.0167, 0.0143, 0.0125, 0.0111$ . The arrow points to the critical packing fraction  $\varphi_{\text{HSS}}^c = 0.516$  for the hard-sphere system. The cross ( $\times$ ) in the curve for  $\delta = 0.025$  indicates the location for the maximum value of  $\lambda = 0.96$ .

which are not shown as a whole for that reason. We restrict the comparison to the respective  $A_4$ -singularities and show the potentials at the point  $\mathbf{V} = \mathbf{V}^*$  in Fig. 4.7. In the region  $1.01 \leq r/d \leq 1.05$ , the potentials are rather close to each other and cross around  $r/d \approx 1.02$  for  $\Gamma \approx 4$ . The volume of the shell  $1.00 < r/d < 1.02$  is smaller than the one for the shell  $1.02 < r/d < 1.04$ . Within the latter, the attraction strength decreases in the sequence SWS, TRI, AOS and HCY. Therefore, the critical packing fraction  $\varphi^*$  for the onset of a glass-glass transition increases in this sequence as seen in the inset and also on page 41 in Tab. 1. For the same reason, the maximum packing fraction of the liquid increases in this sequence. One gets  $\varphi^{\text{max}} = 0.5293, 0.5326, 0.5340, \text{ and } 0.5367$ , respectively. Evaluating the structure factor of the SWS up to next-to-leading order, Eq. (3.16), yields a value of  $\varphi^{\text{max}} = 0.5299$  which is very close to the result when using only the leading order calculation for  $S_q$ .

Structure factors and related  $q$ -dependent quantities at the  $A_4$ -singularities are compared in Figure 4.8. The  $S_q$  for various models mainly differ by a small shift parallel to the  $q$ -axis only. This shift reflects the decrease of the interparticle distance caused by the increase of  $\varphi^*$ . The  $f_q^*$  for all potentials are similar and

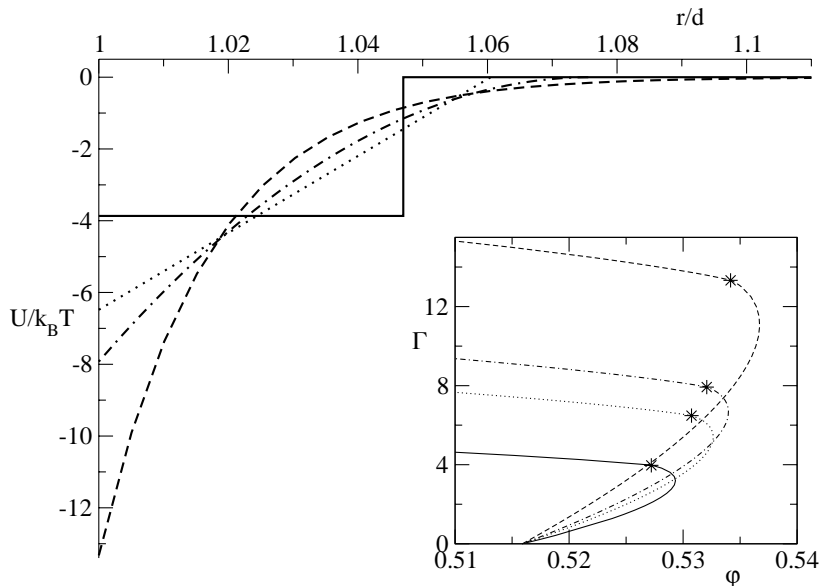


FIGURE 4.7. Attractive potentials  $U$  relative to the thermal energy  $k_B T$  as function of the interparticle distance  $r$  relative to the hard-sphere diameter  $d$  for control parameters  $\mathbf{V}^*$  at the respective  $A_4$ -singularity. The curves refer to the SWS (—), TRI ( $\cdots$ ), AOS ( $- \cdot -$ ) as introduced in Eq. (3.10) and HCY (---) from Eq. (3.27). The inset shows the cuts of the bifurcation surfaces through  $\mathbf{V}^*$  for fixed attraction-range parameter  $\delta = \delta^*$ .

larger than the values  $f_q^c$  for the HSS that is given for reference. Once the system is arrested, the attractive part of the potential leads to a stronger localization than in the HSS where only a repulsive potential is present. Within the wave-vector region around the first peak of  $S_q$ , say  $1 \leq qd \leq 10$ , the glass-form factors of the SWS differ from the ones of the HCY up to about 7% while this difference is minimal at the peak. The corresponding difference for the critical amplitude is about 9% which is maximal at the peak. The inset for the lowest panel of Fig. 4.8 displays the variation of the exponent parameter  $\lambda$  for the liquid-glass transitions on the cuts  $\delta = \delta^*$ . Rescaled as a function of  $\Gamma/\Gamma^*$ , the  $\lambda$  cannot be distinguished on the branch  $\Gamma/\Gamma^* < 1$  dealing with glass transitions. On the branch of gel transitions,  $\Gamma/\Gamma^* > 1$ , the  $\lambda$  for the various models are still very close to each other. Figure 4.8 also shows the results for the structure factor for the SWS evaluated up to next-to-leading order but deviations from the results using the structure factor only in leading-order are negligible.

A quantity that is particularly suited to demonstrate the change of the mechanism of arrest for increasing coupling strength  $\Gamma$ , is the particle's localization length  $r_s$ . Figure 4.9 shows the localization lengths  $r_s^*$  on the transition curves for  $\delta = \delta^*$  for both SWS and HCY. For the HSS,  $\Gamma = 0$ , the localization  $r_s^c/d = 0.0746$  is in agreement with the Lindemann's melting criterion [2, 77]. For  $\Gamma > 0$ , the localization length decreases monotonically and at  $\Gamma = \Gamma^*$ , the variation of  $r_s^c$  experiences the cubic-root singularity already discussed for the  $f_q^c$  in Fig. 4.2. Upon further

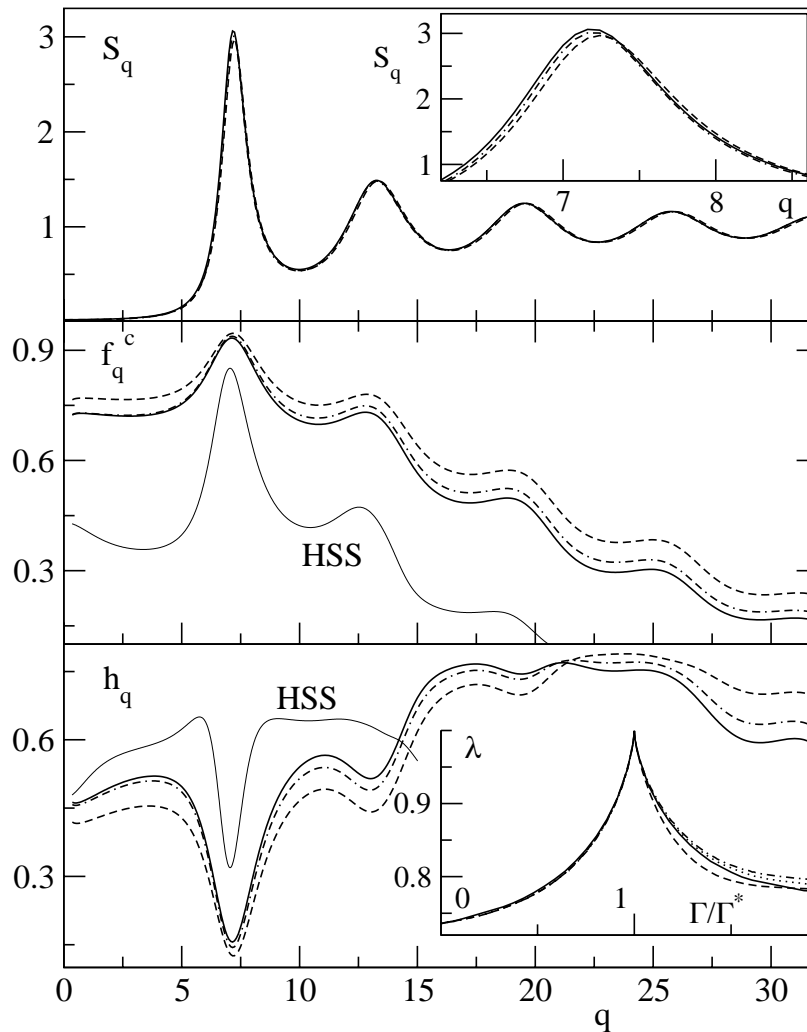


FIGURE 4.8. Structure factors  $S_q$ , critical glass-form factors  $f_q^*$ , and critical amplitudes  $h_q$  for control parameters specifying the  $A_4$ -singularity  $\mathbf{V}^*$ , SWS (—) with  $S_q$  from Eq. (3.13) and HCY (— —) from [67]. The third curve (— · — · —) shows the results for the SWS using the structure-factor up to next-to-leading order in  $\delta$  from Eq. (3.16). The lines denoted by HSS exhibit  $f_q^c$  and  $h_q$  for the critical point of the hard-sphere system. The inset from the lower panel shows the variation of the exponent parameter  $\lambda$  along the liquid-glass transition lines through  $\mathbf{V}^*$  from Fig. 4.7.

increasing  $\Gamma$  the  $r_s^c$  eventually saturate at values of the order of the attraction range. This was first observed in the HCY for  $\delta > \delta^*$  [15].

In Fig. 4.10 the elastic moduli for the SWS are compared with the ones for the HCY. We chose again the cuts incorporating the  $A_4$ -singularities,  $\delta = \delta^*$ . As also seen for crossing the glass-glass transition in the SWS, Fig. 4.3, the compression

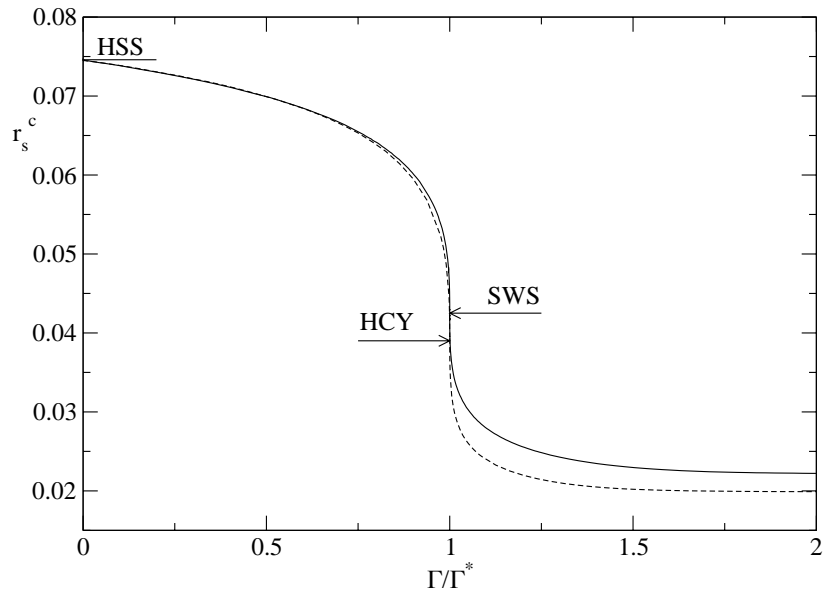


FIGURE 4.9. Localization length  $r_s^c$  of a tagged particle for states on the  $\delta = \delta^*$  transition line for the SWS (HCY) shown as full (dashed) line. At the  $A_4$ -singularity one gets  $r_s^c/d = 0.0425(0.0390)$  as indicated by the arrows. The line labeled HSS marks the localization length  $r_s^c/d = 0.0746$  for the HSS.

modulus  $M_L^0$ , Eq. (2.15), of the liquid varies smoothly throughout. The large variations of  $\delta M_{L,T}$  reflect the strong effect of bonding potentials on restoring forces [15, 16]. The same bonds are resisting shear as well as compression deformations. Therefore, there is no great difference in the behavior of the two moduli. The contributions to  $\delta M_L$  from the first two terms in Eq. (2.17b) are smaller than the one from the last term. Furthermore, these two contributions nearly cancel incidentally. Therefore,  $\delta M_L^c$  differs from  $3\delta M_T^c$  by less than 3% for  $\Gamma < \Gamma^*$  and less than 0.5% for  $\Gamma \geq \Gamma^*$ . This is consistent with the results from a virial expansion in the mode-coupling functional [79]. At the  $A_4$ -singularity we observe once again a cubic-root behavior,  $M(\Gamma) - M(\Gamma^*) \propto (\Gamma - \Gamma^*)^{1/3}$ . The singular increase of  $M$  with  $\Gamma$  increasing through  $\Gamma^*$  is a precursor of the discontinuous increase of  $M$  upon crossing the glass-glass-transition line for  $\delta < \delta^*$ , cf. Fig. 4.3.

To conclude this section, the values for the  $A_4$ -singularity for different potentials and closure relations are summarized in Tab. 1. From the values given for  $\delta^*$  one infers that an effective range of  $0.02d$  as already seen in connection with Fig. 4.7 is a good estimate for the  $A_4$ -singularity. The values for  $\Gamma^*$  follow the same trend for the PYA as they obey for the MSA, however, the actual numbers are about five times larger for MSA than they are for PYA. If a cutoff is introduced in the wave-vector integral for the mode-coupling functional (2.7d), a comparison to the results for the singular potential of the SHSS, cf. Eq. (3.9), with the regular potentials treated above is also possible. The qualitative agreement with the SWS justifies the introduction of a cutoff to renormalize the potential as done in Ref. [14], the quantitative deviations, however, do not fit so easily into the group of potentials



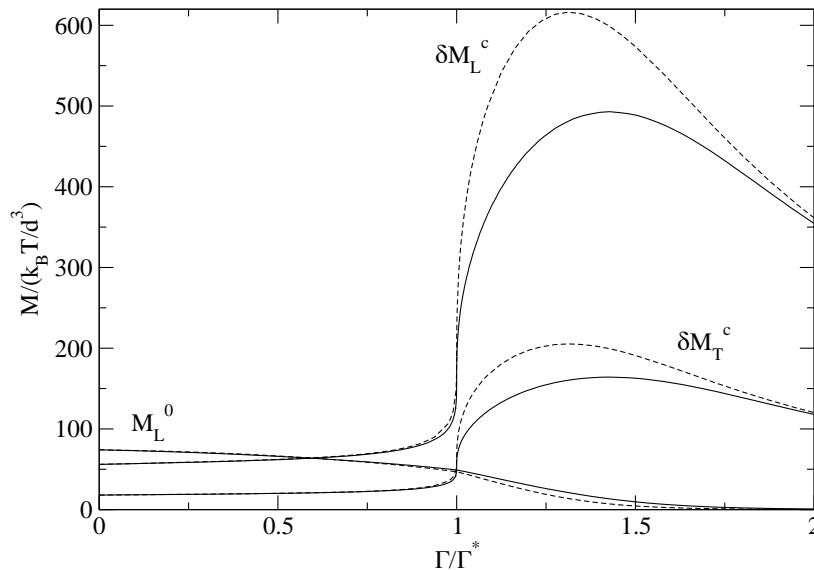


FIGURE 4.10. Longitudinal elastic moduli  $M_L$  and transversal elastic moduli  $M_T$  for the  $\delta = \delta^*$  transition line of the SWS (HCY) shown as full (dashed) lines. For the SWS, the structure factor from Eq. (3.16) was used. In the limiting case of the HSS,  $M_L^0 = 74.1$ ,  $\delta M_T = 18.1$ ,  $\delta M_L = 56.1$  [78]. At the  $A_4$  singularity for the SWS (HCY),  $\delta M_T^* = 54.3(64.4)$ ,  $\delta M_L^* = 163.4(193.6)$ . At the maximum  $\delta M_T = 164.2(205.3)$ ,  $\delta M_L = 493.0(616.3)$ .

	MSA $\varphi^*$	$\Gamma^*$	$\delta^*$	PYA $\varphi^*$	$\Gamma^*$	$\delta^*$
SWS	0.52721	3.967	0.047	0.52851	0.9028	0.0442
TRI	0.53074	6.483	0.0605	0.53306	1.335	0.063
AOS	0.53207	7.926	0.076	0.53419	1.512	0.085
HCY	0.53416	13.33	0.0173			

TABLE 1. Location of  $A_4$ -singularities for various potentials with short-ranged attraction. For the MSA result the structure factor input is taken from the first-order solution, Eq. (3.13), for SWS, TRI and AOS, and from Ref. [67] for the HCY. For the PYA-result, the structure factors were calculated numerically, Eq. (3.18a). For the SWS, the values from Eq. (4.2) are repeated.

discussed above [80]. For the Yukawa system some liquid-glass transitions have been determined within MCT using a more refined structure factor theory [76]. The results are quite similar and do not hint at any serious discrepancies introduced by the simple treatment of the structure factor in this work.

### 3. Reentry phenomenon

The reentry is given by the fact that for positive attraction strength,  $\Gamma^c > 0$ , there is a value  $\varphi_{\max}^c$  of the packing fraction that exceeds the limit of the HSS,

$\varphi_{\max}^c > \varphi_{\text{HSS}}^c$ . Coming from small  $\delta$ , this maximum moves to lower values for  $\Gamma^c$  and is eventually absorbed by the limiting HSS at  $\delta_{\text{reentry}}$ , cf. Figs. 4.1 and 4.6. The existence of a value  $\delta_{\text{reentry}}$  can be understood as follows. In the HSS the particles forming the cage are themselves localized at a length of order  $0.1d$ . The partial dimerization taking place when increasing the attraction is due to the elevated probability of two particles being closer than  $\delta$ . If  $\delta \gtrsim 0.1d$  this is no longer sufficient to cause the dimerization that weakens the cage.

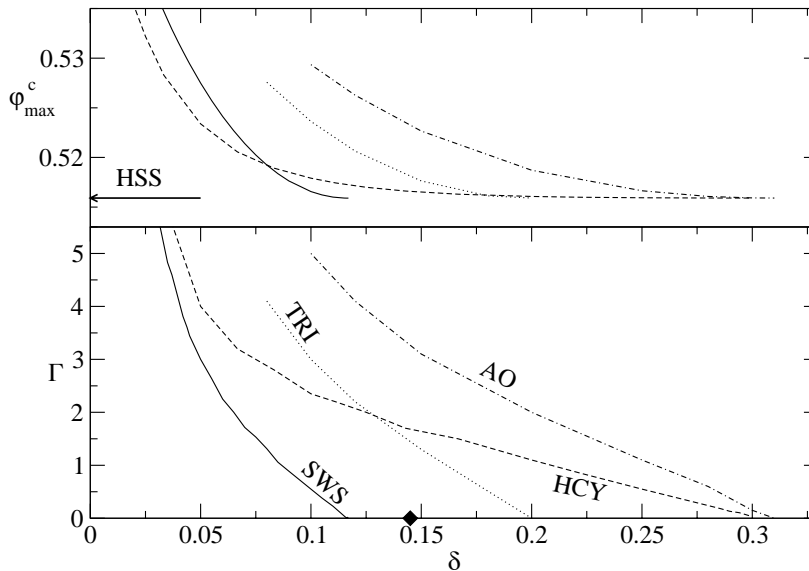


FIGURE 4.11. Location of the point of maximal density in the liquid for SWS, TRI, AOS and HCY using the structure factor in MSA. The upper panel shows the packing fraction  $\varphi_{\max}^c$ , the lower panel the attraction strengths  $\Gamma$  at these points. For the SWS (full line)  $\delta_{\text{reentry}} = 0.117$ , for TRI (dotted)  $\delta_{\text{reentry}} = 0.20$ , for the AOS (chain line)  $\delta_{\text{reentry}} = 0.31$ , and for the HCY (dashed)  $\delta_{\text{reentry}} = 0.30$ . The full diamond marks  $\delta_{\text{reentry}} = 0.145$  for the PYA result for SWS.

The value of  $\delta_{\text{reentry}}$  was already reported for the SWS with  $S_q$  within MSA,  $\delta_{\text{reentry}} = 0.117$ . For the SWS in PYA we find  $\delta_{\text{reentry}} = 0.145$ . Since this is considerably larger than for the MSA we check if the deviation can be traced to the use of an expansion in small  $\delta$  in Eq. (3.16). We repeat the calculation for the MSA this time solving the structure factor numerically, cf. Eq. (3.18b). The result is even smaller,  $\delta_{\text{reentry}} = 0.112$ . We conclude that the difference in  $\delta_{\text{reentry}}$  between PYA and MSA is introduced by the closure relations. The evolution of the reentry is shown for different potentials in Fig. 4.11. The sequence in  $\delta_{\text{reentry}}$  for the different systems reflects the shape of the respective potentials and is the same as discussed in connection with Fig. 4.7. At an effective range of 10% of the particle diameter the reentry phenomenon vanishes in all four potentials.

One encounters a peculiarity when trying to fix the values for  $\delta_{\text{reentry}}$  for the TRI and the AOS using the PYA. For  $\delta \lesssim 0.15$  the behavior of  $\varphi_{\max}^c$  is similar to

the one for the MSA as shown in Fig. 4.11. However, for larger  $\delta$  the  $\varphi_{\max}^c$  do not approach  $\varphi_{\text{HSS}}^c$  but stay at a value  $\varphi_{\max}^c \approx 0.52$ . In addition, for  $0.35 \lesssim \delta \lesssim 0.55$  for the SWS in PYA there is a second enhancement of  $\varphi_{\max}^c$  above the value for the HSS. This enhancement for PYA can be related to a deficiency PYA shows for these potentials. A comparison of computer simulation data from [81] with integral equation theory [65] reveals that for the SWS at  $\delta = 0.5$  the PYA seriously overestimates the contact value  $g_d$  for increased attraction strength. This artificially introduces a similar dimerization as found for small well widths. We can safely ignore that additional reentry effect but note that this prevents us from identifying  $\delta_{\text{reentry}}$  for TRI and AOS within PYA. For completeness we also report a similar possible artifact in the MSA calculations for larger attraction range. For finite strength of the attraction,  $g(r)$  may develop negative values around  $r = d + \Delta$  [65]. The precursor of this failure of the MSA pretends a region depleted of other particles in that range. Within MCT this triggers another enhancement above  $\varphi_{\text{HSS}}^c$  for  $\delta \gtrsim 0.35$ . For both PYA and MSA the effects are small and  $\varphi_{\max}^c \lesssim 0.52$  was never exceeded. Since not vitally connected to the discussion of *short*-ranged attraction, this issue shall not be followed up any further.



## Asymptotic expansions

Close to the glass-transition singularities the equations of motion (2.7) can be expanded in asymptotic series around the critical long-time limit. The asymptotic laws for the decay at  $A_2$ -singularities have been discussed in detail for the HSS [7]. As seen above, systems with short-ranged attraction also exhibit higher-order glass-transition singularities  $A_3$  and  $A_4$ . At these singularities the asymptotic laws known from the  $A_2$ -singularities are no longer valid and different expansions have to be used. These will be derived in the following.

In Sec. 1 the general formalism for the expansion is presented. It is shown in particular how the results for a one-component system are to be extended to the wave-vector dependent case.<sup>1</sup> In Sec. 2 the decay near higher-order singularities is expanded into polynomials of the logarithm of time up to next-to-leading order. This expansion can be applied on a weak-coupling side of the singularity which includes the liquid regime. For the approximation of the decay right at the singularity we need a different expansion. For the latter case the decay is expanded at the  $A_3$ -singularity in inverse powers of the logarithm in time in Sec. 3. Up to six terms of the expansion are considered assure consistency of the approximation. The analogous expansion at an  $A_4$ -singularity is carried out up to next-to-leading order in Sec. 4. To use consistent notation we rewrite the decay laws for an  $A_2$ -singularity and the coupled variables briefly in Sec. 5.

The evaluation of the parameters we need for the approximations can be somewhat involved so it seems desirable to check the formulas in schematic models where one can calculate all these parameters analytically. The laws for an  $A_3$ -singularity are illustrated for a one-component model in Sec. 6. A two-component model allows in addition to demonstrate the results for an  $A_4$ -singularity and to mimic the wave-vector dependence of the approximation, see Sec. 7. The scenarios discussed for the schematic models in this chapter are encountered also later in the analysis of the SWS in Ch. 6.

### 1. General formulas

To discuss the long-time limit of the equations of motion it will be convenient to formulate the equations for the correlators also in the frequency domain. The following convention for the Laplace transform is used,

$$(5.1a) \quad \mathbf{LT}[F(t)](z) = i \int_0^\infty \exp(izt)F(t)dt,$$

---

<sup>1</sup>To avoid confusion, we may clarify that by *component* we always mean a wave-vector component and not a component of some mixture or tensorial quantity. In the latter sense only single-component systems are discussed in this work.

and to simplify notation, the Laplace transform will be modified by a prefactor of  $(-z)$  to define another linear transformation as

$$(5.1b) \quad \mathcal{S}[F(t)](z) = (-iz) \int_0^\infty \exp(izt) F(t) dt .$$

The  $\mathcal{S}$ -transformation leaves constants invariant and the representation of the long-time limit  $\phi_q(t \rightarrow \infty) = f_q$  is equivalent to  $\mathcal{S}[\phi_q(t)](z \rightarrow 0) = f_q$ . The same is true for the long-time limit of the memory kernel,  $\mathcal{S}[\mathcal{F}_q[\mathbf{V}, \phi_k(t)]](z \rightarrow 0) = \mathcal{F}_q[\mathbf{V}, f_k]$ . The equations of motion (2.7) are then reformulated for both Newtonian dynamics,

$$(5.2a) \quad \mathcal{S}[\phi_q(t)](z) = \frac{1}{1 + 1/(\mathcal{S}[m_q(t)](z) - z^2/\Omega_q^2)},$$

and Brownian dynamics,

$$(5.2b) \quad \mathcal{S}[\phi_q(t)](z) = \frac{1}{1 + 1/(\mathcal{S}[m_q(t)](z) - i\tau_q z)} .$$

On the glass side, for the long-time limit,  $z \rightarrow 0$ , the transform of the correlators and the memory kernels assume constant values while the contribution  $z^2/\Omega_q^2$  in Eq. (5.2a) or  $i\tau_q z$  in Eq. (5.2b), respectively, become arbitrarily small. Because of continuity this holds also for states close to the glass states. Under these conditions, the equations of structural relaxation are independent of the short-time dynamics [4] and can be simplified to

$$(5.3) \quad \mathcal{S}[\phi_q(t)](z) = \frac{1}{1 + 1/\mathcal{S}[m_q(t)](z)} .$$

This equation is scale invariant, with  $\phi_q(t)$  also  $\phi_q(x \cdot t)$  is a solution with  $x > 0$ . The transient motion governed by  $\Omega_q$  or  $\tau_q$  has dropped out and Eq. (5.3) fixes the solution only up to an overall time scale. This time scale will be accounted for by matching the result of the asymptotic approximation to the transient dynamics by rescaling the time.

Equation (5.3) can be rewritten in a form which shall be the starting point for the further discussion,

$$(5.4) \quad \frac{\mathcal{S}[\phi_q(t)](z)}{1 - \mathcal{S}[\phi_q(t)](z)} = \mathcal{S}[\mathcal{F}_q[\mathbf{V}, \phi_k(t)]](z) .$$

The long-time limit of the equations of motion is represented by the  $z \rightarrow 0$  limit of Eq. (5.4) and yields a set of implicit equations for the glass form factors  $f_q$  as introduced before in Eq. (2.8),

$$f_q/(1 - f_q) = \mathcal{F}_q[\mathbf{V}, f_k] .$$

To ease the following discussion, the wave-vector domain shall be discretized into  $M$  values and the wave vector  $q$  is now equivalent to an index for the correlation functions,  $q = 1, 2, \dots, M$ .

At some state  $\mathbf{V}^c$  the glass-form factors shall assume the values  $f_q^c$  allowing for the introduction of new functions  $\hat{\phi}_q(t)$  that describe the dynamics around  $f_q^c$ ,

$$(5.5) \quad \phi_q(t) = f_q^c + (1 - f_q^c) \hat{\phi}_q(t) .$$

Equation (5.5) constitutes an expansion of the correlation function  $\phi_q(t)$  in a series around  $f_q^c$  in the small quantity  $\hat{\phi}_q(t)$ . The functional  $\mathcal{S}[\mathcal{F}_q[\mathbf{V}, \phi_k(t)]](z)$  appearing on the rhs of Eq. (5.4) can also be rewritten in that way,

$$(5.6) \quad (1 - f_q^c) \mathcal{S}[\mathcal{F}_q[\mathbf{V}, \phi_k(t)]](z) = \sum_{n=0}^{\infty} A_{qk_1 \dots k_n}^{(n)}(\mathbf{V}) \mathcal{S}[\hat{\phi}_{k_1}(t) \cdots \hat{\phi}_{k_n}(t)](z),$$

and yields the following coefficients

$$(5.7a) \quad A_{qk_1 \dots k_n}^{(n)}(\mathbf{V}) = \frac{1}{n!} (1 - f_q^c) \frac{\partial^n \mathcal{F}_q[\mathbf{V}, f_k^c]}{\partial f_{k_1}^c \cdots \partial f_{k_n}^c} (1 - f_{k_1}^c) \cdots (1 - f_{k_n}^c).$$

These coefficients can be split into the values at  $\mathbf{V}^c$ ,  $A_{qk_1 \dots k_n}^{(n)c} = A_{qk_1 \dots k_n}^{(n)}(\mathbf{V}^c)$ , and the remainders

$$(5.7b) \quad A_{qk_1 \dots k_n}^{(n)}(\mathbf{V}) = A_{qk_1 \dots k_n}^{(n)c} + \hat{A}_{qk_1 \dots k_n}^{(n)}(\mathbf{V}).$$

The control-parameter vector  $\mathbf{V}$  may be parameterized by a distance parameter  $\varepsilon$  which is zero at  $\mathbf{V}^c$  and describes a path in control-parameter space with non-vanishing tangent through  $\mathbf{V}^c$ . Since the functionals are assumed to be smooth in the control parameters they are of order  $\varepsilon$  in the distance parameter,

$$(5.7c) \quad \hat{A}_{qk_1 \dots k_n}^{(n)}(\mathbf{V}) = \mathcal{O}(\varepsilon).$$

The introduction of  $\varepsilon$  facilitates the following expansion where the functions  $\mathcal{S}[\hat{\phi}_q](z)$  and the parameters  $\hat{A}_{qk_1 \dots k_n}^{(n)}(\mathbf{V})$  are treated as small. The lhs of Eq. (5.4) can be expanded in powers of  $\mathcal{S}[\hat{\phi}_q](z)$  resulting in a geometric series,

$$(5.8) \quad (1 - f_q^c) \frac{\mathcal{S}[\phi_q(t)](z)}{1 - \mathcal{S}[\phi_q(t)](z)} = f_q^c + \sum_{n=1}^{\infty} \mathcal{S}[\hat{\phi}_q(t)]^n(z).$$

Equation (5.4) is rephrased in terms of  $\mathcal{S}[\hat{\phi}_q(t)]$  as

$$(5.9a) \quad [\delta_{qk} - A_{qk}^{(1)c}] \mathcal{S}[\hat{\phi}_k(t)](z) = J_q(z),$$

with the inhomogeneity

$$(5.9b) \quad J_q(z) = \hat{A}_q^{(0)}(\mathbf{V}) + \hat{A}_{qk}^{(1)}(\mathbf{V}) \mathcal{S}[\hat{\phi}_k(t)](z) + \sum_{n=2}^{\infty} \{A_{qk_1 \dots k_n}^{(n)}(\mathbf{V}) \mathcal{S}[\hat{\phi}_{k_1}(t) \cdots \hat{\phi}_{k_n}(t)](z) - \mathcal{S}[\hat{\phi}_q(t)]^n(z)\}.$$

where  $A_q^{(0)c} = f_q^c$  was used and summation over repeated indices is implied. Specializing Eqs. (5.9) to the  $z \rightarrow 0$  limit, one gets the equation for  $\hat{f}_q = \hat{\phi}_q(t \rightarrow \infty)$ :

$$(5.10) \quad [\delta_{qk} - A_{qk}^{(1)c}] \hat{f}_k = \hat{A}_q^{(0)}(\mathbf{V}) + \hat{A}_{qk}^{(1)}(\mathbf{V}) \hat{f}_k + \sum_{n=2}^{\infty} [A_{qk_1 \dots k_n}^{(n)}(\mathbf{V}) \hat{f}_{k_1} \cdots \hat{f}_{k_n} - \hat{f}_q^n].$$

The  $M \times M$  matrix  $[\delta_{qk} - A_{qk}^{(1)c}]$  is the Jacobian of the set of implicit equations (2.8) for the solution  $f_q^c$  at  $\mathbf{V} = \mathbf{V}^c$ . Since matrix  $A_{qk}^{(1)c}$  has only positive elements, the Perron-Frobenius theorem implies that, generically, this matrix has a non-degenerate maximum eigenvalue  $E^c > 0$ . All other eigenvalues will be smaller than

$E^c$  [82]. It can be proven for MCT that  $E^c \leq 1$  [57]. Therefore, the Jacobian matrix is no longer invertible if

$$(5.11) \quad E^c = 1,$$

and a bifurcation point  $\mathbf{V}^c$  of Eq. (2.8) results. Since this critical eigenvalue is non-degenerate, only a single critical eigenvector has to be considered and one proceeds in the following way. First, the solution for the critical direction is derived which is equivalent to solving an  $M = 1$  model system that does not contain noncritical directions. Leading results and corrections are determined for that case. Second, the corrections in the noncritical directions are calculated using the leading results from the  $M = 1$  case.

The left and right eigenvectors of matrix  $A_{qk}^{(1)c}$  for the maximum eigenvalue  $E^c = 1$  shall be denoted by  $a_k^*$  and  $a_k$ ,  $k = 1, \dots, M$ , respectively,

$$(5.12) \quad a_q^* A_{qk}^{(1)c} = a_k^*, \quad A_{qk}^{(1)c} a_k = a_q.$$

According to the Frobenius theorems [82], one can require  $a_k^* \geq 0$  and  $a_k \geq 0$ . It will be convenient to fix the eigenvectors uniquely by the conditions  $\sum_q a_q^* a_q = 1$  and  $\sum_q a_q^* a_q^2 = 1$ . The solvability condition for Eq. (5.9a) reads

$$(5.13a) \quad a_q^* J_q(z) = 0,$$

and its general solution can be written as

$$(5.13b) \quad \hat{\phi}_q(t) = a_q \hat{\phi}(t) + \tilde{\phi}_q(t).$$

The splitting of  $\hat{\phi}_q(t)$  in two terms is unique if one imposes the condition  $a_q^* \hat{\phi}_q(t) = \hat{\phi}(t)$ . The part  $\tilde{\phi}_q(t)$  can be expressed by means of the reduced resolvent  $R_{qk}$  of  $A_{qk}^{(1)c}$ :

$$(5.13c) \quad \mathcal{S}[\tilde{\phi}_q(t)](z) = R_{qk} J_k(z).$$

The matrix  $R_{qk}$  can be evaluated from matrix  $A_{qk}^{(1)c}$  and the vectors  $a_k^*$ ,  $a_k$  [82]. The legitimacy of Eq. (5.13b) has to be shown below by explicit construction for the asymptotic series.

For the one-component case the lhs in Eq. (5.10) vanishes and the equation for  $\hat{f}$  reads

$$(5.14a) \quad \varepsilon_1(\mathbf{V}) + \varepsilon_2(\mathbf{V}) \hat{f} + \sum_{n \geq 2} [\hat{A}^{(n)}(\mathbf{V}) - \mu_n] \hat{f}^n = 0$$

where the formulation of the following parameters is straightforward,

$$(5.14b) \quad \mu_n = 1 - A^{(n)c}, \quad \varepsilon_n(\mathbf{V}) = \hat{A}^{(n-1)}(\mathbf{V}), \quad n = 1, 2, \dots$$

The singularity exhibited by  $\hat{f}$  for  $\varepsilon$  tending to zero depends on the number of successive vanishing coefficients  $\mu_n$ . A singularity of index  $l$ ,  $l \geq 2$ , shall be classified by

$$(5.15a) \quad \mu_1 = \mu_2 = \dots = \mu_{l-1} = 0, \quad \mu_l \neq 0.$$

The equation for  $\hat{f}$  reads

$$(5.15b) \quad \begin{aligned} \mu_l \hat{f}^l = & \varepsilon_{l-1}(\mathbf{V}) \hat{f}^{l-2} + \varepsilon_{l-2}(\mathbf{V}) \hat{f}^{l-3} + \dots + \varepsilon_1(\mathbf{V}) \\ & + \{ \varepsilon_l(\mathbf{V}) \hat{f}^{l-1} + \varepsilon_{l+1}(\mathbf{V}) \hat{f}^l + \sum_{n \geq l+1} [A^{(n)}(\mathbf{V}) - 1] \hat{f}^n \}. \end{aligned}$$



The implicit-function theorem can be used to show that there is a smooth invertible transformation of the  $l$  variables  $(\varepsilon_1, \varepsilon_2, \dots, \varepsilon_{l-1}, \hat{f})$  which eliminates the curly bracket in Eq. (5.15b). Thus, the singularities described by this equation are topologically equivalent to the ones described by the first line, i.e. by the zeros of a polynomial of degree  $l$ . Such singularity is referred to as  $A_l$  [5]. The  $\varepsilon_n(\mathbf{V})$  are of order  $\varepsilon$ , Eq. (5.7c), and shall be referred to as separation parameters.

The simplest glass-transition singularity is the  $A_2$  with only one relevant control parameter  $\varepsilon_1(\mathbf{V})$  [3]: There is a discontinuous change of  $\hat{f}$  at the surface specified by  $\varepsilon_1(\mathbf{V}) = 0$ . as one infers from Eq. (5.15b). The dynamics is characterized by power-law decay and power-law dependencies of the relaxation scales on  $|\varepsilon_1(\mathbf{V})|$ . All exponents in these laws are to be calculated from  $\lambda = 1 - \mu_2$ , which is for that reason called the exponent parameter [3]. The transition surface has a boundary that is determined by  $\lambda = 1$ , i.e. by  $\mu_2 = 0$ . These endpoints are the higher-order singularities. The  $A_3$  and  $A_4$  are also referred to as cusp and swallowtail singularities, respectively.

For  $M = 1$  Eqs. (5.9a) and (5.9b) shall be rewritten and grouped for the following expansions as

$$(5.16) \quad \begin{aligned} 0 &= \varepsilon_1(\mathbf{V}) + (1 - \mu_2) \mathcal{S}[\hat{\phi}^2(t)](z) - \mathcal{S}[\hat{\phi}(t)]^2(z) \\ &+ \varepsilon_2(\mathbf{V}) \mathcal{S}[\hat{\phi}(t)](z) + (1 - \mu_3) \mathcal{S}[\hat{\phi}^3(t)](z) - \mathcal{S}[\hat{\phi}(t)]^3(z) \\ &+ \varepsilon_3(\mathbf{V}) \mathcal{S}[\hat{\phi}^2(t)](z) + (1 - \mu_4) \mathcal{S}[\hat{\phi}^4(t)](z) - \mathcal{S}[\hat{\phi}(t)]^4(z) \\ &+ \dots \end{aligned}$$

For  $\mu_2 \neq 0$  the asymptotic expansion for the  $A_2$ -singularity follows from Eq. (5.16) which is summarized in Sec. 5. Specializing to higher-order singularities in Eq. (5.16) requires

$$(5.17) \quad \mu_2 = 0 .$$

## 2. Logarithmic decay

In this section, the expansion in polynomials in  $\ln t$  is derived that generalizes an earlier result [34]. The result will be valid for  $\varepsilon_1 < 0$  and for any higher-order singularity  $A_l$ ,  $l \geq 3$ .

**2.1. One-component case.** First the one-component case will be solved for  $\hat{\phi}(t)$ . As for the case of  $A_2$ -singularities, Eq. (5.16) suggests an expansion of the solution in powers of  $|\varepsilon|^{1/2}$ . With  $G^{(n)}(t) = \mathcal{O}(|\varepsilon|^{n/2})$ , let us write

$$(5.18) \quad \hat{\phi}(t) = G^{(1)}(t) + G^{(2)}(t) + G^{(3)}(t) + \dots .$$

The first line of Eq. (5.16) is of order  $|\varepsilon|$  and it provides a nonlinear integral equation for  $G^{(1)}(t)$ . The contributions to this line which are of order  $|\varepsilon|^{3/2}$  together with the leading terms of the second line provide a linear integral equation for  $G^{(2)}(t)$ , etc. This procedure will yield the desired asymptotic expansion provided the indicated integral equations define meaningful solutions. This is indeed the case as shall be demonstrated below by explicit construction of the  $G^{(n)}(t)$ .

The equation for the leading contribution to the correlator at a glass transition  $A_l$  with  $l \geq 3$  reads

$$(5.19) \quad \varepsilon_1(\mathbf{V}) + \mathcal{S}[G^{(1)2}(t)](z) - \mathcal{S}[G^{(1)}(t)]^2(z) = 0 .$$

The formulas for the Laplace transforms of the logarithm and its square imply  $\mathcal{S}[\ln(t)](z) = \ln(i/z) - \gamma$  and  $\mathcal{S}[\ln^2(t)](z) = \ln^2(i/z) - 2\gamma \ln(i/z) + \gamma^2 + (\pi^2/6)$ , where  $\gamma = 0.577\dots$  is Euler's constant, see Eq. (A.1). Hence, Eq. (5.19) is solved by  $-B \ln(t)$  if  $\varepsilon_1(\mathbf{V}) + (B^2\pi^2/6) = 0$ . Since the correlators are monotonically decreasing functions of  $t$  [57], one must require  $B > 0$ . One concludes that a solution is given by

$$(5.20) \quad G^{(1)}(t) = -B \ln(t) , \quad B = \sqrt{[-6\varepsilon_1(\mathbf{V})/\pi^2]} ,$$

provided the control parameters  $\mathbf{V}$  obey

$$(5.21) \quad \varepsilon_1(\mathbf{V}) < 0 .$$

Ignoring corrections of order  $|\varepsilon|$ , one derives from Eqs. (5.5), (5.18), and (5.20) the leading approximation for the correlator [34]:

$$(5.22) \quad \phi(t) = f^c - (1 - f^c)B \ln(t/\tau) .$$

The time scale  $\tau$  is introduced to take care of the scale invariance of Eq. (5.3). It will be used to match the solution at the plateau  $f^c$ .

In order to solve Eq. (5.16) up to order  $|\varepsilon|^{3/2}$ , one has to incorporate from the first line the contribution  $2\mathcal{S}[G^{(1)}(t)G^{(2)}(t)](z) - 2\mathcal{S}[G^{(1)}](z)\mathcal{S}[G^{(2)}(t)](z)$ , one has to evaluate the second line with  $\hat{\phi}$  replaced by  $G^{(1)}(t)$ , and one can ignore all other terms. Hence, the equation for the leading correction  $G^{(2)}(t)$  can be written in the form

$$(5.23) \quad \mathcal{T} \left[ G^{(2)}(t) \right] (z) = f^{(2)}(z) .$$

Here, the linear integral operator  $\mathcal{T}$  is defined by

$$(5.24) \quad \mathcal{T} [G(t)] (z) = \mathcal{S} [\ln(t)G(t)] (z) - \mathcal{S} [\ln(t)] (z)\mathcal{S} [G(t)] (z) ,$$

and the inhomogeneity of Eq. (5.23) reads

$$(5.25) \quad f^{(2)}(z) = - \left\{ \varepsilon_2(\mathbf{V})\mathcal{S}[G^{(1)}(t)](z) - \mu_3\mathcal{S}[G^{(1)^3}(t)](z) \right. \\ \left. + 2\zeta \{ \mathcal{S}[G^{(1)^3}(t)](z) - \mathcal{S}[G^{(1)}(t)]^3(z) \} \right\} / (2B) .$$

A factor  $2\zeta$  has been introduced for later convenience. For the study of  $M = 1$  models, one has to substitute<sup>2</sup> $\zeta = 1/2$ .

The solution of Eq. (5.19) was built on the equations  $\mathcal{T}[c](z) = 0$  for a constant  $c$  and  $\mathcal{T}[\ln t](z) = \pi^2/6$ . These formulas are generalized in Appendix A by constructing polynomials  $p_n(x)$  of degree  $n \geq 1$  with the properties:

$$(5.26a) \quad p_n(x) = b_{n,1}x + b_{n,2}x^2 + \dots + b_{n,n-1}x^{n-1} + x^n ,$$

$$(5.26b) \quad \mathcal{T} [p_n(\ln(t))] (z) = n(\pi^2/6) \ln^{n-1}(i/z) .$$

These polynomials are a convenient tool to solve the equation

$$(5.27a) \quad \mathcal{T} [g(t)] (z) = f(z)$$

---

<sup>2</sup>In Sec. 3 we will introduce  $\kappa = 2\zeta$ ; here the notation is kept consistent with the notation in [7, 83].

for inhomogeneities  $f(z)$  which are polynomials in  $\ln(i/z)$ ,

$$(5.27b) \quad f(z) = \sum_{n=0}^m a_n \ln^n(i/z) .$$

Obviously, this is solved by a polynomial of degree  $m + 1$ ,

$$(5.27c) \quad g(t) = \sum_{n=1}^{m+1} [a_{n-1}/(n\pi^2/6)] p_n(\ln(t)) .$$

Using Eq. (5.20) and applying Eqs. (A.1) and (A.2) for the evaluation of the transformations of the powers of  $\ln(t)$ , one can write  $f^{(2)}(z)$  in the form of Eq. (5.27b) for  $m = 3$ . The coefficients are linear functions of  $\varepsilon_1(\mathbf{V})$  and  $\varepsilon_2(\mathbf{V})$ :

$$(5.28a) \quad a_0 = [(6\zeta/\pi^2)(\Gamma_3 - \Gamma_1^3) - (3\mu_3/\pi^2)\Gamma_3]\varepsilon_1(\mathbf{V}) - (\Gamma_1/2)\varepsilon_2(\mathbf{V}) ,$$

$$(5.28b) \quad a_1 = [3\zeta - (9\mu_3/\pi^2)\Gamma_2]\varepsilon_1(\mathbf{V}) - (1/2)\varepsilon_2(\mathbf{V}) ,$$

$$(5.28c) \quad a_2 = -(9\mu_3/\pi^2)\Gamma_1\varepsilon_1(\mathbf{V}) , \quad a_3 = -(3\mu_3/\pi^2)\varepsilon_1(\mathbf{V}) .$$

Here,  $\Gamma_k = d^k\Gamma(1)/dx^k$  denotes the  $k$ th derivative of the gamma function at unity. One concludes that  $G^{(2)}(t) = g(t)$ , where Eq. (5.27c) is to be used with  $m = 3$ :

$$(5.29a) \quad G^{(2)}(t) = \sum_{j=1}^4 B_j \ln^j(t) .$$

The coefficients are derived with the aid of Eqs. (A.7a-c):

$$(5.29b) \quad B_1 = (0.44425\zeta - 0.065381\mu_3)\varepsilon_1(\mathbf{V}) - 0.22213\varepsilon_2(\mathbf{V}) ,$$

$$(5.29c) \quad B_2 = (0.91189\zeta + 0.068713\mu_3)\varepsilon_1(\mathbf{V}) - 0.15198\varepsilon_2(\mathbf{V}) ,$$

$$(5.29d) \quad B_3 = -0.13504\mu_3\varepsilon_1(\mathbf{V}) , \quad B_4 = -0.046197\mu_3\varepsilon_1(\mathbf{V}) .$$

The solution up to next-to-leading order reads

$$(5.30) \quad \begin{aligned} \phi(t) - f^c &= (1 - f^c)[(-B + B_1)\ln(t/\tau) + B_2\ln^2(t/\tau) \\ &\quad + B_3\ln^3(t/\tau) + B_4\ln^4(t/\tau)] . \end{aligned}$$

A singularity  $A_l$  with  $l \geq 4$  implies  $\mu_3 = 0$ . In this case, the formula simplifies because  $B_3 = B_4 = 0$ .

The procedure outlined above can be continued. To solve Eq. (5.16) up to order  $\varepsilon^2$ , one derives the analog to Eq. (5.23):  $\mathcal{T}[G^{(3)}(t)](z) = f^{(3)}(z)$ . Function  $f^{(3)}(z)$  has the form of Eq. (5.27b) with  $m = 6$ , where the coefficients  $a_j$  depend on the parameters  $\varepsilon_1(\mathbf{V})$ ,  $\varepsilon_2(\mathbf{V})$ ,  $\varepsilon_3(\mathbf{V})$ ,  $\mu_3$  and  $\mu_4$ . As a result, one gets

$$(5.31) \quad G^{(3)}(t) = \sum_{j=1}^7 C_j \ln^j(i/z) ,$$

where  $C_j = \mathcal{O}(|\varepsilon|^{3/2})$ . The  $C_j$  for a one-component model are summarized in Eq. (A.8).

**2.2. Multi-component case.** Looking back to the splitting in Eq. (5.13b) we recognize that the part  $\hat{\phi}$  proportional to  $a_q$  is solved by the solution for the one-component case, Eq. (5.30), if proper generalizations for the parameters in Eq. (5.14b) and for  $\zeta$  can be defined. Equations (5.9b) and (5.13) suggest an expansion of  $\hat{\phi}(t)$  as in Eq. (5.18) and

$$(5.32a) \quad \tilde{\phi}_q(t) = G_q^{(2)}(t) + G_q^{(3)}(t) + \dots, \quad G_q^{(n)}(t) = \mathcal{O}(|\varepsilon|^{n/2}),$$

$$(5.32b) \quad J_q(t) = J_q^{(2)}(t) + J_q^{(3)}(t) + \dots, \quad J_q^{(n)}(t) = \mathcal{O}(|\varepsilon|^{n/2}).$$

Here, for example,

$$(5.33a) \quad J_q^{(2)}(z) = \hat{A}_q^{(0)}(\mathbf{V}) + A_{qk_1k_2}^{(2)c} a_{k_1} a_{k_2} \mathcal{S}[G^{(1)2}(t)](z) - a_q^2 \mathcal{S}[G^{(1)}(t)]^2(z),$$

$$\begin{aligned} J_q^{(3)}(z) = & 2\{A_{qk_1k_2}^{(2)c} a_{k_1} a_{k_2} \mathcal{S}[G^{(1)}(t)G^{(2)}(t)](z) - a_q^2 \mathcal{S}[G^{(1)}(t)](z)\mathcal{S}[G^{(2)}(t)](z)\} \\ & + \hat{A}_{qk}^{(1)}(\mathbf{V}) a_k \mathcal{S}[G^{(1)}(t)](z) + 2\{A_{qk_1k_2}^{(2)c} a_{k_1} \mathcal{S}[G^{(1)}(t)G_{k_2}^{(2)}(t)](z) \\ & - a_q \mathcal{S}[G^{(1)}(t)](z)\mathcal{S}[G_q^{(2)}(t)](z)\} \end{aligned}$$

$$(5.33b) \quad + A_{qk_1k_2k_3}^{(3)c} a_{k_1} a_{k_2} a_{k_3} \mathcal{S}[G^{(1)3}(t)](z) - a_q^3 \mathcal{S}[G^{(1)}(t)]^3(z).$$

The justification of the preceding expansions shall be given by demonstrating how the equations can be solved recursively.

**2.3. The leading-order contribution.** The leading-order contribution to the solvability condition, Eq. (5.13a), is obtained by substituting Eq. (5.33a) into Eq. (5.13a). One arrives at:  $\varepsilon_1(\mathbf{V}) + \lambda \mathcal{S}[G^{(1)2}(t)](z) - \mathcal{S}[G^{(1)}(t)]^2(z) = 0$ , with the definition of the exponent parameter  $\lambda = 1 - \mu_2$  [3, 7] by

$$(5.34) \quad \mu_2 = 1 - a_q^* A_{qk_1k_2}^{(2)c} a_{k_1} a_{k_2}$$

and the separation parameter

$$(5.35) \quad \varepsilon_1(V) = a_q^* \hat{A}_q^{(0)}(V).$$

According to Eq. (5.17) the parameter  $\mu_2$  has to be zero in order for  $\mathbf{V}^c$  to represent a higher-order singularity. For  $\mu_2 = 0$  the equation found for  $G^{(1)}(t)$  is identical with Eq. (5.19). Thus,  $\varepsilon_1(V)$  is the first separation parameter and Eqs. (5.20) and (5.21) remain valid.

Introducing the critical amplitude  $h_q$  by the same formula as in the theory for the  $A_2$ -singularity [3, 7],

$$(5.36) \quad h_q = (1 - f_q^c) a_q,$$

the leading approximation for the correlators is after Eq. (5.5)

$$(5.37) \quad \phi_q(t) = f_q^c + h_q [-B \ln(t/\tau)].$$

Here,  $B = \sqrt{-6\varepsilon_1(\mathbf{V})}/\pi = \mathcal{O}(|\varepsilon|^{1/2})$ . Equation (5.37) describes the dynamics up to errors of order  $\varepsilon$ ; it is the generalization of the logarithmic decay law [34] to arbitrary wave-vector dependent MCT models.

Substitution of Eq. (5.33a) into Eq. (5.13c) yields the leading-order contribution to  $\tilde{\phi}_q(t)$ , i.e. the function  $G_q^{(2)}(t)$  in Eq. (5.32a). Equation (5.19) is used to express  $\mathcal{S}[G^{(1)}(t)]^2(z)$  in terms of  $\mathcal{S}[G^{(1)}(t)](z)$  so that

$$(5.38a) \quad G_q^{(2)}(t) = X_q G^{(1)2}(t) + \hat{Y}_q(\mathbf{V}) .$$

The amplitude  $X_q$  is independent of separation parameters,

$$(5.38b) \quad X_q = R_{qk} \left[ A_{kk_1k_2}^{(2)c} a_{k_1} a_{k_2} - a_k^2 \right] .$$

$\hat{Y}_q(\mathbf{V}) = \mathcal{O}(\varepsilon)$  and reads

$$(5.38c) \quad \hat{Y}_q(\mathbf{V}) = R_{qk} \left[ \hat{A}_k^{(0)}(\mathbf{V}) - \varepsilon_1(\mathbf{V}) a_k^2 \right] .$$

**2.4. The next-to-leading-order contribution.** If one substitutes (5.38a) into Eq. (5.33b), one gets an expression for  $J_q^{(3)}(z)$  in terms of the known  $G^{(1)}(t)$  and the unknown  $G^{(2)}(t)$ . Therefore, the solvability condition, Eq. (5.13a), evaluated up to order  $\varepsilon^{3/2}$ , yields an equation for  $G^{(2)}(t)$ . The latter has the form of Eq. (5.23), where also the inhomogeneity is given by Eq. (5.25). This holds with the formula

$$(5.39) \quad \begin{aligned} \varepsilon_2(\mathbf{V}) &= \sum_q a_q^* \hat{A}_{qk}^{(1)}(\mathbf{V}) a_k + 2\varepsilon_1(\mathbf{V}) \sum_q a_q^* a_q X_q \\ &+ 2 \sum_q a_q^* \left[ A_{qk_1k_2}^{(2)c} a_{k_1} \hat{Y}_{k_2}(\mathbf{V}) - a_q \hat{Y}_q(\mathbf{V}) \right] \end{aligned}$$

for the second separation parameter, and the constants

$$(5.40) \quad \zeta = \sum_q a_q^* \left[ a_q X_q + a_q^3/2 \right] ,$$

and

$$(5.41) \quad \mu_3 = 2\zeta - \sum_q a_q^* \left[ A_{qk_1k_2k_3}^{(3)c} a_{k_1} a_{k_2} a_{k_3} + 2A_{qk_1k_2}^{(2)c} a_{k_1} X_{k_2} \right] .$$

As a result, Eqs. (5.29) for the function  $G^{(2)}(t)$  remain valid.

Combining the results for  $G^{(1)}(t)$ ,  $G^{(2)}(t)$  and  $G_q^{(2)}(t)$  with Eq. (5.32a), and this with Eq. (5.5), one obtains the solution for logarithmic decay up to order  $|\varepsilon|^{3/2}$ :

$$(5.42) \quad \begin{aligned} \phi_q(t) &= (f_q^c + \hat{f}_q) + h_q \left[ (-B + B_1) \ln(t/\tau) \right. \\ &\quad \left. + (B_2 + K_q B^2) \ln^2(t/\tau) \right. \\ &\quad \left. + B_3 \ln^3(t/\tau) + B_4 \ln^4(t/\tau) \right] . \end{aligned}$$

The relative size of the deviations from the terms proportional to  $B_i$  is the same for all correlators and of order  $\varepsilon$ . The renormalization of the critical glass-form factor is also of order  $\varepsilon$  and derived from Eq. (5.38c),

$$(5.43) \quad \hat{f}_q = (1 - f_q^c) \hat{Y}_q(\mathbf{V}) .$$

The wave-vector dependent correction is the same as in the theory for the  $A_2$ -singularity [7],

$$(5.44) \quad K_q = X_q/a_q .$$

The leading order result (5.37) comprises the factorization theorem of MCT [84]: In leading order  $\phi_q(t) - f_q^c$  factorizes in two terms,  $h_q$  and  $G(t)$ . The factor  $h_q$

is time- and control-parameter-independent and characterizes the specific correlator by its wave-vector dependence. The other factor  $G(t)$  is shared by all correlators and describes the dependence on control parameters and the time. This factorization is a consequence of the center manifold theorem [85]. As a result, the rescaled correlators  $\hat{\phi}_q(t) = [\phi_q(t) - f_q^c]/h_q$  are the same for all  $q$ . However, the function  $G(t)$  is different for the  $A_2$ - and higher-order singularities. In Eq. (5.37),  $G(t) = -B \ln(t/\tau)$ . The  $q$ -dependence of the amplitude  $K_q$  reflects that already the leading corrections to the leading-order logarithmic decay depend on the correlator chosen. Since the leading corrections determine the range of validity for the leading order result this implies that the range where the leading result holds can be quite different for different correlation functions. It is only the term proportional to  $K_q$  that causes a violation of the factorization theorem if we generalize it to  $\phi_q(t) - (f_q^c + \hat{f}_q) = h_q G(t)$  where now  $G(t)$  includes all terms in the square brackets in Eq. (5.42) except the one proportional to  $B^2$ .

### 3. Critical decay at an $A_3$ -singularity

The expansion in the previous section is restricted to the weak-coupling side of the higher-order singularity, cf. Eq. (5.21), and becomes invalid right at the singularity where  $\varepsilon_1(\mathbf{V}) = 0$ . Therefore, a different expansion is needed for that case of a critical decay at a higher-order singularity.

For a discussion of the critical decay at the  $A_3$ -singularity, we set  $\mathbf{V} = \mathbf{V}^c$  in the coefficients of Eq. (5.7b),  $A_{qk_1 \dots k_n}^{(n)}(\mathbf{V}) = A_{qk_1 \dots k_n}^{(n)c}$ . The  $\mathbf{V}$ -dependent terms in the inhomogeneity  $J_q(z)$  in Eq. (5.9b) vanish and the rhs of Eq. (5.9a) can be written as  $J_q(z) = \sum_{n \geq 2} J_q^{(n)}(z)$  with the  $n$ th expansion term given by

$$(5.45) \quad J_q^{(n)}(z) = A_{qk_1 \dots k_n}^{(n)c} \mathcal{S}[\hat{\phi}_{k_1}(t) \cdots \hat{\phi}_{k_n}(t)](z) - \mathcal{S}[\hat{\phi}_q(t)]^n(z).$$

The strategy to find a solution is again to split the problem into a  $q$ -independent part  $\hat{\phi}(t)$  and a  $q$ -dependent part  $\hat{\phi}_q(t)$ . The solution of the  $q$ -independent problem is again equivalent to solving the one-component case, and after having solved the one-component case, parameters like the  $\mu_i$  appearing in the solution for  $\hat{\phi}(t)$  have to be expressed in terms of  $q$ -dependent quantities by applying the solvability condition, Eq. (5.13a). Wave-vector dependent corrections  $\hat{\phi}_q(t)$  are derived with the reduced resolvent  $R_{qk}$  in Eq. (5.13c).

**3.1. One-component case.** At the singularity also all separation parameters are zero in Eq. (5.16) and the latter equation is regrouped for the one-component case as

$$(5.46) \quad 0 = \begin{aligned} & \mathcal{S}[\hat{\phi}^2(t)](z) - \mathcal{S}[\hat{\phi}(t)]^2(z) & - & \mu_3 \mathcal{S}[\hat{\phi}^3(t)](z) \\ & + \kappa \left( \mathcal{S}[\hat{\phi}^3(t)](z) - \mathcal{S}[\hat{\phi}(t)]^3(z) \right) & - & \mu_4 \mathcal{S}[\hat{\phi}^4(t)](z) \\ & & & + \sum_{n=4}^{\infty} K_n(z) . \end{aligned}$$

The parameter  $\kappa$  was introduced for later convenience and is equal to  $2\zeta$ . Some abbreviations were introduced for the terms above which are of order  $n$  in the small quantity  $\hat{\phi}(t)$ ,

$$(5.47a) \quad K_n(z) = \kappa_n \psi_{n-1}(z) - \mu_n \mathcal{S}[\hat{\phi}^n(t)](z), \quad n \geq 4,$$

$$(5.47b) \quad \psi_i(z) = \mathcal{S}[\hat{\phi}^i(t)](z) - \mathcal{S}[\hat{\phi}(t)]^i(z).$$

For the one-component case  $\kappa = \kappa_i = 1$  and the  $\mu_i$  are defined as in Eq. (5.14b).

The problem stated in Eq. (5.46) shall be solved in the following by an extension of the Tauberian theorem for slowly-varying functions introduced in Ref. [35]. A function  $G(t)$  slowly varying for large times is defined by  $\lim_{T \rightarrow \infty} G(tT)/G(T) = 1$  for all  $t > 0$ . This is equivalent to  $\mathcal{S}[G(t)](z)$  being slowly varying for small frequencies,  $\lim_{T \rightarrow \infty} \mathcal{S}[G(t)](z/T)/\mathcal{S}[G(t)](i/T) = 1$ . The Tauberian theorem states that  $\mathcal{S}[G(t)](z)$  is asymptotically equal to  $G(i/z)$  for small frequencies [86],

$$(5.48) \quad \lim_{z \rightarrow 0} \mathcal{S}[G(t)](z)/G(i/z) = 1.$$

Typical examples for slowly varying functions are functions of logarithms. Slowly varying functions that will be used as an Ansatz in the following shall be defined as

$$(5.49a) \quad G(t) = g(x), \quad x = \ln(t/t_0), \quad y = \ln(i/zt_0),$$

where  $g(x)$  is given by a sum of  $g_m(x)$  with polynomials  $p_m$  of order  $l_0$ ,

$$(5.49b) \quad g_m(x) = p_m(\ln x)/x^m, \quad p_m(\xi) = \sum_{l=0}^{l_0} c_{m,l} \xi^l, \quad m = 1, 2, \dots,$$

The function  $g_{m+1}(x)$  is of higher order than  $g_m(x)$  and can be neglected asymptotically,  $\lim_{x \rightarrow \infty} g_{m+1}(x)/g_m(x) = 0$ . We introduce the notation  $f(x) = \mathcal{O}(1/x^m)$  if  $f(x)x^m$  is bounded by some polynomial in  $\ln x$  for large  $x$ . Then, the functions  $g_m(x)$  are of order  $\mathcal{O}(1/x^m)$  and for the derivatives  $d^n g(x)/dx^n = g^{(n)}(x)$ ,  $n = 0, 1, 2 \dots$  one finds

$$(5.50) \quad g_m^{(n)}(x) = \mathcal{O}(1/x^{m+n}).$$

The  $\mathcal{S}$ -transform of Eq. (5.1b) can be written as  $\mathcal{S}[G(t)](z) = \int_0^\infty \exp(-u)g(y + \ln u) du$  and a formal expansion in powers of  $\ln u$  leads to [35]

$$(5.51) \quad \mathcal{S}[G(t)](z) = \sum_{n=0}^{\infty} \frac{1}{n!} \Gamma_n g^{(n)}(y).$$

Here  $\Gamma_n$  denotes again the  $n$ th derivative of the gamma function at unity. Introducing  $G(t) = g_m(x)$  into the expansion Eq. (5.51) results in an asymptotic expansion in increasing orders  $\mathcal{O}(1/y^{m+n})$ . The leading contribution for  $n = 0$  is just the result  $g_m(y)$  from the Tauberian theorem (5.48).

If one replaces the functions  $G(t)$  in expansion (5.51) by a product  $G(t)F(t)$ , one gets the asymptotic expansion

$$(5.52) \quad \mathcal{S}[G(t)F(t)](z) - \mathcal{S}[G(t)](z)\mathcal{S}[F(t)](z) = \sum_{n=2}^{\infty} \sum_{m=1}^{n-1} \frac{[\Gamma_n - \Gamma_{n-m}\Gamma_m]}{(n-m)!m!} g^{(n-m)}(y) f^{(m)}(y).$$

Using  $G(t) = g_{m_1}(x)$  and  $F(t) = g_{m_2}(x)$ , the Tauberian theorem implies that the leading contribution to  $\mathcal{S}[G_{m_1}(t)G_{m_2}(t)](z)$  cancels against the leading contribution to  $\mathcal{S}[G_{m_1}(t)](z)\mathcal{S}[G_{m_2}(t)](z)$ . It is observed in the extension to the Tauberian theorem that also the leading corrections to the Tauberian theorem cancel [35],

$$(5.53) \quad \mathcal{S}[g_{m_1}(t)g_{m_2}(t)](z) - \mathcal{S}[g_{m_1}(t)](z)\mathcal{S}[g_{m_2}(t)](z) = \mathcal{O}(1/y^{m_1+m_2+2}).$$

The difference between the two terms on the left-hand side is two orders smaller for vanishing frequencies than each of the terms separately. This applies in particular to the differences  $\psi_n(z)$  which are of higher order than the individual terms  $\mathcal{S}[\hat{\phi}^n(t)](z)$  or  $\mathcal{S}[\hat{\phi}(t)]^n(z)$  in Eq. (5.47).

3.1.1. *The leading contribution.* To solve Eq. (5.46) in leading order we use the Ansatz  $\hat{\phi}(t) = g_m(x) = c_m/x^m$  where the polynomial in Eq. (5.49b) was chosen to be the constant  $c_m$ . From the expansion (5.51) one infers that  $\mathcal{S}[\hat{\phi}^3(t)](z) = (c_m/y^m)^3 + \mathcal{O}(1/y^{3m+1})$ . Using Eq. (5.52) with  $G(t) = F(t) = g_m(x)$  for calculating  $\psi_2(z)$ , one obtains  $\psi_2(z) = \zeta(2)(mc_m/y^{m+1})^2 + \mathcal{O}(1/y^{2m+3})$ .  $\zeta(k)$  denotes again the zeta function [87]. Choosing  $m = 2$ , both terms in the first line of Eq. (5.46),  $\psi_2(z) - \mu_3\mathcal{S}[\hat{\phi}^3(t)](z)$ , are of the same order  $1/y^6$ . They cancel in this leading order if we set  $\mu_3c_2^3 = 4\zeta(2)c_2^2$ . The expansion in Eq. (5.51) and the cancellation of Eq. (5.53) assert that the terms in the second line of Eq. (5.46) are of order  $1/y^8$  and higher. One concludes that the leading asymptotic behavior of the critical correlator for large times is described by  $\hat{\phi}(t) = g_2(x)$ , where

$$(5.54) \quad g_2(x) = c_2/x^2, \quad c_2 = 4\zeta(2)/\mu_3.$$

3.1.2. *The leading correction.* Let us split the function  $\hat{\phi}(t)$  into its leading term and a correction  $\tilde{g}(x)$ :

$$(5.55) \quad \hat{\phi}(t) = g_2(x) + \tilde{g}(x).$$

Substitution of this formula into the first line of Eq. (5.46), one gets expressions up to third order in  $\tilde{g}$ . The term independent of  $\tilde{g}$  is  $\mathcal{S}[g_2^2(x)](z) - \mathcal{S}[g_2(x)]^2(z) - \mu_3\mathcal{S}[g_2^3(x)](z)$ , and it shall be denoted by  $[(4\zeta(2))^2/\mu_3]F(y)$ . Equations (5.51) and (5.52) are used to derive the asymptotic series

$$(5.56a) \quad F(y) = \sum_{n=3}^{\infty} \frac{(-1)^{n+1}}{\mu_3 y^{4+n}} \left\{ \frac{1}{30} \zeta(2) \frac{(n+3)!}{(n-2)!} \Gamma_{n-2} - \sum_{m=1}^{n-2} (n-m+1)(m+1)(\Gamma_n - \Gamma_{n-m}\Gamma_m) \right\}.$$

The term linear in  $\tilde{g}$  is given by  $2\{\mathcal{S}[g_2(x)\tilde{g}(x)](z) - \mathcal{S}[g_2(x)](z)\mathcal{S}[\tilde{g}(x)](z)\} - 3\mu_3\mathcal{S}[g_2^2(x)\tilde{g}(x)](z)$ . It shall be denoted by  $[(4\zeta(2))^2/\mu_3][\mathcal{D}\tilde{g}(y) + \mathcal{D}'\tilde{g}(y)]$ . Here, the differential operator  $\mathcal{D}$  yields the leading contribution

$$(5.56b) \quad \mathcal{D}\tilde{g}(y) = [y \cdot d\tilde{g}(y)/dy + 3\tilde{g}(y)]/y^4.$$

The correction  $\mathcal{D}'$  is expanded with the aid of Eqs. (5.51) and (5.52):

$$(5.56c) \quad \mathcal{D}'\tilde{g}(y) = [1/2\zeta(2)] \sum_{n=3}^{\infty} \sum_{m=1}^{n-1} (-1)^{n-m} \{ [\tilde{g}^{(m)}(y)/y^{n+2-m}m!](\Gamma_n - \Gamma_{n-m}\Gamma_m) \\ + \zeta(2)\Gamma_{n-2}[\tilde{g}^{(m-1)}(y)/y^{n+3-m}(m-1)!(n-m+1)(n-m)(n-m+1)] \}.$$

With these notations, the equation of motion for  $\tilde{g}(y)$  is reformulated in the form of a linear differential equation with some inhomogeneity  $I(y)$ :

$$(5.57a) \quad \mathcal{D}\tilde{g}(y) = I(y),$$

$$(5.57b) \quad I(y) = F(y) + \mathcal{D}'\tilde{g}(y) \\ + \mathcal{S}[\tilde{g}^2(x)](z) - \mathcal{S}[\tilde{g}(x)]^2(z) - 3\mu_3\mathcal{S}[g_2(x)\tilde{g}^2(x)](z) \\ - \mu_3\mathcal{S}[\tilde{g}^3(x)](z) + \kappa\psi_3(z) - \mu_4\mathcal{S}[\hat{\phi}^4(t)](z) + \sum_{n=4}^{\infty} K_n(z).$$

The iterative solution of Eq. (5.57a) for  $\tilde{g}(x)$  is based on the observation, that one gets for functions  $g_m(y)$  from Eq. (5.49b):

$$(5.58) \quad \mathcal{D}g_m(y) = [p'_m(y) + (3-m)p_m]/y^{m+4}.$$



With  $\tilde{g}(x) = g_3(x)$ ,  $\mathcal{D}g_m(y) = p'_3(y)/y^7$ . In addition, all terms on the right hand side of Eq. (5.57b) are of order  $\mathcal{O}(1/y^8)$  except for the  $n = 4$  contribution to  $F(y)$ , which is  $24\zeta(3)/(\mu_3 y^7) + \mathcal{O}(1/y^8)$ . Hence, the leading order solution for  $\tilde{g}$  reads

$$(5.59) \quad g_3(x) = c_3 \ln(x)/x^3, \quad c_3 = 24\zeta(3)/\mu_3.$$

Combining this finding with Eqs. (5.54) and (5.55) and eliminating all the abbreviations, one reproduces the result of Ref. [35]:

$$(5.60) \quad \phi^c(t) = f^c + (1 - f^c)[c_2/\ln^2(t/t_0)]\{1 + [6\zeta(3)/\zeta(2)] \ln \ln(t/t_0)/\ln(t/t_0)\}.$$

This formula describes the critical correlator up to errors of the order  $1/\ln^4(t/t_0)$ .

**3.1.3. Higher-order corrections.** The equation for  $\tilde{g}(y)$  allows for an iterative solution so that the iteration step with number  $m$  reads  $\tilde{g} = g_3 + g_4 + \dots + g_m$ . Here the numerator polynomial in Eq. (5.49b) is of degree  $l_0 = (m - 2)$ , i.e.,

$$(5.61) \quad g_m(x) = \sum_{l=0}^{m-2} c_{m,l} \ln^l(x)/x^m.$$

Suppose, the procedure had been carried out up to step  $m - 1$ ,  $m = 4, 5, \dots$ , then  $\mathcal{D}\tilde{g}(y) = \mathcal{D}g_m(y) + \mathcal{O}(1/y^{m+3})$ . By construction, all terms up to order  $(m+3)$  cancel against the one appearing in  $I(y)$ . One checks, that the leading contribution to  $I(y)$  reads  $p(\ln y)/y^{m+4}$ , where the degree of the polynomial  $p$  does not exceed  $m - 3$ . Hence, Eq. (5.57a) is equivalent to the linear differential equation  $p'_m + (3 - m)p_m = p$ . This is readily solved by Eq. (5.61), provided the coefficients  $c_{m,l}$  are chosen properly.

In order to determine  $g_4$  and  $g_5$ , one can drop the terms  $\sum_{n=4}^{\infty} K_n(z)$  in Eq. (5.57b). The coefficients  $c_{m,l}$  are given by  $\mu_3$ ,  $\kappa$ , and  $\mu_4$  as follows

$$(5.62a) \quad c_{4,0} = 792 \zeta(3)^2/(\pi^2 \mu_3) + \pi^4 [4\mu_4/(9\mu_3^2) - 4\kappa/(3\mu_3) - 7/6]/\mu_3,$$

$$(5.62b) \quad c_{4,1} = -432 \zeta(3)^2/(\pi^2 \mu_3),$$

$$(5.62c) \quad c_{4,2} = 648 \zeta(3)^2/(\pi^2 \mu_3),$$

$$(5.63a) \quad c_{5,0} = \zeta(3) \pi^2 [400 \kappa \mu_3 + 1551 \mu_3^2 - 160 \mu_4]/(15 \mu_3^3) \\ - [39744 \zeta(3)^3/\pi^4 + 528 \zeta(5)]/\mu_3,$$

$$(5.63b) \quad c_{5,1} = 64800 \zeta(3)^3/(\pi^4 \mu_3) - 4\zeta(3) \pi^2 [21 \mu_3^2 - 24 \kappa \mu_3 + 8 \mu_4]/(\mu_3^3),$$

$$(5.63c) \quad c_{5,2} = -27216 \zeta(3)^3/(\pi^4 \mu_3),$$

$$(5.63d) \quad c_{5,3} = 15552 \zeta(3)^3/(\pi^4 \mu_3).$$

The coefficients for  $g_6$  and  $g_7$  are presented as Eqs. (A.9) and (A.10) in the appendix. The only new model parameters entering the coefficients are  $\mu_5$  and  $\kappa_4$ . In summary, the solution for the critical decay at an  $A_3$ -singularity in the one-component case can be given up to order  $\mathcal{O}(x^{-(n+1)})$  as a sum of functions  $g_m(x)$  of order  $\mathcal{O}(x^{-m})$ ,

$$(5.64) \quad \hat{\phi}(t) = G_n(x) = \sum_{m=2}^n g_m(x), \quad x = \ln(t/t_0).$$

This asymptotic expression replaces the expansion in the power law  $(t/t_0)^{-a}$  which is valid for a generic  $A_2$ -singularity [3]. The solution 5.64 is by itself valid only for  $A_3$ -singularities. For  $\mu_3 \rightarrow 0$  all coefficients  $c_{m,l}$  diverge.

**3.2. Multi-component case.** The starting point of the expansion for the multi-component case is the observation that the leading order of the one-component solution is of quadratic order in the inverse logarithm of time,  $\mathcal{S}[\hat{\phi}(t)](z) = \mathcal{O}(y^{-2})$ . To keep notation concise this will be denoted by  $\mathcal{O}(\hat{\phi})$  in the following. Since the inhomogeneities in Eq. (5.45) are of at least quadratic order in the one-component solution,  $J_q = \mathcal{O}(\hat{\phi}^2)$ , the definition of the  $q$ -dependent corrections, Eq. (5.13c), implies that these are of the same order,  $\tilde{\phi}_q = \mathcal{O}(\hat{\phi}^2)$ .

Substituting the splitting (5.13b) into the inhomogeneity  $J_q^{(2)}(z)$  from Eq. (5.45) yields

$$(5.65) \quad J_q(z) = A_{qk_1k_2}^{(2)c} a_{k_1} a_{k_2} \mathcal{S}[\hat{\phi}(t)^2] - a_q^2 \mathcal{S}[\hat{\phi}(t)]^2 + \mathcal{O}(\hat{\phi}^3).$$

Using the relation of Eq. (5.53) for  $\psi_2(z)$  in Eq. (5.47b) allows to reduce the product of  $\mathcal{S}$ -transforms of  $\hat{\phi}$  to an  $\mathcal{S}$ -transform of products of  $\hat{\phi}$  and a term of higher order,

$$(5.66) \quad J_q(z) = (A_{qk_1k_2}^{(2)c} a_{k_1} a_{k_2} - a_q^2) \mathcal{S}[\hat{\phi}(t)^2] + a_q^2 \psi_2(z) + \mathcal{O}(\hat{\phi}^3).$$

Only the first term in Eq. (5.66) is of order  $\mathcal{O}(\hat{\phi}^2)$  while  $\psi_2(z) = \mathcal{O}(\hat{\phi}^3)$ , cf. Eq. (5.53). The solvability condition requires  $a_q^* J_q(z) = 0$  which in Eq. (5.66) can be fulfilled up to higher orders by the definition of  $\mu_2$  as above in Eq. (5.34), since  $\mu_2 \mathcal{S}[\hat{\phi}(t)^2] = 0$  for higher-order singularities where  $\mu_2 = 0$ . For the  $q$ -dependent correction of order  $\mathcal{O}(\hat{\phi}^2)$ , the reduced resolvent  $R_{qk}$ , Eq. (5.13c), yields

$$(5.67) \quad \tilde{\phi}_q(t) = X_q \hat{\phi}^2(t) + \mathcal{O}(\hat{\phi}^3)$$

with the definition of  $X_q$  introduced in Eq. (5.38b). The solution of the first step in the derivation of  $q$ -dependent corrections is up to order  $\mathcal{O}(\hat{\phi}^3)$ :

$$(5.68) \quad \hat{\phi}_q(t) = a_q \tilde{\phi}_q(t) + X_q \hat{\phi}^2(t) + \tilde{\phi}'_q(t).$$

The next step is started by substituting the result (5.68) into  $J_q(z)$ , Eq. (5.9b). Using the definition of  $\mu_2$ , terms of order  $\mathcal{O}(\hat{\phi}^2)$  vanish altogether as demonstrated above and only  $a_q^2 \psi_2(z)$  and additional terms of order  $\mathcal{O}(\hat{\phi}^3)$  are left from the line  $J_q^{(2)}(z)$ , Eq. (5.66). The repeated use of Eq. (5.47b) to reduce products of  $\mathcal{S}$ -transforms to  $\mathcal{S}$ -transforms of products is again used to collect the appropriate terms, and the inhomogeneity assumes the form

$$(5.69) \quad J_q(z) = \mathcal{S}[\hat{\phi}(t)^3] \left[ A_{qk_1k_2k_3}^{(3)c} a_{k_1} a_{k_2} a_{k_3} + 2(A_{qk_1k_2}^{(2)c} a_{k_1} X_{k_2} - a_q^2) - (a_q^3 + 2a_q X_q) \right] + a_q^2 \psi_2(z) + \mathcal{O}(\hat{\phi}^4).$$

The definition of  $\kappa = 2\zeta$  and  $\mu_3$  as in Eqs. (5.40) and (5.41) is again possible after multiplication of Eq. (5.69) with  $a_q^*$ , and the solvability condition up to order  $\mathcal{O}(\hat{\phi}^4)$  reads

$$(5.70) \quad 0 = \psi_2(z) - \mu_3 \mathcal{S}[\hat{\phi}(t)^3] + \mathcal{O}(\hat{\phi}^4),$$

which reproduces the form of Eq. (5.47a) and was solved for  $\mathcal{S}[\hat{\phi}(t)]$  in Sec. 3.1 for the one-component case. The application of the reduced resolvent  $R_{qk}$  yields  $\tilde{\phi}'_q(t)$  up to order  $\mathcal{O}(\hat{\phi}^4)$  by introducing a new amplitude  $Y_q$  as

$$(5.71) \quad Y_q = R_{qk} \left\{ \left[ A_{kk_1k_2k_3}^{(3)c} a_{k_1} a_{k_2} a_{k_3} - a_k^3 \right] + 2 \left[ A_{kk_1k_2}^{(2)c} a_{k_1} X_{k_2} - a_k X_k \right] + \mu_3 a_k^2 \right\}.$$

For the last term in the curly brackets Eq. (5.70) was used to express the frequency dependence of  $J_q(z)$  in Eq. (5.69) solely by  $\mathcal{S}[\hat{\phi}(t)^3]$ . After this second reduction step the solution reads up to order  $\mathcal{O}(\hat{\phi}^4)$ :

$$(5.72) \quad \hat{\phi}_q(t) = a_q \hat{\phi}_q(t) + X_q \hat{\phi}^2(t) + Y_q \hat{\phi}^3(t) + \tilde{\phi}_q''(t).$$

Here, already the contribution proportional to  $Y_q$  has  $g_2^3$  as the lowest order term and is of higher order than  $g_5$ . However, the calculation of the amplitude  $Y_q$  is a prerequisite to determine the parameter  $\mu_4$  which is necessary for the evaluation of  $g_5$ . To continue we substitute again Eq. (5.72) into the solvability condition (5.9b) which after the same tricks as before is required to yield a definition of  $\mu_4$  which is consistent with the equations for the one-component case. Before adding new terms from the expansion of  $J_q(z)$  in Eq. (5.45), the remaining terms of order  $\mathcal{O}(\hat{\phi}^5)$  in Eq. (5.69) shall be collected from the lines with  $n \leq 3$  discussed above. A new parameter is introduced to shorten notation,

$$(5.73) \quad \kappa' = 2a_q^* a_q X_q,$$

and the contribution to  $J_q(z)$  so far is  $\kappa \psi_3(z) - \kappa' \mathcal{S}[\hat{\phi}] \psi_2(z)$ . Equation (5.70) can be used to eliminate  $\psi_2(z)$  and with the assistance of Eq. (5.47b) this contribution is reduced to  $\kappa \psi_3(z) - \mu_3 \kappa' \mathcal{S}[\hat{\phi}^4] + \mathcal{O}(\hat{\phi}^5)$ . Next, the term from Eq. (5.45) for  $n = 4$  is added and the term with  $\kappa'$  is absorbed in the definition of  $\mu_4$ . Then the solvability condition up to order  $\mathcal{O}(\hat{\phi}^5)$  reads

$$(5.74) \quad 0 = \kappa \psi_3(z) - \mu_4 \mathcal{S}[\hat{\phi}^4] + \mathcal{O}(\hat{\phi}^5).$$

This is solved by the expansion of the one-component solution up to the term  $g_5$ , and the definition for the remaining parameter  $\mu_4$  is

$$(5.75) \quad \mu_4 = a_q^* \{ [a_q^4 - A_{qk_1k_2k_3k_4}^{(4)c} a_{k_1} a_{k_2} a_{k_3} a_{k_4}] + 3[a_q^2 X_q - A_{qk_1k_2k_3}^{(3)c} a_{k_1} a_{k_2} X_{k_3}] \\ + [X_q^2 - A_{qk_1k_2}^{(2)c} X_{k_1} X_{k_2}] + 2[a_q Y_q - A_{qk_1k_2}^{(2)c} a_{k_1} Y_{k_2}] \} + \kappa' \mu_3.$$

After having defined all the necessary parameters, we see that the solution of Sec. 3.1 for  $\hat{\phi}(t)$  is consistent with the solution of the  $q$ -dependent case as formulated in Eq. (5.72). Keeping only terms up to order  $(1/\ln t)^5$ , one finally arrives at the asymptotic solution for the  $q$ -dependent critical correlator at an  $A_3$ -singularity,

$$(5.76) \quad \phi_q^\circ(t) = f_q^\circ + h_q^\circ \{ g_2(x) + g_3(x) \\ + [g_4(x) + K_q^\circ g_2^2(x)] + [g_5(x) + 2K_q^\circ g_2(x)g_3(x)] \}.$$

We recognize that different from the expansion in Sec. 2, the leading correction in Eq. (5.76) is given only by a term respecting the factorization,  $g_3(x)$ . Factorization is first violated in order  $1/\ln^4 t$  and again only the amplitudes  $K_q$  are responsible for that. The expansion for  $\phi_q^\circ(t)$  can be carried out up to order  $1/\ln^5 t$  if  $\mu_4$  is known. The next order would include  $g_6(x)$  and require the additional parameter  $\mu_5$ .

#### 4. Critical decay at an $A_4$ -singularity

The  $A_4$ -singularity is a special case of an  $A_3$ -singularity with  $\mu_3 = 0$ . For the logarithmic decay presented in Sec. 2 it is possible to specialize to the  $A_4$ -singularity by simply setting  $\mu_3 = 0$  in the solution for the parameters  $B_j$  in Eq. (5.29). Different from that, the critical decay for the  $A_4$ -singularity does not follow from the solution for the  $A_3$ -singularity but requires another asymptotic

expansion. However, the tricks for a solution in terms of slowly varying functions are the same for  $A_3$  and  $A_4$ .

**4.1. One-component case.** With vanishing  $\mu_3$  at an  $A_4$ -singularity, (5.16) has yet again to be regrouped,

$$(5.77) \quad \begin{aligned} 0 = & \psi_2(z) & - & \mu_4 \mathcal{S}[\hat{\phi}^4(t)](z) \\ & + & \kappa\psi_3(z) & - & \mu_5 \mathcal{S}[\hat{\phi}^5(t)](z) \\ & + & \kappa_4\psi_4(z) & - & \mu_6 \mathcal{S}[\hat{\phi}^6(t)](z) \\ & & & + & \dots \end{aligned}$$

Using again the Ansatz  $\hat{\phi}(t) = g_m(x) = c_m/x^m$  one arrives for the terms on the first line of Eq. (5.77) at  $\psi_2(z) = \zeta(2)(mc_m/y^{m+1})^2 + \mathcal{O}(1/y^{2m+3})$  and  $\mathcal{S}[\hat{\phi}(t)](z) = (c_m/y^m)^4 + \mathcal{O}(1/y^{4m+1})$ . For  $m = 1$  the first line in Eq. (5.77) is of leading order  $\mathcal{O}(1/y^4)$  with the equation for the coefficient  $(\zeta(2)c_1)^2 = \mu_4$  which results in the leading-order solution [38],

$$(5.78) \quad g_1(x) = c_1/x, \quad c_1 = \sqrt{\zeta(2)/\mu_4}.$$

The corrections may be rephrased in terms of a differential operator again and the solution is straight forward as before. Since for the  $q$ -dependent solution only the first correction will be needed, only the first correction is calculated explicitly here by the linear differential equation for the Ansatz  $\hat{\phi}(t) = g_1(x) + \tilde{g}(x)$ ,

$$(5.79) \quad 2y^3\tilde{g}'(y) + 4y^2\tilde{g} = 4\sqrt{\zeta(2)/\mu_4}\zeta(3)/\zeta(2) + 3\zeta(2)\kappa/\mu_4 - \mu_5\zeta(2)/\mu_4^2.$$

This is solved in leading order by  $g_2(x)$  [41],

$$(5.80)$$

$$g_2(x) = c_2 \ln(x)/x^2, \quad c_2 = 2\sqrt{\zeta(2)/\mu_4}\zeta(3)/\zeta(2) + 3\zeta(2)\kappa/(2\mu_4) - \mu_5\zeta(2)/(2\mu_4^2).$$

Higher-order contributions for  $m \geq 3$  can be written in the form

$$(5.81) \quad g_m(x) = \sum_{l=0}^{m-1} c_{m,l} \ln^l(x)/x^m,$$

and — with the appropriate choice of the parameters  $c_{m,l}$  — the general solution for the critical decay at an  $A_4$ -singularity in the one-component case is represented up to  $\mathcal{O}(\ln^{-(m+1)} t)$  as

$$(5.82) \quad \hat{\phi}(t) = G_n(x) = \sum_{m=1}^n g_m(x), \quad x = \ln(t/t_0).$$

Because the leading order result  $g_1(x)$  is of order  $\mathcal{O}(1/\ln t)$  each higher order solution requires the inclusion of an additional line in Eq. (5.77). This adds new parameters  $\mu_i$  and  $\kappa_{i-2}$  in each step whereas for the  $A_3$ -singularity, Eq. (5.61), additional parameters occur only in every second step in the solution.

**4.2. Multi-component case.** The solution up to the first correction given by  $g_1(x) + g_2(x)$  already requires the evaluation of the parameter  $\mu_5$ . Therefore we need to calculate the amplitudes  $X_q$ ,  $Y_q$ , and  $Z_q$ . The procedure is completely analogous to the solution for the  $A_3$ -singularity. Again,  $J_q = \mathcal{O}(\hat{\phi}^2)$  in Eq. (5.9b), and  $\tilde{\phi}_q = \mathcal{O}(\hat{\phi}^2)$ . Solving the successively higher orders allows for the definition of the quantities above, namely  $X_q$ ,  $Y_q$ ,  $\mu_2$ ,  $\mu_3$  and  $\mu_4$ , together with  $\kappa$  and  $\kappa'$ . The restriction to  $\mu_3 = 0$  simplifies Eqs. (5.71) and (5.75). With however different

terms in  $\hat{\phi}$ , the form of Eq. (5.72) remains valid also for the present expansion. The additional amplitude  $Z_q$  is obtained by also including terms with  $n = 4$  from Eq. (5.45) with all previous results substituted. Applying the same manipulations as above one arrives at  $\tilde{\phi}_q''(t) = Z_q \hat{\phi}^4 + \mathcal{O}(\hat{\phi}^5)$  with the amplitude

$$(5.83) \quad Z_q = R_{qk} \{ [A_{kk_1 k_2 k_3 k_4}^{(4)c} a_{k_1} a_{k_2} a_{k_3} a_{k_4} - a_k^4] + 3[A_{kk_1 k_2 k_3}^{(3)c} a_{k_1} a_{k_2} X_{k_3} - a_k^2 X_k] \\ + [A_{kk_1 k_2}^{(2)c} X_{k_1} X_{k_2} - X_k^2] + 2[A_{kk_1 k_2}^{(2)c} a_{k_1} Y_{k_2} - a_k Y_k] + \mu_4 a_k^2 \}.$$

Introducing the third  $q$ -dependent correction into the solution adds up to

$$(5.84) \quad \hat{\phi}_q(t) = a_q \hat{\phi}(t) + X_q \hat{\phi}^2(t) + Y_q \hat{\phi}^3(t) + Z_q \hat{\phi}^4(t) + \mathcal{O}(\hat{\phi}^5).$$

Collecting all terms of order  $\mathcal{O}(\hat{\phi}^5)$  after including also the line  $n = 5$  from Eq. (5.45) and inserting Eq. (5.84) provides, using the solvability condition (5.9b), a consistent definition of the parameter

$$(5.85) \quad \mu_5 = a_q^* \{ [a_k^5 - A_{kk_1 k_2 k_3 k_4 k_5}^{(5)c} a_{k_1} a_{k_2} a_{k_3} a_{k_4} a_{k_5}] \\ + 4[a_k^3 X_k - A_{kk_1 k_2 k_3 k_4}^{(4)c} a_{k_1} a_{k_2} a_{k_3} X_{k_4}] \\ + 3[a_k X_k^2 + a_k^2 Y_k - A_{kk_1 k_2 k_3}^{(3)c} (a_{k_1} X_{k_2} X_{k_3} + a_{k_1} a_{k_2} Y_{k_3})] \\ + 2[X_k Y_k + a_k Z_k - A_{kk_1 k_2}^{(2)c} (X_{k_1} Y_{k_2} + a_{k_1} Z_{k_2})] \} + \kappa' \mu_4.$$

Having properly defined the parameter  $\mu_5$  and after substituting (5.81) into (5.84) we can write down the asymptotic solution for the critical decay at an  $A_4$ -singularity in next-to-leading order:

$$(5.86) \quad \phi_q^*(t) = f_q^* + h_q \{ g_1(x) + [g_2(x) + K_q g_1^2(x)] \}.$$

We see that the asymptotic solution for the critical decay is getting increasingly more involved for higher-order singularities. However, the expansion can be performed in terms of the solution of the one-component case. The dominant  $q$ -dependent correction for both  $A_3$ - and  $A_4$ -singularities is given by the square of the leading-order solution,  $\hat{\phi}(t)$ , with the amplitude  $K_q$ . The higher-order contributions enter the curly brackets in Eq. (5.86) as  $g_3(x) + 2g_1(x)g_2(x)X_q/a_q + g_1^3(x)Y_q/a_q$  and  $g_4(x) + g_2^2(x)X_q/a_q + 2g_1(x)g_3(x)X_q/a_q + 3g_1^2(x)g_2(x)Y_q/a_q + g_1^4(x)Z_q/a_q$ . However,  $g_3(x)$  requires the evaluation of the parameters  $\mu_6$  and  $\kappa_4$ ,  $g_4(x)$  needs  $\mu_7$  and  $\kappa_5$ .

## 5. $A_2$ -singularity and coupled quantities

For later reference we will briefly reformulate the asymptotic laws at an  $A_2$ -singularity specified by  $\mu_2 > 0$  in Sec. 5.1. The asymptotic approximations for coupled quantities as introduced in Sec. 3 of Ch. 2 closely follow the ones for the density correlation function. These laws are presented in Sec. 5.2 and apply to the  $A_2$ -singularity as well as to the higher-order singularities. We will follow closely the presentation in Refs. [7, 60], adapt the notation and generalize. For the MSD the laws from Sec. 2 shall be specialized further.

**5.1.  $A_2$ -singularity.** The equations from Sec. 1 hold for all  $A_l$ -singularities and are independent of a chosen asymptotic expansion. In particular, the splitting from Eq. (5.13b) applies to the  $A_2$ -singularity as well. The grouping in Eq. (5.16), however, is different depending on the orders in  $\varepsilon$  the specific expansion introduces

as was seen in Sec. 3. For the expansion at the  $A_2$ -singularity the first line of Eq. (5.16) reduces to

$$(5.87) \quad \varepsilon_1(\mathbf{V}) + \lambda \mathcal{S}[G^{(1)^2}(t)](z) - \mathcal{S}[G^{(1)}(t)]^2(z) = 0.$$

For  $\lambda = 1$ , this is identical to Eq. (5.19). The separation parameter  $\varepsilon_1$  was denoted  $\sigma$  in Ref. [7] and is defined in Eq. (5.35). We will use the notation  $\sigma$  when referring to the separation from an  $A_2$ -singularity and  $\varepsilon_1$  when addressing a higher-order singularity. For  $\lambda < 1$  the solution of Eq. (5.87) is known as  $\beta$ -correlation function [3, 88],

$$(5.88) \quad G(t) = \sqrt{|\sigma|} g_\lambda^\pm(t/t_\sigma), \quad t_\sigma = t_0/|\sigma|^{1/2a}, \quad \sigma \gtrless 0,$$

which is a scaling function that depends only on the exponent parameter  $\lambda$ . Changes in the separation parameters enter only via a time scale  $t_\sigma$  that is diverging when the singularity is approached. The exponent  $a$  describing the divergence is also given by  $\lambda$ ,

$$(5.89) \quad \lambda = \Gamma(1-a)^2/\Gamma(1-2a).$$

The correction is given by  $K_q G(t)^2$  and another scaling function [7, 89],

$$(5.90) \quad H(t) = \sigma h_\lambda^\pm(t/t_\sigma), \quad \sigma \gtrless 0.$$

The  $q$ -dependent solution up to  $\mathcal{O}(\sqrt{\sigma}^3)$  reads

$$(5.91) \quad \phi_q(t) = f_q^c + \hat{f}_q + h_q\{G(t) + [H(t) + K_q G(t)^2]\}.$$

The definition of the correction amplitude  $K_q$  is given in Eqs. (5.38b) and (5.44) and the corrections to the plateau of an  $A_2$ -singularity are

$$(5.92) \quad \hat{f}_q = (1 - f_q^c)\{R_{qk}\hat{A}_k^{(0)}(\mathbf{V}) + a_q[\kappa(\mathbf{V}) + \sigma(\lambda\zeta - \xi)/\mu_2^2]\}.$$

The definition of  $\zeta$  is identical to the one in Eq. (5.40) with the first term divided by  $\lambda$  and  $\xi = \zeta - \mu_3/2$  with  $\mu_3$  from Eq. (5.41). The evaluation of  $\kappa(\mathbf{V})$  is somewhat tedious but straightforward when the linearization in  $\sigma$  adopted in Ref. [7] is discarded.

Formula (5.91) represents again a generalized factorization theorem and it can also be read for Eq. (5.42) with the appropriate definition of  $\hat{f}_q$  from Eq. (5.43) and  $G(t) = G^{(1)}(t)$  defined in Eq. (5.20) and  $H(t) = G^{(2)}(t)$ , Eq. (5.29a). For the critical laws at the  $A_2$ -,  $A_3$ -, and  $A_4$ -singularities the plateau corrections are zero. In this sense Eq. (5.91) incorporates also Eqs. (5.76) and (5.86) and the critical law for the  $A_2$ -singularity where

$$(5.93) \quad G(t) = (t_0/t)^a, \quad H(t) = \kappa(a)(t_0/t)^{2a},$$

with a function [7]

$$(5.94) \quad \kappa(x) = [\xi\Gamma(1-3x) - \zeta\Gamma(1-x)^3]/[\Gamma(1-x)\Gamma(1-2x) - \lambda\Gamma(1-3x)].$$

The decay below the plateau  $f_q^c$  is commonly called  $\alpha$  process and its initial part is described by the von Schweidler law [7, 84],

$$(5.95) \quad G(t) = (t/t'_\sigma)^b, \quad H(t) = \kappa(-b)(t/t'_\sigma)^{2b}, \quad \lambda = \Gamma(1+b)^2/\Gamma(1+2b),$$

with  $\kappa(-b)$  given by Eq. (5.94). The time scale  $t'_\sigma$  obeys another power-law scaling,

$$(5.96) \quad t'_\sigma = \frac{t_0}{B^{1/b}|\sigma|^\gamma}, \quad \gamma = \frac{1}{2a} + \frac{1}{2b}.$$

The number  $B$  and exponents  $a$  and  $b$  are given by  $\lambda$ . They are tabulated in Ref. [88]. The precise form of the function  $\kappa(x)$  is found in [7].

Anticipating that several asymptotic expansions can be phrased in that form we shall use Eq. (5.91) to derive the laws for the coupled quantities in the next section.

**5.2. Coupled Quantities.** In general, the approximations to the coupled quantities are derived by inserting the asymptotic approximation for  $\phi_q(t)$  into the memory kernels for the coupled quantities. We demonstrate that explicitly for the tagged particle correlator  $\phi_q^s(t)$  and the mean-squared displacement (MSD). The general form of Eq. (5.91) will be used in the derivations and  $G$  and  $H$

The equations of motion for the tagged particle, Eq. (2.11), can be reformulated using the  $\mathcal{S}$ -transform in a form similar to Eq. (5.4),

$$(5.97) \quad \frac{\mathcal{S}[\phi_q^s(t)](z)}{1 - \mathcal{S}[\phi_q^s(t)](z)} = \mathcal{S}[\mathcal{F}_q^s[\mathbf{V}, \phi_k(t), \phi_p^s(t)]](z).$$

When inserting Eq. (5.91) into Eq. (5.97), using an expansion as for the coherent functionals and collecting terms of the same order, one can write the approximation in next-to-leading order for the tagged particle as [60],

$$(5.98) \quad \phi_q^s(t) = f_q^{s,c} + \hat{f}_q^s + h_q^s \{G(t) + [H(t) + K_q^s G(t)^2]\},$$

with the critical amplitude  $h_q^s = (1 - f_q^{s,c}) a_q^s$ , the correction amplitude  $K_q^s$  and the plateau correction  $\hat{f}_q^s$ . These quantities are given as

$$(5.99a) \quad \sum_k (\delta_{qk} - A_{q,k}^{s,c}) a_k^s = \sum_k A_{qk}^{s,c} a_k,$$

$$(5.99b) \quad \sum_k (\delta_{qk} - A_{q,k}^{s,c}) a_k^s K_k^s = -\lambda a_q^{s2} + \sum_k A_{qk}^{s,c} a_k K_k \\ + \sum_{k,p} [A_{q,kp}^{s,c} a_k^s a_p^s + A_{qkp}^{s,c} a_k a_p + A_{qk,p}^{s,c} a_k a_p^s],$$

$$(5.99c) \quad \sum_k (\delta_{qk} - A_{q,k}^{s,c}) a_k^s \hat{f}_k^s = -\varepsilon_1 a_q^{s2} + \sum_k A_{qk}^{s,c} a_k \hat{f}_k + \hat{A}_q^s(\mathbf{V}).$$

For the higher-order singularities,  $\lambda = 1$ ; for the  $A_2$ -singularity  $\varepsilon_1$  is replaced by  $\sigma$ . The derivatives with respect to the coherent and tagged particle glass-form factors are denoted before and after the comma, respectively. The coefficients are

$$(5.100) \quad A_{qk_1 \dots k_n, p_1 \dots p_m}^s(\mathbf{V}) = \frac{1}{n!} \frac{1}{m!} (1 - f_q^{s,c}) \frac{\partial^n \partial_m \mathcal{F}_q^s[\mathbf{V}, f_k^c, f_q^{s,c}]}{\partial f_{k_1} \dots \partial f_{k_n} \partial f_{p_1}^s \dots \partial f_{p_m}^s} \\ \times (1 - f_{k_1}^c) \dots (1 - f_{k_n}^c) (1 - f_{p_1}^{s,c}) \dots (1 - f_{p_m}^{s,c}) = \\ = A_{qk_1 \dots k_n, p_1 \dots p_m}^{s,c} + \hat{A}_{qk_1 \dots k_n, p_1 \dots p_m}^s(\mathbf{V}).$$

The transformed equation of motion,  $\mathcal{S}[\delta r^2(t)](z) = 6/\mathcal{S}[m^{(0)}(t)](z)$ , and similar arguments as above yield the asymptotic expansion for the MSD,

$$(5.101) \quad \frac{1}{6} \delta r^2(t) = r_s^{c2} - \hat{r}_s^2 - h_{\text{MSD}} \{G(t) + [H(t) + K_{\text{MSD}} G(t)^2]\},$$

with parameters

$$(5.102a) \quad h_{\text{MSD}} = r_s^{c4} \{\mathcal{F}_{\text{MSD}}^c[h_k, f_p^{s,c}] + \mathcal{F}_{\text{MSD}}^c[f_k, h_p^s]\},$$

$$(5.102b) \quad K_{\text{MSD}} = r_s^{c,4} \{ \mathcal{F}_{\text{MSD}}^c[h_k, h_p^s] + \mathcal{F}_{\text{MSD}}^c[h_k K_k, f_p^{s,c}] \\ + \mathcal{F}_{\text{MSD}}^c[f_k^c, h_p^s K_p^s] \} / h_{\text{MSD}} - \lambda h_{\text{MSD}} / r_s^{c,2},$$

$$(5.102c) \quad \hat{r}_{\text{MSD}}^2 = r_s^{c,4} \{ \mathcal{F}_{\text{MSD}}^c[h_k \hat{f}_k, f_p^{s,c}] + \mathcal{F}_{\text{MSD}}^c[f_k^c, h_p^s \hat{f}_p^s] \\ + \mathcal{F}_{\text{MSD}}^c[f_k^c, f_p^{s,c}](\mathbf{V}) - \mathcal{F}_{\text{MSD}}^c[f_k^c, f_p^{s,c}](\mathbf{V}^c) \} / h_{\text{MSD}} \\ - \varepsilon_1(\mathbf{V}) h_{\text{MSD}}^2 / r_s^{c,2}.$$

Again,  $\varepsilon_1$  has to be replaced by  $\sigma$  for an  $A_2$ -singularity and  $\lambda = 1$  for higher-order singularities.

Inserting the critical law (5.93) into (5.101) yields the following form for the description of the MSD at the transition point,

$$(5.103) \quad \frac{1}{6} \delta r^2(t) = r_s^{c,2} - h_{\text{MSD}} (t_0/t)^a \{ 1 + [K_{\text{MSD}} + \kappa(a)](t_0/t)^a \}.$$

The increase of the MSD above the plateau  $r_s^{c,2}$  is given by the von-Schweidler law, Eq. (5.95),

$$(5.104) \quad \frac{1}{6} \delta r^2(t) = r_s^{c,2} + h_{\text{MSD}} (t/t'_\sigma)^b \{ 1 - [K_{\text{MSD}} + \kappa(-b)](t/t'_\sigma)^b \}.$$

**5.3. Power laws in the MSD.** The logarithmic decay laws (5.42) shall be phrased for the MSD in a slightly different form than in Eq. (5.101) to account for the fact that the MSD is conveniently shown in a double-logarithmic plot and this representation is more sensitive to the detection of power laws. The asymptotic approximation (5.42) for the MSD can be written as

$$(5.105a) \quad z = a_0 + a_1 y + a_2 y^2 + a_3 y^3 + a_4 y^4, \quad z = \delta r^2(t)/6, \quad y = \ln(t/\tau).$$

The constant term represents the square of the localization length,  $a_0 = r_s^{c,2} - \hat{r}_s^2$ , the coefficients  $a_1 = h_{\text{MSD}}(B - B_1)$ ,  $a_2 = -h_{\text{MSD}}(B_2 + K_{\text{MSD}}B^2)$  as well as  $a_3$  and  $a_4$  are separation dependent prefactors for the leading- and next-to-leading order logarithmic terms. Expanding the asymptotic solution (5.105a) for  $\ln z$  close to the plateau yields

$$(5.105b) \quad \ln z = \ln a_0 + b'_1 y + b_2 y^2 + \mathcal{O}(y^3), \quad b'_1 = \frac{a_1}{a_0}, \quad b_2 = \frac{2a_0 a_2 - a_1^2}{2a_0^2}.$$

For vanishing coefficient  $b_2$ , the linear term in Eq. (5.105b) is equivalent to a power law. In leading order in  $\sqrt{\varepsilon}$  this power law for the MSD reads

$$(5.106a) \quad \delta r^2(t)/6 = r_s^{c,2} (t/\tau)^{b_1},$$

with an exponent

$$(5.106b) \quad b_1 = h_{\text{MSD}} B / r_s^{c,2}.$$

Exponent  $b_1$  varies with the square-root in the separation parameter  $\varepsilon_1$ , cf. (5.20), and Eq. (5.106) constitutes a leading-order approximation for the MSD equivalent to Eq. (5.37). In particular the quadratic correction proportional to  $b_2$  is of higher order in  $\sqrt{\varepsilon}$  than the linear term  $b_1$ . Including the next-to-leading order the prefactor  $r_s^{c,2}$  to the power law is rescaled to  $r_s^{c,2} - \hat{r}_s^2$  and the corrected exponent is

$$(5.107) \quad b'_1 = h_{\text{MSD}}(B - B_1) / (r_s^{c,2} - \hat{r}_s^2).$$



### 6. Dynamics in a one-component model

For the demonstration of the results above a simple  $M = 1$  model is used in the following which has two control parameters  $\mathbf{V} = (v_1, v_3)$ ,  $v_1 \geq 0$  and  $v_3 \geq 0$ , and was derived within a theory for spin-glass transitions [90]. We use the model with Brownian microscopic dynamics. Equations (2.7b) and (2.7c) then specialize to

$$(5.108a) \quad \tau_1 \partial_t \phi(t) + \phi(t) + \int_0^t m(t-t') \partial_{t'} \phi(t') dt' = 0 ,$$

$$(5.108b) \quad m(t) = v_1 \phi(t) + v_3 \phi^3(t) .$$

Referencing the powers occurring in the memory kernel (5.108b) the model is also called  $F_{13}$ -model. The discussion below is closely following the one in Ref. [83]. At the appropriate points we extend the discussion or cut it shorter to make the comparison to the SWS easier. In particular, we do not consider the frequency domain in the following for which we refer to Ref. [83].

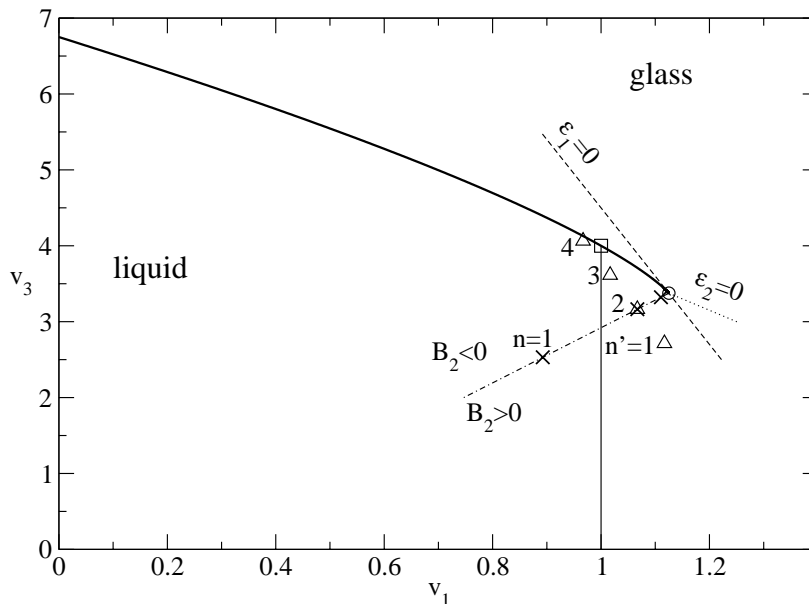


FIGURE 5.1. Glass-transition diagram for the  $F_{13}$ -model defined in Eq. (5.108). The vertical full line shows the liquid-glass-transition singularities connected with a continuous variation of the glass-form factors. The heavy full line represents the set of  $A_2$ -singularities that ends at an  $A_3$ -singularity marked by the circle ( $\circ$ ). The square ( $\square$ ) indicates where the two lines cross. The dashed line presents the boundary where the separation parameter  $\varepsilon_1 = 0$ . The dotted line is the analog for  $\varepsilon_2 = 0$  which is shown only for  $v_1 > 9/8$ . The chain line describes the points of vanishing coefficients  $B_2$ , and crosses ( $\times$ ) and triangles ( $\triangle$ ) denote the states  $n$  and  $n'$  for the discussion in Figs. 5.2 and 5.3, respectively.

The glass-transition diagram for the model in Eq. (5.108) is reproduced in Fig. 5.1 [3, 34]. It is obtained from the largest of the solutions for  $f^c$  of Eq. (2.8), i.e.,  $v_1^c f^c + v_3^c f^{c3} = f^c / (1 - f^c)$ , and Eq. (5.11). There are two transition lines that we plot in a way to enforce the similarity to the glass-transition diagrams of Ch. 4. The first one is the straight vertical line of degenerate  $A_2$ -bifurcations:  $v_1^c = 1$ ,  $0 \leq v_3^c \leq 4$ ,  $f^c = 0$ . Crossing this line by increasing  $v_1$ ,  $f = \phi(t \rightarrow \infty)$  increases continuously. The second one is the smooth curve of  $A_2$ -singularities shown as a heavy full line. It starts at  $v_1^c = 0$ ,  $v_3^c = 27/4$ ,  $f^c = 2/3$ . With decreasing  $v_3^c$ ,  $f^c$  decreases along the line. For  $v_1^c = 1$ ,  $v_3^c = 4$  one crosses the first line for  $f^c = 1/2$ . Decreasing  $f^c$  further, the line reaches the endpoint that is marked by a circle. This is the  $A_3$ -singularity  $\mathbf{V}^\circ$  specified by

$$(5.109) \quad v_1^\circ = 9/8, \quad v_3^\circ = 27/8, \quad f^\circ = 1/3, \quad \mu_3 = 1/3.$$

At the  $A_3$ -singularity,  $\mu_2 = 0$  and for decreasing  $v_1^c$  this parameter increases along the line of transition points as  $\mu_2(v_1^c) = 1 + (3\sqrt{9 - 8v_1^c} - 9)/(8v_1^c)$ . From an expansion for small distances  $\hat{v}_1$  we find  $\mu_2 \propto \sqrt{\hat{v}_1}$ , which is generic at an  $A_3$ -singularity as  $\mu_2$  and  $f$  vary regular but the control parameters assume extreme values as functions of  $f^c$ .

The two separation parameters obtained from Eqs. (5.7b) and (5.14b) are linear functions of the parameters differences  $\hat{v}_{1,3} = v_{1,3} - v_{1,3}^\circ$ :

$$(5.110) \quad \varepsilon_1(\mathbf{V}) = (2/81)[9\hat{v}_1 + \hat{v}_3], \quad \varepsilon_2(\mathbf{V}) = (4/27)[3\hat{v}_1 + \hat{v}_3].$$

The lines  $\varepsilon_i(\mathbf{V}) = 0$  define local coordinates at the  $A_3$ -singularity and condition  $\varepsilon_1 < 0$ , (5.21), is fulfilled below the line  $\varepsilon_1 = 0$  in Fig. 5.1. The formulas (5.110) determine the coefficient  $B$  in Eq. (5.20) and  $B_1$  to  $B_4$  in Eqs. (5.29). The scales  $\tau$  for the results in Eqs. (5.22), (5.30), and (5.31) are determined as the time where the correlator crosses the critical form factor:  $\phi(\tau) = f^\circ$ .

**6.1. Logarithmic decay.** The term  $B_2 \ln^2(t/\tau)$  in Eq. (5.30) is responsible for the dominant deviation of the correlators from the logarithmic-decay law (5.22). Setting  $B_2 = 0$  defines a line (dash-dotted in Fig. 5.1) where the logarithmic-decay law is seen best. Figure 5.2 demonstrates the evolution of the dynamics upon shifting states on this line toward the  $A_3$ -singularity. The time intervals, where the leading order (5.22) or next-to-leading order approximation (5.30) describe the correlators within an error margin of 5%, are marked by closed and open symbols, respectively. For  $n \geq 2$ , these intervals increase with decreasing  $\mathbf{V} - \mathbf{V}^\circ$ .

There are two peculiarities concerning the range of applicability of the asymptotic expansions. First, it can happen that for sufficiently large separation  $\varepsilon$  the range shrinks if one proceeds from the leading approximation to the next-to-leading one as is demonstrated in Fig. 5.2 for the  $n = 1, 2$  results. This is caused by a cancellation of errors due to neglecting the  $B_1$ -correction in the prefactor of the  $\ln(t/\tau)$  term in Eq. (5.30) and due to neglecting the terms proportional to  $B_3$  and  $B_4$ . This peculiarity would disappear if the tolerated error margin were decreased sufficiently below the 5% used. Second, for small  $\mathbf{V} - \mathbf{V}^\circ$ , the interval of decay for  $\phi(t)$  below the critical form factor  $f^c$  that is described by the asymptotic expansion shrinks with decreasing separation. This is inferred by comparing the  $n = 3$  with the  $n = 4$  results. The reason is the following. The correlator  $\phi(t)$  decreases monotonically towards its long-time limit  $f$  [57]. For the liquid state  $n = 1$  the plateau value is zero. After crossing the vertical line in Fig. 5.1 the plateau increases continuously

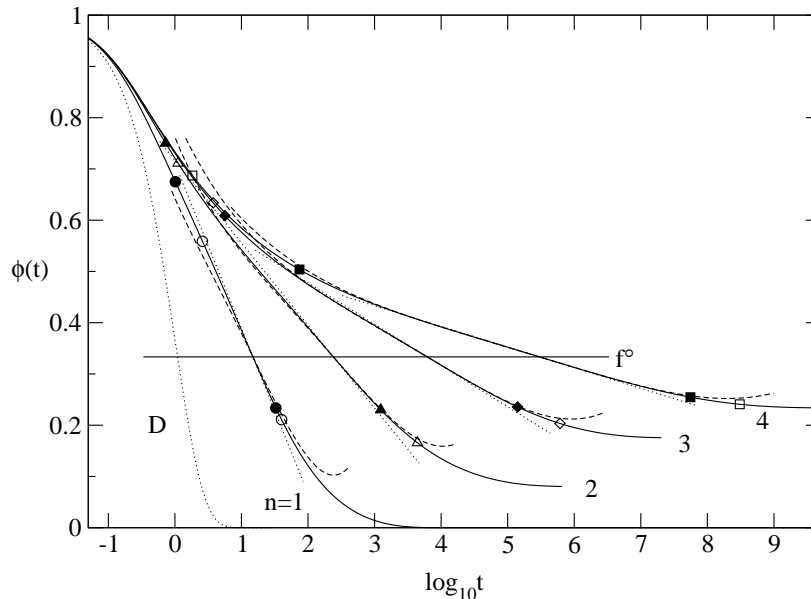


FIGURE 5.2. Correlators  $\phi(t)$  for the one-component model defined in Eq. (5.108). The states are located on the line  $B_2 = 0$  with coupling constants:  $v_1^c - v_1 = 0.9298/4^n$ ,  $v_3^c - v_3 = 3.3750/4^n$ ,  $n = 1, \dots, 4$ , marked by crosses in Fig. 5.1. The full lines are the solutions of Eqs. (5.108a, b) with  $\tau_1 = 1$  as unit of time as also in the following figures. The dotted straight lines exhibit the leading approximation, Eq. (5.22), the dashed lines the leading correction, Eq. (5.30). The filled and open symbols, respectively, mark the times where these approximations deviate from the solution by 5%. The dotted line marked by D is the Debye law  $\exp[-t/\tau_1]$ . The horizontal line shows the critical form factor  $f^\circ = 1/3$ .

from  $f = f^c = 0$  to  $f = f^\circ$  and the interval for the logarithmic decay below  $f^\circ$  decreases.

Figure 5.2 demonstrates that the transient regime extends to about  $t/\tau_1 = 1$ . For vanishing mode-coupling functional, the correlator describes a Debye process:  $\phi(t) = \exp(-t/\tau_1)$ . Mode-coupling effects cause a slower decay for  $t/\tau_1 \geq 1$ . But for  $\mathbf{V}$  close to  $\mathbf{V}^\circ$ , the transient dynamics is rather insensitive to changes of the coupling constants. There is a crossover interval, say  $\tau_1 < t < \tau^*$ , before the decay of  $\phi(t)$  towards  $f^c$  can be described by the  $\ln(t/\tau)$  law. The beginning  $\tau^*$  of the range of validity of Eq. (5.22) is indicated by the filled symbols. There are two subtleties demonstrated for  $n \geq 2$ . First, the time  $\tau^*$  increases upon approaching the  $A_3$ -singularity, and therefore the decay interval  $\phi(\tau^*) - f^\circ$  which is described by the logarithmic law shrinks with decreasing separation parameters. The control-parameter sensitive structural relaxation is governed by the two time scales  $\tau^*$  and  $\tau$ . Both times become large, but  $\tau/\tau^*$  becomes large as well for  $\varepsilon \rightarrow 0$ . Second, the beginning of the range of applicability of the leading correction Eq. (5.30) is almost

control-parameter insensitive, as is shown by the open symbols on the short-time part of the decay curves.

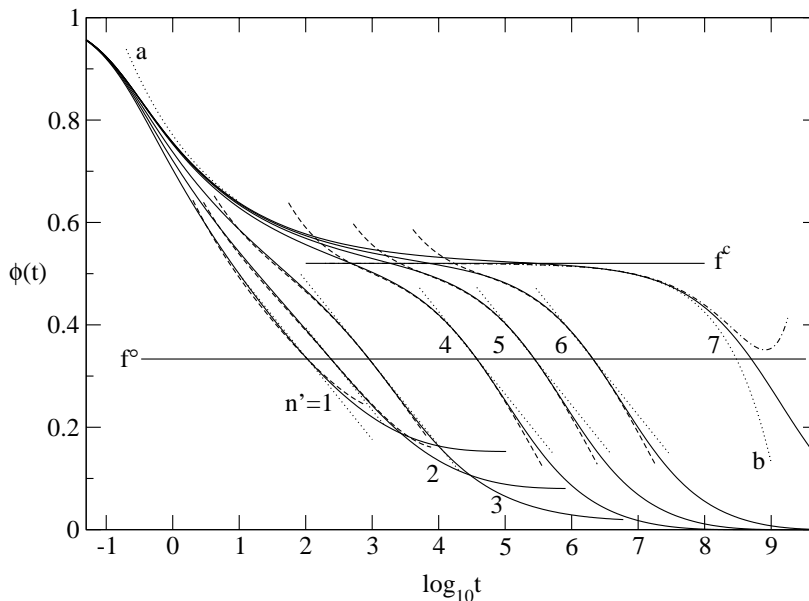


FIGURE 5.3. Correlators  $\phi(t)$  for the one-component model defined in Eq. (5.108) for states located on the line  $\varepsilon_1 = -0.0182$ . The states with labels  $n' = 1-4$  have the coordinates  $(v_1, v_3) = (1.1169, 2.7141)$ ,  $(1.0669, 3.1641)$ ,  $(1.0169, 3.6141)$ ,  $(0.9669, 4.0641)$ , respectively, and they are marked by triangles in Fig. 5.1. The state labeled  $n' = 2$  is identical with the state discussed in Figs. 5.1, 5.2 with label  $n = 2$ . The states with labels 5, 6, and 7 have the coordinates  $(0.9599, 4.1271)$ ,  $(0.9569, 4.1541)$ , and  $(0.9549, 4.1721)$ , respectively. The straight line in Fig. 5.1 through the states 1 to 7 crosses the liquid-glass-transition curve at  $\mathbf{V}^c = (0.95466, 4.17407)$ , where the critical glass-form factor has the value  $f^c = 0.520$  and  $\lambda = 0.719$  implying a critical exponent  $a = 0.318$  and a von Schweidler exponent  $b = 0.608$ . The leading order of the critical decay law, Eq. 5.93 and the von Schweidler law, Eq. (5.95) are shown by dotted lines labeled a and b, respectively; the constants of proportionality are fitted to curve 7. The dashed-dotted curve extends the von Schweidler expansion for curve 7 to the second order, cf. Eq. (5.95). The horizontal lines mark the critical glass-form factors  $f^\circ$  and  $f^c$ , respectively. The dotted straight lines and the dashed curves are the leading asymptotic laws, Eq. (5.22), and the leading correction, Eq. (5.30), respectively.

Let us consider the states labeled  $n' = 1-3$  and shown by triangles in Fig. 5.1 in order to analyze the implications of the correction term in Eq. (5.30) proportional to  $B_2$ . These states are chosen on the line  $\varepsilon_1 = -0.0182$  and state  $n' = 2$  is identical

with state  $n = 2$  considered in Fig. 5.2 as example for  $B_2 = 0$ . Figure 5.3 exhibits the correlators together with their approximations. For  $B_2 > 0$ , the  $\phi(t)$  versus  $\log(t)$  diagram is convex for all times outside the transient, since a parabola with positive curvature is added to the leading linear variation described by Eq. (5.22). The formula with the leading correction describes the complete structural relaxation, except for the very last piece for the approach to the long-time limit  $f$ , as shown by curve  $n' = 1$ . This observation also holds for cases with  $B_2 < 0$  as is demonstrated for state  $n' = 3$ . However, for negative  $B_2$ , the  $\phi(t)$  versus  $\log(t)$  curve exhibits two inflection points because  $\phi(t)$  crosses the critical form factor  $f^\circ$  with negative curvature. Since the  $\phi(t)$  versus  $\log(t)$  curve is concave for  $\phi(t) \approx f^\circ$ , it has to have an inflection point for  $\phi(t) < f^\circ$  in order to approach the exponential, i.e. convex, long-time asymptote. It has to exhibit an inflection point also for  $\phi(t) > f^\circ$  in order to approach the convex critical correlator for short times. The described alternation of concave and convex parts is identical to the behavior discussed earlier for the MCT correlators for states near an  $A_2$ -singularity [3, 7]. But contrary to the characteristic decay pattern found for the MCT liquid-glass transition, curve  $n' = 3$  does not show a two step relaxation scenario, even though there is a huge stretching of the dynamics. For the decay from 0.80 to 0.05 a dynamical window of 5 orders of magnitude is required. Within this large window, the correlator follows closely the law  $\phi(t) \propto \ln(t/\tau_{\text{eff}})$ .

The qualitative features described above for state  $n' = 3$  are more pronounced for state  $n' = 4$ , since  $B_2$  is decreased to larger negative values. The relaxation curve 4 has the form expected for states near a liquid-glass transition. To corroborate this statement, further states  $n' = 5$  to 7 are considered on the line  $\epsilon_1 = -0.0182$  between the state 4 and the intersection  $\mathbf{V}^c$  of this line with the liquid-glass transition curve. The transition point  $\mathbf{V}^c$  is characterized by a critical glass-form factor  $f^c > f^\circ$ . The decay of the correlator from the value  $f^c$  to zero is the corresponding  $\alpha$ -process. Its initial part is described by the von Schweidler power law, as indicated in Fig. 5.3 for curve  $n' = 7$  by the dotted line. In this case, the von Schweidler law accounts for the decay from  $f^c$  to about 0.45, i.e. for about 15% of the  $\alpha$ -relaxation. The analytical description of the  $\alpha$ -process can be expanded by using the correction of von Schweidler law, Eq. (5.95), as shown by the dashed-dotted line. Asymptotically, the  $\alpha$ -process obeys the superposition principle:  $\phi(t) = \tilde{\phi}(t/\tau_\alpha)$ , where  $\tilde{\phi}$  is the control-parameter-independent shape function. The  $\phi(t)$  versus  $\log(t)$  curves for the  $\alpha$ -process can be superimposed by rescaling the time, i.e. by shifts parallel to the  $\log(t)$ -axis. It is easy to check that the curves  $n' = 4-7$  have the same shape for  $\phi(t) < f^c$ . Outside the transient for  $\phi(t) > f^c$ , the correlator follows the critical decay law for the fold bifurcation  $\phi(t) - f^c \propto 1/t^a$ , as is also demonstrated for curve 7. The results for states 4-7 exemplify the well understood scenario for the evolution of structural relaxation near a liquid-glass transition. The formula (5.30) provides an accurate description of 60% of the  $\alpha$ -process.

Comparison of the results for states  $n' = 1-3$  with the second-correction formula based on Eq. (5.31) does not alter seriously the fit quality for the long-time part of the curves  $n' = 4-6$  in Fig. 5.3. However, for  $\phi(t) \approx f^c$ , the extended formula yields slightly worse results than Eq. (5.30). This is so, since for  $\phi(t) \gtrsim f^c$ , the dynamics is governed by the  $A_2$ -singularity  $\mathbf{V}^c$  whose existence is ignored in the expansions near the higher-order singularity. The number  $f^c - f^\circ$  marks the limit where the expansion in the small parameter  $\phi(t) - f^\circ$  makes sense. The opposite conclusion

holds for the description of the  $\alpha$ -process for  $\phi(t) \approx f^\circ$ . The von Schweidler law results from an expansion for states  $\mathbf{V}$  near  $\mathbf{V}^c$  in terms of the small parameter  $f^c - \phi(t)$ . This number becomes too large if  $\phi(t) \approx f^\circ$ . It is the dynamics dominated by the higher-order glass-transition singularity  $\mathbf{V}^\circ$  that ruins the relevance of the expansion resulting in the von Schweidler law. The stretching of the  $\alpha$ -process connected with the transition of  $\mathbf{V}^c$  is larger than estimated by von Schweidler's law, because of the logarithmic-decay effects.

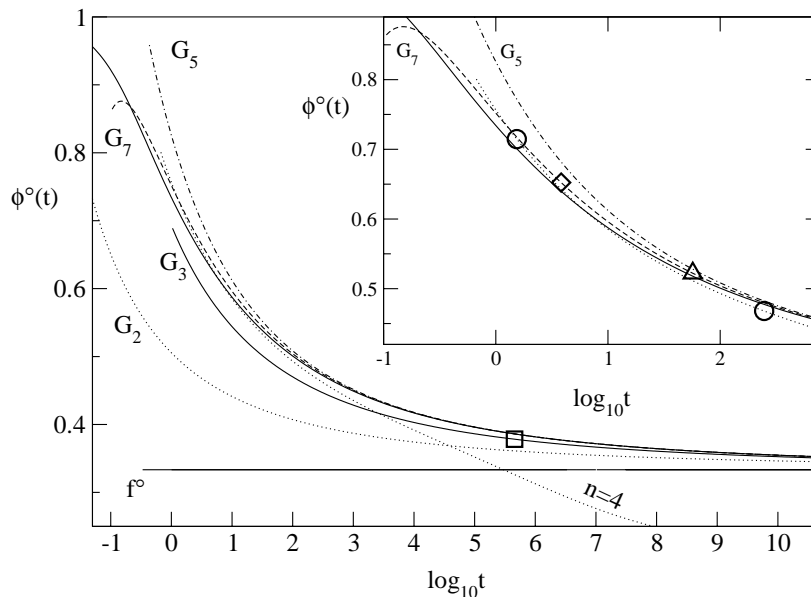


FIGURE 5.4. Critical decay at the  $A_3$ -singularity in the  $F_{13}$ -model. The full line shows the solution for  $\phi^\circ(t)$  of Eq. (5.108) at  $\mathbf{V} = \mathbf{V}^\circ$ . The lines labeled  $G_n$ , for  $n = 2, 3, 5, 7$ , show the approximations from Eq. (5.64) with the time scale  $t_0 = 1.6 \cdot 10^{-4}$ . The dotted line labeled  $n = 4$  is the next-to-leading-order correction, Eq. (5.31), to the decay for  $n = 4$  in Fig. 5.2. The point where  $G_3$  deviates by 2% from  $\phi^\circ(t)$  is marked by a square ( $\square$ ). The inset reproduces the upper part of the decay using the same line styles. The diamond ( $\diamond$ ), the triangle ( $\triangle$ ) and the circles ( $\circ$ ) mark the locations where  $G_7$ ,  $G_5$ , and  $n = 4$  deviate by 2% from  $\phi^\circ(t)$ , respectively.

**6.2. Critical decay.** We conclude the discussion of the one-component model with an analysis of the critical decay at the  $A_3$ -singularity in Fig. 5.4. The solution for the state  $\mathbf{V} = \mathbf{V}^\circ$  (full line) does no longer cross the plateau but approaches it asymptotically. For an  $A_2$ -singularity the critical decay is described by the power law  $(t/t_0)^{-a}$ , cf. Eq. (5.93), but for the  $A_3$ -singularity this has to be replaced by the inverse logarithms in Eq. (5.64). The approach to the critical plateau is significantly slower than for a typical  $A_2$ -singularity where the decay comes close to the plateau within a few decades when a deviation of 5% is used as a measure, cf. curve a in Fig. 5.3. This criterion is not met by the decay in Fig. 5.4 for the entire window in time shown. For  $t = 10^{11}$  the critical correlator  $\phi^\circ(t)$  is still 5.5% above

$f^\circ = 1/3$ . To apply the asymptotic approximation provided by Sec. 3.1 one has to evaluate the parameters appearing in Eq. (5.64) and find the time scale  $t_0$ . The first requirement is fulfilled straightforwardly by  $\mu_3 = 1/3$ ,  $\mu_4 = \mu_5 = \kappa = \kappa_4 = 1$  and summarized by the explicit formula for  $G_7(x)$  for the  $F_{13}$ -model in Eq. (A.11). In contrast, matching consistently the time scale  $t_0$  presents a challenge as this has to be done at large times. It has been recognized earlier that this is not possible when using only  $G_2(x)$  or  $G_3(x)$  [35, 41].

Using terms up to  $G_7(x)$  from the asymptotic expansion and extending the numerical solution to  $t = 10^{38}$ , it is possible to consistently fix  $t_0 = 1.6 \cdot 10^{-4}$ . After having matched  $t_0$ , the successive asymptotic approximations can be drawn into Fig. 5.4. The leading approximation from Eq. (5.54), labeled  $G_2$ , deviates from the critical correlator strongly indicating that more terms from the asymptotic series are necessary. Including the next-to-leading term  $g_3(x)$  from Eq. (5.59) yields the approximation labeled  $G_3$ . A square indicates where  $G_3$  deviates from the critical correlator by less than 2% for  $t \gtrsim 5 \cdot 10^5$ . If that criterion were relaxed to 5%,  $G_3$  would obey it for  $t \gtrsim 10^3$ . For  $t < 10^3$  the approximation  $G_3$  stays close to the critical correlator within 6%. Even if it is not possible to match the time scale  $t_0$  using the approximation up to the first correction, after correctly matching  $t_0$ , the approximation by  $G_3$  provides a first reasonable approximation to  $\phi^\circ(t)$ . Including further terms of the expansion improves the approximation as is seen for  $G_5$  and  $G_7$  in Fig. 5.4 by the curves labeled accordingly. The 2% deviations from  $\phi^\circ(t)$  are shown in the inset by a triangle for  $G_5$  and a diamond for  $G_7$ . We recognize that the inclusion of  $g_6(x)$  and  $g_7(x)$  into  $G_7$  of Eq. (5.64) still improves the range of applicability by one order of magnitude in time. One concludes that the asymptotic expansion presented in Sec. 3 describes the critical decay at an  $A_3$ -singularity up to the transient regime.

For approaching the  $A_3$ -singularity, but  $\mathbf{V} \neq \mathbf{V}^\circ$ , the correlators  $\phi(t)$  share an increasingly larger window in time with the critical correlator  $\phi^\circ(t)$  and the expansion of Sec. 2 can be applied. Fig. 5.4 shows the approximation including also Eq. (5.31) to the curve for  $n = 4$  from Fig. 5.2. We observe that the asymptotic description in terms of powers of the logarithm describes a large part of the critical decay. The inset of Fig. 5.4 shows the 2%-deviation of the approximation (dotted) from the critical correlators by two circles. By this criterion the approximation is acceptable for two orders of magnitude in time and covers a comparably large amplitude of 30% of the decay. Describing the critical correlator by the logarithmic decay laws of Sec. 2 is possible for an increasing interval in time as we approach the  $A_3$ -singularity. However, for  $\tau \rightarrow \infty$  the range of applicability shrinks with respect to the amplitude in  $\phi(t)$  that is covered.

It is obvious that matching a time scale  $t_0$  at  $t = 10^{40}$  and using six terms of the expansion in Eq. (5.64) is not useful for fitting data. However, the expansion in Eq. (5.64) leads to a reasonable approximation also for short times. We may depart from the procedure to match  $t_0$  at large times and try to fit the time scale instead for shorter times. Figure 5.5 shows the values obtained for  $t_0$  when matching the approximations at large times ( $\times$ ) as described above. That  $t_0$  is practically the same for  $n \geq 5$  justifies the use of the series (5.64) as an approximation. We will consider two procedures for fitting. The first shall define a scale  $t'_0$  by matching the critical correlator and the approximation at  $t = 10^6$ , namely  $G_i(10^6/t'_0) = \phi^\circ(10^6)$ . The second time scale  $t''_0$  is obtained from matching at 50% of the decay,

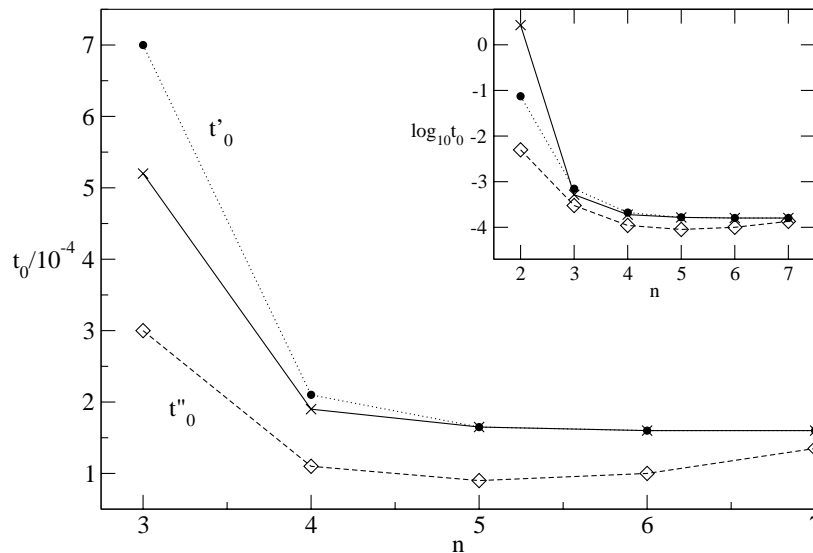


FIGURE 5.5. Time scale  $t_0$  for the approximation of the critical decay at the  $A_3$ -singularity in the  $F_{13}$ -model for including  $n$  orders of the asymptotic expansion (5.64). Time scales obtained by comparison at large time,  $35 \lesssim \log_{10} t \lesssim 38$  are shown by crosses ( $\times$ ). The time  $t'_0$  resulting from matching the solutions at  $t = 10^6$  is shown by filled circles ( $\bullet$ ). The diamonds ( $\diamond$ ) show the time scale  $t''_0$  resulting from matching at 50% of the decay where  $\phi(t) = 2/3$ . The inset shows  $t_0$  on logarithmic scale to include the larger deviations for  $n = 2$ .

$G_i(2.5/t''_0) = 2/3$ . We infer from the inset of Fig. 5.5 that all methods to fix  $t_0$  based on the term  $G_2(x)$  alone are off by orders of magnitude. The approximation up to  $G_3(x)$  yields the correct order of magnitude for  $t_0$  in all three approaches. Starting with  $n = 5$ , the scales  $t_0$  and  $t'_0$  can no longer be distinguished, therefore matching the approximation at  $10^6$  is comparable to a true asymptotic approximation. We see that fixing at  $10^6$  is superior to using  $t''_0$  which implies matching at too short times.

## 7. Dynamics in a two-component model

To mimic the  $q$ -dependence, which is crucial for the asymptotic expansions above, we use a two-component model that was introduced for the description of a symmetric molten salt [91]. The model has three control parameters we combine to the vector  $\mathbf{V} = (v_1, v_2, v_3)$ . We will again use Brownian dynamics, so the equations of motion for the correlators  $\phi_q(t)$ ,  $q = 1, 2$ , read

$$(5.111a) \quad \tau_q \partial_t \phi_q(t) + \phi_q(t) + \int_0^t m_q(t-t') \partial_{t'} \phi_q(t') dt' = 0,$$

$$(5.111b) \quad m_1(t) = v_1 \phi_1^2(t) + v_2 \phi_2^2(t),$$

$$(5.111c) \quad m_2(t) = v_3 \phi_1(t) \phi_2(t).$$



The glass-transition diagram for the above model has been calculated before [3, 34]. This can be done analytically what will allow also for an accurate determination of the higher-order singularities. We restrict ourselves to  $v_3 > 4$ . Equation (2.8) for the second form factor implies  $f_2 = [v_3 f_1 - 1]/(v_3 f_1)$ , and this result can be used to eliminate  $f_2$  in the following expressions. Equation (2.8) for the first form factor,  $f_1/(1 - f_1) = v_1 f_1^2 + v_2 f_2^2$ , is a linear equation for  $(v_1, v_2)$  with coefficients that are nonlinear in  $f_1$  and  $v_3$ . The same holds for  $E^c = 1$ , Eq. (5.11), for a singularity which is equivalent to  $f_1^c/(1 - f_1^c)^2 = 2v_1^c f_1^{c2} + 2v_2^{c2} f_2^c(1 - f_2^c)$ . These equations can be used to express  $v_1^c$  and  $v_2^c$  in terms of  $v_3^c$  and  $f_1^c$ . To ease the notation, variables  $x$  and  $y$  shall be introduced as

$$(5.112a) \quad v_3^c = x, \quad f_1^c = y.$$

One gets a parameterized representation of the transition surface,

$$(5.112b) \quad v_1^c = \frac{3 - (2 + x)y}{2(1 - y)^2 y(2 - xy)},$$

$$(5.112c) \quad v_2^c = \frac{x^2 y(y^2 - 2y^3)}{2(1 - y)^2(x^2 y^2 - 3xy + 2)}.$$

The variables  $x$  and  $y$  with  $x > 4$  and  $1/2 \leq y \leq 3/(2 + x)$  serve as surface parameters. The exponent parameter  $\lambda = 1 - \mu_2$  is determined by

$$(5.112d) \quad \mu_2 = \frac{(3x^2 + 6x)y^3 - (x^2 + 18x + 8)y^2 + (6x + 18)y - 6}{(2x^2 + 4x)y^3 - 12xy^2 + (2x + 4)y}.$$

The maximum theorem, Eq. (2.9), has to be used to identify among the points  $(v_1^c, v_2^c, v_3^c)$  those that are glass-transition singularities.

**7.1.  $A_3$ -singularity.** A typical cut through the three dimensional glass-transition diagram containing higher-order singularities will contain either a smooth line of  $A_2$ -singularities or a crossing of lines with an associated  $A_3$ -singularity. Hitting the  $A_4$ -singularity on the liquid-glass-transition line requires fine tuning of the third parameter and will be considered in Sec. 7.2. Figure 5.6 shows a cut through the glass transition diagram for the model defined in Eq. (5.111) for  $v_3^c = 45$  which exhibits a generic  $A_3$ -singularity. Since all steps can be carried out analytically it is particularly transparent to follow the evolution of the higher-order singularities in the two-component model of Eq. (5.111). For the existence of a cusp singularity,  $x$  needs to be sufficiently large which is fulfilled for  $v_3^c = 45$ . In this case, the cubic numerator polynomial in Eq. (5.112d) has two zeros  $y_1(x) < y_2(x)$  above some  $y_0$ ; they can be evaluated straightforwardly [87]. The transition line consists of several pieces. The first one, obtained for  $y_2(x) < y \leq 1/2$ , is shown in Fig. 5.6 as heavy full line. It starts at  $v_1^c = 4$ ,  $v_2^c = 0$  and ends at the  $A_3$ -singularity marked by a circle. The second piece describes bifurcations with  $\mu_2 < 0$  for  $y_1(x) < y < y_2(x)$ . It connects the mentioned  $A_3$ -singularity with a second  $A_3$ -singularity of Eq. (2.8) that is shown as a shaded circle. This piece of the line is shown dotted. Decreasing  $y$  further, one gets a curve with  $\mu_2 > 0$  that joins the second  $A_3$ -singularity with the point  $v_1^c = 0$ ,  $v_2^c = 3/(2 + x)$ . This line exhibits a crossing point with the first line piece mentioned above, that is shown as a square. The part between the second  $A_3$ -singularity and the crossing point is shown dotted, and the final piece is shown as light full line. The dotted bifurcation lines and the second  $A_3$ -singularity are excluded from the set of glass-transition singularities because of the maximum

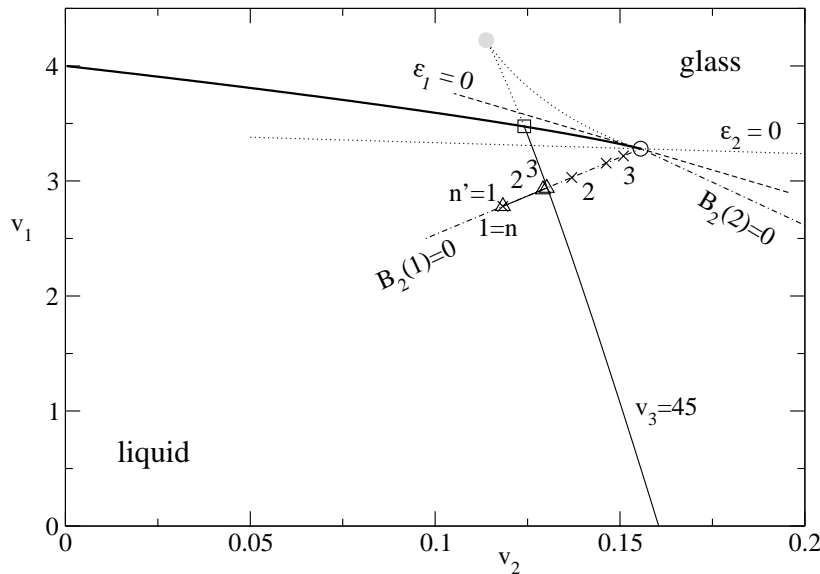


FIGURE 5.6. Glass-transition diagram for the two-component model for  $v_3 = 45$ . The light full line represents the glass-transition singularities with the lower glass-form factors, the heavy full line the singularities with the higher glass-form factors. The latter line crosses the former one ( $\square$ ) and extends as line of glass-glass transitions until it terminates in an  $A_3$ -singularity ( $\circ$ ). The dotted lines that join in the cusp singularity marked by a shaded circle complete the bifurcation diagram but they have no relevance for the discussion of the MCT solutions. The straight dashed and dotted lines show where the separation parameters  $\varepsilon_1$  and  $\varepsilon_2$  vanish. The chain lines are the cuts  $v_3 = 45$  through the surfaces of vanishing correction term  $B_2(q) = B_2 + K_q B^2$  in Eq. (5.42),  $q = 1, 2$ . The crosses labeled  $n = 1, 2, \dots$  and triangles labeled  $n' = 1, 2, 3$  mark states whose dynamics is discussed in Figs. 5.7, and 5.8, respectively.

theorem. These items have been added to the figure in order to illustrate the familiar swallowtail scenario [5]. The line between the crossing point and  $v_1 = 0$  is also representing generic liquid-glass transitions with a finite critical glass-form factor,  $f_q^c > 0$ .

7.1.1. *Logarithmic decay.* Figure 5.7 demonstrates the validity of the factorization theorem for states close enough to a cusp singularity  $\mathbf{V}^\circ$  and its violation for states sufficiently away from it. For the  $A_3$ -singularity with  $v_3^c = 45$ , the correction amplitudes calculated from Eq. (5.44) are quite different for the two correlators:  $K_1 = 0.06857$ ,  $K_2 = -2.049$ . Therefore, the lines for vanishing dominant correction, i.e. the cut of the surfaces  $B_2(q) = B_2 + K_q B^2 = 0$ ,  $q = 1, 2$ , with the plane  $v_3 = 45$  are quite different as well, as shown by the chain lines in Fig. 5.6. The four states discussed in Fig. 5.7 are chosen on the surface  $B_2(1) = 0$ . Thus, the

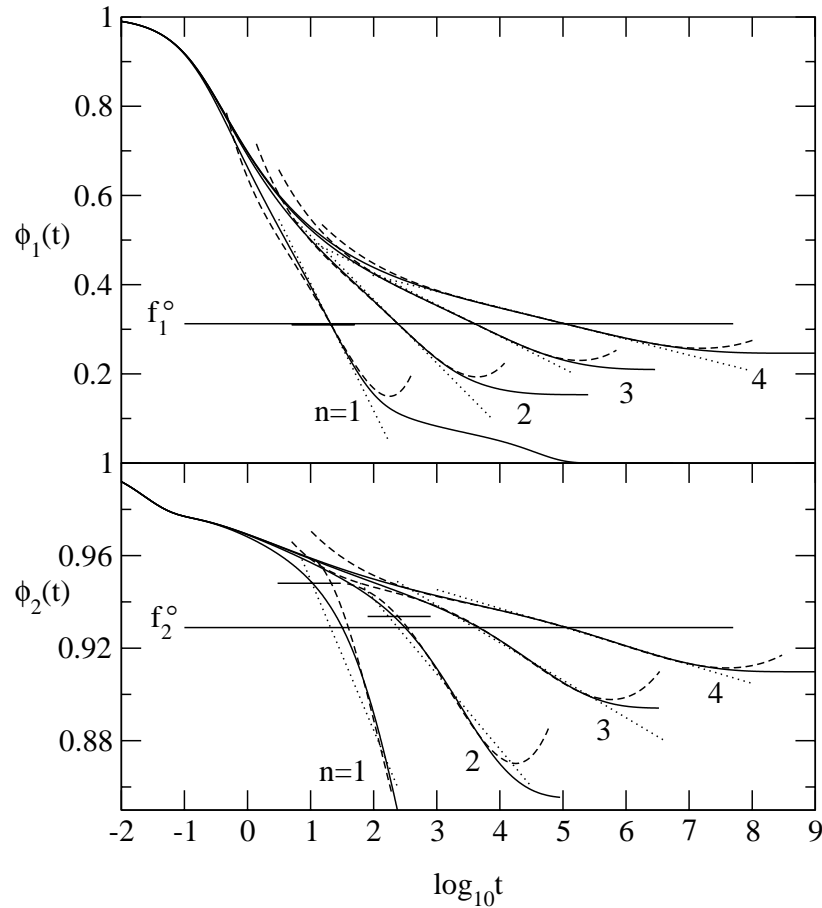


FIGURE 5.7. Correlators  $\phi_{1,2}(t)$  for the two-component model defined in Eq. (5.111). The states labeled  $n = 1, \dots, 4$  are located on the cut  $v_3 = 45$  through the surface of vanishing dominant correction for the first correlator,  $B_2(1) = B_2 + K_1 B^2 = 0$ . The coupling constants are  $v_1^\circ - v_1 = 2/4^n$ ,  $v_2^\circ - v_2 = 0.14907/4^n$  and the states for  $n = 1, 2$ , and  $3$  are shown in Fig. 5.6 by crosses. The full lines are the solution of Eqs. (5.111a-c). The dotted straight lines show the leading approximation, Eq. (5.37) and the dashed ones the leading correction, Eq. (5.42). The long horizontal lines show the critical glass-form factors  $f_1^\circ = 0.312507$ ,  $f_2^\circ = 0.92889$  and the short horizontal lines shown for the states  $n = 1, 2$ , denote the renormalized form factors  $f_{1,2}^\circ + \hat{f}_{1,2}$  according to Eq. (5.43). Here and in the following figures, the model is used with  $\tau_1 = \tau_2 = 1$ .

scenario for the evolution of the  $\ln(t/\tau)$  law shown for  $\phi_1(t)$  is in qualitative agreement with the one discussed for the  $F_{13}$ -model in Fig. 5.2. The states with labels  $n = 3$  and  $4$  are so close to the singularity, that the correction term in Eq. (5.42) proportional to  $B_2(2) = \mathcal{O}(\epsilon)$  is not important. As a result, the rescaled functions  $(\phi_q(t) - f_q^c)/h_q$ ,  $q = 1$  and  $2$  agree for the states  $n = 3$  and  $4$ , and the same holds for

the corresponding approximations. However, for the states with labels  $n = 1$  and  $2$ , the negative coefficient  $B_2(2)$  is so large that the  $\phi_2(t)$  versus  $\log(t)$  curve does not exhibit the straight line obtained for  $\phi_1(t)$  versus  $\log(t)$ . Rather, the correlator  $\phi_2(t)$  exhibits changes of the curvature and inflection points as explained above in Fig. 5.3 for state  $n' = 3$ .

Figure 5.7 also exemplifies a problem concerning the choice of the time scale  $\tau$ . The complete solution of the equations of motion is unique up to the choice of a control-parameter independent time scale. The nonlinear coupling of the correlators of different index  $q$  requires scale universality. However, if a time scale like  $\tau$  is deduced from some approximation to the equation of motion, the error of the approximation will result in violations of the scale universality for the approximate solutions. Constructing the approximate solutions in Fig. 5.7 — and also in the upper panel of Fig. 5.8 — the time  $\tau$  was fixed for the leading approximation from  $\phi_1(\tau) = f_1^\circ$  and for the leading correction from  $\phi_1(\tau) = f_1^\circ + \hat{f}_1$ . The errors explained lead to offsets for the second correlator:  $\phi_2(\tau) \neq f_2^\circ$  and  $\phi_2(\tau) \neq f_2^\circ + \hat{f}_2$ , respectively, for the two approximations studied. This explains, e.g., that the dashed line for  $\phi_2(t)$  for the state  $n = 1$  does not coincide with the full one. One could also choose  $\tau$  differently, e.g. by requesting  $\phi_2(\tau) = f_2^\circ + \hat{f}_2$  as done in the lower panel of Fig. 5.8. For the discussion of the  $A_4$ -singularity in Sec. 7.2 the time scales are fixed independently for both correlators and the deviation is taken as measure for the violation of the scale universality.

The transition line which is shown in Fig. 5.6 by the light full and almost vertical curve intersects the line  $B_2(1) = 0$  at some liquid-glass-transition singularity  $\mathbf{V}^c = (2.94\dots, 0.130\dots, 45.0)$ . For states on the line  $B_2(1) = 0$  that are close enough to this singularity, one gets the standard liquid-glass transition scenario, e.g., the evolution of a plateau of the  $\phi_q(t)$  versus  $\log(t)$  diagram at the critical glass-form factor  $f_q^c$  and an  $\alpha$ -process for the decay below this plateau. The universal bifurcation results for an  $A_4$ -singularity require that the plateau values are below the critical form factors of the nearby  $A_3$ -singularity:  $f_q^c < f_q^\circ$ . For the example under discussion, one gets  $f_1^c = 0.0747$ ,  $f_2^c = 0.7027$  and  $f_1^\circ = 0.3125$ ,  $f_2^\circ = 0.9289$ . The liquid-glass transition point is connected with an exponent parameter  $\lambda = 0.603$ , leading to the exponents  $a = 0.363$  and  $b = 0.807$ . The precursor of the liquid-glass transition at  $\mathbf{V}^c$  explains the stretched tail exhibited in Fig. 5.7 for the decay of  $\phi_1(t)$  below  $0.1$  for the state  $n = 1$ . To corroborate the discussion of the preceding paragraph, the correlators with label  $n = 1$  are reproduced as curves with label  $n' = 1$  in Fig. 5.8. Two further curves with labels  $n' = 2$  and  $3$  are added. They refer to states between state 1 and the transition point  $V^c$  as noted in Fig. 5.6 by triangles. The curves for  $\phi_1(t)$  for states 2 and 3 exhibit the two-step-relaxation scenario characteristic for an  $A_2$ -bifurcation. The decay for  $\phi_q(t) < f_q^c$  demonstrates the superposition principle for the  $\alpha$ -process, and its initial part can be described by von Schweidler's power law with a time scale fitted for curve  $n' = 3$ . The decay towards the plateaus  $f_q^c$  for  $t > 1000$  follows the critical law for the  $A_2$ -singularity  $\mathbf{V}^c$ , Eq. (5.93). The universal laws for the dynamics near a fold bifurcation imply that the correlators follow the asymptote of the critical law,  $(\phi_q(t) - f_q^c)/h_q = (t/t_0)^{-a}$ , for short times down to about one decade above the end of the transient dynamics, i.e. until about  $t = 10$ . In particular, for small times, the correlator for state  $n' = 2$  should approach the one for state  $n' = 3$ . However, these features are not exhibited in Fig. 5.8. Rather, the  $t^{-a}$  law becomes irrelevant for the description of the

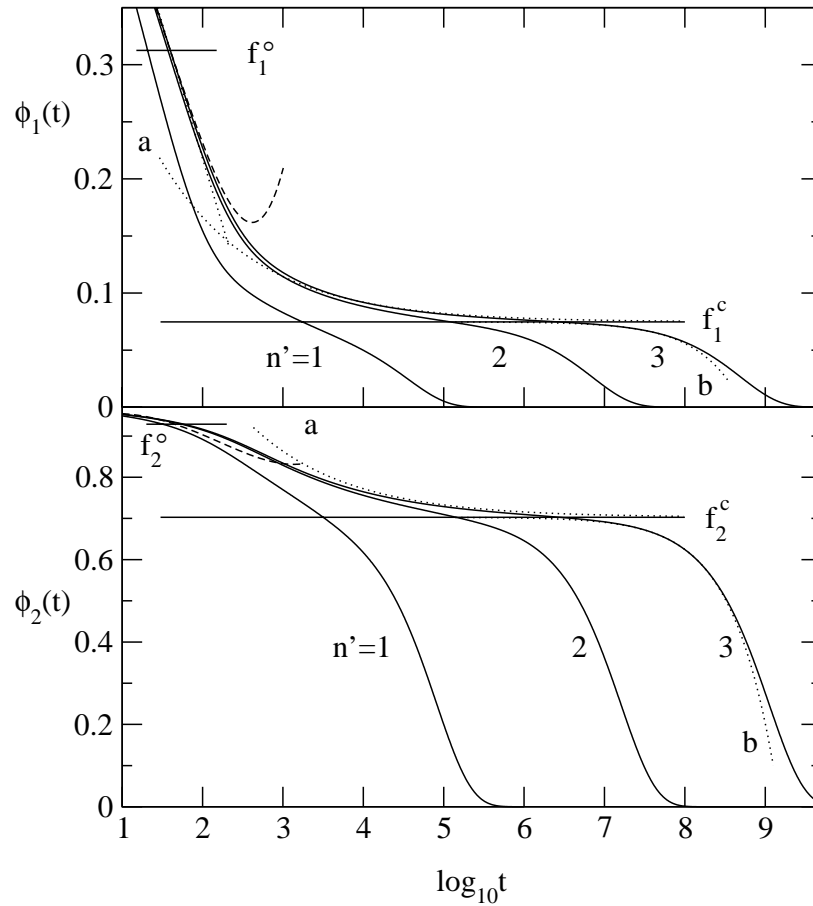


FIGURE 5.8. Correlators for the two-component model defined in Eq. (5.111). The states with labels  $n' = 1, 2,$  and  $3$  are located on the line defined by  $v_3 = 45, B_2(1) = 0$  and have coordinates  $(v_1, v_2) = (2.7799, 0.1183), (2.9254, 0.1292),$  and  $(2.9391, 0.1302),$  respectively. They are indicated in Fig. 5.6 by triangles and approach the liquid-glass transition point  $\mathbf{V}^c$  with coordinates  $v_1^c = 2.941029, v_2^c = 0.130326.$  The horizontal lines show the critical glass-form factors  $f_q^\circ$  and  $f_q^c, q = 1, 2,$  for the cusp singularity  $\mathbf{V}^\circ$  and the fold singularity  $\mathbf{V}^c,$  respectively. The critical decay laws  $(\phi_q(t) - f_q^c) = h_q^c(t_0/t)^a$  are shown as dotted lines labeled a. The von Schweidler laws  $(\phi_q(t) - f_q^c)/h_q^c \propto -t^b$  are shown as dotted lines with label b (see text). The straight dotted line in the upper panel exhibits the leading asymptotic law, Eq. (5.37), for  $\phi_1(t)$  and state  $n' = 3;$  the dashed line shows the result of Eq. (5.42). The dashed lines in the lower panel exhibit the leading-correction formulas, Eq. (5.42), for  $\phi_2(t)$  and states  $n' = 1$  and  $3,$  respectively.

dynamics below times around  $10^3,$  where the  $A_2$  critical curve crosses the curves describing the logarithmic laws for the  $A_3$ -singularity. As a result, there appears a

window between the end of the transient and the beginning of the description by the  $A_2$ -singularity results where the correlators are described by Eq. (5.42). This window deals with an increase in time over about two orders of magnitude. In this window, the logarithmic decay processes destroy the manifestation of the  $t^{-a}$  law.

The lower panel of Fig. 5.8 demonstrates a further implication of  $\mathbf{V}^\circ$ -dynamics on the precursors of the liquid-glass transition dynamics. Even though the time scale for the  $\alpha$ -process for states  $n' = 1$  or  $2$  exceeds the one for the transient by factors  $10^4$  and  $10^6$ , respectively, the correlator  $\phi_2(t)$  does not exhibit the two-step scenario for these states. Rather, there is a large time interval where the approach towards the plateau  $f_2^c$  follows closely the law  $(\phi_2(t) - f_2^c) \propto \ln(t/\tau_{\text{eff}})$ . This is due to a crossover from the asymptotes for the  $\mathbf{V}^\circ$  dynamics and the  $\mathbf{V}^c$  dynamics. The resulting nearly linear-log( $t$ ) variation must not be mistaken as the asymptotic logarithmic law given by Eq. (5.37).

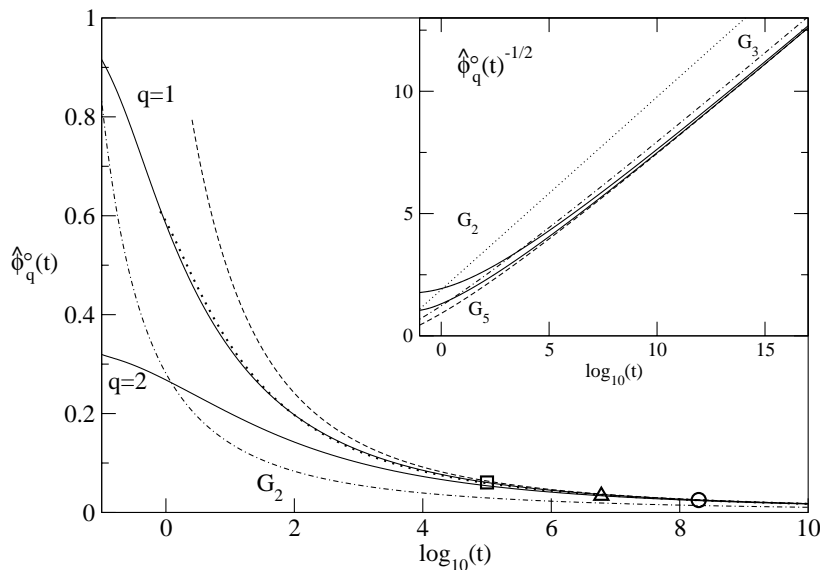


FIGURE 5.9. Critical decay at the  $A_3$ -singularity in the two-component model, Eq. (5.111). The rescaled solutions  $(\hat{\phi}_q^\circ(t) - f_q^\circ)/h_q$ ,  $q = 1, 2$ , are shown for as full lines. The asymptotic approximation (5.76) is shown dashed for  $q = 1$  and dotted for  $q = 2$ . The points where the approximation deviates by 5% from the solution for  $q = 1, 2$ , and the point where the solutions differ by 5% from each other are marked by a square, a triangle and a circle, respectively. The inset shows as full lines the rectification,  $\hat{\phi}_q^\circ(t)^{-1/2}$  for  $q = 1$  (lower full line) and  $q = 2$  (upper full line). The  $q$ -independent part  $G_5$  of the approximation in Eq. (5.76) is given by the dashed line. The dotted and the chain line show the leading and next-to-leading order approximations  $G_2$  and  $G_3$ , Eq. (5.64). The time scale  $t_0 = 4.07 \cdot 10^{-3}$  was matched in the interval  $t = 10^{20} \dots 10^{25}$ .

7.1.2. *Critical decay.* As for the one-component case, the logarithmic decay laws are no longer applicable at the critical point and we turn to the expansion for the critical decay, Eq. (5.76). In comparison to the  $F_{13}$ -model demonstrated in Fig. 5.4 we now have two correlators, so we will use the rescaled correlators  $\hat{\phi}_q^\circ(t) = (\phi_q^\circ(t) - f_q^\circ)/h_q$  for the following considerations. The factorization theorem can be stated after the rescaling as  $\hat{\phi}_q^\circ(t) = G_5(x) + K_q \tilde{G}_5(x)$  with  $G_5(x)$  from Eq. (5.64) and  $\tilde{G}_5(x) = g_2^2(x) + 2g_2(x)g_3(x)$  with  $x = \ln(t/t_0)$ . Since  $\tilde{G}_5(x)$  is of higher order than  $G_5(x)$  whose lowest-order contribution is  $g_2(x)$ , Eq. (5.54), correlators for different  $q$  approach each other for sufficiently large time. This is demonstrated in Fig. 5.9 for the two correlators of model (5.111). The time  $t \approx 2 \cdot 10^8$  where  $\hat{\phi}_2^\circ$  deviates by 5% from  $\hat{\phi}_1^\circ$  is marked by a circle. The amplitude  $K_q$  introduces the  $q$ -dependent corrections which are again small for  $q = 1$  and large for  $q = 2$ . To evaluate  $G_5(x)$  and  $\tilde{G}_5(x)$  we need to specify the following parameters,  $\mu_3 = 0.772$ ,  $\kappa = 0.888$ , and  $\mu_4 = 1.38$ . The larger value for  $\mu_3$  indicates that the present  $A_3$ -singularity is further away from an  $A_4$ -singularity where  $\mu_3 = 0$  than the  $A_3$ -singularity in the  $F_{13}$ -model where  $\mu_3 = 1/3$ . Since the coefficients  $c_{m,l}$  in Eq. (5.61) contain powers of  $\mu_3$  in the denominator, corrections are larger if  $\mu_3$  is smaller, cf. Eqs. (5.62) and (5.63). Because of the smaller corrections the time scale can be matched using terms up to  $G_5(x)$  between  $t = 10^{20}$  and  $10^{25}$  which is significantly earlier than for the  $F_{13}$ -model in Fig. 5.4. We get  $t_0 = 4.07 \cdot 10^{-3}$ .

The asymptotic approximation (5.76) is shown as a dashed line for  $q = 1$  in Fig. 5.9, it deviates by more than 5% from the solution if  $t \lesssim 10^5$  ( $\square$ ). The approximation for  $q = 2$  (dotted) deviates by more than 5% for  $t \lesssim 6 \cdot 10^6$  ( $\triangle$ ). This difference in the range of validity can be understood qualitatively by considering the  $q$ -dependent corrections of higher order in Eq. (5.72),  $K_q[g_3^2(x) + 2g_2(x)g_4(x)] + Y_q g_2^3(x)/a_q$  with  $Y_q$  from Eq. (5.71). Both  $K_q$  and  $Y_q/a_q$  are smaller for the first correlator,  $Y_1/a_1 = -0.1928$  and  $Y_2/a_2 = 5.761$ , and introduce less deviations from the  $q$ -independent part  $G_6(x)$  of the approximation in higher order.

The  $q$ -independent function  $G_5(x)$  would lie on top of the dashed line in Fig. 5.9 and is therefore shown only in the inset which also displays the critical correlators and the  $q$ -independent functions  $G_2(x)$  and  $G_3(x)$ , Eq. (5.64). Plotting  $\hat{\phi}_q^\circ(t)^{-1/2}$  we can identify  $1/\ln^2 t$ -behavior as straight line. The critical correlators exhibit a straight line starting from  $t \approx 10^9$ . The leading approximation  $G_2(x)$  is a straight line by definition but has a slope slightly larger than the solution. The first correction  $G_3(x)$  resembles the slope of the solution but is offset from the solution by a shift of the time scale. This was observed before in Fig. 5.4. Since  $G_5(x) + \tilde{G}_5(x)$  was used to match the time scale  $t_0$  and as  $\tilde{G}_5(x)$  decays faster than the  $q$ -independent part,  $G_5(x)$  coincides with the solution for larger times.

**7.2. Two component model at the  $A_4$ -singularity.** Decreasing the parameter  $x$  in Eq. (5.112) from large values to smaller ones, the two cusp values  $y_1(x)$  and  $y_2(x)$  determining the two  $A_3$ -singularities in Fig. 5.6 approach each other. The corresponding parameter vectors  $V^c = (v_1^c(x), v_2^c(x), v_3^c(x))$  form curves that approach each other with decreasing  $x$  and join at a certain value  $x^*$ :  $y_1(x^*) = y_2(x^*) = y^*$ . The pair  $(x^*, y^*)$  defines the  $A_4$ -singularity for the model. The parameters for this singularity are obtained when the derivative of the numerator polynomial in Eq. (5.112d) is zero for  $\mu_2 = 0$ . This leads to  $(x^* - 2)(x^* - 4)(x^{*4} - 30x^{*3} + 136x^{*2} - 168x^* + 88) = 0$ . The elementary solution

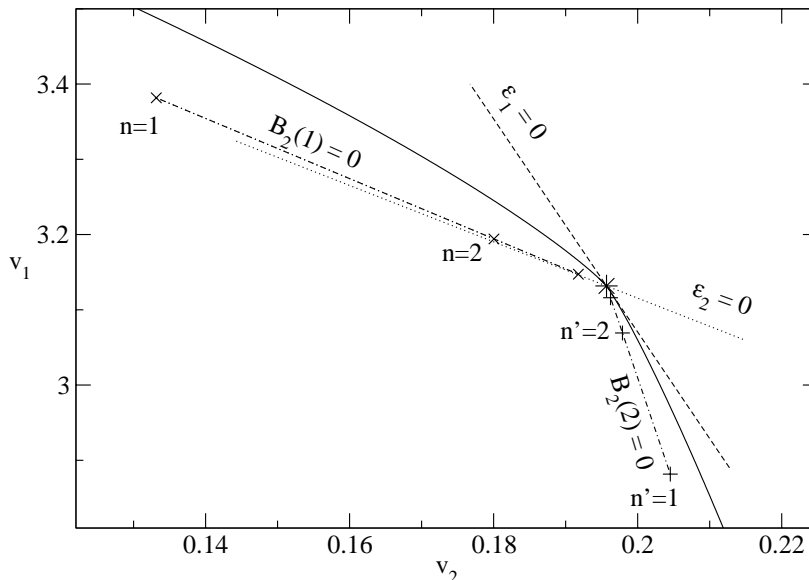


FIGURE 5.10. Glass-transition diagram for the two-component model defined in Eq. (5.108) for the cut  $v_3 = v_3^*$ . The full line shows the liquid-glass-transition singularities, the  $A_4$ -singularity is marked by a star (\*). The chain lines labeled  $B_2(i) = 0$ ,  $i = 1, 2$ , represent control-parameter values of vanishing quadratic correction for the correlator  $\phi_i(t)$ . The paths labeled  $n$  ( $\times$ ) and  $n'$  ( $+$ ) are discussed in Figs. 5.11 and 5.12, respectively. The dashed line marks the boundary where  $\varepsilon_1(\mathbf{V}) = 0$ , and the dotted line the location for  $\varepsilon_2(\mathbf{V}) = 0$ .

for the zeros of the quartic polynomial [87] determines the coordinates of the swallowtail singularity  $x^* = 24.779392\dots$ ,  $y^* = 0.24266325\dots$ . The cut through the transition surface for  $v_3 = x^*$  is shown in Fig. 5.10 as pair of light full lines joining at the  $A_4$ -singularity which is indicated by a star,  $(v_1^*, v_2^*, v_3^*) = (3.132, 0.1957, 24.78)$ . Attached to the  $A_4$ -singularity we find the lines of vanishing separation parameters,  $\varepsilon_1(\mathbf{V}) = 0$  (dashed) and  $\varepsilon_2(\mathbf{V}) = 0$  (dotted), which represent the local coordinate system. These lines are obtained by smooth transformation from the ones in Fig. 5.6.

7.2.1. *Logarithmic decay.* The correction amplitudes are also not changing drastically in comparison to the  $A_3$ -singularity above; at the  $A_4$ -singularity,  $K_1 = 0.3244$  and  $K_2 = -2.109$ . Therefore also the lines where the quadratic corrections vanish are smooth transformations of the ones before; these are shown by the chain lines in Fig. 5.10. We notice that different from the situation in Fig. 5.6, the path obeying the condition  $B_2(2) = 0$  is now also located within the liquid regime for  $v_3 = v_3^*$ .

We first analyze the path labeled  $n$  in Fig. 5.10 which is the analog of the one carrying the same labels in Fig. 5.6. The solutions corresponding to the ones discussed in Fig. 5.7 are shown in Fig. 5.11. As before the logarithmic decay in the first correlator is accompanied by a decay in the second correlator that is concave in



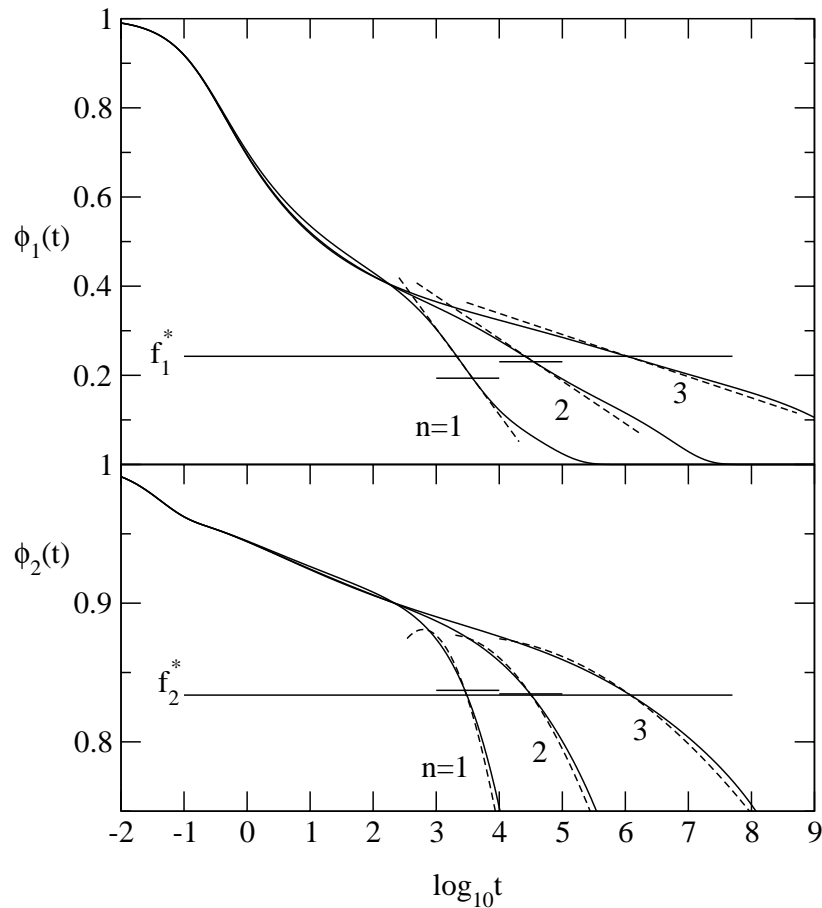


FIGURE 5.11. Logarithmic decay at the  $A_4$ -singularity on the path  $(\times)$  with  $n = 1, 2, 3$  in Fig. 5.10 with  $v_1 - v_1^* = 1/2^{n+1}$ ,  $v_2 - v_2 = 0.25009/2^{n+1}$ . The solutions of Eq. (5.111) are shown as full lines, the approximation (5.42) as dashed lines. Long horizontal lines exhibit the critical plateau values  $f_q^*$ , short lines the corrected plateau values  $f_q^* + \hat{f}_q$ .

the logarithm of time. The approximations (5.42) for the correlators are displayed as dashed lines. The time scale  $\tau$  was matched for  $\phi_1(t)$  and  $\phi_2(t)$  independently at the corrected plateau values. The approximation describes the decay around the plateaus  $f_q^*$  again reasonably for both correlators. But whereas in Fig. 5.7 the asymptotic laws extended up to the end of the transient  $t \approx 1$ , in Fig. 5.11 there appears now a window in time between  $t \approx 1$  and  $t \approx 10^3$  where the description by Eq. (5.42) is not applicable. In addition, for the same distance from the singularity  $\hat{v}_1 = 1/8$ , the correlators cross the plateau two decades later in Fig. 5.11 than in Fig. 5.7 for the states labeled  $n = 2$ . This is caused by the close-by  $A_2$ -singularities with  $f_q^c > f_q^*$ ,  $q = 1, 2$  which introduce an additional slowing down before the logarithmic decay is encountered. This is reminiscent of the situation in Fig. 5.3 where a decay around the plateau of an  $A_2$ -singularity shifts the logarithmic decay

to later times. We observe that  $\phi_2(t)$  varies almost linearly in  $\ln t$  in for  $t = 1 \dots 250$  but it is easy to distinguish that effective logarithmic variation that stays the same upon further approaching the singularity from the characteristic behavior around the plateau.

Comparing the solutions with the approximations (5.42) in Fig. 5.11 is less satisfactory than in Fig. 5.7. The next-to-leading-order approximation shown by the dashed lines overestimates the absolute value of the slope at  $f_q^*$  for both  $q$ . One can attribute that to the neglect of higher-order contributions to the asymptotic expansion which renormalize the prefactor for the logarithmic decay to  $(B - B_1 - C_1)$ , cf. Eq. (5.31).  $C_1$  in Eq. (A.8a) depends in a quite involved way on the different separation parameters but mainly on  $\varepsilon_1(\mathbf{V})$  and  $\varepsilon_2(\mathbf{V})$ . The path taken in Fig. 5.11 is closer to  $\varepsilon_2 = 0$  than to  $\varepsilon_1 = 0$  as can be seen in Fig. 5.10. The largest contribution to  $C_1$  is given by the difference  $0.308\varepsilon_2(\mathbf{V}) - 0.217\varepsilon_1(\mathbf{V})$  which is positive on the present path and explains the deviations seen in Fig. 5.11. The

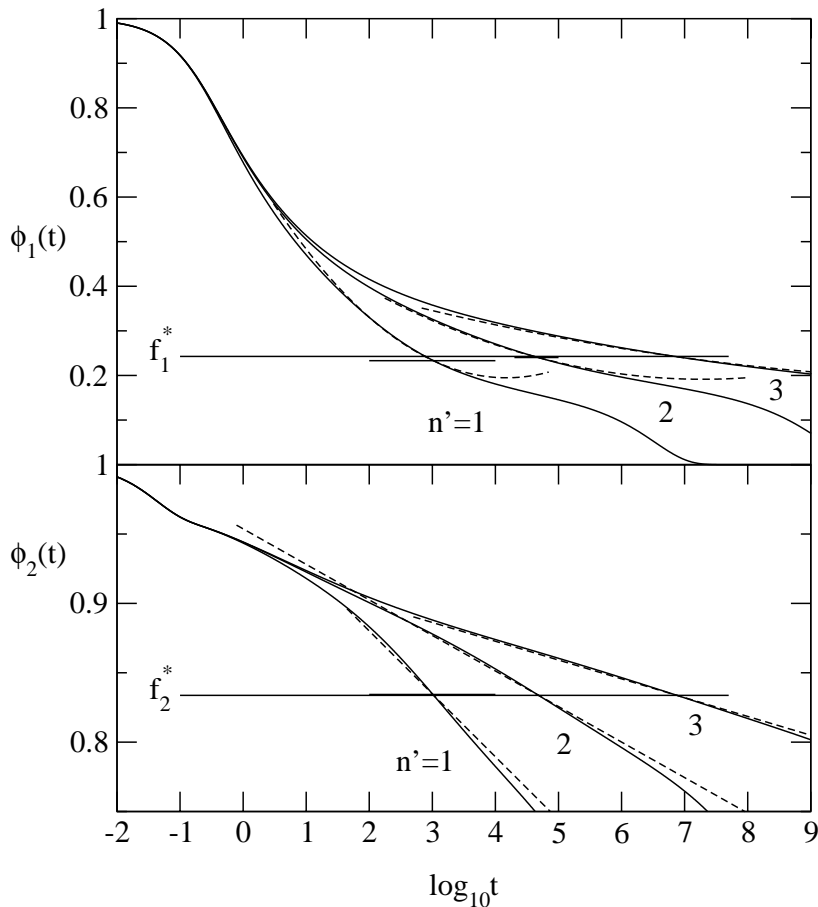


FIGURE 5.12. Logarithmic decay on the path (+) for  $n' = 1, 2, 3$  in Fig. 5.10.  $v_1^* - v_1 = 1/4^n$ ,  $v_2 - v_2^* = 0.3541/4^n$ . Line styles and notation are the same as in Fig. 5.11.

estimate for the sign of  $C_1$  can be verified in Fig. 5.12 where the situation is reversed

as the path labeled  $n'$  in Fig. 5.10 is now closer to the line  $\varepsilon_1 = 0$  than to  $\varepsilon_2 = 0$ . Indeed, the comparison of solutions and approximations (5.42) now indicates a negative value for  $C_1$  to account for a steeper slope ( $B - B_1 - C_1$ ).

In Fig. 5.12 the quadratic corrections in Eq. (5.42) for the correlator  $\phi_2(t)$  are zero up to higher orders. The quadratic corrections to the first correlator are positive,  $B_2(1) > 0$ , and  $\phi_1(t)$  is convex in  $\ln t$  around  $f_1^*$ . There are close-by  $A_2$ -singularities with  $f_q^c < f_q^*$ ,  $q = 1, 2$  causing a decay which is encountered after the logarithmic decay. The decay of  $\phi_1(t)$  from 0.1 to zero at the state  $n = 1$  in Fig. 5.7 is in that respect similar as the decay in  $\phi_1(t)$  for  $n' = 1$  in Fig. 5.12. In both cases the validity of the logarithmic laws is limited below  $f_q^\circ$  or  $f_q^*$ , respectively, by an interfering  $A_2$ -singularity. Above the plateaus  $f_q^*$ , the asymptotic approximation extends up to shorter times and the range of validity is only limited by the shrinking amplitude in  $\phi_q$  as explained in connection with Fig. 5.2.

The comparison of Figs. 5.11 and 5.12 is summarized as follows. For each value for  $q$  there exists a line with vanishing quadratic correction for the specified  $q$  in the approximation of Eq. (5.42). On this line the logarithmic decay is displayed best for the correlator specified by  $q$ . Moving to control parameter values above this line,  $B_2(q) < 0$ , introduces concave decay of the correlator in  $\ln t$ . Going below the line,  $B_2(q) > 0$ , yields a convex decay in the correlator. For increasing the value of  $K_q$  the curve specified by  $B_2(q) = 0$  and  $\varepsilon_1(\mathbf{V}) < 0$  rotates clockwise around the  $A_4$ -singularity.

**7.2.2. Critical decay.** Figure 5.13 shows the critical decay at the  $A_4$ -singularity. We use again the rescaled correlator  $\hat{\phi}_q^*(t) = (\phi_q^*(t) - f_q^*)/h_q$  and check first the validity of the factorization in Eq. (5.86) in the form  $\hat{\phi}_q^*(t) = G_2(x) + K_q \tilde{G}_2(x)$ ,  $x = \ln(t/t_0)$  where  $G_2(x) = g_1(x) + g_2(x)$  and  $\tilde{G}_2(x) = g_1^2(x)$ . The point, where the solutions for  $q = 1, 2$ , differ by 5% is only reached at  $t \approx 10^{23}$ . The circle marks the point where the deviation is still 10% at  $t = 10^{12}$ . The parameters for the evaluation of  $g_1(x)$  and  $g_2(x)$  are  $\mu_3 = 0$ ,  $\mu_4 = 1.53$ ,  $\mu_5 = 0.962$ , and  $\kappa = 0.386$ . We can then use the approximation (5.86) to fix the time scale at  $t_0 = 2.0$  which then yields the dashed and dotted curves for  $q = 1, 2$ , accordingly. For  $q = 1$  this approximation deviates by 5% from the solution at  $t \approx 8.2 \cdot 10^4$  ( $\square$ ). For  $q = 2$  we find  $t \approx 1.8 \cdot 10^8$  ( $\triangle$ ). This is again plausible when appealing to the  $q$ -dependent higher-order correction in Eq. (5.84), which incorporates in addition to drastically different values for  $K_q$  also the values  $Y_1/a_1 = -0.579$  and  $Y_2/a_2 = 3.76$ .

A rectified representation of the critical decay and the approximation in the inset of Fig. 5.13 shows again the leading-order  $G_1(x)$  (dotted) as a straight line of different slope than the solution (full lines) and the second correction  $G_2(x)$  (dashed). In this plot the critical correlators for different  $q$  are still significantly different in the entire window but Eq. (5.86) can account for that difference as is shown by the good agreement of the curve labeled  $G_2 + \tilde{G}_2 K_2$  that describes the second correlator where the deviations due to the correction amplitudes are largest.

**7.3. Characteristic Parameters.** To conclude the present chapter we shall have a look at the parameters characterizing the singularities in a glass-transition diagram with a swallowtail bifurcation. Since we know the properties of the singularities exactly in the schematic models, we can check the accuracy of the asymptotic description. The inverse of that procedure can be used later to check the accuracy of the numerical solution that is known with limited numerical precision only.

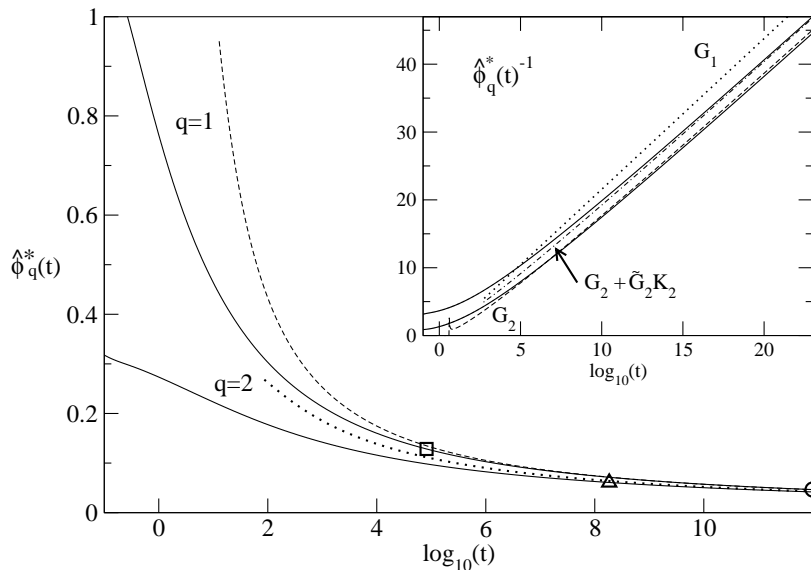


FIGURE 5.13. Critical decay at the  $A_4$ -singularity in the two-component model. Full lines show the solution of Eq. (5.111) for  $q = 1, 2$ , at  $\mathbf{V} = \mathbf{V}^*$ . The asymptotic approximations, Eq. (5.86), for  $q = 1, 2$ , are represented by the dashed and dotted curve, respectively. For  $q = 1$  ( $\square$ ) and  $q = 2$  ( $\triangle$ ), the points are marked where the solution and the approximation deviate by 5%. An additional point is indicated where the solution for  $q = 2$  differs from the one for  $q = 1$  by 10% ( $\circ$ ). The inset displays the rectified representation of the solutions for  $q = 1$  (lower full line) and  $q = 2$  (upper full line) together with the  $q$ -independent parts of the approximations,  $G_1$  and  $G_2$ , cf. Eq. (5.82), and  $G_2 + K_2 \tilde{G}_2$  (see text). The time scale  $t_0 = 2.0$  was matched at  $t = 10^{20} \dots 10^{25}$ .

In principle, Eq. (5.15b) could be used to derive the scaling laws at  $A_l$ -singularities. This yields multi-parameter laws that simplify on the special lines where some separation parameter  $\varepsilon_i$  vanishes. Since we are primarily interested in the behavior on the transition surface, a different approach is taken which is motivated by the representation in Eq. (5.112). It was seen above that the numerator of Eq. (5.112d) allows for two distinct zeros  $y_1(x) < y_2(x)$  for  $x > x^*$  which is connected with a minimum  $\mu_2 \leq 0$ . For an  $A_3$ -singularity only the root  $y_2(x)$  has to be considered because of the maximum theorem. Around  $y_2(x)$  the parameter  $\mu_2$  varies linearly in  $y - y_2(x)$  according to Taylor's theorem. The control parameter  $v_1^c$ , Eq. (5.112b), is a smooth function of  $y$  and  $x$  and since  $y_2(x)$  represents a cusp,  $v_1^c$  assumes a local maximum or minimum there. Therefore we conclude  $[v_1^c - v_1^o] \propto [y - y_2(x)]^2$  and hence  $\mu_2 \propto [v_1^c - v_1^o]^{1/2}$ . This is generic also for the second control parameter  $v_2^c$ . In Fig. 5.14 the solution of Eq. (5.112d) for  $x = v_3$  is shown as full line in panel A. The dashed line represents the square-root behavior at the  $A_3$ -singularity, which describes the solution with an accuracy of 5% up to  $\lambda = 1 - \mu_2 \approx 0.8$ .

At an  $A_4$ -singularity, the two roots merge,  $y_1(x) = y_2(x) = y^*(x^*)$ . This implies a quadratic variation of  $\mu_2$  with  $y - y^*(x^*)$  and a cubic-root behavior of  $f_1^c = y$  with the control parameters, e.g.  $v_1^c$ . This cubic-root variation of the glass-form factors was demonstrated already in Fig. 4.2 for the SWS. For the control-parameter dependence we get  $\mu_2 \propto |v_1^c - v_1^*|^{2/3}$ . For  $\mu_2$  in the two-component model we obtain the solution shown in panel B in Fig. 5.14. The full line for  $v_1 < v_1^*$  is the analog of the line of transitions displayed also in panel A, the dotted line for  $v_1 > v_1^*$  has no analog at the  $A_3$ -singularity due to the maximum property. Asymptotically close to the  $A_4$ -singularity both solutions follow the same variation in the control parameter. The deviations from the asymptotic behavior are different for  $v_1 < v_1^*$  and  $v_1 > v_1^*$  as can be seen by the symbols marking the 5%-accuracy level. This is explained by higher order terms in the Taylor expansion of  $\mu_2(y - y^*)$  which need not be symmetric in  $(y - y^*)$ .

Finally, the evolution of  $\mu_3$  along the line of  $A_3$ -singularities is considered in panel C of Fig. 5.14. We get a square-root law for  $\mu_3$  from Eq. (5.112) observing that at  $v_3 = v_3^*$  the parameter  $\mu_3$  has a zero which is non-degenerate for  $\mu_4 > 0$ , and that  $x - x^*$  varies quadratically in  $y^\circ(x) - y^*$ . The asymptotic approximation works on the 5%-accuracy level up to  $\mu_3 \approx 0.15$  ( $\square$ ). The double-logarithmic representation in the inset confirms that this is indeed valid asymptotically.

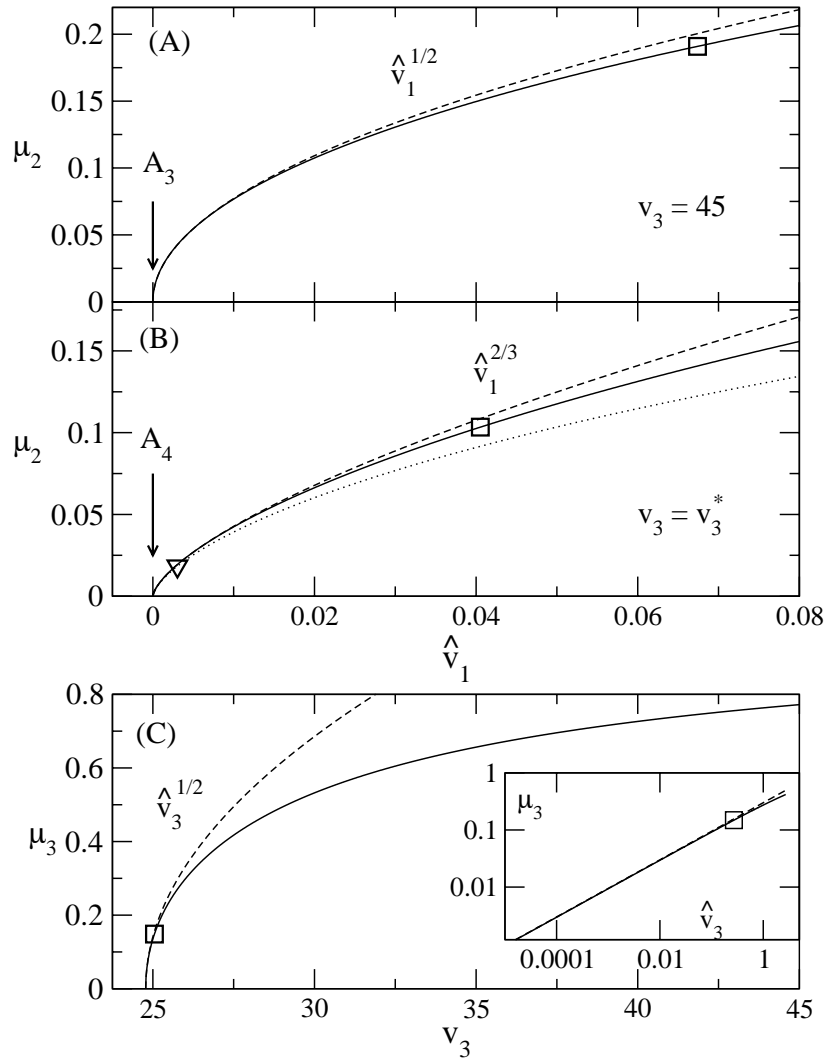


FIGURE 5.14. Parameters  $\mu_2$  and  $\mu_3$  for the two-component model. Panel A shows the evolution of  $\mu_2$  along the line of liquid-glass transitions in Fig. 5.6 starting from the  $A_3$ -singularity,  $\Delta v_1 = v_1^\circ - v_1$ . The asymptotic square-root law is shown dashed. It deviates by 5% from the solution at the point indicated by a square. In panel B,  $\Delta v_1 = |v_1^* - v_1|$ , the full line shows  $\mu_2$  for  $v_1 > v_1^*$ , the dotted line for  $v_1 < v_1^*$ . The dashed line exhibits the  $\Delta v_1^{2/3}$ -law which deviates by 5% from the solutions for  $v_1 < v_1^*$  and  $v_1 > v_1^*$  at the points marked by a square and a triangle, respectively. The variation of  $\mu_3$  with  $\Delta v_3 = v_3 - v_3^*$  is shown in panel C as full line together with the asymptotic approximation as dashed line. The 5%-accuracy level of the approximation is indicated by the square. The inset displays solution and approximation in a double-logarithmic representation.

## Logarithmic relaxation in the SWS

In principle the numerical solution of the equations of motion (2.7) gives the definitive answer what dynamics is expected for the correlation functions according to MCT when the structure of a certain system is used as input. However, the case of the SWS is a good example that it might not be easy to distill the relevant features from an analysis of the numerical solution only. The possible changes in three control parameters and an additional variation in the wave vector illustrates that even for a theoretical analysis the asymptotic approximation is a helpful guide to the relevant features that are displayed by the numerical solution of the theory.

The asymptotic expansion (5.42) shall be applied to the SWS in Sec. 1 with the focus on the laws at the  $A_4$ -singularity. We will discuss in detail the logarithmic decay of the correlation functions and the wave-vector dependence. We identify the lines of vanishing corrections in the glass-transition diagram as done for the schematic models in Ch. 5. These lines are located in the liquid regime only for relatively large wave vectors. As a second variable the mean-squared displacement (MSD) is discussed in Sec. 2 which displays a subdiffusive power law that is the analog of the logarithmic decay in the correlation functions. Deviations from this power law can be convex or concave in a double logarithmic representation depending on the control parameters and it is possible to identify a line in the liquid regime where the corrections vanish and the power law is shown best. The situation for the  $A_3$ -singularity for  $\delta = 0.03$  is very similar to the case of the  $A_4$ -singularity and different only in the wave-vector dependence as shown in Sec. 3. The lines of vanishing correction in the liquid regime are seen at higher  $q$  for the correlators but the power law in the MSD is not altered significantly. The critical decay laws at the  $A_3$ - and the  $A_4$ -singularity are however different and shall be discussed in Sec. 4. With the approximations available it is possible to describe the decay at the  $A_3$ , for the  $A_4$ -singularity only qualitative trends can be corroborated.

### 1. Logarithmic decay at the $A_4$ -singularity

Before we can apply the asymptotic expansion of Eq. (5.42), we need to specify the values for  $\mu_3$  and  $\zeta$  appearing in the prefactors of Eqs. (5.29). Figure 6.1 shows these parameters and the parameter  $\mu_4$  for the critical decay laws in Eqs. (5.76) and (5.86) at the  $A_3$ -singularities for various  $\delta$ . All parameters are evaluated using the structure factor in MSA given by Eq. (3.16). The  $\mu_3$  vanish when we approach the  $A_4$ -singularity. The decrease close to  $\delta^*$  is described by a square-root variation,  $\mu_3 \propto \sqrt{\delta^* - \delta}$ , shown by the dashed line. One has to take into account that the evaluation of the  $\mu_3$  in the SWS involves the inversion of several  $M \times M$  matrices for calculating the reduced resolvent  $R_{qk}$  in Eq. (5.13c), where  $M$  ranges from  $M = 300$  at  $\delta = \delta^*$  up to  $M = 750$  for  $\delta = 0.02$ . Given the rather involved

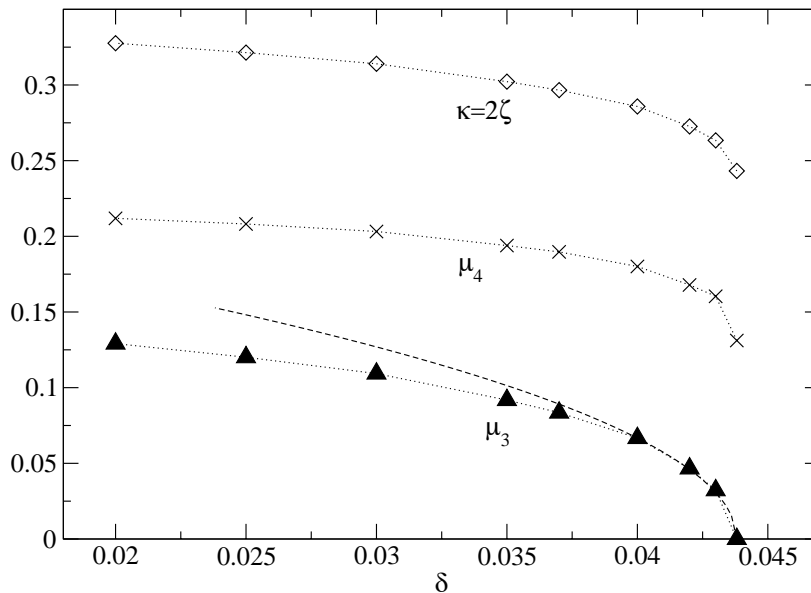


FIGURE 6.1. Parameters  $\mu_3$  (▲), Eq. (5.41),  $\mu_4$  (×), Eq. (5.75), and  $\kappa = 2\zeta$  (◇), Eq. (5.40), at the  $A_3$ -singularities for varying  $\delta$  in the SWS. The dotted lines connecting the points are guides to the eye. The dashed curve shows the  $\sqrt{\delta^* - \delta}$ -law for the  $\mu_3$  at  $\delta^*$ .

numerical procedure to obtain  $\mu_3$ , the square-root law for the  $\mu_3$  close to the  $A_4$ -singularity is realized to a good degree, which can be used as a consistency check for the numerical algorithms. The deviation from the asymptotic variation in  $\mu_3$  is similar to the one observed for the schematic model in panel C of Fig. 5.14 and can be interpreted in the same way. The  $A_4$ -singularity is not only characterized by  $\mu_2 = 0$  but also has to fulfill the requirement  $\mu_3 = 0$ . This was achieved up to  $|\mu_3| < 5 \cdot 10^{-4}$  at the control-parameter values specified in Eq. (4.1). Since the parameters  $\mu_4$  and  $\kappa$  contain  $\mu_3$  in their definition, cf. Eqs. (5.75) and (5.41), they share part of the behavior of  $\mu_3$  at  $\delta^*$  but remain finite at  $\delta^*$ .

That the values of  $\mu_3$  are altogether rather small indicates that all the  $A_3$ -singularities that can be studied in the SWS are already influenced by the proximity of the close-by  $A_4$ -singularity. One can take advantage of this finding and conclude that the terms proportional to  $\mu_3$  in Eq. (5.29a) are small, moreover one may neglect  $B_3$  and  $B_4$  in Eq. (5.29d) entirely without introducing large additional errors. The leading correction to the logarithmic decay laws is then only quadratic also for the  $A_3$ -singularities. The  $\mu_3$  being small has a different impact on the approximation of the critical decay where  $\mu_3$  appears in the denominators for the coefficients  $c_2$  of Eq. (5.54),  $c_3$  of Eq. (5.59) and all higher  $c_{m,l}$ , cf. Eqs. (5.62), (5.63), (A.9), and (A.10). The same applies to the critical law for the  $A_4$ -singularity, Eq. (5.86), where  $\mu_4$  is in the denominators. For the description of the  $A_3$ -singularities,  $\delta \neq \delta^*$ , the  $\mu_4$  introduce only regular terms as do the terms proportional to  $\kappa$ , which are smaller than in the HSS, but of the same order of magnitude,  $\kappa_{\text{HSS}} = 0.54$  [7].

The second prerequisite for the asymptotic description according to Eq. (5.42) are the wave-vector dependent amplitudes  $f_q^*$ ,  $h_q^*$  and  $K_q^*$ . These are shown for the



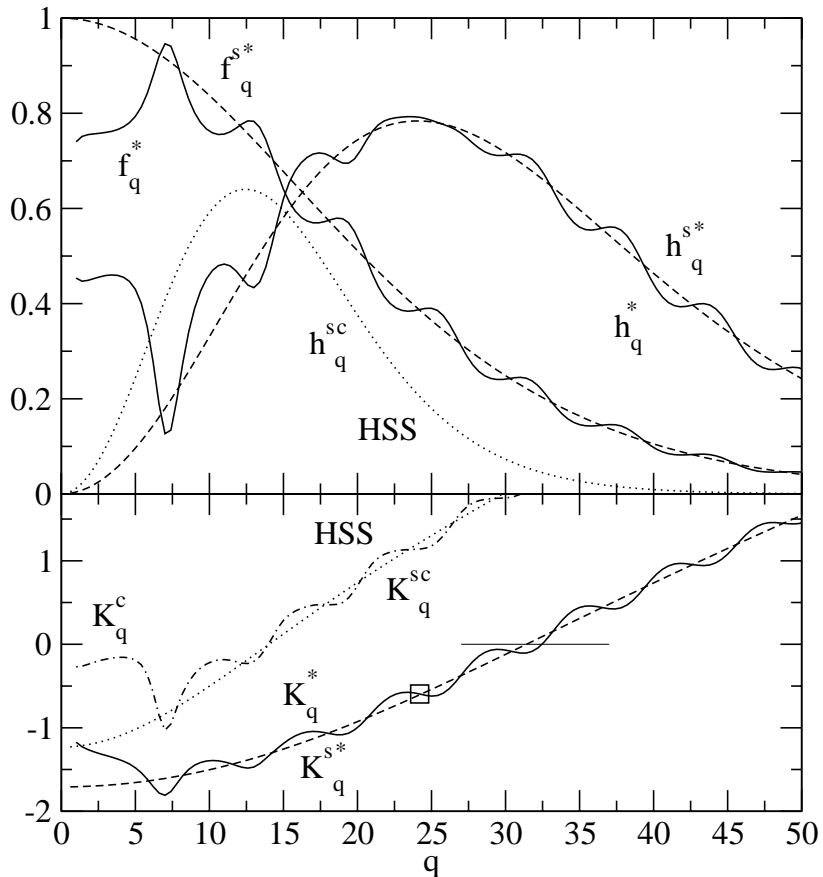


FIGURE 6.2. Wave-vector dependent amplitudes at the  $A_4$ -singularity for coherent and tagged particle correlators. In the upper panel the critical glass-form factors  $f_q^*$  and the amplitudes  $h_q^*$  are shown as full lines. The dashed lines represent the respective values for  $f_q^{s*}$ , Eq. (2.12), and  $h_q^{s*}$ , Eq. (5.99a). For the HSS,  $h_q^{sc}$  is shown dotted. The lower panel shows the correction amplitudes  $K_q^*$ , Eq. (5.44) and (5.38b), and  $K_q^{s*}$ , Eq. (5.99b), as full and dashed lines, respectively. A short horizontal line marks the location for  $K_q^* = 0$  and  $K_q^{s*} = 0$ . A square at  $q = 24.2$  indicates the corrections for the path calculated for Fig. 6.3 and the correlators shown in Fig. 6.4. The values for  $K_q^c$  ( $- \cdot -$ ) and  $K_q^{sc}$  ( $\cdot \cdot \cdot$ ) for the HSS are shown for comparison.

$A_4$ -singularity in Fig. 6.2 together with the related values for the tagged-particle correlator  $\phi_q^s(t)$ , Eq. (5.98). The quantities for the tagged particle motion are close to the ones for the coherent correlator  $\phi_q(t)$  except for values of  $q$  smaller than say  $q = 10$ . This difference was observed already for the HSS [60] and since we will not be concerned with small  $q$  in the following, we restrict the discussion to the coherent dynamics and imply that the same is applicable also to the incoherent part with only minor changes. In comparison to the HSS the distributions  $f_q$ ,  $h_q$ ,

$f_q^s$  and  $h_q^s$  are broader with the maximum in  $h_q^s$  shifted from  $q \approx 13$  to  $q \approx 25$  reflecting the smaller localization length in the SWS as noticed before, cf. [16] and Ch. 4. We see in the lower panel of Fig. 6.2 that the distributions of the correction amplitudes  $K_q$  and  $K_q^s$  share that trend of becoming broader from the HSS to the  $A_4$ -singularity of the SWS. The zero in  $K_q$  moves from around  $q \approx 14$  in the HSS to  $q \approx 32$  in the SWS which is indicated by the horizontal rule. In addition, the correction amplitudes are shifted to lower values for small  $q$ .

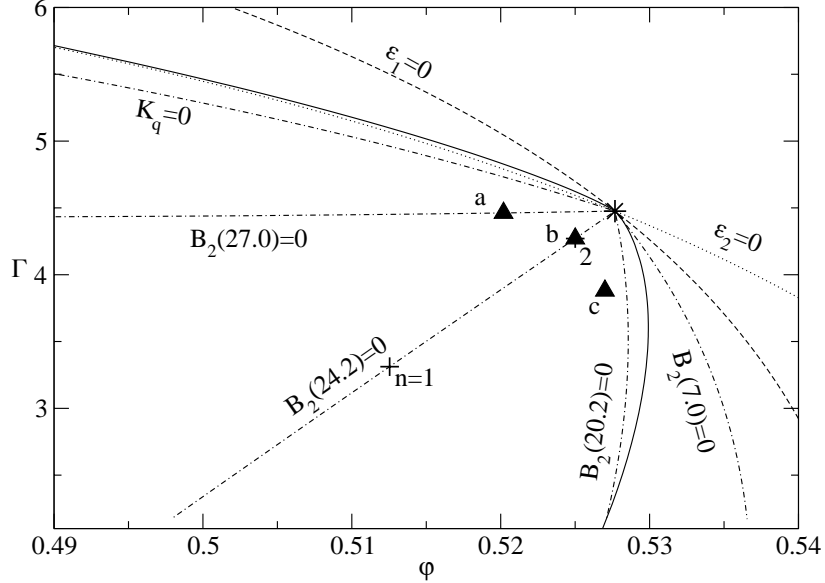


FIGURE 6.3. Curves of vanishing quadratic correction at the  $A_4$ -singularity (dash-dotted),  $B_2(q) = 0$  for  $q = 7.0, 20.2, 24.2, 27.0$ , and for  $K_q = 0$  as labeled. The full line shows a part of the glass-transition diagram from Fig. 4.1 for constant  $\delta = \delta^*$ . The lines of vanishing separation parameters  $\varepsilon_1(\mathbf{V})$  and  $\varepsilon_2(\mathbf{V})$  are shown by a broken and a dotted line, respectively. For the wave vector  $q = 24.2$ , a path on the curve  $B_2(24.2) = 0$  is marked (+) and labeled by  $n$ , for which the correlators are shown in Fig. 6.4. State  $n = 2$  is analyzed also in Fig. 6.5. For the points (▲) labeled a, b, and c the decay is shown in Fig. 6.6.

As done for the schematic models in Ch. 5, we set the quadratic corrections in Eq. (5.42) to zero,  $B_2(q) = 0$ , and calculate the curves in the control-parameter space where the logarithmic decay is expected to show up as straight line around the plateau  $f_q^*$ . We get a different curve for each wave vector  $q$  and show typical examples in Fig. 6.3. We start with  $q = 7.0$  where  $K_q = -1.81$  assumes the smallest value. The solution of  $B_2(\mathbf{V}) + K_q B(\mathbf{V})^2 = 0$  yields the chain line labeled  $B_2(7.0) = 0$  in Fig. 6.3 and is lying in the arrested region close to the line of liquid-glass transitions. Since the  $K_q$  depend smoothly on  $q$ , the evolution of the curve where  $B_2(q) = 0$  can be understood by inspecting the parameters  $B$  and  $B_2$ . The square  $B^2$  is always positive and proportional to  $\varepsilon_1(\mathbf{V})$ , cf. Eq. (5.20); therefore

$K_q B^2$  is proportional to  $K_q |\varepsilon_1(\mathbf{V})|$  and shares the sign of  $K_q$ . Inserting  $\mu_3 = 0$  and  $\zeta = 0.1216$  into Eq. (5.29c) yields  $B_2(\mathbf{V}) = 0.111 \varepsilon_1(\mathbf{V}) - 0.152 \varepsilon_2(\mathbf{V})$ , which has to be positive to comply with  $B_2(q) = 0$ . Indeed,  $\varepsilon_2(\mathbf{V}) < 0$  below the dotted curve for  $\varepsilon_2 = 0$  in Fig. 6.3. In addition, the value  $|\varepsilon_2(\mathbf{V})|$  on the line  $B_2(7.0) = 0$  is larger than  $|\varepsilon_1(\mathbf{V})|$  which we can also infer from the fact that the line  $\varepsilon_1 = 0$  is closer than the line  $\varepsilon_2 = 0$ . We now chose a point on the line  $B_2(7.0) = 0$ , keep the first separation parameter fixed, say  $\varepsilon_1 = \varepsilon'_1$ , and move to higher values for  $K_q$ , e.g., for  $q = 20.2$  where  $K_q = -0.966$ . Since  $B^2$  stays the same, the term  $K_q B^2$  increases. To ensure that  $B_2(20.2) = 0$ , the value  $B_2(\mathbf{V})$  has to decrease. We can only achieve that by moving closer to the line  $\varepsilon_2 = 0$ . For fixed  $\varepsilon'_1$  this implies a shift to lower  $\varphi$  and higher  $\Gamma$ . Consequently the entire  $B_2(q) = 0$  line is rotating clockwise around the  $A_4$ -singularity as  $K_q$  increases. This is seen for the chain line  $B_2(20.2) = 0$  in Fig. 6.3. Since  $K_q^s$  is monotonic increasing with  $q$  and  $K_q$  has the same trend when neglecting the small oscillations, Fig. 6.2, the line  $B_2(q) = B_2(\mathbf{V}) + B(\mathbf{V})^2 K_q^s = 0$  also rotates clockwise with increasing wave-vector  $q$ .

The variation of the lines  $B_2(q) = 0$  described above depends only on the angle at which the lines  $\varepsilon_1 = 0$  and  $\varepsilon_2 = 0$  intersect at the  $A_4$ -singularity. This intersection is in a sense generic that it is shared by the close-by  $A_3$ -singularities of the SWS. It applies also to the  $A_4$ -singularities of the other potentials discussed in Ch. 4, since the functionals determining the separation parameters depend on quantities like the structure factors and the glass-form factors which are similar for different potentials as shown Fig. 4.8. We observe that the lines  $\varepsilon_1 = 0$  and  $\varepsilon_2 = 0$  intersect at an angle of the same sign as in Fig. 6.3 also in the two-component model, cf. Figs. 5.6 and 5.10, and in the one-component model, Fig. 5.1. For a given wave vector  $q$ , the line  $B_2(q) = 0$  may or may not lie in the liquid regime depending on  $K_q$ . For the SWS at  $\delta = \delta^*$  we get a range of  $-1 \lesssim K_q \lesssim 0$  corresponding to  $20 \lesssim q \lesssim 30$ , where a line  $B_2(q) = 0$  is found in the liquid regime. We illustrate this by adding lines for  $q = 24.2$ ,  $q = 27.0$  and for  $K_q = 0$  to Fig. 6.3. The vanishing  $K_q$  is corresponding to  $q \approx 32.3$ .

We select a wave vector  $q = 24.2$  with  $K_q = -0.596$  as indicated in Fig. 6.2 by a square and choose a path on the line  $B_2(24.2) = 0$  marked by the plus symbols in Fig. 6.3. For  $n = 1, 2, 3$ , the control parameters are  $(\Gamma, \varphi) = (3.312, 0.5125)$ ,  $(4.271, 0.5250)$ , and  $(4.453, 0.5274)$ , respectively. The solutions are shown in Fig. 6.4 together with the leading approximation (5.37) (dotted) and the next-to-leading approximation (5.42) (dashed). The time scales  $\tau$  are matched at the plateau  $f_q^*$  for the leading approximation and at the renormalized plateaus  $f_q^* + \hat{f}_q$  for the first correction. We recognize that for  $n = 3$  the correction covers more than ten decades in time with an accuracy better than 5%, the leading approximation is acceptable on that level for nine decades. For  $n = 1$  two and more than one decade are covered, respectively. Five and three orders of magnitude in time are achieved for  $n = 2$ . For  $n = 1, 2, 3$ , the leading approximation describes at least 30% of the complete decay and when including the correction, 65% are covered on the chosen accuracy level. The distance in the control parameter  $\Gamma$  from the value at the  $A_4$ -singularity is 25% for  $n = 1$  and 4% for  $n = 2$ , so no fine-tuning was necessary to obtain such large windows for the logarithmic decay. The curve  $n = 1$  requires about five decades for the complete decay which is well in the reach of today's computer simulation techniques [92].

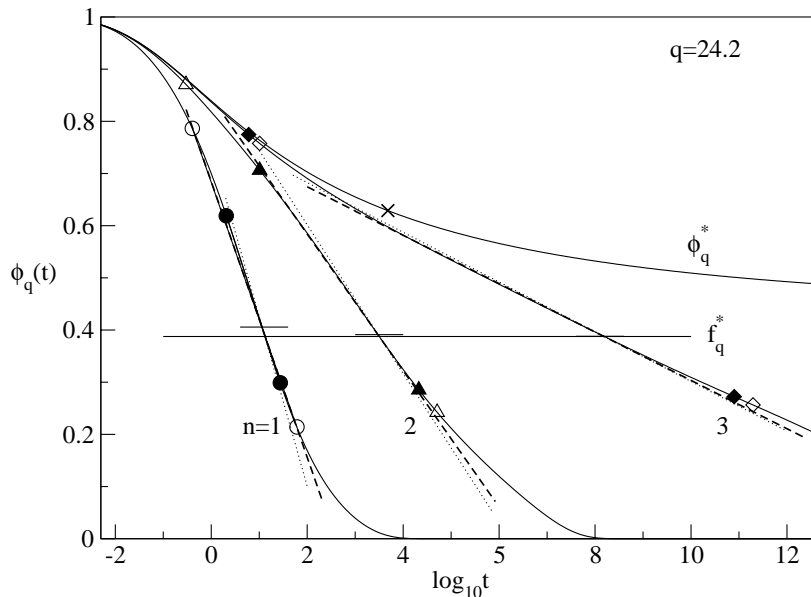


FIGURE 6.4. Logarithmic decay at the  $A_4$ -singularity for  $q = 24.2$  on the path indicated in Fig. 6.3. The correlation functions are shown as full lines for the states  $n = 1, 2, 3$  (see text) and at  $\mathbf{V} = \mathbf{V}^*$  which is labeled  $\phi_q^*$ . The horizontal line indicates the critical plateau value  $f_q^*$  for  $q = 24.2$ , short lines the renormalized plateaus  $f_q^* + \hat{f}_q$ . Broken lines show the approximation of Eq. (5.42),  $-(B - B_1) \ln(t/\tau)$ , dotted lines the approximation of Eq. (5.37). Filled and open symbols, respectively, mark the points where the approximations deviate by 5% from the solution. The cross indicates the time when the solution for  $n = 3$  and the critical correlator differ by 5%.

The scenario in Fig. 6.4 is reminiscent of the one for the one-component model in Fig. 5.2 and in Fig. 5.4 it was possible to describe part of the critical decay in the model by the expansion in polynomials in  $\ln t$  at a point away from the singularity. We therefore compare the critical decay  $\phi_q^*(t)$  with the decay for  $n = 3$  and indicate the point at  $t \approx 5000$  where both differ by 5% in Fig. 6.4. With only the leading correction at our disposal, a 2%-criterion was not fulfilled as for the one-component model, where the next-to-leading correction (5.31) could be used. The dashed line for  $n = 3$  does not come closer to the critical decay than 4%. Allowing for 5%, the interval from  $t \approx 20$  to  $t \approx 4000$  could be described. However, at the  $A_4$ -singularity the approximation in Eq. (5.42) always yields a straight  $\ln t$ -decay as approximation on the chosen path with  $B_2(q) = 0$ . This disagrees qualitatively with the critical decay.

To identify correctly some decay that is linear in the  $\phi_q(t)$  versus  $\ln t$  diagram with the logarithmic decay predicted by the asymptotic laws, Eq. (5.42), we check if a different correlator with a different correction amplitude  $K_q$  is *not* linear in  $\ln t$  at the same point in the control-parameter space unless one is very close to the

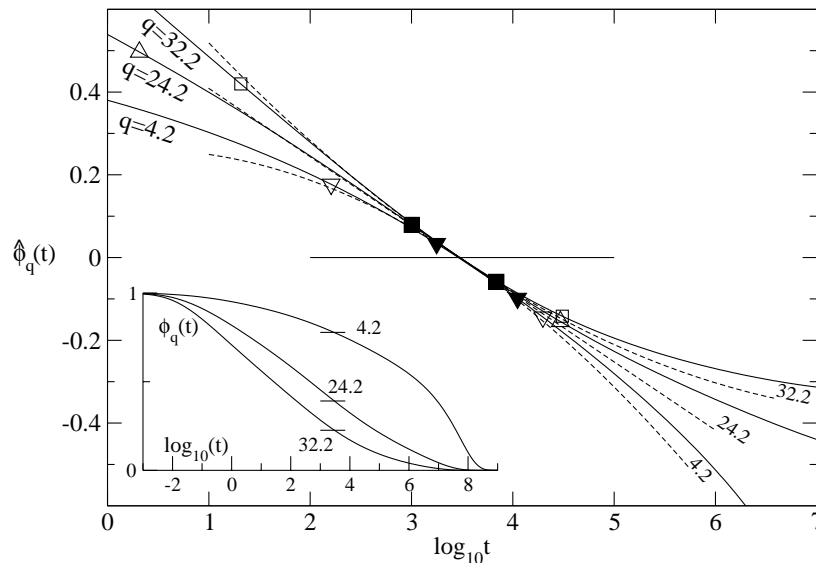


FIGURE 6.5. Logarithmic decay at the  $A_4$ -singularity for varying wave vector  $q$ . The inset shows the correlation functions  $\phi_q(t)$  at state  $n = 2$  from Fig. 6.3 for wave vectors  $q = 4.2, 24.2$ , and  $32.2$  from top to bottom and the short horizontal lines show the corresponding critical plateau values  $f_q^*$ . The full panel shows the same correlation functions rescaled according to  $\hat{\phi}_q(t) = (\phi_q(t) - f_q^* - \hat{f}_q)/h_q$  as full lines and labeled by the respective wave vectors. Dashed lines show the asymptotic laws of Eq. (5.42) for the different wave vectors which are indicated in the right lower corner by the value for  $q$  placed between the solution and the approximation. The deviations of the approximations from the solutions of 5% are marked by the open symbols. Filled symbols for  $q = 4.2$  ( $\blacktriangledown$ ) and  $q = 32.2$  ( $\blacksquare$ ) show the 5% deviation from the additional approximation of neglecting quadratic terms (see text).

higher-order singularity. For the two-component model a characteristic alternation of concave, linear and convex decay in  $\ln t$  was found, cf. Figs. 5.11 and 5.12. As the values for  $K_q$  differed from each other by  $K_1 - K_2 \approx 2$ , not both correlators could be linear in  $\ln t$  at the same time. In the SWS this check is performed at the point  $n = 2$  from Fig. 6.3 by variation of the wave vector  $q$  in Fig. 6.5. For the wave vectors  $q = 4.2$  and  $32.2$  the correction amplitudes are  $K_q = -1.400, -0.0413$ , respectively. Therefore  $B_2(4.2) < 0$  and  $B_2(32.2) > 0$  and we expect  $\phi_q(t)$  to be concave or convex, accordingly. This is indeed found in Fig. 6.5. That the curvature is different for the decay around the plateaus is already recognized directly from the inset where  $\phi_q(t)$  is shown. The rescaled correlators  $\hat{\phi}_q(t)$  displayed in the full panel allow for a more detailed analysis. We see that the solutions as well as the approximations clearly exhibit increased curvature for larger  $q$ . Since the coefficient linear in  $\ln t$  is not depending on  $q$ , cf. Eq. (5.42), the middle dashed line represents the leading correction to all three correlators when the quadratic terms are neglected. For

$q = 24.2$  we observe good agreement over almost 5 decades as before, cf. Fig. 6.4. For  $q = 4.2$  and  $32.2$ , however, the additional approximation reduces the range of applicability to less than one decade as marked by the filled symbols. Including the quadratic terms from the approximation (5.42) extends this range by half a decade to later times and to earlier times by one and almost two decades for  $q = 4.2$  and  $32.2$ , respectively. The time window defined by a 5% deviation from the approximation (5.42) is larger by one and two orders of magnitude for  $q = 24.2$  than for  $q = 32.2$  and  $q = 4.2$ , respectively, what indicates that  $q$ -dependent higher-order corrections significantly influence the range of applicability for the leading correction (5.42).

The time scale  $\tau$  in Fig. 6.5 was matched for  $q = 24.2$ , so the violation of scale universality discussed in Ch. 5 leads to different times  $\tau_q$ , where the correlators for different  $q$  cross their respective renormalized plateau  $f_q^* + \hat{f}_q$ . The representation with the rescaled  $\hat{\phi}_q(t)$  is particularly sensitive to these deviations since the point where the plateau is crossed is required to be zero,  $\hat{\phi}_q(t/\tau) = 0$ . In Fig. 6.5 we see that the line crossing the zero is slightly broader than a single curve. The deviations in  $\tau_q$  are small enough to not exceed the grid for the time axis which around  $\tau = 2988$  is given by  $\Delta t = 172$ . So we interpolate to get for  $q = 4.2, 24.2$ , and  $32.2$ ,  $\tau_q = 2899, 2988$ , and  $3017$ , respectively. These difference do not introduce larger errors in the analysis carried out above.

In order to change from convex to concave behavior we can also change the control parameters which was exercised already in detail in the schematic models in Ch. 5. For states above the line  $B_2(24.2) = 0$ , we expect concave behavior,  $B_2(q) < 0$ , for states below, convex decay,  $B_2(24.2) > 0$ . For a test of these expectation, the rescaled correlators  $\hat{\phi}_q(t/\tau)$  at the states labeled a, b, c from Fig. 6.3 are divided by the prefactor  $(B - B_1)$  of Eq. (5.42). This way the part of the decay that is linear in  $\ln t$  shows up as straight line with slope  $-\ln 10$  in Fig. 6.6. The approximations (5.42) are shown as dashed lines for each state representing  $-\ln(t/\tau) + [B_2(24.2)/(B - B_1)] \ln^2(t/\tau)$ . For state b the approximation is identical to  $-\ln(t/\tau)$  and the solution follows that line over 5 decades before 5% deviation is reached. The states a and c are chosen to have the same value for  $B - B_1 \approx 0.015$  and  $B_2(24.2) = \mp 0.0020$ , respectively. The solutions at state a and c follow the  $-\ln t$ -law closely within a 5% margin for two decades or one decade, respectively, which is significantly less than found for state b. We can infer from Fig. 6.3 that at state a the quadratic corrections would vanish again if we went from  $q = 24.2$  to the higher wave vector  $q = 27.0$ . A scenario similar to the one shown in Fig. 6.4 can be found.

The procedure outlined in Figs. 6.3, 6.4, 6.5, and 6.6 can be summarized as follows. From the higher-order singularities there emanate surfaces in the control-parameter space for a specific wave vector  $\bar{q}$  where the quadratic term in Eq. (5.42) is zero, cf. Fig. 6.3, and the decay is linear in  $\ln t$ . Moving closer to the singularity on that surface, the window in time where the logarithmic decay is a valid approximation increases, cf. Fig. 6.4. On a fixed point on that surface the decay is concave for  $q < \bar{q}$  and convex for  $q > \bar{q}$ , cf. Fig. 6.5. For fixed  $\bar{q}$  the change from concave to convex is achieved by crossing the mentioned surface from above in the sense exemplified in Fig. 6.6.

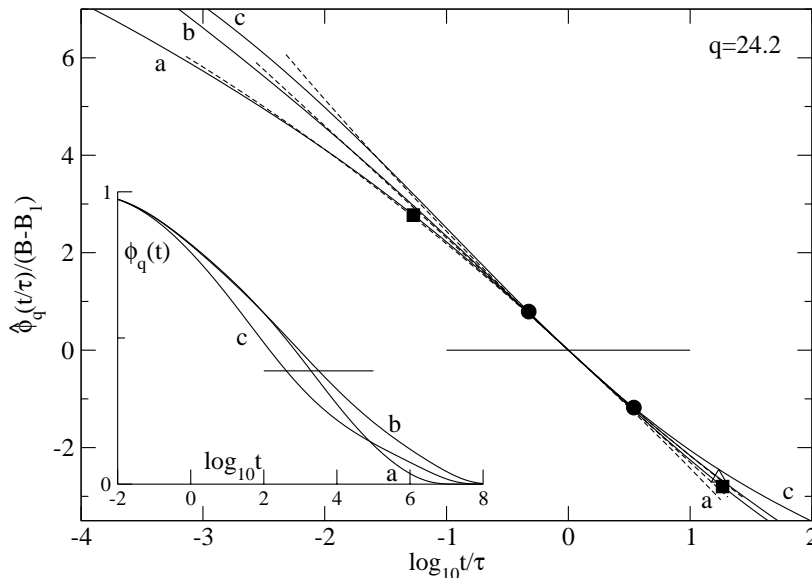


FIGURE 6.6. Logarithmic decay at the  $A_4$ -singularity for the three states marked by triangles in Fig. 6.3. The inset shows the correlation functions  $\phi_q(t)$  for  $q = 24.2$ . The plateau value  $f_q^*$  is indicated by the short horizontal line in both the inset and the full panel. The full panel shows  $\hat{\phi}_q(t) = (\phi_q(t) - f_q^* - \hat{f}_q)/h_q$  divided by the respective values for  $(B - B_1)$  at the three states specified. The dashed curves show the result from Eq. (5.42). Filled squares and bullets mark the points where curve a and c deviate by 5% from  $-\ln(t/\tau)$ , respectively. The deviation for curve b ( $\Delta$ ) for short times is at  $t \approx 10^{-4}$  and not included in the figure.

## 2. Subdiffusive power law in the MSD

It was demonstrated in Sec. 5.2 of Ch. 5 that the coupled quantities share the leading asymptotic behavior of the density correlators. As a consequence of the factorization theorem only the glass-form factors and the critical amplitudes  $h_q$  are different for the coupled quantities. In the sense of Eq. (5.91) the leading correction violating a generalized factorization theorem is proportional to the correction amplitude  $K_q$ . Since for large wave vectors, say  $q > 10$ , the quantities  $f_q^s$ ,  $h_q^s$ , and  $K_q^s$  are close to the ones for the coherent correlator, the approximation for the tagged particle correlation functions  $\phi_q^s(t)$  for these large  $q$  is the same as for  $\phi_q(t)$ . So the discussion for  $\phi_q^s(t)$  is already exhausted by Fig. 6.2 and not much could be gained from repeating the same discussion as in the previous section.

We turn instead to the MSD as a second variable to be examined for the manifestation of the logarithmic decay laws. It was derived in Sec. 5.3 of Ch. 5 that  $\delta r^2(t)$  is expected to exhibit power-law behavior around the plateau  $6 r_g^c{}^2$  provided the term  $b_2$  in Eq. (5.105b) vanishes. The power-law exponent  $b_1$  is determined explicitly in Eq. (5.106b) by the localization length and the critical amplitude,

which are

$$(6.1) \quad r_s^* = 0.04255, \quad h_{\text{MSD}}^* = 0.004051$$

for the  $A_4$ -singularity.

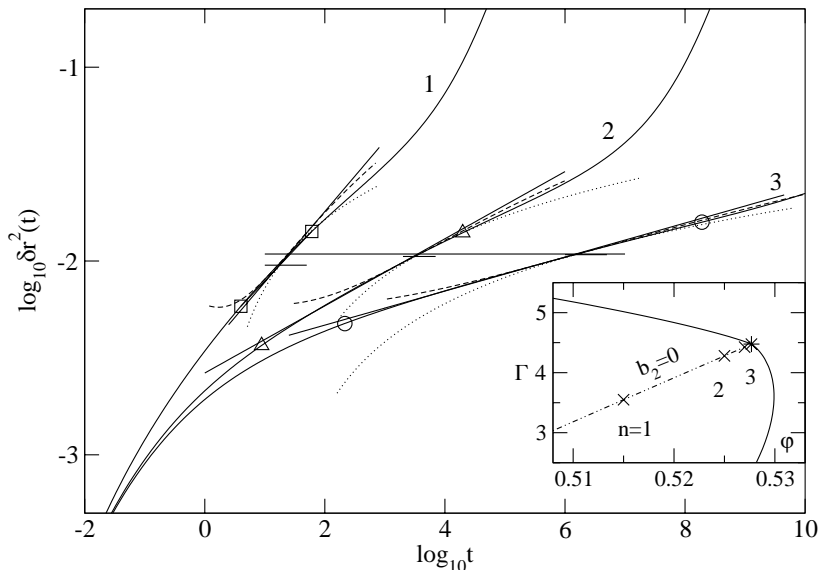


FIGURE 6.7. Subdiffusive power law in the MSD. The solutions for states 1, 2, and 3 in the inset are shown as full lines in the full panel together with the leading (dotted) and next-to-leading (dashed) approximation by Eqs. (5.37) and (5.42), respectively. The long horizontal line represents  $6r_s^{*2} = 0.01086$ , the short horizontal lines the corrections to the plateau,  $6(r_s^{*2} - \hat{r}_s^2)$ . The straight full lines show the power law  $(t/\tau)^{b_1}$ , Eq. (5.106a), with exponents  $b_1 = 0.365, 0.173$  and  $0.0878$  for states  $n = 1, 2, 3$ . The open symbols show the points where the solutions deviate by 5% from the leading-order power laws. The inset shows part of the glass-transition diagram for  $\delta = \delta^*$  and a chain line where  $b_2 = 0$  (see text).

The line where  $b_2$  from Eq. (5.105b) vanishes is found in the liquid regime as shown in the inset of Fig. 6.7. Accidentally, this line is almost identical to the one for  $B_2(24.2) = 0$  for the correlators  $\phi_q(t)$ . The MSD for three states on that line is shown in the full panel and described well by the approximation (5.42) substituted into Eq. (5.101). For states  $n = 1, 2, 3$ , one, three and six decades are covered with deviations less than 5%, so the approximation yields a description of similar accuracy as for the correlation functions in Fig. 6.4. The leading result from Eq. (5.37) describes the relaxation proportional to  $\ln t$  (dotted) which always has negative curvature in the double-logarithmic representation and does not provide a valid description for  $n = 1$  and 2. The reason for the qualitative difference between the solution for the MSD and the leading logarithmic law is that the corrections proportional to  $K_{\text{MSD}} = -1.708$  are so large that  $K_{\text{MSD}}B^2 + B_2$  is never close to



zero in the liquid regime except very close to the  $A_4$ -singularity, which is seen for  $n = 3$  in Fig. 6.7 where  $\ln t$  develops a straightened decay around the plateau.

The power law (5.106) provides a different formulation of a leading order approximation and is shown as straight line for  $n = 1, 2, 3$ . For  $n = 1$  this describes the MSD for more than a decade as indicated by the squares. For  $n = 2$  three decades are covered and six decades of power-law behavior are identified for curve  $n = 3$ . So the accuracy is similar to the one provided by the approximation in next-to-leading order by Eq. (5.42). Both asymptotic descriptions fall on top of each other around the plateau and therefore corroborate that the reformulation (5.105b) is justified. The interpretation of the behavior of the MSD is then much simpler when considering the power laws instead of the logarithms of time. The decreasing slope of the relaxation when approaching the  $A_4$ -singularity as in Fig. 6.7 is just the exponent  $b_1$  from Eq. (5.106b) which decreases as  $B$  with the square-root of the separation parameter  $\varepsilon_1$ , cf. Eq. (5.20). The same parameter  $B$  is the prefactor of the leading-order logarithmic decay in Eq. (5.37). In that sense Fig. 6.7 is the analog of Fig. 6.4.

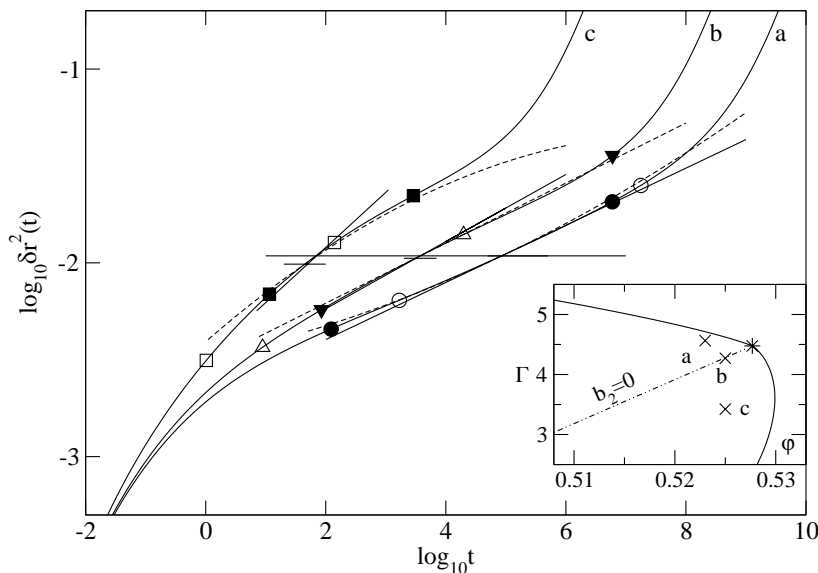


FIGURE 6.8. Concave and convex deviations from the power law (5.106) in the MSD. Solutions for the states a, b, and c are shown as full lines, the approximation (5.106) as straight full lines for exponents  $b_1 = 0.147, 0.173,$  and  $0.285,$  respectively. Open symbols denote the 5% deviation of the solutions from the leading-order power law. For state b, the dashed line exhibits the corrected power law with  $b'_1 = 0.155,$  Eq. (5.107), and the filled triangle the 5% deviations of the solution from it. Dashed lines show the approximation by Eq. (5.105b) for a and c with  $b_2 = 0.00363$  and  $-0.00735,$  respectively, and  $b'_1 = 0.143$  and  $0.214.$  The filled symbols mark the 5% deviations. The inset replots the one from Fig. 6.7 and shows the state points a, b, and c.

Since the term  $b_2$  in Eq. (5.105b) varies regularly in the separation parameters  $\varepsilon_1$  and  $\varepsilon_2$ , the sign of  $b_2$  is positive above the line  $b_2 = 0$  and negative below. Therefore, similar to the case for the correlators in the linear-log representation, in the double-logarithmic representation, the behavior of the MSD can be changed from convex to concave when crossing the line where the respective quadratic correction  $b_2$  vanishes. For the  $A_4$ -singularity the change in curvature is demonstrated for three states in Fig. 6.8. State b is identical to the state  $n = 2$  in Fig. 6.7 and obeys  $b_2 = 0$ . The power law  $(t/\tau)^{b_1}$  is shown as straight full line. The time scale  $\tau$  is matched at the plateau  $6r_s^{*2}$ . Moving to state c below the chain line,  $(\Gamma, \varphi) = (3.42, 0.525)$ , a relaxation is obtained which clearly exhibits negative curvature and is consistent with the calculated value  $b_2 = -0.00735$ . The leading-order power law with exponent  $b_1 = 0.285$  fulfills a 5%-deviation criterion for two decades which accidentally extends to short times as the approximation crosses the solution twice. Reducing the allowed deviation to 4% would reduce that interval to less than a decade. If we include the term proportional to  $b_2$  from Eq. (5.105b) and renormalize the exponent to  $b'_1$ , Eq. (5.107), the approximation agrees with the solution for three decades. It is obvious from a comparison with curve 1 in Fig. 6.7, that the leading-order power law describes that solution better than it describes the solution at state c in Fig. 6.8 for comparable values for  $\tau$  and the plateau correction. The deviation to convex behavior is demonstrated by the dashed line to curve a,  $(\Gamma, \varphi) = (4.57, 0.523)$ . Again the range of validity is extended to earlier times but for later times no improvement can be found.

In Fig. 6.7 the dashed line, which describes the next-to-leading order approximation of Eq. (5.42), deviates from the leading order power law (5.106a) below the plateau where the range of validity for the power law extends to much smaller times than justified by its derivation. We also recognize that the exponent  $b_1$  overestimates the slope of the relaxation in Figs. 6.7 and 6.8. In Eq. (5.106b) only the term  $B$  from the leading order approximation is present. Taking into account the renormalization of this prefactor to  $B - B_1$  in Eq. (5.107) changes the exponent for state b from  $b_1 = 0.173$  to  $b'_1 = 0.155$ . By comparing the full line for the leading result and the dashed line for the corrected one in Fig. 6.8 we find that the range of applicability is shifted to later times by one decade and extended by two decades. The corrected power law is valid from  $10^2$  to  $5 \cdot 10^6$  and comparison to Fig. 6.7 shows that approximation (5.42) covers a similar range. The accidental extension to shorter times is removed. The approximation now covers the range also a naive power-law fit would yield.

In summary, we can interpret Fig. 6.8 as the analog of Fig. 6.6. Some quadratic correction to a leading-order linear behavior can be set to zero on a surface in control-parameter space. Departing from that surface in opposite directions introduces either positive or negative corrections and the linear behavior is changed to convex or concave.

### 3. Logarithmic decay at an $A_3$ -singularity

For the discussion of the logarithmic decay laws at the  $A_3$ -singularity the  $q$ -dependent amplitudes are shown in Fig. 6.9. No qualitative changes are obvious from a comparison of Fig. 6.9 with Fig. 6.2 for the  $A_4$ . The smaller length scale  $\delta = 0.03$  introduces a smaller localization length that is reflected in the broader distributions in wave vector space. So the trend seen when changing from the HSS

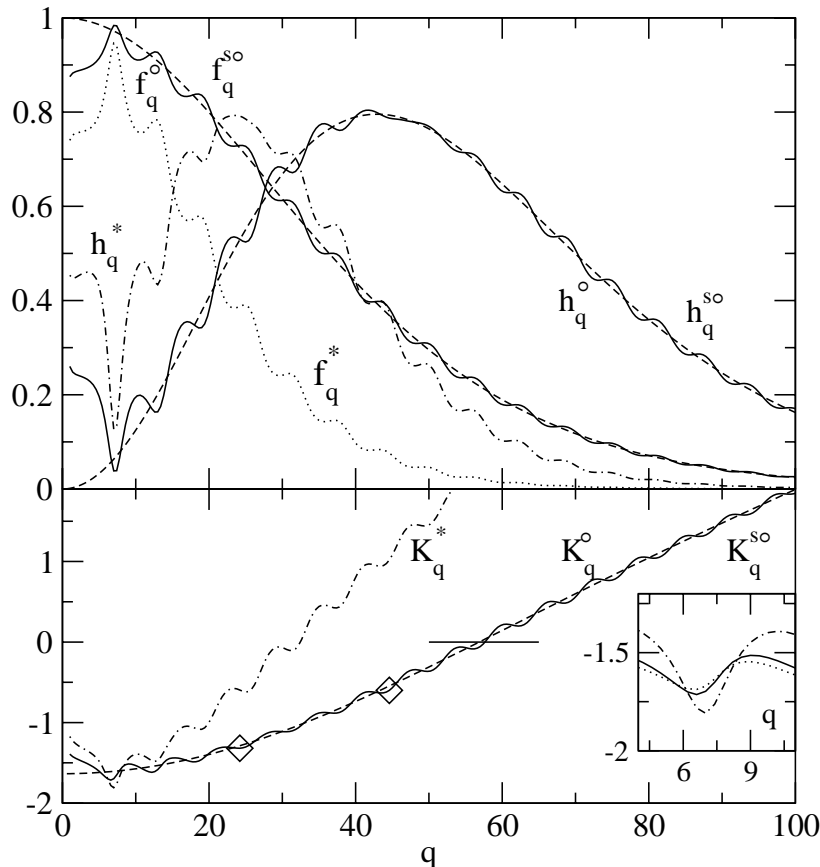


FIGURE 6.9. Glass-form factors and wave-vector dependent amplitudes at the  $A_3$ -singularity for  $\delta = 0.03$ . Line styles are the same as in Fig. 6.2. The values at the  $A_4$ -singularity,  $f_q^*$ ,  $h_q^*$ , and  $K_q^*$ , are shown for comparison. At  $q \approx 57.5$  a short line indicates where  $K_q^o = 0$ . The values for  $q = 24.2$  and  $45.0$  are marked by diamonds. The inset shows  $K_q$  for  $4 < q < 11$  for  $\delta = \delta^*$  (chain line),  $0.03$  (full line) and  $0.02$  (dotted line).

to the  $A_4$  of the SWS is continued when approaching  $A_3$ -singularities at smaller  $\delta$ . There are only two notable exceptions at smaller  $q$ . First, the value for  $K_q$  at the position of the structure factor peak is minimal for the  $A_4$ ,  $-1.81 = K_q^* < K_q^o = -1.72$ . The inset shows this region enlarged for  $\delta = \delta^*$ ,  $0.03$  and  $0.02$ , demonstrating that  $K_q$  at the peak is again larger for the  $A_3$ -singularity with smaller well width  $0.02$ , where  $K_q = -1.69$ . Second, the zero-wave-vector limit of  $K_q^s$  is also smallest at the  $A_4$ -singularity. The respective values for  $\delta = \delta^*$ ,  $0.03$  and  $0.02$  are  $-1.71$ ,  $-1.64$ , and  $-1.62$ . Therefore, one experiences the strongest  $q$ -dependent corrections at the  $A_4$ -singularity.

Figure 6.10 shows the analog of Fig. 6.3 for a cut through the glass-transition diagram at  $\delta = 0.03$ . The lines  $\varepsilon_1 = 0$  and  $\varepsilon_2 = 0$  for the  $A_3$ -singularity are obtained from a smooth transformation from the corresponding lines at the  $A_4$ -singularity

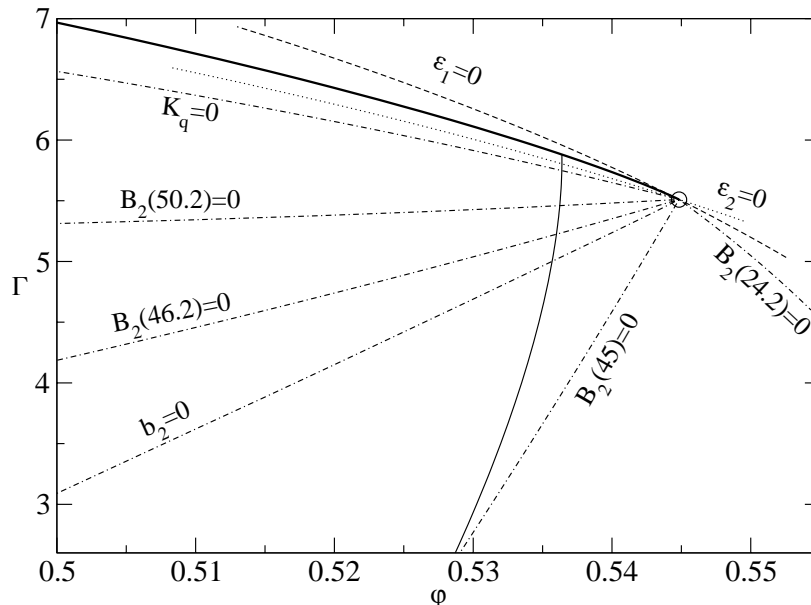


FIGURE 6.10. Lines of vanishing quadratic correction for the  $A_3$ -singularity ( $\circ$ ) at  $\delta = 0.03$ . The  $\delta = 0.03$  cut through the glass-transition diagram is displayed by full lines. The lines of vanishing separation parameters and quadratic corrections,  $B_2(q) = 0$ , are shown in the same style as in Fig. 6.3 and labeled accordingly. The line  $b_2 = 0$  indicates the analogous line for the MSD, cf. inset of Fig. 6.7.

and appear in similar locations in the diagram. The line  $\varepsilon_2 = 0$  is again very close to the line of gel transitions. Just below, we find again the line where  $B_2(q) = 0$  when  $K_q = 0$ . However, this now represents  $q \approx 57.5$ , cf. Fig. 6.9, which is a value almost twice as large as for the corresponding line in Fig. 6.3. For the wave vector  $q = 24.2$  we find the line where  $B_2(24.2) = 0$  completely in the glass state. Taking the same value for the correction amplitude as at  $q = 24.2$  at the  $A_4$ ,  $K_q^* \approx -0.6$ , instead of  $q$  we obtain  $q = 45.0$  in Fig. 6.9 and the line labeled accordingly in Fig. 6.10. Since the latter line comes close to the liquid-glass-transition line we take that as a reference and estimate the range of wave-vectors where the quadratic corrections can be put to zero in the liquid regime to  $45 \lesssim q \lesssim 58$ . The lines where  $B_2(q) = 0$  can be rather sensitive to  $q$ -variation. This is demonstrated by the curve  $B_2(46.2) = 0$ . Although the change in the wave vector is small, the values for  $K_q$  differ by more than 20% and induce a rotation of the line  $B_2(q) = 0$  by quite a significant angle in Fig. 6.10.

Having in mind the drastic changes in the lines where  $B_2(q) = 0$  for a given wave vector  $q$  it may come with some surprise that the line for the MSD, where  $b_2 = 0$ , stays rather robust in the accessible liquid regime as seen in Fig. 6.10 from the line labeled MSD. The variation in  $q$  for the amplitudes is reflected in changes of the localization lengths. For the  $A_3$ -singularity at  $\delta = 0.03$  we get

$$(6.2) \quad r_s^\circ = 0.0243, \quad h_{\text{MSD}}^\circ = 0.00136.$$

From Eq. (6.1) one gets  $r_s^*/r_s^\circ = 1.75$  and the square of the latter ratio,  $r_s^{*2}/r_s^{\circ 2} \approx 3$ , is the same as  $h_{\text{MSD}}^*/h_{\text{MSD}}^\circ$ . Since only the fraction  $h_{\text{MSD}}/r_s^2$  could introduce larger modifications in Eq. (5.105b), the changes in  $b_2$  cancel approximately and the line specified by  $b_2 = 0$  experiences only minor deformations when  $\delta$  is varied.

In summary one finds for the case of an  $A_3$ -singularity the same scenarios for the correlators and the MSD as presented in Sec. 1 for the  $A_4$ -singularity. There arise more complex scenarios near an  $A_3$ -singularity because of the crossing of lines in the vicinity which shall be considered in the next chapter.

#### 4. Critical decay at higher-order singularities

We now turn to the critical decay at the higher-order singularities in the SWS which is described by the expansions in Ch. 5 Secs. 3 and 4. Recalling the discussion for the  $F_{13}$ -model in connection with Fig. 5.4 we expect that a good and consistent approximation might not be achieved for the decay at shorter times. We start with the discussion for the  $A_3$ -singularity at  $\delta = 0.03$ .

**4.1. Critical decay at the  $A_3$ -singularity.** For the discussion of the critical decay, the solution is calculated at the  $A_3$ -singularity specified by  $(\varphi^\circ, \Gamma^\circ, \delta^\circ) = (0.5448, 5.509, 0.03)$  and shall be denoted by  $\phi_q^\circ(t)$ . It will be convenient to use the rescaled correlators given by  $\hat{\phi}_q^\circ(t) = (\phi_q^\circ(t) - f_q^\circ)/h_q^\circ$ . For the evaluation of the approximation (5.76) we need the correction amplitudes  $K_q^\circ$  which are shown in Fig. 6.9 and the parameters characteristic for the  $A_3$ -singularity under discussion,

$$(6.3) \quad \mu_3 = 0.109, \quad \kappa = 0.314, \quad \mu_4 = 0.204.$$

The  $q$ -dependent asymptotic approximation for the critical decay at the  $A_3$ -singularity for  $\delta = 0.03$  in the SWS after substituting all parameters into Eq. (5.76) reads

$$(6.4) \quad \begin{aligned} \hat{\phi}_q^\circ(t) = & 60.4/x^2 + 264.7 \ln x/x^3 \\ & + [3374.9 - 580.2 \ln x + 870.4 \ln^2 x]/x^4 \\ & + [-11745.7 - 27952.1 \ln x - 4452.2 \ln^2 x + 2544.1 \ln^3 x]/x^5 \\ & + K_q^\circ \{3643.9/x^4 + 31953.7 \ln x/x^5\} + \mathcal{O}(x^{-6}), \quad x = \ln(t/t_0). \end{aligned}$$

The first line in Eq. (6.4) represents  $g_2(x)$  and  $g_3(x)$ , Eqs. (5.54) and (5.59). The second and third line exhibit the contribution up to order  $\mathcal{O}(x^{-6})$ ,  $g_4(x)$  and  $g_5(x)$ , which are independent of the wave vector. The  $q$ -dependent correction terms up to order  $\mathcal{O}(x^{-6})$  are given by the prefactor  $K_q^\circ$  and the terms in the curly brackets, which are positive for  $t/t_0 > 2.5$  and monotonic decreasing for  $t/t_0 > 3.1$ .

Figure 6.11 shows the critical decay  $\hat{\phi}_q^\circ(t)$  for correlators having different correction amplitudes  $K_q^\circ$ . At the peak of the structure factor,  $q = 7$ , the amplitude is negative, for  $q = 57.4$  the correction amplitude is close to zero, and for the highest wave vector  $q = 172.2$  the amplitude is positive. The respective rescaled correlation functions  $\hat{\phi}_q^\circ(t)$  (full lines) deviate strongly from each other in the window of time presented, showing that the factorization property is violated. The leading contribution to this violation comes from the terms in curly brackets in Eq. (6.4). If the deviations among the correlation functions for different wave vectors cannot be assigned to the  $q$ -dependent corrections in Eq. (6.4) within an accessible window in time, we cannot expect that Eq. (6.4) will be sufficient to describe the critical

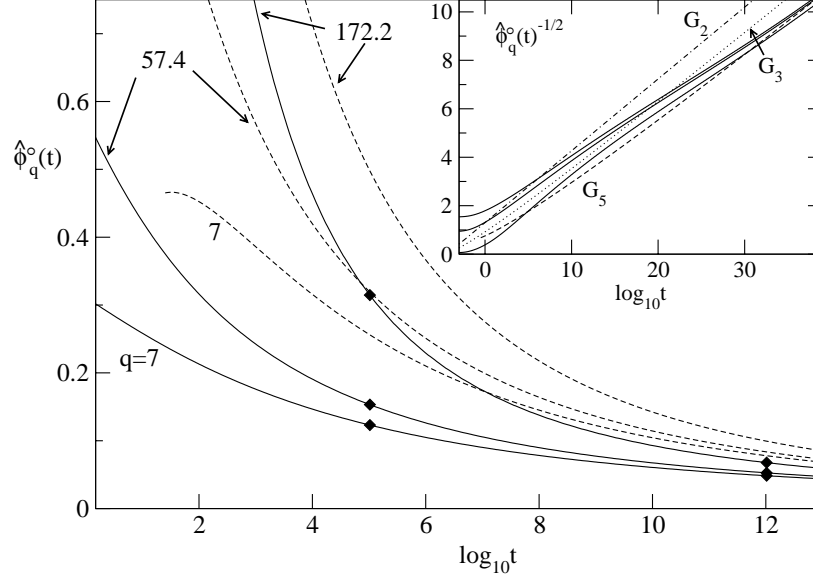


FIGURE 6.11. Critical decay at the  $A_3$ -singularity of the SWS for  $\delta = 0.03$ . Full lines show the rescaled correlation functions at  $\mathbf{V}^\circ$ ,  $\hat{\phi}_q^\circ(t) = (\phi_q^\circ(t) - f_q^\circ)/h_q^\circ$ , for the wave-vector values  $q = 7, 57.4$ , and  $172.2$  as indicated. The dashed lines exhibit the asymptotic approximation of Eq. (6.4) with a time scale  $t_0 = 4 \cdot 10^{-5}$  matched in the interval  $t = 10^{40} \dots 10^{45}$ . For  $q = 7.0, 57.4$ , and  $q = 172.2$ , the correction amplitudes are  $K_q^\circ = -1.704, -0.00224$ , and  $4.814$ , respectively. The filled diamonds for  $t = 10^5$  and  $t = 10^{12}$  mark the values for  $\hat{\phi}_q^\circ(t)$  for the three  $q$ -values. The inset shows  $\hat{\phi}_q^\circ(t)^{-1/2}$  for the  $q$ -values above from top to bottom and the  $q$ -independent approximations defined in Eq. (5.64) in the same representation,  $G_2(t/t_0)^{-1/2}$ ,  $G_3(t/t_0)^{-1/2}$  and  $G_5(t/t_0)^{-1/2}$ , respectively.

decay. For this reason we look at the correlators themselves before trying to match any approximation to the solution.

Suppose the critical correlators  $\hat{\phi}_q^\circ(t)$  for different wave vectors are approximated by Eq. (6.4). Then for arbitrarily chosen wave vectors  $q_1$  and  $q_2$  the difference  $\hat{\Delta}[q_1, q_2](t) = \hat{\phi}_{q_1}^\circ(t) - \hat{\phi}_{q_2}^\circ(t)$  is given in leading order by the difference in the correction amplitudes,  $K_{q_1}^\circ - K_{q_2}^\circ$ , and the terms in the curly brackets in Eq. (6.4). From Fig. 6.11 we infer that  $\hat{\Delta}[q_1, q_2](t)$  is not yet close to zero to neglect the terms in the curly brackets in Eq. (6.4). The values of  $\hat{\phi}_q^\circ(t)$  for the three chosen  $q$ -values are marked by diamonds in Fig. 6.11 for  $t = 10^5$  and  $10^{12}$  and show large deviations. We get  $\hat{\Delta}[7, 57.4](10^5) = -0.030$  and  $\hat{\Delta}[172.2, 57.4](10^5) = 0.161$ . These differences are large but however reflect the ordering in the values for  $K_q^\circ$  which increase with  $q$ . From that we conclude that the treatment of the  $q$ -dependence in Eq. (6.4) is qualitatively correct. If the correlators  $\hat{\phi}_q^\circ(t)$  for different  $q$  would intersect, higher  $q$ -dependent corrections were relevant for the given window in time

since the subtraction inherent to  $\hat{\Delta}[q_1, q_2](t)$  also cancels higher order corrections that are independent of  $q$ .

Having established the qualitative consistency we proceed to check the quantitative agreement. If the time dependence of  $\hat{\Delta}[q_1, q_2](t)$  were given exclusively by the terms in curly brackets in Eq. (6.4), then the differences among the  $K_q^\circ$  would explain the amplitudes of the decay in  $\hat{\Delta}[q_1, q_2](t)$ . To quantify deviations from that case we introduce the ratio  $\nu[q_1, q_2, q_3](t) = \hat{\Delta}[q_1, q_2](t)/\hat{\Delta}[q_2, q_3](t)$ . For  $t \rightarrow \infty$  this ratio goes to  $\nu_\infty = (K_{q_1}^\circ - K_{q_2}^\circ)/(K_{q_2}^\circ - K_{q_3}^\circ)$ . Deviations from  $\nu_\infty$  hence indicate that higher-order  $q$ -dependent corrections are present in addition to the terms in Eq. (6.4). For the  $q$ -values used in Fig. 6.11 we get  $\nu_\infty = (K_7^\circ - K_{57.4}^\circ)/(K_{57.4}^\circ - K_{172.2}^\circ) = 0.354$ . Since  $K_{57.4}^\circ \approx 0$ , this ratio is almost equivalent to  $-K_7^\circ/K_{172.2}^\circ$ . The ratio at time  $t = 10^5$  is  $\nu[7, 57.4, 172.2](10^5) = 0.187$  and therefore deviates by 90% from  $\nu_\infty$ . Hence, we cannot expect Eq. (6.4) to describe the critical decay in Fig. 6.11 at that time as additional  $q$ -dependent corrections are still large there.

At  $t = 10^{12}$  the ratio has decayed to  $\nu[7, 57.4, 172.2](10^{12}) = 0.280$  which is close to  $\nu_\infty$  within 20%. Here, the  $q$ -dependent corrections are also in reasonable quantitative agreement with the approximation in Eq. (6.4). To determine  $t_0$ , we go again to large times. The inset of Fig. 6.11 displays the rescaled correlators as  $\hat{\phi}_q^\circ(t)^{-1/2}$ . In this representation the leading term  $g_2(x)$  in Eq. (6.11) yields a straight line. We see that for large times the correlators for different  $q$  indeed come closer together and the ratio at  $t = 10^{40}$  is  $\nu[7, 57.4, 172.2](10^{40}) = 0.341$  which is 1% from  $\nu_\infty$ . For the determination of  $t_0$  we use Eq. (6.11) for  $q = 7, 57.4$ , and  $172.2$  and match the asymptotic approximation to the numerical solutions in the interval from  $t = 10^{40}$  to  $t = 10^{45}$ . This results in a value  $t_0 = 4 \cdot 10^{-5}$ . For times larger than  $t \approx 10^{50}$  the numerical solution does no longer follow the approximation. In that region inaccuracies in the control-parameter values lead to deviations from the asymptotic behavior. These inaccuracies prevent us also from fixing more than just one digit of  $t_0$ . This is well known from the  $A_2$ -singularities, e.g. in the HSS, where the control parameter  $\varphi$  has to be calculated up to ten digits to fix  $t_0$  up to three digits. The dashed line in the inset labeled  $G_5$  shows the result for neglecting the last line of Eq. (6.11). Within the error margin this also describes the correlator for  $q = 57.4$  where  $K_q$  is close to zero. Taking into account only the first line of Eq. (6.11) but staying at the value for  $t_0$  yields the dotted curve labeled  $G_3$  which is clearly inferior but captures the slope of the solution still better than  $G_2$ .

In the full panel of Fig. 6.11 we can compare the critical correlators with the approximation (dashed) by Eq. (6.11). We observe that the asymptotic expression in Eq. (6.11) describes the critical correlators at the  $A_3$ -singularity of the SWS quantitatively but only at large times. For smaller times comparable to experimental windows the description is still reasonable qualitatively. Especially the leading  $q$ -dependent corrections describe the variations seen in the correlators correctly down to relatively short times.

The accuracy of the approximation that was obtained in the schematic models, cf. Figs. 5.9 and 5.4, is far better than seen in Fig. 6.11 for the SWS. This difference is mainly due to different values of the parameter  $\mu_3$  that characterizes the various  $A_3$ -singularities. For the two-component model we had  $\mu_3 = 0.77$  and for the one-component model there was  $\mu_3 = 1/3$ . Moreover, in Fig. 5.4 additional terms of the expansion for one-component systems could be applied. The value of  $\mu_3 = 0.109$

for the SWS implies large correction terms in Eq. (6.11) and in additional terms that are not included in Eq. (6.11).

**4.2. Critical decay at the  $A_4$ -singularity.** For the application of Eq. (5.86) we need the parameters characterizing the  $A_4$ -singularity,

$$(6.5) \quad \mu_4 = 0.131, \quad \kappa = 0.243, \quad \mu_5 = 1.21.$$

The rather small value of  $\mu_4$  signals that in the SWS the  $A_4$ -singularity is already close to the yet again higher-order singularity  $A_5$ , the *butterfly*, where  $\mu_4$  vanishes. This generates particularly large coefficients in the expansion of the critical decay in Eq. (5.81) where  $\mu_4$  appears in the denominators. This is quite the same as for the  $A_3$ -singularities that are close to the  $A_4$ -singularity taking the distance of  $\mu_3$  from zero as measure, cf. Fig. 6.1.

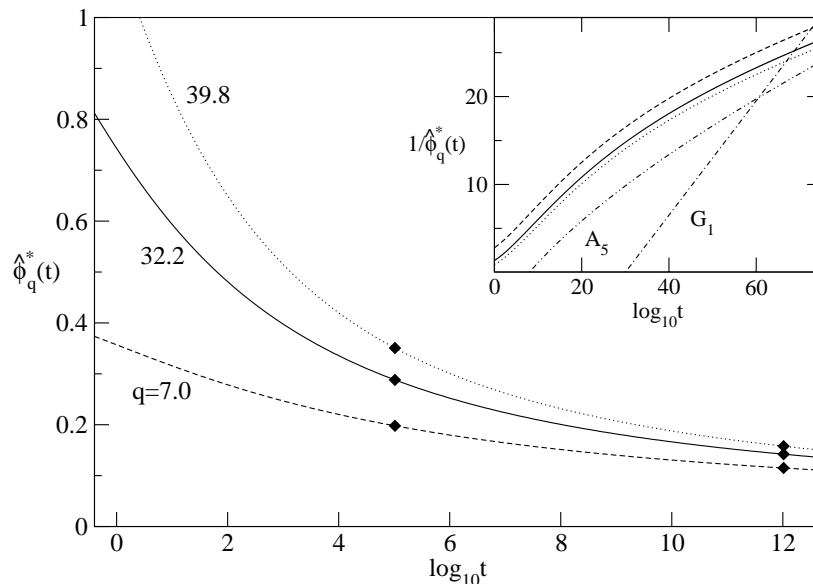


FIGURE 6.12. Critical decay at the  $A_4$ -singularity of the SWS for  $q = 7.0$  (dashed), 32.2 (full line), 39.8 (dotted). The correction amplitudes are  $K_q = -1.81, -0.04, \text{ and } 0.77$ , respectively. The filled diamonds mark the values at  $t = 10^5$  and  $t = 10^{12}$  where the ratios  $\nu(t)$  are 1.44 and 1.72, respectively (see text). The inset replots the curves from the full panel in the same linestyle and shows the first term of Eq. (6.6) labeled  $G_1$  and the law  $\ln(t/\tau)^{-2/3}$  labeled  $A_5$ , both with an arbitrary time scale.

The asymptotic approximation for the critical decay at the  $A_4$ -singularity in the SWS after inserting all parameters into Eq. (5.86) yields a particular simple formula for the rescaled correlators  $\hat{\phi}_q^*(t) = (\phi_q^*(t) - f_q^*)/h_q^*(t)$ ,

$$(6.6) \quad \hat{\phi}_q^*(t) = 3.54/x - 50.7 \ln x/x^2 + 12.5 K_q^*/x^2 + \mathcal{O}(x^{-3}), \quad x = \ln(t/t_0).$$



The above expression has yet again only a single source for the violation of the factorization property – the correction amplitude  $K_q$ . This motivates an analysis of the critical correlator  $\hat{\phi}_q^*(t)$  for different wave vectors as done before for the  $A_3$ -singularity. We chose again values for  $q$  where  $K_q^*$  is negative, almost zero and positive. Figure 6.12 demonstrates that again the factorization is violated. Comparing the solutions  $\hat{\phi}_q^*(t)$  for  $t = 10^5$  we find a ratio defined as in the previous section of  $\nu[7, 32.2, 39.8](10^5) = 1.439$  which is more than 30% off the ratio for the correction amplitudes  $\nu_\infty = 2.185$ . At  $t = 10^{12}$  we find  $\nu[7, 32.2, 39.8](10^{12}) = 1.723$  which achieves 20% accuracy. So the critical decay at the  $A_4$ -singularity shown in Fig. 6.12 is in qualitative accord with Eq. (6.6) with respect to the variation in  $q$ . However, due to the small value of  $\mu_4$ , the differences among the correlators for different  $q$  do not decay fast enough to allow for a consistent determination of  $t_0$  for the maximum value in time that could be reached, numerically we find  $\nu[7, 32.2, 39.8](10^{128}) = 2.076$  which is still 5% off from  $\nu_\infty$ , and  $\hat{\phi}_q^*(t)$  itself deviates from zero by 5%. This illustrates drastically how slow the critical decay at the  $A_4$ -singularity is.

The inset of Fig. 6.12 demonstrates that the critical decay  $\hat{\phi}_q^*(t)$  in the entire window in time is qualitatively different from the leading order  $1/\ln t$ -law. For the  $A_3$ -singularity in Fig. 6.11 it was still possible to argue that curve  $G_2$  is in accord with the decay qualitatively at least for large times and attribute deviations for shorter times to the proximity of the  $A_4$ -singularity. In Fig. 6.12 the leading order shown as  $G_1$  with an arbitrary time scale  $t_0$  does not allow for such an interpretation. The curves  $1/\hat{\phi}_q^*(t)$  have a slope smaller than  $1/G_1$  over the complete window in time and imply a slower decay than given by the leading order in Eq. (6.6). To make plausible that the proximity to an  $A_5$ -singularity with a critical decay law  $\ln(t)^{-2/3}$  [41] induces that behavior, we plot the law  $\ln(t)^{2/3}$  in the inset as chain line labeled  $A_5$  and observe at least some qualitative similarity. So the failure of the critical law at the  $A_4$ -singularity in the SWS is explained by the low value of  $\mu_4$ . If  $\mu_4$  is larger as in the two-component model, Eq. (5.86) offers a valid description of the critical decay, cf. Fig. 5.13.

To check if the value for  $\mu_4$  in Eq. (6.5) is exceptionally small for the SWS, the calculation was repeated for the HCY. We find the even smaller value  $\mu_4 = 0.080$  and conclude that the shape of the potentials discussed in Ch. 4 does not change the character of the  $A_4$ -singularity found for the SWS.



## Line crossing in the SWS

In the previous chapter the dynamics at and close to the  $A_3$ - and  $A_4$ -singularities in the SWS was analyzed. These higher-order singularities do not occur isolated but are accompanied by lines of nearby  $A_2$ -singularities we identified with transitions to a glass state, transitions to a gel state and glass-glass transitions between glass and gel. How the interplay of the various singularities rules the dynamics at the line crossing near an  $A_3$ -singularity shall be analyzed in the following. Since the wave-vector dependence was already discussed extensively, we restrict ourselves to the MSD in Sec. 1. The discussion of the crossing at  $\delta = 0.03$  is partly motivated by a recent MD simulation [93] where a subdiffusive power law in the MSD was reported. It was shown in Ch. 6 that power-law behavior in the MSD is an implication of the logarithmic decay at the higher-order singularities. It is shown that effective power laws can result from a crossover from  $A_3$ - to  $A_2$ -dynamics.

In Sec. 2, a crossing scenario containing an effective logarithmic decay predicted for the correlation function at small wave vectors in Ref. [16] is reconsidered and explained in terms of asymptotic expansions. Similar scenarios have been reported in photon-correlation spectroscopy in micellar systems [42, 43], in light scattering from a colloidal systems with attraction [30] and also in MD simulation [93].

### 1. MSD at a crossing

When considering multiple glass-transition singularities on a cut through the glass-transition diagram as shown for Fig. 7.1, the distance to the liquid-glass transition is no longer unique but depends on the choice of a specific point on the liquid-glass transition line. The relative size of the diffusivity  $D^s$  compared to the short-time diffusion coefficient  $D_0^s$  can be used instead to characterize the distance of a chosen state to the liquid-glass-transition line. The dashed lines in Fig. 7.1 show lines for constant  $D_0^s/D^s$  with  $D^s$  defined in Eq. (2.14). These lines are plotted for the cut  $\delta = 0.03$  from Fig. 4.1 using the MSA for the evaluation of the structure factor. The lines can be interpreted as precursors of the liquid-glass-transition line and display the reentry phenomenon.

Three paths are marked in Fig. 7.1 for the discussion of the dynamics. The first path for  $\Gamma = 1.67$  is relatively far from the crossing point, the path for  $\Gamma = 5.50$  is close to but below the crossing point and close to the  $A_3$ -singularity, and the third path is connected to a gel transition beyond the crossing point. All paths end at an  $A_2$ -singularity given by the respective  $\Gamma$ , and the changes in the MSD when approaching the different liquid-glass-transition points shall be analyzed using the asymptotic laws for the  $A_2$ -singularity.

The asymptotic laws for the critical relaxation at  $A_2$ -singularities from Eq. (5.103) are compared with the full MCT result in Fig. 7.2. For  $\Gamma = 1.67$  (panel A) the description is similar to that found for the HSS [60]. The exponent parameter

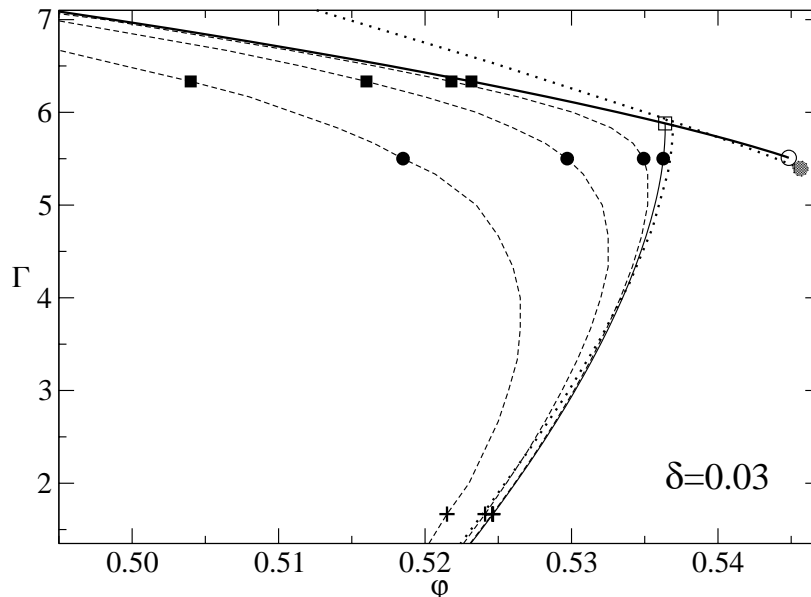


FIGURE 7.1. Glass-transition diagram for the SWS at  $\delta = 0.03$  together with isodiffusivity lines for  $D_0^s/D^s = 10^5, 10^7, 10^{10}$  based on the structure factor using MSA. Full curves show the glass-transition lines exhibiting an  $A_3$ -singularity ( $\circ$ ) and a crossing point ( $\square$ ). On the isodiffusivity lines (dashed), paths are marked for the dynamics discussed in Fig. 7.2 for  $\Gamma = 1.67$  ( $+$ ),  $5.50$  ( $\bullet$ ), and  $6.33$  ( $\blacksquare$ ). The dotted lines with the shaded circle as endpoint show the glass-transition singularities for  $\delta = 0.03$  based on the structure factor using PYA rescaled in  $\Gamma$  by a factor 5.88 to match the crossing point.

$\lambda^A = 0.750$  is still close to the one for the HSS,  $\lambda = 0.735$ . But the time scale  $t_0^A = 1.95$  differs considerably from the value  $t_0 = 0.425$  for the HSS. This is due to a slowing down of the dynamics for times where  $\delta r^2(t)$  is smaller than  $r_s^{c_2}$  caused by the attractive forces on smaller length scale. The exponent for the critical relaxation is  $a = 0.305$ . The point where correction and numerical solution deviate by 20% of the critical plateau value  $6 r_s^{c_2}$  is marked by a square at  $t \approx 18 \approx 9 t_0$ .

Panel B shows the scenario for an approach to an  $A_2$ -singularity on the path closer to the  $A_3$ -singularity. The exponent parameter is increased to  $\lambda^B = 0.857$  corresponding to a decrease of the critical exponent to  $a = 0.243$ . The increasing importance of the attraction is seen in a decrease of the critical localization length representing the plateaus for the MSD (labeled by  $+$  in panel A) from  $6 r_s^{c_2} = 0.0318$  to  $6 r_s^{c_2} = 0.0245$  (marked by  $\bullet$  in panel B). However, the major new phenomenon is the drastic increase of the time scale  $t_0$  to  $t_0^B = 4 \cdot 10^3$ . The critical decay for the  $A_2$ -singularity sets in only for times around  $10^6$  as indicated by the square in Fig. 7.2 B. There is an additional relaxation process outside the transient ruling the dynamics within the window  $0 \leq \log_1 0(t) \leq 4.5$ . The critical localization length of the nearby gel transition causes a plateau around  $\delta r^2 \approx 10^{-3}$  so the anomalous decay process is not the one related to the gel transition. Rather, it

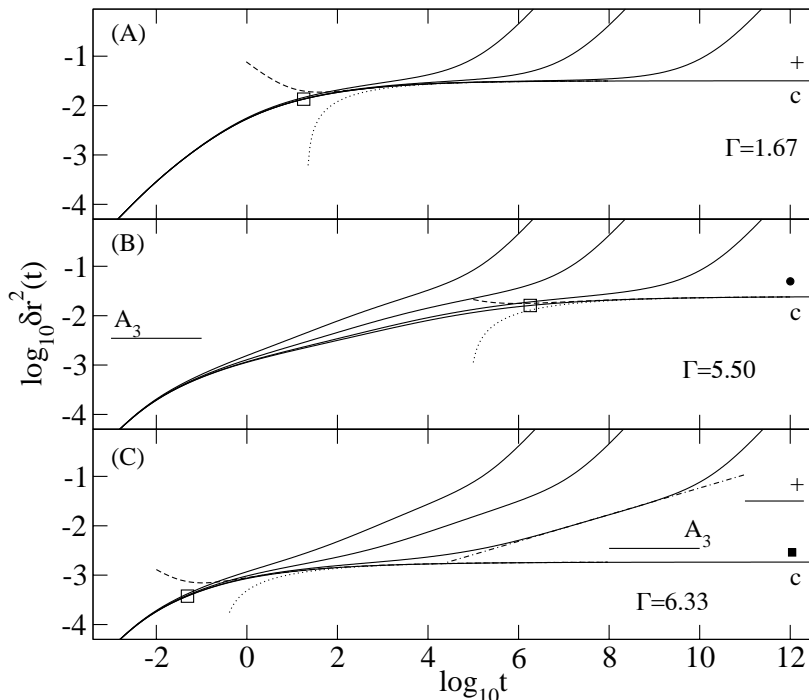


FIGURE 7.2. MSD for the SWS at the crossing. Full curves are the results for states on the isodiffusivity lines for  $D_0^s/D^s = 10^5, 10^7, 10^{10}$  marked in Fig. 7.1. The curves with label  $c$  refer to the transition points for the value of  $\Gamma$  indicated. Respective values for the plateaus  $6r_s^{c^2}$  are marked by the symbols  $+$ ,  $\bullet$  and  $\blacksquare$  introduced in Fig. 7.1. The plateau is also shown as horizontal line for the  $A_3$ -singularity for the lower two panels. Dotted curves show the leading solution to the critical law,  $(t_0/t)^a$ , dashed curves the next-to-leading order for the  $A_2$ -singularities, Eq. (5.103). Open squares ( $\square$ ) denote the time where the solution deviates by 20% from the asymptotic result in Eq. (5.103). An effective power law for exponent  $x = 0.27$  appearing at  $\Gamma = 6.63$  is shown by the dash-dotted line (see text).

is the decay around the plateau of the close-by  $A_3$ -singularity as described in the previous chapter.

In panel C for  $\Gamma = 6.33$ , the gel plateau is approached with  $t_0 = 6 \cdot 10^{-3}$  and the critical relaxation for  $\lambda = 0.873$  and  $a = 0.232$  is described with similar accuracy as for  $\Gamma = 1.67$  in panel A, the deviation of 20% is at  $t = 0.048 = 8t_0$  and again indicated by a square. The comparably large value of  $\lambda$  causes the leading asymptotic approximation (dotted curve) to deviate further from the next-to-leading order result. The amplitude  $[K_{\text{MSD}} + \kappa(a)]$  in Eq. (5.103) is around  $-1$  in both A and C. In this sense one concludes that the critical dynamics for the gel transition is quite similar to the one observed for the glass transition.

The dynamics for the  $\delta r^2(t)$  exceeding the respective plateaus is quite different for the glass transition shown in panel A from the gel transition in panel C. If one, as usual, refers to the process with  $\delta r^2(t) > 6r_s^{c2}$  as an  $\alpha$ -process, in A the  $\alpha$ -process is similar to the one in the HSS. The crossing of the plateau is followed by a von Schweidler relaxation and a crossover to long-time diffusion [60]. A shift in time can condense the curves after the plateau on top of each other, a property known as  $\alpha$ -scaling. For the dynamics at the gel transition (C) the lower plateau (■) defines the onset of the  $\alpha$ -process. It is different in shape compared to A. The relaxation around the  $A_3$ -singularity plateau causes effective power-law behavior with  $x = 0.27$  as shown by the dash-dotted line. It is the same phenomenon as discussed above for panel B. On approaching the gel transition, this subdiffusive regime scales as part of the  $\alpha$ -process if one is so close to the gel transition that separations to the  $A_3$ -singularity and the  $A_2$ -glass-transition singularity are kept fixed.  $A_3$ -singularity and the glass-transition singularity determine only the shape of the  $\alpha$ -relaxation. If the distance between the two singularities is changed on the path taken, the form of the  $\alpha$ -process is also changed. In this case the  $A_3$ -singularity is manifested in a violation of the  $\alpha$ -scaling for the gel transition. If the separation from the  $A_3$ -singularity and the glass-transition singularity is sufficiently large, which is true for small  $\varphi$ , the dynamics is affected only by the gel plateau and directly crosses over from the von Schweidler relaxation at the gel plateau to the long-time diffusion. For this reason the exponent of the effective power law approaches unity.

Figure 7.3 shows the parameters for the asymptotic description via Eq. (5.103) along the liquid-glass-transition lines for  $\delta = 0.03$  with increasing  $\Gamma$ . The localization lengths  $r_s^c$  in panel A exhibit a jump at the crossing point  $\Gamma^\times$  reflecting the discontinuous change of both  $f_q$  and  $f_q^s$ . The values for the glass-glass transition are also shown down to the  $A_3$ -singularity at  $\Gamma^\circ$ . The critical amplitudes  $h_{\text{MSD}}$  follow the same trend as  $r_s^c$  signaling that a change in the localization length also sets the amplitude for the relaxation around  $r_s^c$ . Panel B shows the two quantities in the correction to the critical law.  $K_{\text{MSD}}$  shows only small deviations from the value in the HSS,  $K_{\text{MSD}}^{\text{HSS}} = -1.23$ . At the crossing on the glass  $K_{\text{MSD}} = -1.57$ , on the gel-line it reaches  $K_{\text{MSD}} = -1.31$  and at the  $A_3$ -singularity  $K_{\text{MSD}} = -1.64$ . Since away from crossing and higher-order singularities  $\kappa(a)$  is always close to zero, the correction to the critical law in Eq. (5.103) is dominated by the amplitude  $K_{\text{MSD}}$  which is negative and of order unity there. For this reason including the correction to the critical law in Fig. 7.2 increases the range of applicability considerably in comparison to the leading approximation. At higher-order singularities,  $\lambda \rightarrow 1$ , and  $\kappa(a)$  diverges which is responsible for the increase of the corrections at the crossing. These corrections change sign when  $\kappa(a)$  starts to increase. For the present case of  $\delta = 0.03$ , this happens only on the glass-glass-transition line between  $\Gamma^\circ$  and  $\Gamma^\times$ .

Panel C of Fig. 7.3 points out the difference in the time scale  $t_0$  when coming from small  $\Gamma$  in the HSS limit or from high  $\Gamma$ , respectively. In the first case  $t_0$  for the critical law at the glass-transition plateau is increasing and eventually diverging when the gel transition at the crossing is approached. This is because the glassy dynamics of the gel transition determines  $t_0$ . For  $\Gamma > \Gamma^\circ$ ,  $t_0$  is orders of magnitude smaller than in the HSS since the relevant localization for the gel is encountered much earlier in time. On this line of transitions  $t_0$  is regular at the crossing but

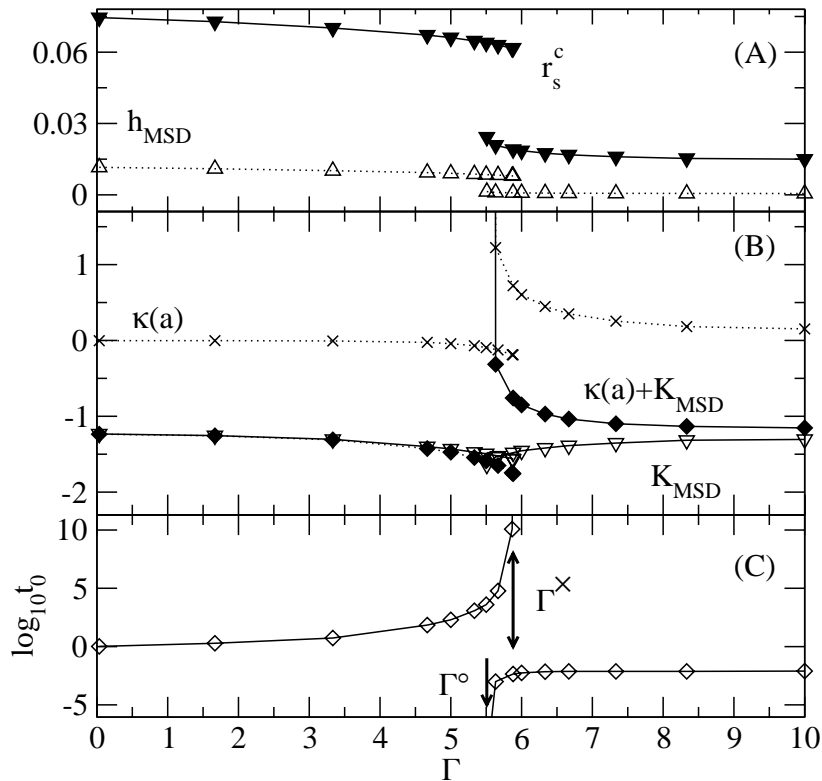


FIGURE 7.3. Parameters for the critical decay at  $A_2$ -singularities according to Eq. (5.103);  $r_s^c$  ( $\blacktriangledown$ ) and  $h_{\text{MSD}}$  ( $\triangle$ ) in panel A;  $\kappa(a)$  ( $\times$ ) from Eq. (5.94),  $K_{\text{MSD}}$  ( $\nabla$ ), and  $\kappa(a) + K_{\text{MSD}}$  ( $\blacklozenge$ ) in panel B; and  $t_0$  ( $\diamond$ ) in the panel C. The arrow labeled  $\Gamma^\circ$  marks the value for the  $A_3$ -singularity,  $\Gamma^\times$  the crossing point. Full and dotted lines are guides to the eye to join points on different parts of the glass-transition line for  $0 \leq \Gamma \leq \Gamma^\times$  and the gel-transition line for  $\Gamma^\circ \leq \Gamma$ , respectively.

diverges at the  $A_3$ -singularity. This indicates that power laws are an inadequate description of the critical relaxation at a higher-order singularity.

Figure 7.4 displays the parameters quantifying the influence from the  $A_3$ -singularity and the von Schweidler relaxation in Eq. (5.104). Panel A refers to states on the isodiffusivity line  $D_0^s/D^s = 10^{10}$  in Fig. 7.1. The isodiffusivity lines bend away from the crossing and this translates into the separation parameters  $|\sigma|$  being maximal there. On the same curve, the separation from the  $A_3$ -singularity  $|\varepsilon_1|$  has a minimum at the crossing. This also shows that distance in control-parameter space as seen in Fig. 7.1 need not reflect the relevant separation parameters of the singularity. The distances of the liquid-glass-transition point for  $\Gamma = 5.50$  from the  $A_3$  are  $(\Delta\phi, \Delta\Gamma) = (0.085, 0.01)$  while for the crossing point  $(\Delta\phi, \Delta\Gamma) = (0.084, -0.37)$ . The separations, however, are  $\varepsilon_1 = -0.028$  and  $-0.015$ , respectively. Panel B of Fig. 7.4 displays the correction amplitudes in Eq. (5.104).  $K_{\text{MSD}}$  is the same as in Fig. 7.3 and  $\kappa(-b)$  shows similar behavior as  $\kappa(a)$  in Fig. 7.3. However, as  $\kappa(-b)$  is

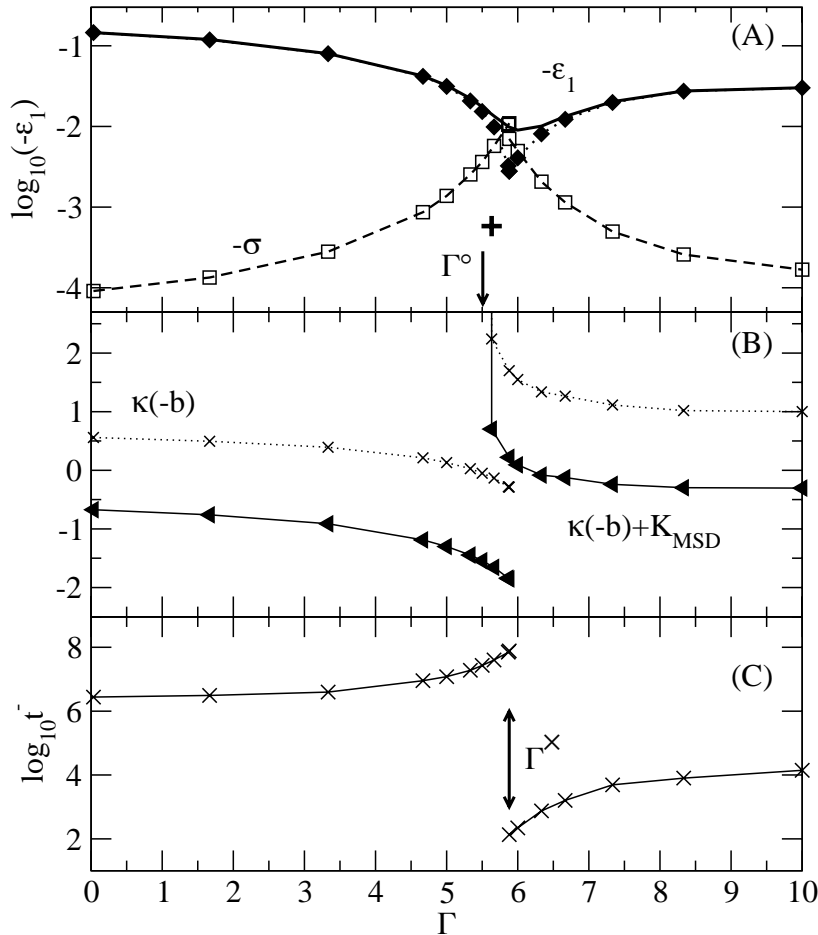


FIGURE 7.4. Parameters for the von Schweidler-law description, Eq. (5.104), for  $\delta = 0.03$ . Panel A shows the separation parameters  $\sigma$  for points on the isodiffusivity line for  $D_0^s/D^s = 10^{10}$  ( $\square - \square$ ). The separation of the same points from the  $A_3$ -singularity,  $\varepsilon_1$ , is shown by the full line. The separation  $\varepsilon_1$  of points on the liquid-glass-transition for given  $\Gamma$  is shown by filled symbols ( $\blacklozenge \cdots \blacklozenge$ ), the plus symbol marks  $\varepsilon_1$  for the glass-glass transition for  $\Gamma = 5.63$ . Panel B exhibits the amplitudes of the correction in Eq. (5.104),  $\kappa(-b) + K_{\text{MSD}}$  ( $\blacktriangleleft$ ) and  $\kappa(-b)$  ( $\times$ ), cf. Eq. (5.94). The values for  $K_{\text{MSD}}$  are the same as shown in Fig. 7.3. Panel C shows the time  $t^-$  where the respective critical  $A_2$ -plateau is crossed by the MSD for  $D_0^s/D^s = 10^{10}$ .

larger than  $\kappa(a)$  on the gel line it almost compensates the negative values of  $K_{\text{MSD}}$  and  $K_{\text{MSD}} + \kappa(-b)$  is close to zero.

The time  $t^-$  for the onset of the  $\alpha$ -process, i.e. the time where the critical plateau is crossed, is shown in panel C. When the long-time diffusion is given by the ratio  $D_0^s/D^s = 10^{10}$ , the plateau in the localization is encountered by the MSD



for the HSS at  $t^- = 3 \cdot 10^6$ . This is the time when the cage around a tagged particle disintegrates and the particle starts to diffuse. The increasing attraction for  $\Gamma > 0$  introduces short-ranged bonding among the particles before the particles experience the cage. Hence, for the same reason as for the increase of  $t_0$ , this bonding process shifts  $t^-$  to higher values. When comparing the lower panels of Figs. 7.3 and 7.4 we observe that for  $0 \leq \Gamma \leq 5$ , the time scales  $t_0$  and  $t^-$  run almost parallel and define a window of six orders of magnitude in time where the cage effect dominates the dynamics. For large coupling,  $8 \leq \Gamma$ , we observe a comparable window for the dynamics around the gel plateau, where bonding rules the dynamics. Therefore, in both cases the stretching of the dynamics is the same what is corroborated by observing that  $\lambda \lesssim 0.8$  in the mentioned regions, cf. Fig. 4.4. In this sense also the  $\alpha$ -process of glass- and gel-transition singularities are similar if one is unaffected by the other. For  $5 \lesssim \Gamma \lesssim 7$ , or  $\lambda \gtrsim 0.8$ , the dynamics is governed by the interference of both mechanisms and the emergence of the  $A_3$ -singularity.

Figure 7.5 shows the asymptotic approximation of the  $\alpha$ -process on the path for  $\Gamma = 6.67$  from Fig. 7.1. Three plateaus organize the relaxation. First, the gel plateau is encountered. Shown here as dash-dotted curve, labeled  $\beta$ , is the first order description by the full  $\beta$ -correlation function from Eq. (5.88). It continues the description by the critical law discussed in Eq. (7.2). The correction in Eq. (5.104) for that  $A_2$ -singularity is close to zero as for almost all gel transitions for  $\delta = 0.03$ , cf. Fig. 7.4. This explains why the first-order description is so successful in the regime after crossing the plateau. After the plateau the curve for the  $\beta$ -correlator cannot be discerned from the full solution. It extends, accidentally, also beyond the region of applicability which is limited by the  $A_3$ -plateau. To demonstrate, that upon closer approach to the  $A_2$ -singularity for the gel transition, the  $\alpha$ -scaling picture from Fig. 7.2 A reemerges, we show an additional relaxation for  $\varphi = 0.5231$ , which has a similar separation parameter,  $\sigma = -10^{-4}$ , as the curve  $D_0^s/D^s = 10^{10}$  in Fig. 7.2 A. This last curve in Fig. 7.5 clearly displays the two-step relaxation and is described well by the von Schweidler law (5.104).

The second plateau is associated with the logarithmic relaxation laws. The curvature in the double-logarithmic representation is positive around the plateau and therefore the leading approximation, Eq. (5.37), qualitatively disagrees. The correction (5.42) covers two decades in time for all curves shown when requiring 5% accuracy. The asymptotic laws for the  $A_3$ -singularity describe approximately half of the relaxation between the gel and the glass plateau. In particular the onset of the effective power law discussed in Fig. 7.2 is captured by the asymptotic approximation. However, the range of applicability for the logarithmic laws is bound by the neighboring plateaus for gel and glass transition. For this reason the approximations for the  $A_3$ -singularity do not extend beyond the range shown in the figure and can therefore not cover the complete effective power law.

To differentiate the effective power law from the power laws discussed for the MSD in the previous chapter, we show the latter for comparison and note first, that the path in the control-parameter space taken in Fig. 7.5 is above the line  $b_2 = 0$  specified in Fig. 6.10, therefore  $b_2 > 0$ . The approximation by the leading order power law (5.106a) describes one and a half decades on the 5%-level as seen for the curve  $D_0^s/D^s = 10^{10}$ . The exponents capture the diminishing slope upon approaching the  $A_3$ -singularity by decreasing from left to right,  $b_1 = 0.331, 0.243, 0.181, 0.163$ . The corrected power law, Eq. (5.107), yields an exponent  $b'_1 = 0.178$

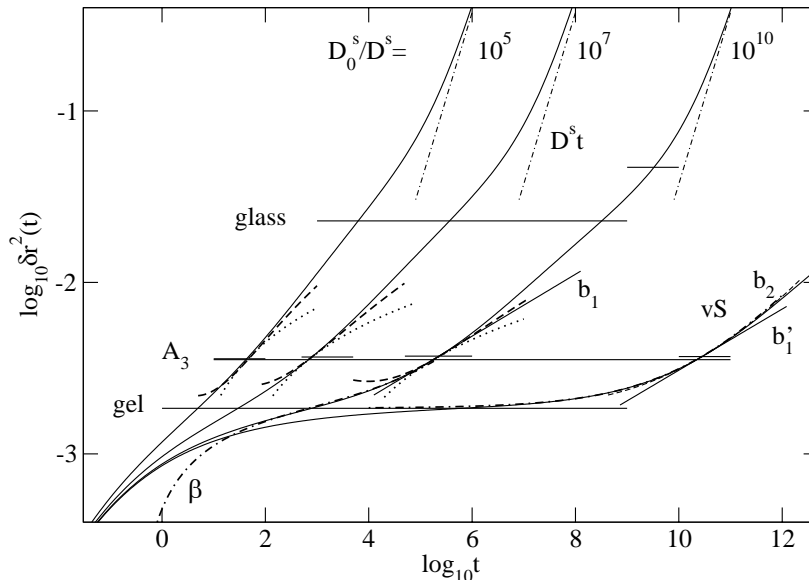


FIGURE 7.5. Subdiffusive power law at the  $A_3$ -singularity. The full lines are the MSD for states with  $\Gamma = 6.33$  and increasing  $\varphi$ . Three curves reproduce the results from Fig. 7.2 C and the last one refers to  $\varphi = 0.5231$ . The long horizontal lines show the critical plateaus  $6r_s^{c,2}$  for the gel transition at  $\Gamma = 6.33$ , the  $A_3$ -singularity and the glass transition at the crossing point for  $\Gamma = 5.88$ . The short horizontal lines indicate the corrected plateau  $6(r_s^{c,2} - \hat{r}_s^2)$  for the asymptotic laws associated with the respective relaxation. The  $\beta$ -relaxation asymptote around the gel plateau is drawn as chain curve labeled  $\beta$  for the solution at  $D_0^s/D^s = 10^{10}$ . The chain line labeled vS represents the von Schweidler description for the state at  $\varphi = 0.5231$ . For  $D_0^s/D^s = 10^5$ ,  $10^7$ , and  $10^{10}$  dotted and dashed lines show the leading, Eq. (5.37), and next-to-leading approximation, Eq. (5.42), near the  $A_3$ -plateau, respectively. The straight full line labeled  $b_1$  shows the approximation by Eq. (5.106),  $b_1'$  the corrected power law (5.107), and the dashed line labeled  $b_2$  the approximation by Eq. (5.105b). The straight dash-dotted lines show the asymptotic long-time diffusion  $D^s t$  for the respective curves.

for the last relaxation. This correction comes closer to the effective exponent  $x = 0.27$ , but improves the description of the effective power law only little, as can be seen in the straight full line with label  $b_1'$ . When including the curvature  $b_2 = 0.0132$  in the approximation, cf. Eq. (5.105b), we find the dashed curve  $b_2$ , that describes the relaxation over three decades in time. But again it covers only the onset of the effective power law. In that sense the effective power law is the analog of the effective logarithmic decay discussed in connection with Fig. 5.8, where a crossover from  $A_3$ - to  $A_2$ -dynamics could explain the observed decay.

As the distance to the  $A_3$ -singularity is no longer changed significantly for  $D_0^s/D^s \geq 10^7$ , the solutions as well as the approximations do no longer change in shape and the decay around the  $A_3$ -plateau is part of the  $\alpha$ -process for the gel transition. This  $\alpha$ -process contains also the relaxation around the third plateau in Fig. 7.5 that represents the glass transition at the crossing point and is modified by a rather large correction, since the distance to this point is large. Despite the larger distance the last relaxation still slows down the dynamics by one decade before the final crossover to the long-time diffusion.

To demonstrate how the crossing scenario in Fig. 7.5 changes when  $\delta$  is varied, Fig. 7.6 exhibits the parameters relevant for the description of the relaxation. The three plateaus in Fig. 7.5 are defined by the localization lengths  $r_s^c$ . Panel A in Fig. 7.6 shows the variation of the localization lengths. At the  $A_4$ -singularity,  $\delta = \delta^*$ , all three plateaus join in a single localization length and the relaxation is just the logarithmic decay described in Ch. 6. For  $\delta > \delta^*$ , the localization of a glass state at the crossing is larger than the localization of the gel state. This difference is becoming more pronounced as  $\delta$  decreases. For the gel the localization follows  $\delta$  and for the glass the localization approaches the value for the HSS. In between there is the plateau for the  $A_3$ -singularity, which closely follows the localization for the gel. This limits the regime for the von Schweidler relaxation after the gel plateau, as observed in connection with Fig. 7.5, if the  $A_3$ -singularity is close. Sufficiently far from higher-order singularities the amplitude in  $\delta r^2$  delimited by the localization lengths of gel and glass transition exhibits the dynamics defined by a crossover of two different  $A_2$ -singularities. If the  $A_3$ -singularity is close as in Fig. 7.5, logarithmic laws influence the relaxation.

The influence of the  $A_3$ -singularity is quantified by the separation parameter  $\varepsilon_1^{\text{cross}}$ , shown for the various crossing points in panel B. For smaller  $\delta$ , the separation increases and limits the  $A_3$ -dynamics visible in the relaxation at the crossing. The minimal exponent  $b_1$ , cf. Eq. (5.106b), in the liquid regime is assumed at the crossing point. Therefore this exponent can be used as an estimate for the separation from the  $A_3$ -singularity. For  $\delta = 0.02$  we find  $b_1 = 0.169$  and for  $\delta = 0.03$  the minimal exponent is  $b_1 = 0.095$ . Moreover, if in an experiment one can only come close to the crossing limited by say  $D_0^s/D^s = 10^{10}$ , this implies further restrictions to the detection of the higher-order singularities.

By comparing the lines where  $b_2 = 0$  for the  $A_4$ -singularity and the  $A_3$ -singularity for  $\delta = 0.03$ , cf. Figs. 6.7 and 6.10, we found that this line would not change its location in control-parameter space, when both  $K_{\text{MSD}}^\circ$  and the ratio  $h_{\text{MSD}}^\circ/r_{\text{MSD}}^{\circ 2}$  varied only little. This is indeed, what we can infer from panel C and D.  $K_{\text{MSD}}^\circ$  exhibits only small changes and is minimal at the  $A_4$ -singularity, which was already noticed for the  $K_q$  in Fig. 6.9. The variation in  $h_{\text{MSD}}^\circ/r_{\text{MSD}}^{\circ 2}$  is only 5%. Thus, we conclude that the power-law behavior in the MSD as a clear signature of the dynamical anomalies due to higher-order singularities should be well accessible in the liquid regime without extensive fine tuning of the control parameters.

## 2. Correlation function at a crossing

The last section showed that the dynamical laws at a crossing of liquid-glass transition lines can be quite intriguing since upon variation of control parameters the separation to three different singularities is changed. Allowing now also for a variation in the wave vector  $q$ , combines the subtle  $q$ -variation for the logarithmic

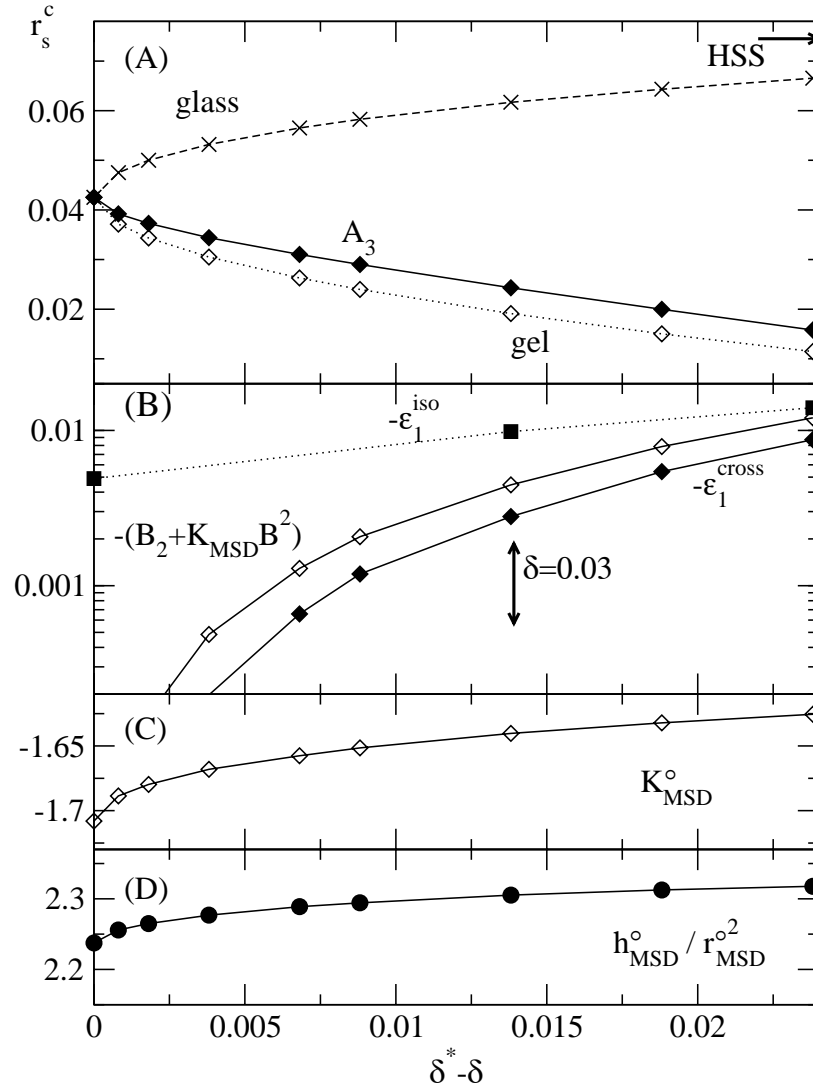


FIGURE 7.6. Parameters for the description asymptotic at the crossing. Panel A shows the localization length  $r_s^c$  at the crossing point for the glass ( $\times$ ) and the gel state ( $\diamond$ ) as a function of  $\delta^* - \delta$  together with the value at the  $A_3$ -singularity ( $\diamond$ ). The value of  $r_s^c$  in the HSS is indicated by the arrow. Panel B displays the separation parameter  $-\varepsilon_1$  ( $\diamond$ ) and the quadratic corrections to the logarithmic relaxation at the crossing point. For  $\delta = \delta^*$ , 0.03, 0.02, the minimal  $|\varepsilon_1|$  is displayed ( $\blacksquare$ ) which can be reached on the isodiffusivity line  $D_0^s/D^s = 10^{10}$ . The correction amplitudes  $K_{\text{MSD}}^{\circ}$  and the ratios  $h_{\text{MSD}}^{\circ}/r_{\text{MSD}}^{\circ 2}$  are shown in panels C and D.

decay, see Ch. 6, with the  $q$ -dependences of the decay at  $A_2$ -singularities. We shall

select only one such scenario which was proposed in [16] and subsequently found in an experiment [42, 43] and also in MD simulation [93].

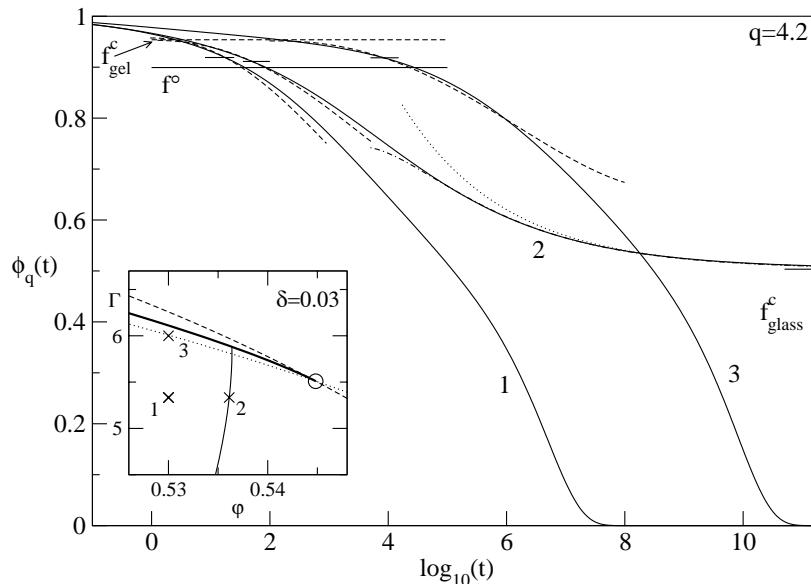


FIGURE 7.7. Logarithmic decay of the density correlation function for  $q = 4.2$  at the crossing point for  $\delta = 0.03$ . The full curves display the solutions for states  $n = 1, 2, 3$ :  $(\Gamma, \varphi) = (0.53, 5.33)$ ,  $(5.33, 0.5361)$ , and  $(0.53, 6)$  which are marked in the inset. Three relevant plateaus are indicated by horizontal lines for the gel transition (dashed) at  $(0.530, 6.1)$  labeled  $f_{\text{gel}}^c$ , for the  $A_3$ -singularity (full line) labeled  $f^\circ$ , and for the glass transition at  $(0.536, 5.33)$  (short full line) labeled  $f_{\text{glass}}^c$ . The plateau values are  $f_{\text{gel}}^c = 0.954$ ,  $f^\circ = 0.899$ , and  $f_{\text{glass}}^c = 0.503$ . Short lines show the plateau corrections for the plateau  $f^\circ$ . Broken curves show the next-to-leading approximation (5.42) for the logarithmic decay, dotted and dash-dotted curves the leading and next-to-leading approximation for the critical decay (5.93) in curve 2 at  $f_{\text{glass}}^c$ . The inset shows part of the glass-transition diagram for  $\delta = 0.03$  including the lines  $\varepsilon_1 = 0$  (dashed) and  $\varepsilon_2 = 0$  (dotted).

Figure 7.7 shows how the dynamics for the states specified in the inset is described by the asymptotic laws for different singularities. The dominant feature is the straight line decay displays for  $0.8 \gtrsim \phi_q(t) \gtrsim 0.6$ . One may interpret this as logarithmic decay around an estimated plateau  $f' \approx 0.7$ . However, the appropriate plateau value connected with the  $A_3$ -singularity is higher,  $f_q^\circ = 0.899$ , and close to the plateau for gel transitions and the  $A_3$ -singularity are close for any wave vector is seen in Fig. 4.2 and reflected in the localization lengths in Fig. 7.6 (A). Therefore the logarithmic laws of Eq. (5.42) have an asymmetric range of applicability. The range is rather small for shorter times since the gel transition interferes, and considerably larger for longer times as the critical decay due to the glass transition has a more distant plateau.

The evolution of the dynamics when moving from state 1 to state 2 is the analog of the dynamics seen in the MSD in Fig. 7.2 (B). Only a minor part of the slowing down takes place at the gel plateau, the major part from  $t \approx 8$  to  $t \approx 10^4$  is described by the logarithmic laws around  $f_q^\circ$ . For the solutions 1 and 2, the approximation (5.42) is valid from  $t \approx 10$  to  $t \approx 10^3$  and  $10^4$ , respectively. At the  $A_2$ -singularity for the glass transition, the critical law (5.93) is observed. The exponent parameter  $\lambda = 0.847$  implies an exponent  $a = 0.250$ . The leading  $t^{-a}$ -law (dotted) describes curve 2 successfully for  $t \gtrsim 10^6$  and adding the correction (dash-dotted) improves that range by almost two decades. Curve 2 demonstrates how different asymptotic expansions complement one another: Eq. (5.42) describes the decay from above  $f_q^\circ$  down to  $\phi_q(t) \gtrsim 0.7$  and Eq. (5.93) approximates successfully the region from  $\phi_q(t) \lesssim 0.7$  to the critical plateau  $f_{\text{glass}}^c$ . That the slope of the decay becomes smaller below  $f_q^\circ$  is a clear indication of a closer approach to a higher-order singularity, as prefactor  $B$  in Eq. (5.42) vanishes with the square-root of the distance from the  $A_3$ -singularity, cf. Eq. (5.20).

When taking another path from 1 to state 3, the distance to the  $A_3$ -singularity remains largely unaltered and we find the counterpart of Fig. 7.5 for the MSD. The dynamics is ruled by an approach to the gel transition and the complete decay below  $f_{\text{gel}}^c$  is part of the  $\alpha$ -process and scales by a shift along this plateau with only minor deviations due to changing separations to the glass-transition line and the  $A_3$ -singularity. No clear two-step process is observed for curve 3 for two reasons. First, the  $A_2$ -dynamics below  $f_{\text{gel}}^c$  is limited by the logarithmic laws for the  $A_3$ -singularity. Second, the complete decay seen in curve 3 requires more than ten decades, but only for  $t \lesssim 10^2$  the decay takes place above the plateau  $f_{\text{gel}}^c$  and this is too close to the transient dynamics to exhibit a clear critical decay. Moreover, the exponent parameter in the vicinity of the  $A_3$ -singularity is already rather high,  $\lambda = 0.89$ , so the critical law  $t^{-a}$  is stretched considerably. As in the MSD shown in Fig. 7.5 for the last curve, moving closer to the gel transition, the two-step process typical for an  $A_2$ -singularity reemerges.

One recognizes for all three curves in Fig. 7.7 that the logarithmic decay around  $f^\circ$  is approximated by a too steep slope in Eq. (5.42). As all states are close to the lines  $\varepsilon_1 = 0$  and  $\varepsilon_2 = 0$ , cf. inset of Fig. 7.7, we face a similar situation as in Fig. 5.10 where a positive renormalization of the linear term by  $C_1$  could be assumed to explain similar deviations in the approximation in Fig. 5.11.

From the asymptotic approximation in Fig. 7.7 we find that the effective logarithmic behavior is similar to one observed in Fig. 5.8. To demonstrate that a variation of the wave vector can be used as a test if the observed decay is indeed compatible with the asymptotic expansion (5.42) or due to some crossover, we try to fit the decay for state 2 with the assumption that the logarithmic decay for  $q = 4.2$  is taking place around  $f'_q = 0.7$ . This choice yields a time scale  $\tau' = 3.8 \cdot 10^4$  and the values for  $f'_q$  for different  $q$  are read off at the same time. This yields values shown by the filled circles in the inset of Fig. 7.8, for all wave vectors,  $f'_q < f_q^\circ$ , cf. inset of Fig. 7.8. To achieve a rescaled plot similar to  $(\phi_q(t) - f_q^\circ)/h_q^\circ$  in Fig. 6.5, we determine the coefficient  $h'_q$  for the decay linear in  $\ln(t/\tau')$  around zero for  $\phi_q(t) - f'_q$ . This amplitude is the equivalent of  $(B - B_1)h_q^\circ$  in Eq. (5.42) and is shown as diamonds in the inset of Fig. 7.8. The variation in  $q$  of the factors  $f'_q$  and  $h'_q$  suggest a reasonable albeit narrower distribution in  $q$  as the true values  $f_q^\circ$  and  $h_q^\circ$ . The full panel of Fig. 6.5 shows a rescaled plot of  $(\phi_q(t) - f'_q)/h'_q$  which should

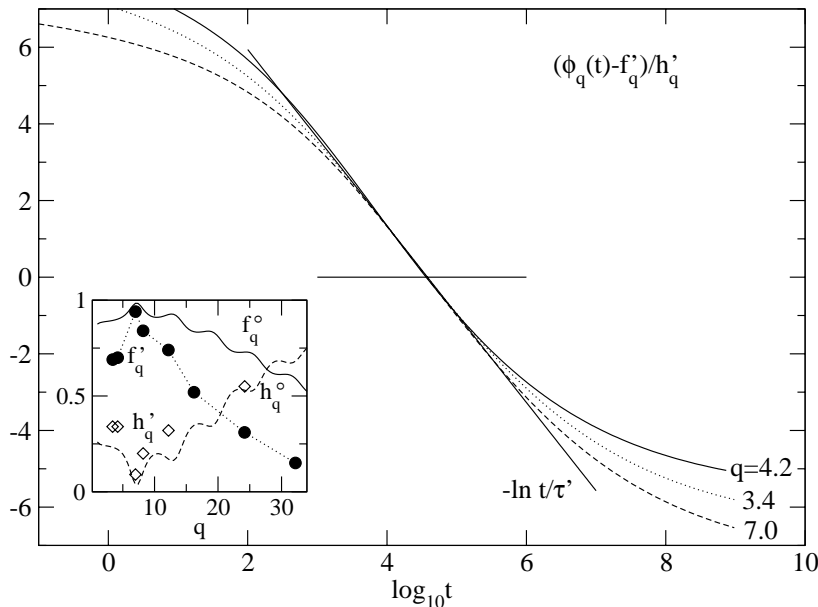


FIGURE 7.8. Wave-vector test for the logarithmic decay at state 2 in Fig. 7.7. The correlators  $(\phi_q(t) - f'_q)/h'_q$  are shown as dotted, full and dashed lines for  $q = 3.4, 4.2, 7.0$  and labeled accordingly. The full straight line displays the  $\ln t/\tau'$  decay for  $\tau' = 3.8 \cdot 10^4$ . The inset shows the glass-form factors  $f_q^\circ$  and critical amplitudes  $h_q^\circ$  at the  $A_3$ -singularity, cf. Fig. 6.9. The filled circles mark the fitted plateau values  $f'_q$  and the diamonds show  $10 h'_q$  (see text).

be equivalent to Fig. 6.5. In contrast, Fig. 7.8 does not exhibit the characteristic concave/convex behavior. Moreover, the deviations from the  $-\ln t$ -behavior are asymmetric, curves deviating first before crossing the zero, deviate last after the zero. Therefore the range for the logarithmic decay in time does not show the dependence to be expected from Eq. (5.42). It is therefore possible to differentiate the results for the choice  $f'_q$  from the results for a correct choice as in Fig. 6.5.





## Experimental aspects

The previous chapters have outlined a number of predictions of MCT in systems with higher-order glass-transition singularities. We shall now assess the experimental situation. Section 1 introduces to colloidal dispersion that are expected to be close to the model potentials studied above. For the reentry phenomenon there is already evidence coming from several independent sources so we can simply review the development in Sec. 2. In order to locate the higher-order singularities in the control-parameter space a mapping is suggested in Sec. 3 which is based on a recent MD study [33]. Section 4 interprets for the logarithmic decay in a different MD simulation [44].

### 1. Depletion Attraction

The range of the attraction in the potentials discussed above needs to be very small compared to the particle diameter. This rules out the important case of the Lennard-Jones potential encountered in molecular systems. Besides computer simulation studies it is possible to find such potentials in colloidal suspensions which provide a testbed for theoretical predictions as the interaction potentials are tunable to a large extent. A colloidal system that is used frequently to model the HSS comprises particles made of polymethyl methacrylate (PMMA) in a hydrocarbon solvent [8]. When adding polymer to the solution an entropically driven imbalance in the osmotic pressure causes the so-called depletion attraction [19, 21]. The concentration of polymer governs the strength of this attraction and the radius of gyration of the polymer can be used as range of the effective attraction. By adding polymer chains of different lengths and varying the concentration of both polymer and colloids, three control parameters can be changed that are present also in the SWS. For modeling the interaction often not the SWS but the form introduced by Asakura and Oosawa is used [20]. For small interaction range  $\delta$ , this depletion potential can be identified with Eq. (3.10) for  $n = 2$  with  $\Gamma = 3\varphi_P/(2\delta)$  and the polymer packing fraction  $\varphi_P$ . The treatment as two-body interaction is exact for  $\delta < 2/\sqrt{3} - 1 \approx 0.1547$  [22]. The experimental techniques for colloid-polymer mixtures are by now well under control and the thermodynamic behavior of these systems is established [94]. However, isostructural phase transition were so far only found in computer simulation [23–26]. To investigate the correlation function dynamic light scattering is already used in such systems [29, 30, 42]. Direct imaging techniques are available to determine also the MSD with high precision [95–97].

### 2. Reentry phenomenon

The prediction of the reentry phenomenon by MCT [14] and its explanation by corresponding changes in the static structure factor [16] was found in a system

of crosslinked microgel colloids with linear polystyrene chains added to induce the depletion attraction [29]. The radius of gyration for the polymer was  $\delta = 0.054$ . Upon addition of these polymer chains an acceleration of the decay of the correlation function by three orders of magnitude was observed. The measurement of the static structure factor revealed that indeed changes at the peak of the structure factor can be related to the reentry in that system.

An earlier investigation in a similar system with crosslinked microgel colloids but without added polymer revealed significant differences from the behavior of the HSS as seen in the PMMA system [98]. The glass transition was found at much higher volume fractions, and to interpret the dynamical data within MCT a considerably higher value for the exponent parameter,  $\lambda = 0.88$ , had to be assumed. It was found recently that in this system imperfections during the process of crosslinking in the colloidal particles released free polystyrene into the solvent and thus induced depletion attraction by accident [99]. Therefore, in this earlier experiment the deviation in the packing fraction can be explained partly by the reentry phenomenon and the high value of  $\lambda$  might be taken as indication of higher-order singularities.

A different study using the PMMA colloidal suspension inferred the reentrant behavior of the liquid-glass transition from the fact that homogeneous nucleation of colloidal crystals is no longer observed when a glass transition is reached [30]. In computer simulation, enhanced diffusion was found when increasing the attraction strength into the reentry regime [30, 31, 33]. In conclusion the reentry phenomenon was predicted successfully by MCT.

### 3. Location of the glass-transition diagram in the phase diagram

One cannot expect a theory for a singularity to predict accurate numbers for the control parameters where the singularities occur. For that reason the distance from the singularity,  $\mathbf{V}^* - \mathbf{V}$ , should be used for a comparison with data from experiments or computer simulation. The isodiffusivity curves in Fig. 7.1 motivate a comparison between MCT and computer simulation based on the ratio  $D_0^s/D^s$  [33].

A slight reservation has to be made since the simulation data refer to a binary mixture while the present theory deals with a monodisperse system. However, comparing the data from the simulation of the monodisperse case [31] indicated by crosses in Fig. 8.1 with the ones for the mixture, the isodiffusivity for  $D_0^s/D^s = 2.4 \cdot 10^2$  seems to fit nicely into the picture. Data for lower  $D_0^s/D^s$  from [31] have the same trend in  $\Gamma$  but apparently do not occur at control parameter values for the same diffusivity as extrapolated from the mixture. The MD studies were performed using Newtonian dynamics where an appropriate definition of  $D_0^s$  is impossible; the value  $d\sqrt{k_B T/m}$  is taken instead of  $D_0^s$  as reference which introduces a reasonable microscopic time scale [31, 33]. This problem in the definition of the analog of  $D_0^s$  introduces less deviations for larger ratios of the diffusivity  $D_0^s/D^s$  since only the order of magnitude is important for the definition of the isodiffusivity curves. A deviation in  $\log D_0^s$  would stay the same for both large and small differences in  $\log D_0^s - \log D^s$  and the result can be more accurate the larger the ratio  $D_0^s/D^s$  is. Therefore, putting emphasis on the data with high ratios of  $D_0^s/D^s$  is justified.

Figure. 8.1 shows that an acceptable fit of data for the diffusivity in [33] and the theoretical data calculated using the structure factor evaluated in PYA is achieved

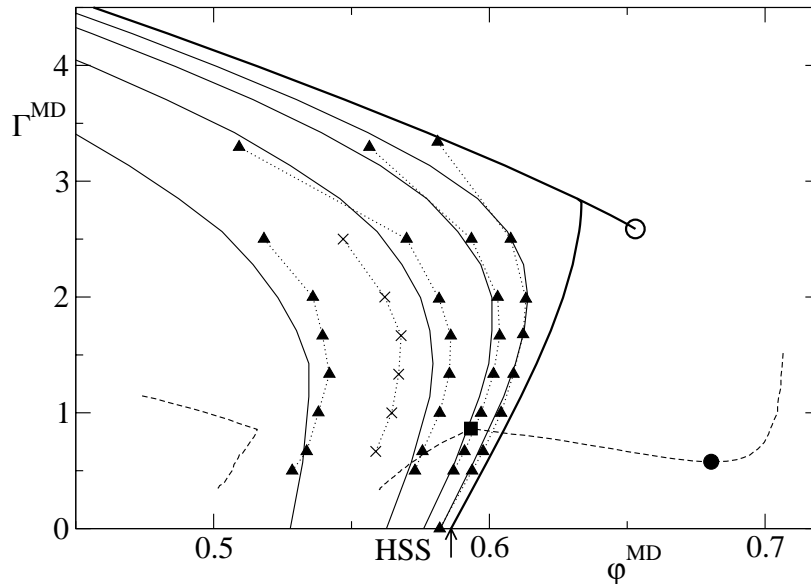


FIGURE 8.1. Theoretical glass-transition diagram of the SWS compared to computer simulation data at  $\delta = 0.03$ . Triangles ( $\blacktriangle$ ) mark the isodiffusivity curves from the simulation in [33] from left to right for  $D_0^s/D^s = 2 \cdot 10^2, 2 \cdot 10^3, 2 \cdot 10^4, 2 \cdot 10^5$ , respectively. Crosses ( $\times$ ) show the isodiffusivity curve for  $D_0^s/D^s = 2.4 \cdot 10^2$  from the simulation of the monodisperse system [31]. Dotted lines are guides to the eye for the simulated isodiffusivity curves. Dashed lines indicate the data for melting, freezing and solid-solid binodal together with the solid-solid triple point ( $\blacksquare$ ) and critical point ( $\bullet$ ) from [23]. The theoretical calculations within MCT using the structure factor solved numerically in PYA, cf. Eq. (3.18a), are shown as full lines for liquid-glass transitions, the glass-glass transition with endpoint  $A_3$  ( $\circ$ ) and the respective isodiffusivity curves for  $D_0^s/D^s = 2 \cdot 10^2, 2 \cdot 10^3, 2 \cdot 10^4, 2 \cdot 10^5$ . The arrow labeled HSS indicates the limit of the hard-sphere system from [33]. The MCT results are based on the PYA and the control parameters  $\varphi^{\text{PYA}}$  and  $\Gamma^{\text{PYA}}$  are transformed by  $\varphi^{\text{MD}} = 2.25 \varphi^{\text{PYA}} - 0.5747$  and  $\Gamma^{\text{MD}} = 2.85 \Gamma^{\text{PYA}}$  to match the isodiffusivity curves from the simulation.

by keeping the well width fixed at  $\delta = 0.03$  and scaling the axis of the inverse temperature by  $\Gamma^{\text{MD}} = 2.85 \Gamma^{\text{PYA}}$ . This preserves the limiting case for the HSS as done above for the comparison of PYA and MSA, cf. Fig. 4.5. Trying to match reasonably at least the two curves with the highest ratio of  $D_0^s/D^s$ , the packing fraction has to be taken  $\varphi^{\text{MD}} = 2.25 \varphi^{\text{PYA}} - 0.5747$  in order to keep a value for HSS of  $\varphi_{\text{HSS}}^c = 0.586$ . This is consistent with the diffusivity data and experiments done in colloids [11, 12]. The prefactor of 2.25 seems somewhat large. It is already

seen in Fig. 8.1 that this overestimates the differences in  $\varphi$  further from the singularities. But taking the diffusivity data for granted this large prefactor is required. A modification of the third coupling parameter  $\delta$  was not necessary in the fit.

Figure 8.1 demonstrates a reasonable fit between theory and data starting from the HSS and extending up to the crossing point. For the gel-transitions, there are not enough data to make a definite statement. For this high values of  $\Gamma$  it is also difficult to obtain accurate values for  $D^s$  with good statistics from the simulation [33]. These points are only fitted qualitatively in Fig. 8.1. A comparison of the fit in Fig. 8.1 which uses the PYA for the theoretical curves with Fig. 7.1 indicates that using MSA for the structure factor would also properly fit the data from the HSS limit up to the crossing but would be worse than PYA for the gel line. The indication of the  $A_3$ -singularity in Fig. 8.1 has to be understood as an extrapolation of the transformation scheme outlined above.

The fit in Fig. 8.1 corroborates that in general MCT overestimates the trend to freezing when coupling parameters are increased [6]. This is already found in the HSS [11] and in a binary Lennard-Jones mixture [100]. Yet, for a Lennard-Jones potential the mechanism of arrest is still dominated by repulsion, so the control parameter is effectively only density also in that system. For the SWS near the line crossing, necessarily both mechanisms of arrest have to be of the same importance and the approximation inherent to MCT has to preserve the relative importance of both mechanisms. In the case of the SWS, MCT has apparently the same trend in the error for the treatment of couplings in  $\varphi$  and  $\Gamma$ . The mapping of the MCT results to higher values in both packing fraction and attraction strength is in agreement with a recent experimental analysis of a colloid-polymer mixture with the theoretical results for the AOS [101]. By comparison with the data for the phase transitions [23], we recognize that the crossing of lines and the  $A_3$ -singularity are located in the metastable region. The  $A_3$ -singularity differs by 4% in  $\varphi$  and by a factor of 4.5 in  $\Gamma$  from the solid-solid critical point.

#### 4. Logarithmic decay in MD

To demonstrate how the logarithmic decay laws in Eq. (5.42) can be used for the interpretation of data we apply these laws to data taken from a recent molecular dynamics simulation<sup>1</sup> [44]. The simulated system comprises a mixture of particles interacting with an  $r^{-36}$ -repulsion and an attraction of the Asakura-Oosawa form. An additional small repulsive barrier is introduced to avoid liquid-gas separation. Matching the peak of the structure factor for the equivalent of the HSS, we rescale the wave vectors by 7.8/7.0 in the following to be compatible with the notation in other chapters.

Logarithmic decay was observed for a state point with packing fraction  $\varphi = 0.55$  and polymer concentration  $\varphi_P = 0.375$  for an attraction range of  $\delta = 0.1$  [44]. The system is reasonably close to the SWS to motivate a comparison in the vicinity of the  $A_4$ -singularity of the SWS. Because of better statistics the correlation functions for a tagged particle are investigated. The asymptotic approximation for tagged particle correlation functions is given by Eq. (5.98) which is easily adapted to incorporate Eq. (5.42). Anticipating the results of Ch. 6 that also for close-by  $A_3$ -singularities the dominant correction to logarithmic decay is quadratic in  $\ln(t/\tau)$  and that the

<sup>1</sup>The authors provided refined data with better statistics for the final fit what is gratefully acknowledged. Changes in comparison to the fits using the published data are small.

corrections to the plateau are small, the following function is used for fitting the data,

$$(8.1) \quad \phi_q^s(t) = f_q^s - a_1(q) \ln(t/\tau) + a_2(q) \ln^2(t/\tau).$$

The first step in the fitting is choosing an appropriate time scale  $\tau$  that also fixes the values for  $f_q^s$ . For a generic liquid-glass transition exhibiting the  $A_2$ -two-step decay, the  $f_q^s$  are in principle apparent from the plateau or can at least be inferred from an inflection point in the decay. It is inherent to Eq. (5.42) that neither a plateau nor an inflection point is expected. Therefore one has to estimate  $\tau$  and check if that guess yields a consistent fit of the data available. We try three different time scales,  $\tau = 5, 10,$  and  $25$ . For each choice of  $\tau$ , a least-square fit to the polynomial in Eq. (8.1) covering two decades symmetrically around  $\tau$  yields three  $q$ -dependent coefficients. The constants and the prefactors to the linear term are used to rescale the correlators in the form  $(\phi_q^s(t) - f_q^s)/a_1(q)$ . This representation can be compared directly to the theoretical results in Fig. 6.5.

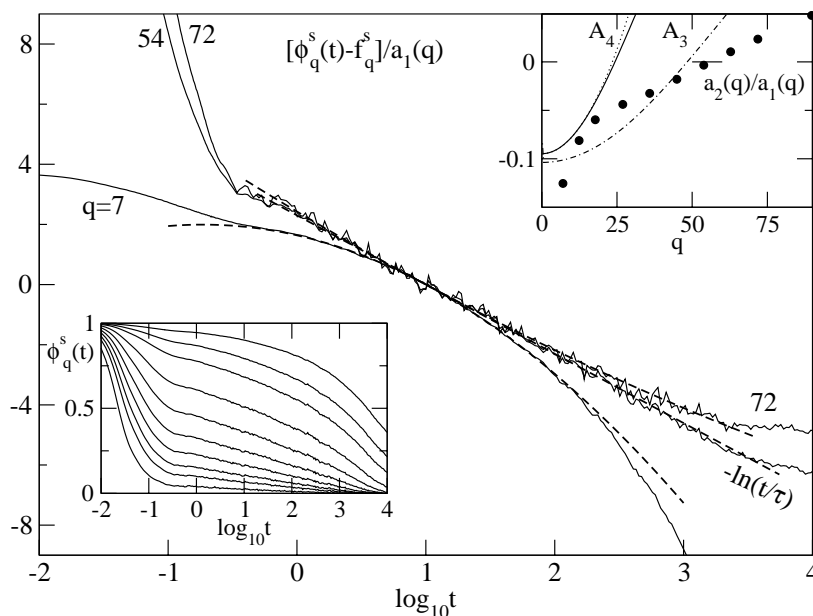


FIGURE 8.2. Correlators from simulation data [44] rescaled as  $(\phi_q^s(t) - f_q^s)/a_1(q)$ , cf. Eq. (8.1), for  $q = 7, 54,$  and  $72$ , as full curves, with parameters taken from the fit using  $\tau = 10$  (see text). The dashed curves show the fits to the data according to Eq. (8.1), the straight dashed line represents the function  $-\ln(t/10)$ . The lower inset reproduces the correlation function  $\phi_q^s(t)$  from Ref. [44] from top to bottom for  $q = 7, 12.5, 18, 27, 36, 45, 63, 72, 89.5$ , and the upper inset shows the factors  $a_2(q)/a_1(q)$  ( $\bullet$ ) from the data. For the SWS the value for  $B_2(q)/(B - B_1)$  is shown for the state  $(\varphi, \Gamma, \delta) = (0.54, 5.48, 0.03)$  as dash-dotted curve, and for the state  $n = 2$  from Fig. 6.3 as full line, and the Gaussian approximation to the latter as dotted line.

Figure 8.2 shows that the data are consistent with theoretical predictions. Starting from smaller wave vectors, the rescaled curves are concave in the given representation and change to convex behavior when increasing the wave vector. The curve closest to linear-log  $t$  decay is found for  $q = 54$ . This high value for  $q$  is compatible with the findings for the SWS close to higher-order singularities, Ch. 6. For increasing  $q$  beyond 54, the curvature becomes positive. However, the noise level increases considerably and in the lower inset we see that for wave vectors that large, the glass-form factors are quite small. The variation in the prefactor of the quadratic term is monotonic as seen in the upper inset and resembles qualitatively the variation expected for the correction amplitude  $K_q^s$ , cf. Fig. 6.2.

Before the comparison of the glass-form factors and the critical amplitudes from the SWS to the data we introduce the Gaussian approximation that is frequently examined in computer simulation. For the tagged particle quantities we get [60],

$$(8.2a) \quad f_q^s = \exp[-r_s^{c2} q^2],$$

$$(8.2b) \quad h_q^s = \exp[-r_s^{c2} q^2] q^2 h_{\text{MSD}},$$

$$(8.2c) \quad K_q^s = K_{\text{MSD}} + \frac{q^2}{2} h_{\text{MSD}}.$$

For small wave vectors, the Gaussian approximation was found to be a reasonable description for the results from MCT for the HSS [60].

The deviations from the Gaussian approximation for larger wave vectors are more pronounced for the results of MCT for the higher-order singularities in the SWS than for the HSS which is inferred from the upper panel in Fig. 8.3. Large non-Gaussianity was also observed for the gel states in the present system [32, 44]. Therefore, we assume that the suspected  $A_3$ -singularity shares that trend and accept the values for  $f_q^s$  in Fig. 8.3 found from the fitting procedure. We find that the simulation suggests that the Gaussian approximation is violated much more than MCT predicts. The latter is independent on the time scale  $\tau$  we chose for the analysis as the comparison for the three different choices for  $\tau$  reveals. A smaller value than  $\tau = 5$  can be ruled out when taking the distribution  $f_q^s$  found for a gel transition in the present system as upper bound. Taking larger values of  $\tau$  than above would yield smaller values for  $f_q^s$  and these would eventually cross the distribution for the HSS. Since we can safely assume smaller localization this case can be refuted. Time scale  $\tau$  is then bound to at least the decade between  $\tau = 5$  and  $\tau = 50$  by taking into account only the data for a single point. This estimate could be improved by considering different state points.

The lower panel of Fig. 8.3 shows the critical amplitudes  $h_q^s$ . The results from MCT are described reasonably by the Gaussian approximation up to  $q \approx 40$  for the  $A_4$ -singularity and  $q \approx 60$  for the  $A_3$ -singularity. The deviations from Gaussian behavior have the same qualitative trend in theory and data but are again larger for the simulation results. In Fig. 8.3 the fitted value for  $h_q^s$  is taken to be  $15 a_1(q)$ . This is at first just a mapping to the distributions found in the SWS. However, it can be justified further by considering the implications of this transformation to the dynamics. From Eq. (5.42) we know that  $a_1(q)/h_q^s = (B - B_1)$  and the scaling of  $a_1(q)$  onto  $h_q^s$  hence suggests  $(B - B_1) = 1/15 \approx 0.07$ . Neglecting the higher-order term  $B_1$ , Eq. (5.20) yields an estimate for the separation parameter  $\varepsilon_1 \approx 0.007$ . These values are close to the ones describing state  $n = 2$  in Fig. 6.3 whose dynamics is shown as curve 2 in Fig. 6.4, where for  $(\Gamma, \varphi) = (4.271, 0.5250)$  we

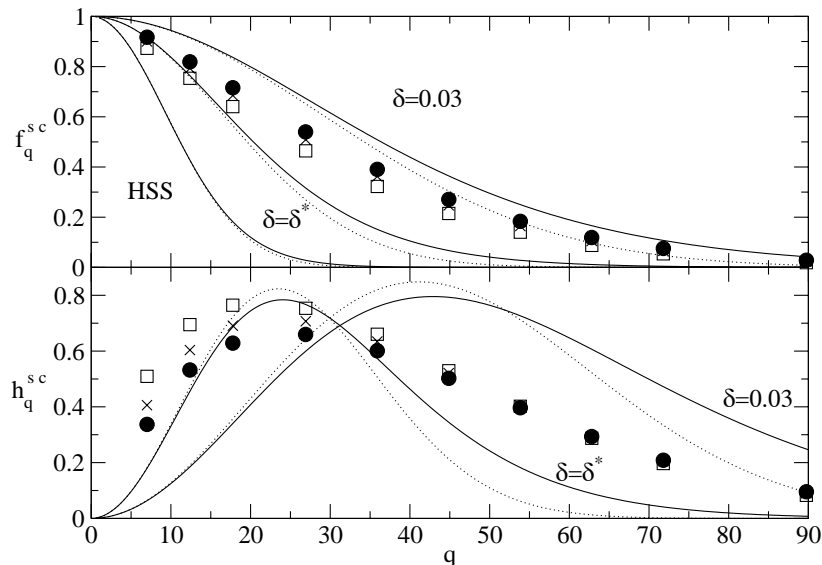


FIGURE 8.3. Glass-form factors  $f_q^s$  and critical amplitudes  $h_q^s$  determined from the fit (8.1) to the data from [44] for  $\tau = 5$  ( $\bullet$ ),  $\tau = 10$  ( $\times$ ) and  $\tau = 25$  ( $\square$ ). MCT results are shown for the  $A_4$ -singularity and the  $A_3$ -singularity at  $\delta = 0.03$  in the SWS as full lines. The dotted lines represent the respective Gaussian approximations, Eq. (8.2), to the theoretical curves. The upper panel shows in addition the glass-form factors for the HSS and their Gaussian approximation. The fitted critical amplitudes are given by  $15 a_1(q)$  (see text).

find  $(B - B_1) = 0.072$  and  $\varepsilon_1 \approx 0.010$ . Both curve 2 in Fig. 6.4 and Fig. 8.2 exhibit three decades of logarithmic behavior in the correlator with vanishing quadratic correction. In both cases, the window is considerably smaller for smaller wave vectors, cf. Fig. 6.5. For the  $A_3$ -singularity at  $\delta = 0.03$  a state with  $\varepsilon_1 \lesssim 0.01$ , would be inside the arrested regime or very close to the transition, cf. Fig. 7.4. Since the decay shown in the lower inset of Fig. 8.2 does not indicate the presence of a finite long-time limit, the decay takes place at a point closer to an  $A_4$ -singularity.

The upper inset in Fig. 8.3 displays the quadratic corrections fitted according to Eq. (8.1) in the form  $a_2(q)/a_1(q)$ . These have to be compared to the corrections amplitudes  $K_q$ . For a comparison we use the values  $B_2(q)/(B - B_1)$  which are shown as full line for the point close to the  $A_4$ -singularity discussed above. Deviations from the Gaussian approximation are again apparent for larger  $q$ . A second point is chosen for  $\delta = 0.03$  on the line  $B_2(50.2) = 0$  in Fig. 6.10 at  $\Gamma = 5.48$  and  $\varphi = 0.54$ . The separation parameter is  $\varepsilon_1 = -0.0097$  and the prefactor  $B - B_1 = 0.0072$ . The fitted values show a broader distribution in  $q$  than expected from the comparison with the  $A_4$ -singularity and therefore the quadratic corrections have a zero at higher wave vectors. The comparison with the  $A_3$ -singularity yields better agreement for  $K_q$  but the corresponding dynamics is incompatible with the simulation as argued above. Given the necessary crudeness of the fit when using only a single state

point, the noise in the data for larger wave vectors, and the large deviations from the Gaussian approximation in the data, the accordance is still acceptable.

We conclude that the logarithmic decay found in the computer simulation [44] is compatible with MCT predictions when allowing for larger deviations from Gaussian behavior than the theory predicts. The qualitative trends are consistent with theory and robust to changes in the fitting procedure.



## Conclusion

Mode-coupling theory for ideal glass transitions (MCT) predicts for systems with hard-core repulsion and an additional short-ranged attraction the existence of higher-order glass-transition singularities. The correlation functions close to these singularities exhibit anomalous logarithmic behavior. It was the objective of this work to analyze the dynamics close to higher-order singularities in terms of asymptotic expansions of the correlation functions.

Static structure factors for short-ranged attractive potentials were derived in Ch. 3 extending a result for the square-well system (SWS). In particular, the case of the frequently used Asakura-Oosawa potential is included in the solution. These structure factors were used as input to the MCT and the resulting glass-transition diagrams corroborate the prediction of topologically stable higher-order singularities in these systems, Ch. 4. Quantitative deviations from the SWS for different potentials can be understood by recognizing the stronger localization, e.g., a Yukawa potential introduces compared to the SWS, cf. Fig. 4.7 on page 38.

Two different asymptotic expansions were carried out in Ch. 5. The first one involves polynomials of the logarithm in time and leads to the result in Eq. (5.42) on page 53, which is valid for both  $A_3$ - and  $A_4$ -singularities for non-vanishing distance from the singularity. The second expansion describes the critical decay at the singularities and is performed in inverse powers of the logarithm. The result for the  $A_3$ -singularity starts with inverse quadratic power in  $\ln t$ , cf. Eq. (5.76) on page 59, and the leading term at the  $A_3$ -singularity is the inverse of the logarithm, Eq. (5.86) on page 61. In both expansions earlier results were extended to higher orders and generalized to wave-vector dependent systems. Using the newly derived terms the validity of all expansions as asymptotic approximations was demonstrated in schematic model systems in Ch. 5, Secs. 6 and 7. Including terms up to the first wave-vector-dependent correction, all the asymptotic series mentioned above and the corresponding expansions for the  $A_2$ -singularity can be cast in a generalized factorization theorem, Eq. (5.91) on page 62. In all expansions the violation of the factorization is given by the same correction amplitude  $K_q$  and the square of the leading term.

For the decay in powers of  $\ln t$  generic scenarios were discussed for the schematic models that are easily transferred to wave-vector-dependent models. In particular a characteristic change from convex to concave decay in  $\ln t$  was presented in Ch. 5 Sec. 7

The application of the critical decay laws to the square-well system (SWS) leads to a consistent description at the  $A_3$ -singularity in Fig. 6.11, which, however, does not yield a satisfactory approximation for times relevant in experiment. For the  $A_4$ -singularity the dynamics is so slow that only qualitative consistency with the asymptotic approximation could be observed.

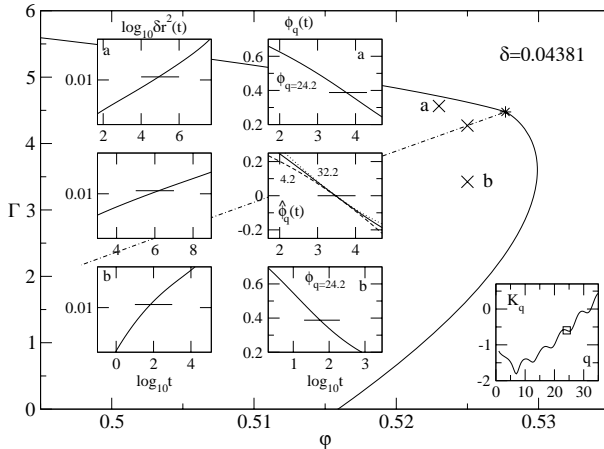
Different from the critical laws, a number of testable predictions stem from the asymptotic description in terms of logarithms, which shall be summarized using the schematic drawing below which shows a cut through the glass-transition diagram containing the  $A_4$ -singularity (\*), cf. Fig. 4.1. The logarithmic decay is dependent on the wave vector  $q$  and there are lines in control-parameter space, where the quadratic corrections to the logarithmic decay vanish for a specified  $q$  (chain line). These lines emanate from the higher-order singularity and rotate clockwise around the higher-order singularity with increasing correction amplitude  $K_q$ , which in general grows with  $q$ , cf. lower right inset and Fig. 6.3 on page 90.

The correlation functions for states on these lines exhibit decays that are linear in the logarithm for several orders of magnitude in time, cf. Fig. 6.4 on page 92. In leading order the slope of the decay is given by the square-root of the distance from the singularity. For smaller  $K_q$  or for state points above (a) the chain line in the glass-transition diagram the decay is concave. For larger  $K_q$  or states below the line (b), the decay is convex, cf. Fig. 6.5 on page 93 and Fig. 6.6 on page 95.

The logarithmic laws are reflected in a subdiffusive power law for the mean-squared displacement (MSD) and the results in a double-logarithmic representation for the MSD are analogous to the ones in a semi-logarithmic representation for the correlation functions, cf. Fig. 6.7 on page 96 and Fig. 6.8 on page 97. The relaxation of the MSD is convex above (a) and concave below (b) a specified line.

The dynamics at a crossing of glass-transition lines can be understood by the interplay of different singularities and their asymptotic description. Chapter 7 revealed crossover scenarios that are consistent with the results from experiment [42], cf. Fig. 7.7, and computer simulation [33], cf. Fig. 7.2.

The logarithm in the correlation functions is expected to be accessible to molecular dynamics simulation, whereas the power laws in the MSD might also be in reach for experiments in colloidal dispersions. Two recent computer simulation studies were analyzed in Ch. 8. The first [33] could be used to estimate the location of the higher-order singularities in Fig. 8.1 on page 123. The dynamics from the second study [44] is compatible with the logarithmic decay laws of MCT, cf. Fig. 6.5 on page 93 with Fig. 8.2 on page 125.



*Make everything as simple as possible,  
but not simpler.*

ALBERT EINSTEIN

## Comments on the asymptotic expansion

Some formulae needed for the asymptotic expansions in Ch. 5 shall be compiled in this appendix. Also more involved expressions are given here for reference which would unnecessarily obscure the presentation above.

### 1. Laplace transform of logarithms

The modification of the Laplace transform, introduced in Eq. (5.1b), shall be used to invertibly map functions  $F(t)$  of time to functions of the complex frequency  $z$ . The functions are defined for  $t > 0$  and  $\text{Im } z > 0$ , respectively. Euler's second integral for the gamma function  $\Gamma(y)$  implies  $\mathcal{S}[t^x](z) = (i/z)^x \Gamma(1+x)$  if  $x > -1$ . Differentiating this identity  $n$  times for  $x = 0, n = 0, 1, 2, \dots$ , one arrives at the formula:

$$(A.1) \quad \mathcal{S}[\ln^n(t)](z) = \sum_k \binom{n}{k} \Gamma_k \ln^{n-k}(i/z).$$

Here  $\binom{n}{k} = n!/[k!(n-k)!]$  and  $\Gamma_k = d^k \Gamma(x=1)/dx^k$ . One gets in particular  $\Gamma_0 = 1$  and  $\Gamma_1 = -\gamma$ , where  $\gamma$  is Euler's constant. If  $\psi(y)$  denotes the digamma function, one can write  $\Gamma'(y) = \Gamma(y)\psi(y)$ . Iterating this formula, one can express  $\Gamma_k$  in terms of the first  $(k-1)$  derivatives of  $\psi(y)$  for  $y = 1$ . The latter are given by the values of the zeta function  $\zeta(k)$  [87]; for example,  $\Gamma_2 - \Gamma_1^2 = \zeta(2) = \pi^2/6$ . Implications of Eq. (A.1) read with  $n \geq 1, n_1 \geq 1, n_2 \geq 1$ :

$$(A.2) \quad \begin{aligned} & \mathcal{S}[\ln^n(t)](z) - \mathcal{S}[\ln(t)]^n(z) = \\ & \frac{\pi^2}{12} n(n-1) \ln^{n-2}\left(\frac{i}{z}\right) + \sum_{k=3}^n \binom{n}{k} [\Gamma_k - \Gamma_1^k] \ln^{n-k}\left(\frac{i}{z}\right), \\ & \mathcal{S}[\ln^{n_1+n_2}(t)](z) - \mathcal{S}[\ln^{n_1}(t)](z) \mathcal{S}[\ln^{n_2}(t)](z) = \\ & (\pi^2/6) n_1 n_2 \ln^{n_1+n_2-2}(i/z) \\ & + \sum_{k=3}^{n_1+n_2} \left[ \binom{n_1+n_2}{k} \Gamma_k - \sum_l \binom{n_1}{k-l} \binom{n_2}{l} \Gamma_{k-l} \Gamma_l \right] \\ & \times \ln^{n_1+n_2-k}(i/z). \end{aligned} \tag{A.3}$$

These formulas are needed for the evaluation of the function  $f^{(2)}(z)$  in Eq. (5.25).

Specializing Eq. (A.3) to  $n_1 = n$  and  $n_2 = 1$  and using the definition of the linear operator  $\mathcal{T}$  from Eq. (5.24), one gets

$$(A.4) \quad \begin{aligned} \mathcal{T}[\ln^n(t)](z) &= (\pi^2/6) [n \ln^{n-1}(i/z) \\ &+ \sum_{k=2}^n (n-k+1) \Gamma_{n,k} \ln^{(n-k)}(i/z)], \end{aligned}$$

where the coefficients are

$$(A.5) \quad \Gamma_{n,k} = \binom{n}{k} [\Gamma_{k+1} - \Gamma_k \Gamma_1] / [(\pi^2/6)(n-k+1)] .$$

Let us construct polynomials  $p_n(x)$  of degree  $n = 1, 2, \dots$  obeying Eqs. (5.26). Specializing Eq. (A.4) to  $n = 1$  shows that one can choose  $p_1(x) = x$ . Assuming the polynomials for degree  $l < n$  to be known, Eq. (A.4) provides the formula for the degree  $n$

$$(A.6) \quad p_n(x) = x^n - \sum_{k=2}^n \Gamma_{n,k} p_{n+1-k}(x) .$$

Thus, the sequence of  $p_n(x)$  can be constructed recursively in terms of the coefficients  $\Gamma_{n,k}$ . To derive Eqs. (5.29b-d), one needs:

$$(A.7a) \quad p_2(x) = 2.6160x + x^2 ,$$

$$(A.7b) \quad p_3(x) = -2.1482x + 3.9239x^2 + x^3 ,$$

$$(A.7c) \quad p_4(x) = -12.813x - 4.2964x^2 + 5.2319x^3 + x^4 .$$

## 2. Parameters $C_j$ for Eq. (5.31)

The parameters  $C_j$  from Eq. (5.31) are a bit more involved than the  $B_j$  but shall be given explicitly here for completeness for the one-component case.

$$(A.8a) \quad C_1 = [0.0671 \mu_3^2 + 0.205 \mu_3 - 0.115 \mu_4 \\ + 0.0433 \mu_3 \varepsilon_2(\mathbf{V})/\varepsilon_1(\mathbf{V})] \sqrt{-\varepsilon_1(\mathbf{V})^3} \\ + [-0.217 \varepsilon_1(\mathbf{V}) + 0.308 \varepsilon_2(\mathbf{V}) - 0.0588 \varepsilon_3(\mathbf{V}) \\ + 0.0852 \varepsilon_2(\mathbf{V})^2/\varepsilon_1(\mathbf{V})] \sqrt{-\varepsilon_1(\mathbf{V})} ,$$

$$(A.8b) \quad C_2 = [-0.00600 \mu_3^2 - 0.237 \mu_3 + 0.102 \mu_4 \\ - 0.0373 \mu_3 \varepsilon_2(\mathbf{V})/\varepsilon_1(\mathbf{V})] \sqrt{-\varepsilon_1(\mathbf{V})^3} \\ + [0.303 \varepsilon_1(\mathbf{V}) - 0.520 \varepsilon_2(\mathbf{V}) + 0.173 \varepsilon_3(\mathbf{V}) \\ + 0.0433 \varepsilon_2(\mathbf{V})^2/\varepsilon_1(\mathbf{V})] \sqrt{-\varepsilon_1(\mathbf{V})} ,$$

$$(A.8c) \quad C_3 = (0.0221 \mu_3^2 + 0.296 \mu_3 - 0.0714 \mu_4) \sqrt{-\varepsilon_1(\mathbf{V})^3} \\ + [0.237 \varepsilon_1(\mathbf{V}) - 0.237 \varepsilon_2(\mathbf{V}) + 0.0790 \varepsilon_3(\mathbf{V})] \sqrt{-\varepsilon_1(\mathbf{V})} ,$$

$$(A.8d) \quad C_4 = (-0.0387 \mu_3^2 - 0.446 \mu_3 + 0.105 \mu_4) \sqrt{-\varepsilon_1(\mathbf{V})^3} \\ + 0.0872 \mu_3 \sqrt{-\varepsilon_1(\mathbf{V})} \varepsilon_2(\mathbf{V}) ,$$

$$(A.8e) \quad C_5 = (0.0642 \mu_3^2 - 0.136 \mu_3 + 0.0288 \mu_4) \sqrt{-\varepsilon_1(\mathbf{V})^3} \\ + 0.0167 \mu_3 \sqrt{-\varepsilon_1(\mathbf{V})} \varepsilon_2(\mathbf{V}) ,$$

$$(A.8f) \quad C_6 = (0.02340 \mu_3^2 - 0.00400 \mu_3) \sqrt{-\varepsilon_1(\mathbf{V})^3} \\ + 0.00133 \mu_3 \sqrt{-\varepsilon_1(\mathbf{V})} \varepsilon_2(\mathbf{V}) ,$$

$$(A.8g) \quad C_7 = 0.00156 \mu_3^2 \sqrt{-\varepsilon_1(\mathbf{V})^3} .$$

## 3. Critical decay for the $F_{13}$ -model

The expansion for the critical decay at an  $A_3$ -singularity yields increasingly more involved expressions for the coefficients. For  $g_6(x) = \sum_{i=0}^4 c_{6,i} \ln^i x/x^6$  the

coefficients read

$$(A.9a) \quad c_{6,0} = 19\pi^6/(8\mu_3) - 57384\zeta(3)^2/(5\mu_3) + 3322944\zeta(3)^4/(\pi^6\mu_3) \\ + 56736\zeta(3)\zeta(5)/(\pi^2\mu_3) \\ + 32\pi^6/(9\mu_3^3) + 62\pi^6/(9\mu_3^2) - 56\mu_4\pi^6/(27\mu_3^4) \\ - 314\mu_4\pi^6/(135\mu_3^3) + 8\mu_4^2\pi^6/(27\mu_3^5) - 16\pi^6\kappa_4/(27\mu_3^3) \\ + 8\pi^6\mu_5/(81\mu_3^4) - 4928\zeta(3)^2/\mu_3^2 \\ + 1760\mu_4\zeta(3)^2/\mu_3^3,$$

$$(A.9b) \quad c_{6,1} = 10818\zeta(3)^2/\mu_3 - 4743360\zeta(3)^4/(\pi^6\mu_3) \\ - 47520\zeta(3)\zeta(5)/(\pi^2\mu_3) \\ + 4128\zeta(3)^2/\mu_3^2 - 1536\mu_4\zeta(3)^2/\mu_3^3,$$

$$(A.9c) \quad c_{6,2} = 3405888\zeta(3)^4/(\pi^6\mu_3) - 3780\zeta(3)^2\mu_3 \\ - 4320\zeta(3)^2/\mu_3^2 + 1440\mu_4\zeta(3)^2/\mu_3^3,$$

$$(A.9d) \quad c_{6,3} = -1096416\zeta(3)^4/(\pi^6\mu_3),$$

$$(A.9e) \quad c_{6,4} = 349920\zeta(3)^4/(\pi^6\mu_3).$$

The coefficients for  $g_7(x) = \sum_{i=0}^5 c_{7,i} \ln^i x/x^7$  are

$$(A.10a) \quad c_{7,0} = -194879\pi^4\zeta(3)/(280\mu_3) - 7647048\zeta(3)^2\zeta(5)/(\pi^4\mu_3) \\ - 18720\zeta(7)/\mu_3 - 464\pi^4\zeta(3)/(3\mu_3^3) \\ - 13664\pi^4\zeta(3)/(15\mu_3^2) + 320\mu_4\pi^4\zeta(3)/(3\mu_3^4) \\ + 1004\mu_4\pi^4\zeta(3)/(3\mu_3^3) - 160\mu_4^2\pi^4\zeta(3)/(9\mu_3^5) \\ - 32\mu_5\pi^4\zeta(3)/(9\mu_3^4) + 128\pi^4\kappa_4\zeta(3)/(9\mu_3^3) \\ + 6419304\zeta(3)^3/(5\pi^2\mu_3) + 383616\zeta(3)^3/(\pi^2\mu_3^2) \\ - 142848\mu_4\zeta(3)^3/(\pi^2\mu_3^3) - 281802240\zeta(3)^5/(\pi^8\mu_3) \\ + 6480\pi^2\zeta(5)/\mu_3 + 4152\pi^2\zeta(5)/\mu_3^2 - 1520\mu_4\pi^2\zeta(5)/\mu_3^3,$$

$$(A.10b) \quad c_{7,1} = 513\pi^4\zeta(3)/(2\mu_3) - 7171092\zeta(3)^3/(5\pi^2\mu_3) \\ + 6982848\zeta(3)^2\zeta(5)/(\pi^4\mu_3) + 444258432\zeta(3)^5/(\pi^8\mu_3) \\ + 384\pi^4\zeta(3)/\mu_3^3 + 744\pi^4\zeta(3)/\mu_3^2 - 224\mu_4\pi^4\zeta(3)/\mu_3^4 \\ - 1256\mu_4\pi^4\zeta(3)/(5\mu_3^3) + 32\mu_4^2\pi^4\zeta(3)/\mu_3^5 \\ - 64\pi^4\kappa_4\zeta(3)/\mu_3^3 + 32\pi^4\mu_5\zeta(3)/(3\mu_3^4) \\ - 606528\zeta(3)^3/(\pi^2\mu_3^2) + 217728\mu_4\zeta(3)^3/(\pi^2\mu_3^3),$$

$$(A.10c) \quad c_{7,2} = 652212\zeta(3)^3/(\pi^2\mu_3) - 317447424\zeta(3)^5/(\pi^8\mu_3) \\ - 2566080\zeta(3)^2\zeta(5)/(\pi^4\mu_3) + 300672\zeta(3)^3/(\pi^2\mu_3^2) \\ - 108864\mu_4\zeta(3)^3/(\pi^2\mu_3^3),$$

$$(A.10d) \quad c_{7,3} = -136080\zeta(3)^3/(\pi^2\mu_3) + 142347456\zeta(3)^5/(\pi^8\mu_3) \\ - 155520\zeta(3)^3/(\pi^2\mu_3^2) + 51840\mu_4\zeta(3)^3/(\pi^2\mu_3^3),$$

$$(A.10e) \quad c_{7,4} = -35901792\zeta(3)^5/(\pi^8\mu_3),$$

$$(A.10f) \quad c_{7,5} = 7558272\zeta(3)^5/(\pi^8\mu_3).$$

If we introduce the model parameters  $\mu_3 = 1/3$ ,  $\mu_4 = \mu_5 = 1$ , and  $\kappa = \kappa_4 = 1$ , the critical correlation function for the  $F_{13}$  model in Eq. (5.108) up to errors of order

$\mathcal{O}(x^{-8})$  can be given a concise form,

$$\begin{aligned}
 (A.11) \quad g(x) &= \frac{6.58}{x^2} + \frac{28.85 \ln x}{x^3} + \frac{2.31 - 63.25 \ln x + 94.87 \ln^2 x}{x^4} \\
 &+ \frac{-219.28 + 158.89 \ln x - 485.29 \ln^2 x + 277.31 \ln^3 x}{x^5} \\
 &+ \frac{-1212.5 - 2751.9 \ln x + 1934.7 \ln^2 x - 2381.1 \ln^3 x + 759.9 \ln^4 x}{x^6} \\
 &+ \frac{5538.2 - 9915.8 \ln x - 22340.3 \ln^2 x + 13702.9 \ln^3 x}{x^7} \\
 &+ \frac{-9496.0 \ln^4 x + 1999.2 \ln^5 x}{x^7}, \quad x = \ln(t/t_0).
 \end{aligned}$$

## Numerical Algorithms

For the numerical solution of the equations of motion (2.7) refined algorithms are applied that have been developed in the recent years. The memory kernel  $\mathcal{F}_q[\mathbf{V}, \phi]$  is calculated on a grid of  $M$  values for the wave vector  $q$  as used for the HSS [7]. Only the cutoff in  $q$  needs to be varied and cutoff values equivalent to  $M = 3000$  were used to check the precision of the calculations. Routinely  $M = 300$  is used for the calculations around  $\delta \approx \delta^*$  and up to  $M = 750$  for  $\delta = 0.02$ . Refining the grid in  $q$  did not alter the results noteworthy. To extend the calculation to large logarithmic times, the grid on the time axis is doubled in step size after 512 steps in time [102]. The convolution integral in Eqs. 2.7a and 2.7b is treated as introduced in Ref [103]. The details for the implementation are documented, e.g., in [41].

We shall only discuss only two aspects related to the determination of glass-glass-transition singularities and higher-order glass-transition singularities.

### 1. Determination of glass-glass transitions

For the determination of liquid-glass-transition points a robust method of nested intervals can be applied adopting the discontinuity in the glass-form factors  $f_q$  at the  $A_2$ -singularity. An initial interval  $I^{(0)} = [\mathbf{V}_1^{(0)}, \mathbf{V}_2^{(0)}]$  is chosen sufficiently large to include the transition point  $\mathbf{V}^c$ . Let's assume  $f_q[\mathbf{V}_1^{(0)}] = 0$  and  $f_q[\mathbf{V}_2^{(0)}] > 0$ , and that only a single control parameter, say  $v$ , is changed. A new point at  $v'$  is evaluated with  $v_1^{(0)} < v' < v_2^{(0)}$ . If  $f_q[v'] = 0$  the subdivision of the interval is given by  $v_1^{(1)} = v'$ , if  $f_q[v'] > 0$  we set  $v_2^{(1)} = v'$ . This procedure works also at an  $A_4$ -singularity which is also a liquid-glass-transition point. For a glass-glass-transition point the discontinuity in the glass-form factors takes place between finite values and the jump in the  $f_q$  becomes smaller when approaching the  $A_3$ -singularity and observing a discontinuity in the glass-form factors becomes more and more difficult. Therefore a different criterion is used. At the glass-transition singularities the critical eigenvalue  $E^c$  has a maximum that is unity, cf. Eq (5.11). The evolution of  $E$  in the vicinity of an  $A_2$ -singularity is given by a square-root,  $1 - E \propto \sqrt{v - v^c}$ , for the strong-coupling side. Monitoring the eigenvalues can be done with high precision and allows in addition for an extrapolation in control parameters. At an  $A_3$ -singularity the eigenvalue is approaching unity from either side in a generic path in control-parameter space through the singularity. The variation is given by  $1 - E \propto (v - v^o)^{2/3}$  which follows, as the square-root above, from considerations similar to the ones for the parameters  $\mu_i$ .

It is clearly seen in Fig. B.1 that at a glass-glass transition only the eigenvalues for the strong coupling side,  $\varphi > \varphi^c$  go to unity and follow the square-root law ( $\bullet$ ). At a liquid-glass transition the eigenvalues for  $\varphi < \varphi^c$  would be zero, however, in the glass due to continuity they are finite, smaller than unity and jump to a

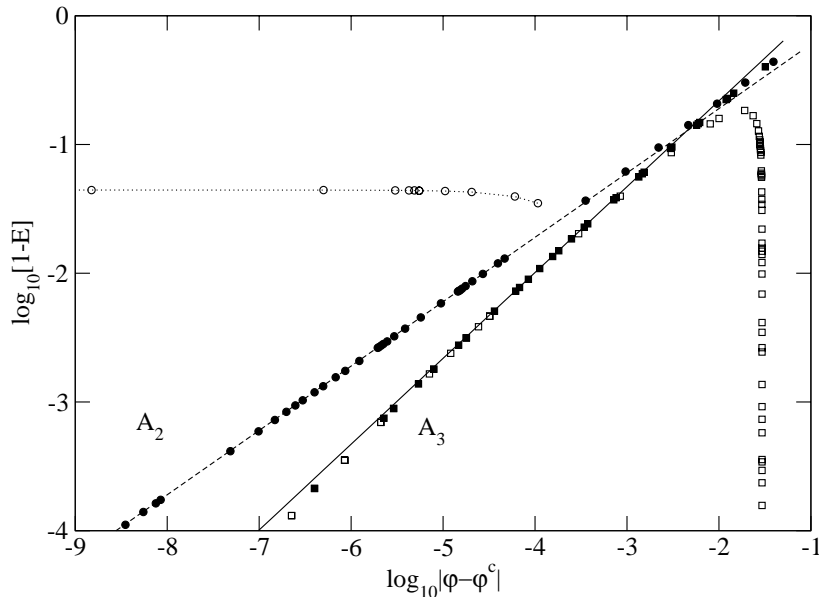


FIGURE B.1. Eigenvalues  $E$  upon approaching a glass-glass transition for  $\delta = 0.02$ ,  $\Gamma = 7.75$ , and  $\varphi^c = 0.540965015$ . The deviation from unity,  $1 - E$ , is shown for  $\varphi < \varphi^c$  (open circles) and for  $\varphi > \varphi^c$  (filled circles) together with the square-root  $\sqrt{|\varphi - \varphi^c|}$  (dashed). The corresponding eigenvalues for the  $A_3$ -singularity at  $\delta = 0.02$ ,  $\Gamma^\circ = 6.646$ , and  $\varphi^\circ = 0.5680321$  are denoted by open squares for  $\varphi < \varphi^\circ$  and by the filled squares for  $\varphi > \varphi^\circ$ . The full line shows the power law  $|\varphi - \varphi^\circ|^{2/3}$ .

critical value only at the glass-glass-transition points. For the  $A_3$ -singularity this discontinuity vanishes and the eigenvalues show the variation with the power  $2/3$  on both sides of  $\varphi^\circ$ . The deviation from that law for larger distances  $\varphi < \varphi^\circ$  is due to the increase of the eigenvalues at the liquid-glass transition at  $\varphi = 0.540693$ . Deviations close to the  $A_3$ -singularity indicate the precision of five digits in the control parameter  $\varphi$  for the determination of  $\mathbf{V}^\circ$ .

The deviation of  $E^c$  from unity is a measure for the accuracy of the critical points. In this work a value of  $1 - E^c \leq 10^{-3}$  was assured for all the values shown. For the higher-order singularities and the determination of the parameters for the asymptotic expansions the higher accuracy of  $1 - E^c \leq 10^{-4}$  was required. For the discussion of the critical decay in Fig. 6.12 values for the  $A_4$ -singularity in Eq. (4.1) were calculated until  $1 - E^c \leq 3 \cdot 10^{-6}$  was accomplished.

## 2. Characteristic parameters for higher-order singularities

To avoid lengthy discussion about details of the implementation that are easily found in textbooks, we show checks for the final results instead. We therefore replot the parameters  $\mu_2$  from Fig. 4.4 and fit the asymptotic laws as in Fig. 5.14 (A) and (B) in Fig. B.2. The analog of Fig. 5.14 (C) for the characteristic parameters for the higher-order singularities is shown already in Fig. 6.1.



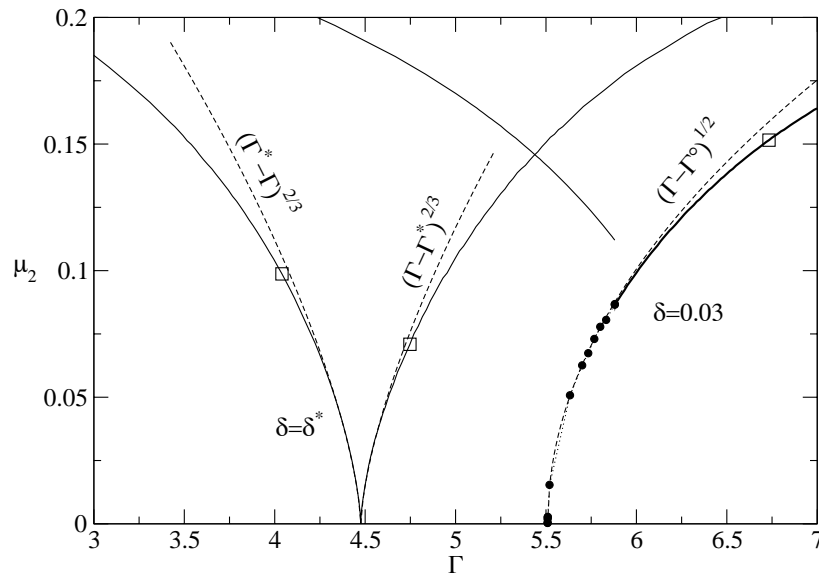


FIGURE B.2. Parameter  $\mu_2$  in the SWS for  $\delta = \delta^*$  and 0.03. Liquid-glass transitions are shown as full lines, glass-glass transitions as filled circles. The dashed lines show the laws  $\mu_2 \propto (\Gamma - \Gamma^*)^{2/3}$  for the  $A_4$ -singularity and  $\mu_2 \propto (\Gamma - \Gamma^o)^{1/2}$  for the  $A_3$ -singularity. The squares indicate a deviation between result and approximation of 5%.

Figure B.2 shows that close to higher-order glass-transition singularities the exponent parameters  $\lambda = 1 - \mu_2$  calculated numerically obey the asymptotic approximation with similar accuracy as for the schematic models. For the  $A_3$ -singularity the description works down to  $\lambda = 0.85$  and includes both glass-glass transitions and liquid-gel transitions. The  $A_4$ -singularity is described by the asymptotic law for  $\lambda \geq 0.93$  on the line of gel transitions and for  $\lambda \geq 0.9$  on the line of glass transitions. The exponent parameters for different potentials in the inset Fig. 4.8 fall on top of each other for the region where the asymptotic approximation is applicable and therefore underline the universality of the  $A_4$ -singularity.



## Bibliography

- [1] J.-P. Boon and S. Yip, *Molecular Hydrodynamics* (McGraw-Hill, New York, 1980).
- [2] U. Bengtzelius, W. Götze, and A. Sjölander, *J. Phys. C* **17**, 5915 (1984).
- [3] W. Götze, in *Liquids, Freezing and Glass Transition*, edited by J. P. Hansen, D. Levesque, and J. Zinn-Justin (North Holland, Amsterdam, 1991), vol. Session LI (1989) of *Les Houches Summer Schools of Theoretical Physics*, pp. 287–503.
- [4] W. Götze and L. Sjögren, *Rep. Prog. Phys.* **55**, 241 (1992).
- [5] V. I. Arnol'd, *Catastrophe Theory* (Springer, Berlin, 1992), 3rd ed.
- [6] W. Götze, *J. Phys.: Condens. Matter* **11**, A1 (1999).
- [7] T. Franosch, M. Fuchs, W. Götze, M. R. Mayr, and A. P. Singh, *Phys. Rev. E* **55**, 7153 (1997).
- [8] P. N. Pusey and W. van Meegen, *Nature* **320**, 340 (1986).
- [9] P. N. Pusey and W. van Meegen, *Phys. Rev. Lett.* **59**, 2083 (1987).
- [10] W. van Meegen, S. M. Underwood, and P. N. Pusey, *Phys. Rev. Lett.* **67**, 1586 (1991).
- [11] W. van Meegen and S. M. Underwood, *Phys. Rev. Lett.* **70**, 2766 (1993).
- [12] W. van Meegen and S. M. Underwood, *Phys. Rev. E* **49**, 4206 (1994).
- [13] W. van Meegen, *Transp. Theory Stat. Phys.* **24**, 1017 (1995).
- [14] L. Fabbian, W. Götze, F. Sciortino, P. Tartaglia, and F. Thiery, *Phys. Rev. E* **59**, R1347 (1999), **60**, 2430(E).
- [15] J. Bergenholtz and M. Fuchs, *Phys. Rev. E* **59**, 5706 (1999).
- [16] K. Dawson, G. Foffi, M. Fuchs, W. Götze, F. Sciortino, M. Sperl, P. Tartaglia, T. Voigtmann, and E. Zaccarelli, *Phys. Rev. E* **63**, 011401 (2001).
- [17] H. Verduin and J. K. G. Dhont, *J. Colloid Interface Sci.* **172**, 425 (1995).
- [18] P. N. Segrè, V. Prasad, A. B. Schofield, and D. A. Weitz, *Phys. Rev. Lett.* **86**, 6042 (2001).
- [19] S. Asakura and F. Oosawa, *J. Chem. Phys.* **22**, 1255 (1954).
- [20] S. Asakura and F. Oosawa, *J. Polym. Sci.* **33**, 183 (1958).
- [21] W. B. Russel, D. A. Saville, and W. R. Schowalter, *Colloidal Dispersions* (Cambridge University Press, New York, 1989).
- [22] A. P. Gast, C. K. Hall, and W. B. Russel, *J. Colloid Interface Sci.* **96**, 251 (1983).
- [23] P. Bolhuis, M. Hagen, and D. Frenkel, *Phys. Rev. E* **50**, 4880 (1994).
- [24] P. Bolhuis and D. Frenkel, *Phys. Rev. Lett.* **72**, 2211 (1994).
- [25] C. F. Tejero, A. Daanoun, H. N. W. Lekkerkerker, and M. Baus, *Phys. Rev. Lett.* **73**, 752 (1994).
- [26] C. F. Tejero, A. Daanoun, H. N. W. Lekkerkerker, and M. Baus, *Phys. Rev. E* **51**, 558 (1995).
- [27] C. Rascón, L. Mederos, and G. Navascués, *J. Chem. Phys.* **103**, 9795 (1995).
- [28] C. N. Likos, Z. T. Watzlawek, and H. Löwen, *J. Phys.: Condens. Matter* **6**, 10965 (1994).
- [29] T. Eckert and E. Bartsch, *Phys. Rev. Lett.* **89**, 125701 (2002).
- [30] K. N. Pham, A. M. Puertas, J. Bergenholtz, S. U. Egelhaaf, A. Moussaïd, P. N. Pusey, A. B. Schofield, M. E. Cates, M. Fuchs, and W. C. K. Poon, *Science* **296**, 104 (2002).

- [31] G. Foffi, K. A. Dawson, S. V. Buldyrev, F. Sciortino, E. Zaccarelli, and P. Tartaglia, *Phys. Rev. E* **65**, 050802 (2002).
- [32] A. M. Puertas, M. Fuchs, and M. E. Cates, *Phys. Rev. E* **67**, 031406 (2003).
- [33] E. Zaccarelli, G. Foffi, K. A. Dawson, S. V. Buldyrev, F. Sciortino, and P. Tartaglia, *Phys. Rev. E* **66**, 041402 (2002).
- [34] W. Götze and R. Haussmann, *Z. Phys. B* **72**, 403 (1988).
- [35] W. Götze and L. Sjögren, *J. Phys.: Condens. Matter* **1**, 4203 (1989).
- [36] L. Sjögren, *J. Phys.: Condens. Matter* **3**, 5023 (1991).
- [37] H. Eliasson, B.-E. Mellander, and L. Sjögren, *J. Non-Cryst. Solids* **235–237**, 101 (1998).
- [38] S. Flach, W. Götze, and L. Sjögren, *Z. Phys. B* **87**, 29 (1992).
- [39] I. C. Halalay, *J. Phys.: Condens. Matter* **8**, 6157 (1996).
- [40] H. Eliasson, *Phys. Rev. E* **64**, 011802 (2001).
- [41] M. Sperl, Diploma thesis, TU München (2000).
- [42] F. Mallamace, P. Gambadauro, N. Micali, P. Tartaglia, C. Liao, and S.-H. Chen, *Phys. Rev. Lett.* **84**, 5431 (2000).
- [43] W.-R. Chen, S.-H. Chen, and F. Mallamace, *Phys. Rev. E* **66**, 021403 (2002).
- [44] A. M. Puertas, M. Fuchs, and M. E. Cates, *Phys. Rev. Lett.* **88**, 098301 (2002).
- [45] J.-P. Hansen and I. R. McDonald, *Theory of Simple Liquids* (Academic Press, London, 1986), 2nd ed.
- [46] D. Forster, *Hydrodynamic Fluctuations, Broken Symmetry, and Correlation Functions* (Benjamin, Reading, MA, 1975).
- [47] K. Kawasaki, *Phys. Rev.* **150**, 291 (1966).
- [48] W. Götze, *Solid State Commun.* **27**, 1393 (1978).
- [49] W. Götze, in *Amorphous and Liquid Materials*, edited by E. Lüscher, G. Fritsch, and G. Jacucci (Nijhoff Publishers, Dordrecht, 1987), vol. 118 of *NATO ASI Series E*, pp. 34–81.
- [50] G. Szamel and H. Löwen, *Phys. Rev. A* **44**, 8215 (1991).
- [51] M. Fuchs, Ph.D. thesis, TU München (1993).
- [52] W. Götze and M. Lücke, *Phys. Rev. B* **13**, 3825 (1976).
- [53] L. Sjögren, *Phys. Rev. A* **22**, 2883 (1980).
- [54] A. R. Denton and N. W. Ashcroft, *Phys. Rev. A* **39**, 426 (1989).
- [55] J.-L. Barrat, W. Götze, and A. Latz, *J. Phys.: Condens. Matter* **1**, 7163 (1989).
- [56] F. Sciortino and W. Kob, *Phys. Rev. Lett.* **86**, 648 (2001).
- [57] W. Götze and L. Sjögren, *J. Math. Analysis and Appl.* **195**, 230 (1995).
- [58] M. S. Wertheim, *Phys. Rev. Lett.* **10**, 321 (1963).
- [59] E. Thiele, *J. Chem. Phys.* **39**, 474 (1963).
- [60] M. Fuchs, W. Götze, and M. R. Mayr, *Phys. Rev. E* **58**, 3384 (1998).
- [61] C. Caccamo, *Phys. Rep.* **274**, 1 (1996).
- [62] L. S. Ornstein and F. Zernike, *Proc. Acad. Sci. (Amsterdam)* **17**, 793 (1914).
- [63] J. K. Percus and G. J. Yevick, *Phys. Rev.* **110**, 1 (1958).
- [64] J. L. Lebowitz and J. K. Percus, *Phys. Rev.* **144**, 251 (1966).
- [65] W. R. Smith, D. Henderson, and Y. Tago, *J. Chem. Phys.* **67**, 5308 (1977).
- [66] A. Lang, G. Kahl, C. N. Likos, H. Löwen, and M. Watzlawek, *J. Phys.: Condens. Matter* **11**, 10143 (1999).
- [67] P. T. Cummings and E. R. Smith, *Chem. Phys.* **42**, 241 (1979).
- [68] R. J. Baxter, *Aust. J. Phys.* **21**, 563 (1968).
- [69] K. Hiroike, *Prog. Theor. Phys.* **62**, 91 (1979).
- [70] R. J. Baxter, *J. Chem. Phys.* **49**, 2770 (1968).
- [71] L. Vega, E. de Miguel, L. F., G. Jackson, and I. A. McLure, *J. Chem. Phys.* **96**, 2296 (1992).
- [72] E. O. Tuck, *Math. Comp.* **21**, 239 (1967).

- [73] M. J. Lighthill, *Introduction to Fourier Analysis and Generalized Functions* (Cambridge University Press, Cambridge, 1962).
- [74] G. A. Vliegthart and H. N. W. Lekkerkerker, *J. Chem. Phys.* **112**, 5364 (2000).
- [75] K. A. Dawson, G. Foffi, G. D. McCullagh, F. Sciortino, P. Tartaglia, and E. Zaccarelli, *J. Phys.: Condens. Matter* **14**, 2223 (2002).
- [76] G. Foffi, G. D. McCullagh, A. Lawlor, E. Zaccarelli, K. A. Dawson, F. Sciortino, P. Tartaglia, D. Pini, and G. Stell, *Phys. Rev. E* **65**, 031407 (2002).
- [77] F. A. Lindemann, *Phys. Z.* **11**, 609 (1910).
- [78] M. Fuchs, I. Hofacker, and A. Latz, *Phys. Rev. A* **45**, 898 (1992).
- [79] J. Bergenholtz, M. Fuchs, and T. Voigtmann, *J. Phys.: Condens. Matter* **12**, 6575 (2000).
- [80] W. Götze and M. Sperl, *J. Phys.: Condens. Matter* **15**, S869 (2003).
- [81] D. Henderson, W. G. Madden, and D. D. Fitts, *J. Chem. Phys.* **64**, 5026 (1976).
- [82] F. R. Gantmacher, *The Theory of Matrices*, vol. II (Chelsea Publishing, New York, 1974).
- [83] W. Götze and M. Sperl, *Phys. Rev. E* **66**, 011405 (2002).
- [84] W. Götze, *Z. Phys. B* **60**, 195 (1985).
- [85] S.-N. Chow and J. K. Hale, *Methods of Bifurcation Theory* (Springer, Berlin, 1982).
- [86] W. Feller, *An Introduction to Probability Theory and Its Applications*, vol. II (Wiley & Sons, New York, 1971), 2nd ed.
- [87] M. Abramowitz and I. A. Stegun, *Handbook of Mathematical Functions* (Dover, New York, 1970), 7th ed.
- [88] W. Götze, *J. Phys.: Condens. Matter* **2**, 8485 (1990).
- [89] W. Götze and L. Sjögren, *J. Phys.: Condens. Matter* **1**, 4183 (1989).
- [90] W. Götze and L. Sjögren, *J. Phys. C* **17**, 5759 (1984).
- [91] J. Bosse and U. Krieger, *J. Phys. C* **19**, L609 (1987).
- [92] W. Kob, in *Slow Relaxations and Nonequilibrium Dynamics in Condensed Matter*, edited by J.-L. Barrat, M. Feigelman, and J. Kurchan (Springer, Berlin, 2003), vol. Session LXXVII (2002) of *Les Houches Summer Schools of Theoretical Physics*.
- [93] E. Zaccarelli, G. Foffi, P. D. Gregorio, F. Sciortino, P. Tartaglia, and K. A. Dawson, *J. Phys.: Condens. Matter* **14**, 2413 (2002).
- [94] W. C. K. Poon, *J. Phys.: Condens. Matter* **14**, R859 (2002).
- [95] W. K. Kegel and A. van Blaaderen, *Science* **287**, 290 (2000).
- [96] E. R. Weeks, J. C. Crocker, A. C. Levitt, A. Schofield, and D. A. Weitz, *Science* **287**, 627 (2000).
- [97] E. R. Weeks and D. A. Weitz, *Phys. Rev. Lett.* **89**, 095704 (2002).
- [98] E. Bartsch, M. Antonietti, W. Schupp, and H. Sillescu, *J. Chem. Phys.* **97**, 3950 (1992).
- [99] E. Bartsch, T. Eckert, C. Pies, and H. Sillescu, *J. Non-Cryst. Solids* **307–310**, 802 (2002).
- [100] M. Nauroth and W. Kob, *Phys. Rev. E* **55**, 657 (1997).
- [101] J. Bergenholtz, W. C. K. Poon, and M. Fuchs (2003), to be published.
- [102] W. Götze, *J. Stat. Phys.* **83**, 1183 (1996).
- [103] M. Fuchs, W. Götze, I. Hofacker, and A. Latz, *J. Phys.: Condens. Matter* **3**, 5047 (1991).

## Curriculum Vitae

27. 1. 1974 born in Dingolfing, Bavaria  
1984–1993 Gymnasium Landau a.d. Isar  
1993 Abitur (High School Diploma), Landau  
1993–1997 studies in physics, TU München  
1997 final examination, TU München  
1998 studies at the University of Illinois at Urbana-Champaign  
and at the Santa Fe Institute, New Mexico  
1999–2000 Diploma work at the Institute for theoretical physics,  
Prof. Dr. W. Götze  
2000 Diploma, TU München  
2000–2003 PhD work at the Institute for theoretical physics,  
Prof. Dr. W. Götze  
April 2003 completion of PhD thesis

## Publications related to the thesis

K. Dawson, G. Foffi, M. Fuchs, W. Götze, F. Sciortino, M. Sperl, P. Tartaglia, Th. Voigtmann, and E. Zaccarelli, *Higher order glass-transition singularities in colloidal systems with attractive interactions*. Phys. Rev. **E** 63, 011401 (2001).

W. Götze and M. Sperl, *Logarithmic Relaxation in Glass-Forming Systems*. Phys. Rev. E **66**, 011405 (2002).

W. Götze and M. Sperl, *Higher-order glass-transition singularities in systems with short-ranged attractive potentials*. J. Phys.: Condens. Matter **15**(11), S869-S879 (2003).

## Acknowledgments

I thank first and foremost Prof. Dr. W. Götze for the opportunity to work on this subject that turned out to be both challenging and fruitful.

This work has benefited a lot from collaboration and discussion with my colleagues. I thank Dr. Song-Ho Chong, Dr. Thomas Franosch for a lot of guidance, Dr. Matthias Fuchs especially for introducing me to integral equation theory, and Dr. Thomas Voigtmann who shared among many other things a lot of his programming experience with me.

Frau Sprzagala deserves credit for countless things – thank you very much!

I also want to thank Gisela Wolf and Dr. Herbert Müller for smooth access to printed and electronic resources.

I thank Dr. Antonio Manuel Puertas for providing partially unpublished computer simulation data and I gratefully acknowledge assistance from Dr. Johan Bergenholtz while implementing the HCY structure factor.

The work was financially supported by the Deutsche Forschungsgemeinschaft under Grant No. Go154/13-1.

I thank my family for ongoing support and Brigitte for her enduring patience and great help.